

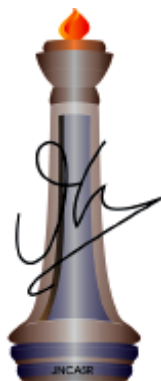
Investigations on Layered Materials for Adsorption, Dispersion and Gas Separation

A Thesis Submitted for the Degree of

Doctor of Philosophy

By

Amritroop Achari



Chemistry and Physics of Materials Unit

Jawaharlal Nehru Centre for Advanced Scientific Research

(A Deemed University)

Bangalore - 560064 (INDIA)

April 2016

*Investigations on Layered Materials for
Adsorption, Dispersion and Gas Separation*

A Thesis Submitted for the Degree of

Doctor of Philosophy

By

Amritroop Achari

UNDER THE SUPERVISION OF

Prof. M. Eswaramoorthy

Chemistry and Physics of Materials Unit

Jawaharlal Nehru Centre for Advanced Scientific Research

(A Deemed University)

Bangalore-560064 (INDIA)

April 2016

DECLARATION

I hereby declare that the thesis entitled “*Investigations on layered materials for adsorption, dispersion and gas separation.*” is an authentic record of research work carried out by me at the Chemistry and Physics of Materials Unit, Jawaharlal Nehru Centre for Advanced Scientific Research, Bangalore, India under the supervision of **Prof. M. Eswaramoorthy** and that it has not been submitted elsewhere for the award of any degree or diploma.

In keeping with the general practice in reporting scientific observations, due acknowledgment has been made whenever the work described is based on the findings of other investigators. Any omission that might have occurred due to oversight or error in judgment is regretted.

Amritroop Achari



**Jawaharlal Nehru Centre for
Advanced Scientific Research**

Prof. M. Eswaramoorthy
Chemistry and Physics of Materials Unit
Jawaharlal Nehru Centre for Advanced
Scientific Research (JNCASR)
Bangalore-560064,India
Phone : +91 80 2208 2870
Fax: + 91 80 22082766
E-mail: eswar@jncasr.ac.in

Date

April 6, 2016

CERTIFICATE

I hereby certify that the work described in this thesis titled “*Investigations on layered materials for adsorption, dispersion and gas separation.*” has been carried out by **Amritroop Achari** at the Chemistry and Physics of Materials Unit, Jawaharlal Nehru Centre for Advanced Scientific Research, Bangalore, India under my supervision and it has not been submitted elsewhere for the award of any degree or diploma.

M. Eswaramoorthy

(Research Supervisor)

ACKNOWLEDGEMENTS

*During the course of my Ph.D., I have been helped by a large number of people, to whom I will always be grateful. Firstly, I would like to offer my most sincere thanks to one person who has stayed with me from the beginning to the end of Ph.D., my research supervisor, **Prof. M. Eswaramoorthy**. I am thankful to him for introducing me to the field of materials science and for giving me the freedom to work on various problems. His ever-enthusiastic nature, constant encouragement and support has helped me in successful completion of this work.*

*I would like to express my gratitude to **Prof. C. N. R. Rao, FRS** for being a constant source of inspiration. I am also grateful to him for creating such a vibrant research atmosphere to carry out this work.*

I thank the past and present chairmen of CPMU for allowing me to use the various facilities of the centre.

I am thankful to Prof. A. Sundaresan, Prof. U. V. Waghmare, Prof. S. M. Shiva Prasad, Prof. G. U. Kulkarni, Prof. T. K. Maji, Prof. C. Narayana, from JNCASR and Prof. N. Ravishankar from IISc for their coursework.

My special thanks to my labmates, the “Nanocat” group members: Dr. Dinesh, Dr. Sai Krishna, Dr. K.K.R. Datta, Dr. B.V.V.S. Pawan Kumar, Dr. Piyush Chaturbedy, Josena, Sisir, Sonu Dheeraj and Suchi for their cooperation, useful discussions and for creating a friendly atmosphere in the lab. Working with them was a real pleasure.

It is a great pleasure to thank my collaborators: Prof. Subi J. George (JNCASR), Ankit Jain (JNCASR) and Prof. V. P. Dravid and Dr. M. De (Northwestern University) for fruitful collaborations.

I am thankful to my friends Mohit, Ankit, Chidambar, Satya, Nitesh, and Urmi, for useful discussions.

I am thankful to the following people for various technical assistance: Mrs. Usha (TEM); Mr. Jay, Mr. Karthik and Mr. Kanan (TEM) Mrs. Selvi (FESEM); Mr. Vasu (UV, PL, IR, TGA); Mohit, Chidambar, (NMR); and Ankit (TCSPC)

I am grateful to Nitya (SRF-2011,2012); Komal (SRF- 2013); Sahana and Krishnachary (Project assistant) for working with me on various projects.

I am thankful to academic and administrative staff of JNCASR for their assistance.

I thank all my friends from JNCASR for their company in various activities.

Besides the research life, I am thankful to Prof. M. Eswaramoorthy and his family members for their hospitality and affection.

Financial assistance from Council of Scientific and Industrial Research (CSIR), is gratefully acknowledged.

A deep sense of gratitude to my family for their support, love and affection throughout my life.

Amrit

Preface

This thesis is divided into two parts. Part 1 focuses on different clay-carbon hybrid materials for diverse applications. Part 2 deals with gas permeation and separation through layered material membranes.

Chapter 1.1 briefly introduces layered materials with emphasis on clays and their hybrid materials for multifaceted applications. Use of aminoclay and laponite in hybrid materials is discussed in detail in this chapter as these are the clay materials used in this thesis.

Chapter 1.2 presents a new strategy to disperse reduced graphene oxide (RGO) in water by aminoclay- RGO hybrid. The hybrids were synthesized by in-situ synthesis of aminoclay over graphene oxide (GO) followed by reduction with hydrazine hydrate. The resultant hybrids are stable in aqueous medium even at concentrations up to 7.5 mg RGO/mL. The hybrids are amphiphilic in nature and show simultaneous adsorption of Cytochrome C through hydrophobic interaction and DNA through electrostatic interaction.

Chapter 1.3 discusses the water dispersion of clay-fullerene hybrids. In this chapter we show Fullerenes, otherwise insoluble in aqueous phase, while being immobilized in an inorganic clay matrix (Laponite) can be dispersed in aqueous phase. We have also demonstrated that the Laponite- fullerene hybrids can quench dithiacyanine dyes embedded on the clay surface by ground state charge transfer.

Chapter 1.4 describes synthesis and application of clay-carbon hybrids for CO₂ capture. Self-assembly of laponite and aminoclay has been used to create a laponite-aminoclay hybrid and then carbonized under nitrogen atmosphere to achieve clay-carbon hybrids. These hybrids show high uptake of CO₂ due to their hierarchical porous structure and low diffusion length.

Chapter 2.1 briefly introduces the concepts of membrane based gas separation. The history and main mechanisms of gas separation through membranes are discussed. H₂/CO₂ separation through different porous membranes such as silica, zeolite and metal organic frameworks have been discussed in detail.

Chapter 2.2 discusses gas permeation through graphene oxide membranes. The huge increase in permeability (Up to 20 times) was demonstrated by formation of oxygen rich and graphitic domains on GO surface without sacrificing their selectivity. The performance of such membranes in H₂/CO₂ separation compared to previously reported membranes was investigated and found to be well above the upper bound of polymeric membranes.

In **Chapter 2.3** MoS₂ membranes were investigated for their gas permeation properties and efficiency of H₂/CO₂ separation. It was found that these membranes show high H₂/CO₂ separation at very high H₂ permeability. Thermal stability of the membrane and the effect of phase transition of MoS₂ from 1T to 2H phase on gas permeability and H₂/CO₂ separation was investigated by heating the membranes at different temperatures. The MoS₂ membranes were found to be thermally stable up to 160 °C and a significant increase in gas permeability was observed.

PART 1

Chapter 1.1. *Introduction to clays and clay based hybrid materials.*

Chapter 1.2. *Amphiphilic Aminoclay-RGO hybrids: A simple strategy to disperse high concentration of RGO in water.*

Chapter 1.3. *Highly water dispersible clay- Fullerene hybrids: Surface mediated quenching of cyanine dyes.*

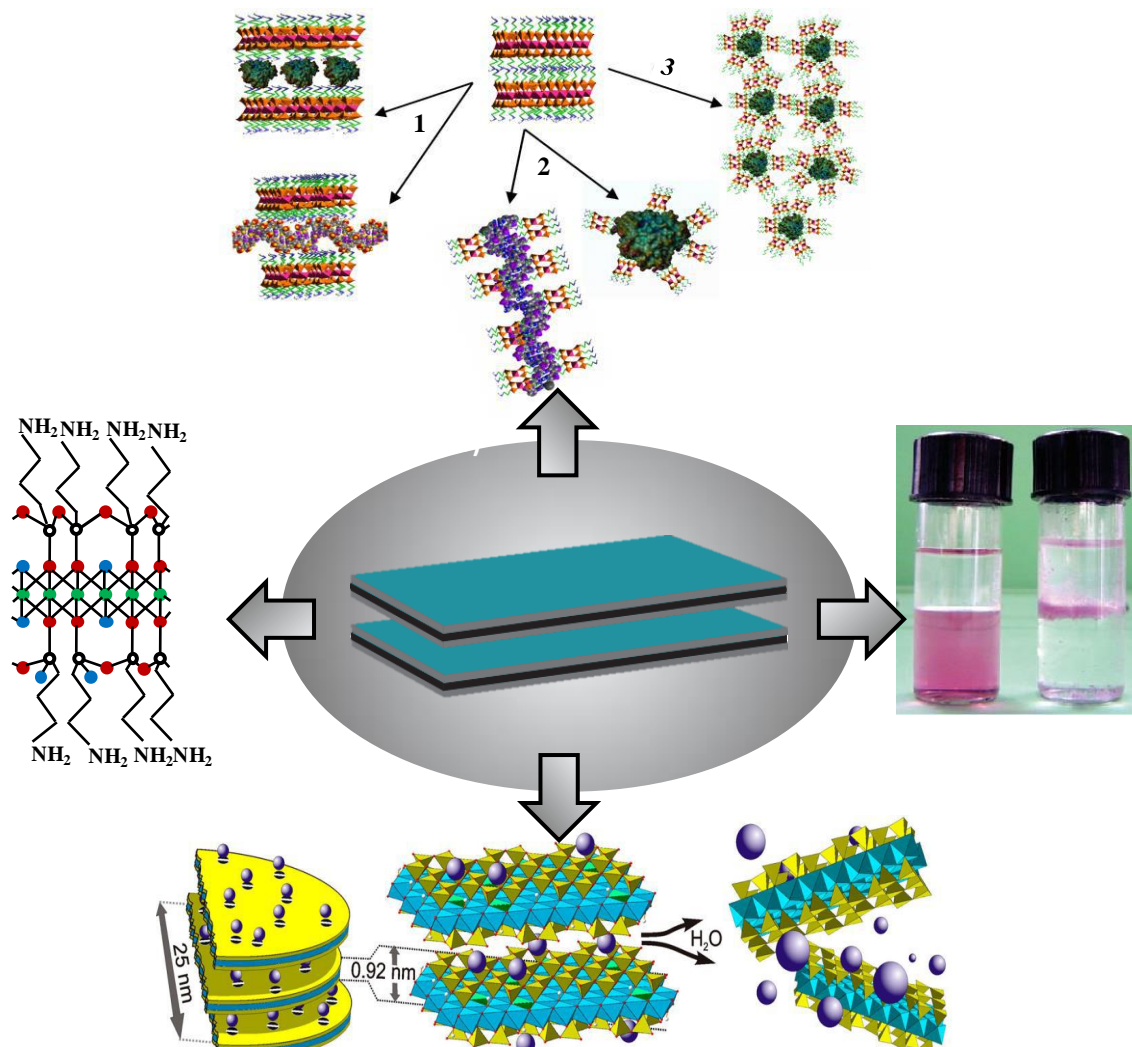
Chapter 1.4. *Clay- Carbon hybrid materials for CO₂ capture.*

Chapter-1.1

Introduction to Clays and Clay Based Hybrid Materials

Summary:

This chapter gives a short introduction about clays and clay based hybrid materials. Their structure and classification are described in brief. Several examples of clay based (mainly aminoclay and laponite) hybrid materials are discussed.



1.1.1. Clay:

The term 'clay' can be interpreted in many ways depending on the point of view of the interpreter. Geologists, mineralogists, soil scientists and chemists approach clay from very different perspectives. Historically the term 'clay' was referred to soil fraction of < 2 nm in size irrespective of their crystallinity and composition. A more recent definition of clay is much more precise. According to Encyclopaedia Britannica, clay or clay mineral is referred to very fine mineral fragments or particles (< 2 nm) composed mostly of hydrous layered silicates of aluminium, though occasionally containing iron, alkali metals or alkaline earth metals.(1)

The usage of clay in human civilization dates back to antiquity. The first known application of clay in prehistoric times was as clay bricks. Even in the ancient civilizations of Cyprus and Greece clays were used as bleaching material and as soaps for removing grease and stains 5000 years ago. Mankind has come a long way from then regarding the applications of clays. In modern civilization clays find their use in a tremendous number of places. From toothpaste, pencils (laponite), paint and plastic additives (kaolinite), household ceramics (kaolinite) to the cores of dams or as a barrier against toxic and radioactive leakage (bentonite) clays are literally everywhere.

1.1.1.1. Structure of clay:

The essential features of hydrous-layer silicates (clay minerals) were revealed by various scientists including Charles Mauguin, Linus C. Pauling, W.W. Jackson, J. West, and John W. Gruner through the late 1920s to mid-1930s. Clay minerals mostly consist of two types of sheets- tetrahedral and octahedral.(Figure 1.1.1) Tetrahedral sheets contain silicate layers of composition Si_4O_{10} , where SiO_4 tetrahedrons are linked with one another via oxygen atoms by sharing three corners of each tetrahedron in a hexagonal mesh pattern to form the basal plane. The remaining apical oxygens are shared with another layer of cations forming octahedral sheet. The octahedral sheets have cations (usually magnesium or aluminium) that are coordinated with six oxygen groups. These octahedrons are joined with each other by sharing the edges, thus forming an octahedral sheet. Natural minerals made up with only octahedral sheets are gibbsite $[\text{Al}(\text{OH})_3]$ and brucite $[\text{Mg}(\text{OH})_2]$. In gibbsite, only two third of the octahedral positions are filled with aluminium, therefore clay minerals based on this structure are

called dioctahedral. On the other hand, in case of brucite all the octahedral positions are occupied, therefore clay minerals based on this structure are called trioctahedral.(2)

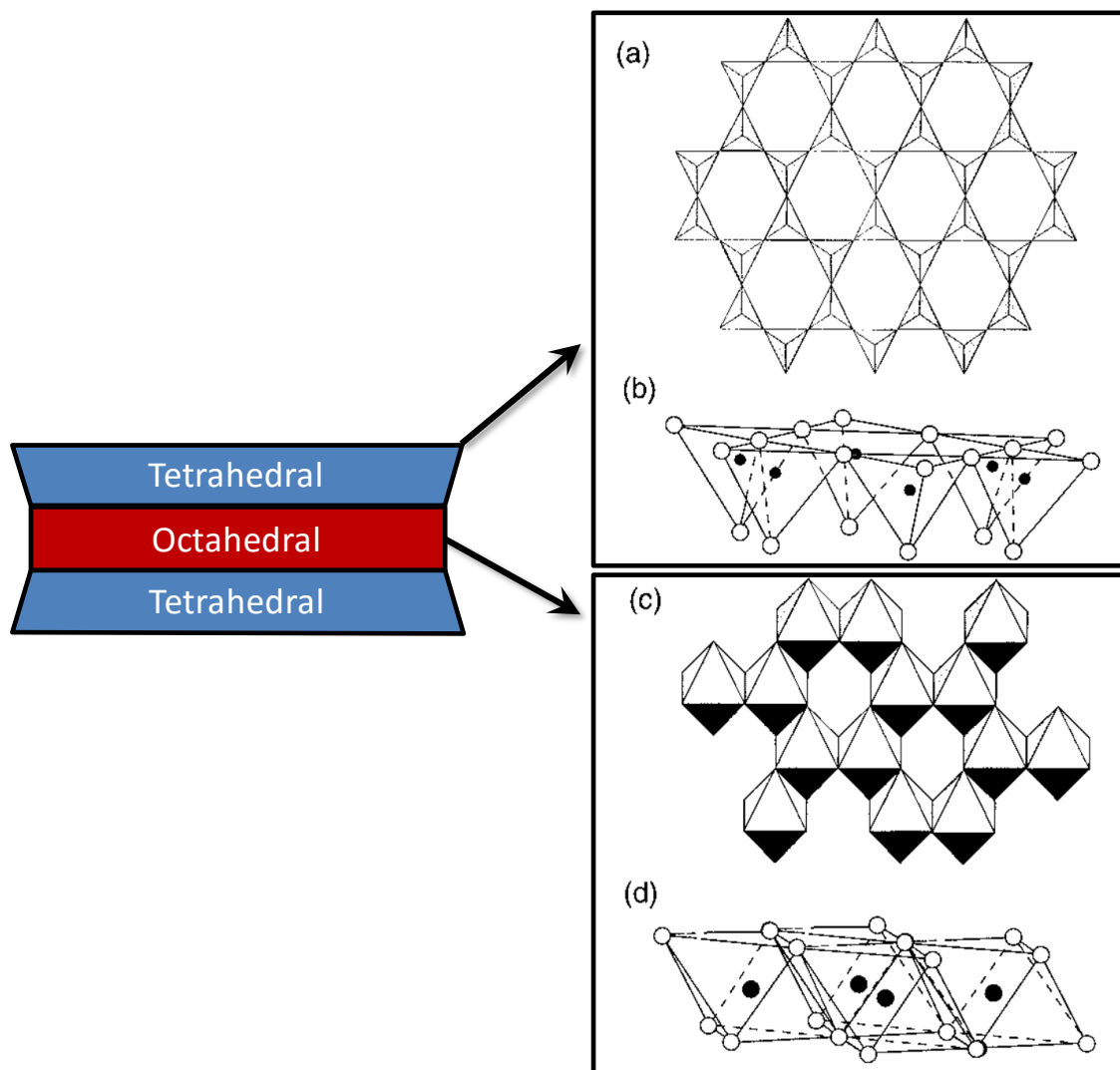


Figure 1.1.1: A clay structure comprised of tetrahedral and octahedral sheets. Silicate $[\text{Si}_4\text{O}_{10}]^{4-}$ tetrahedral sheet in (a) top view and (b) side view, and a clay octahedral sheet in (c) top view and (d) side view. The $[\text{Al}_4\text{O}_{12}]^{12+}$ dioctahedral top view is shown in (c); a $[\text{Mg}_6\text{O}_{12}]^{12+}$ trioctahedral top view would show a continuous sheet of octahedral units. Adapted from ref (2)

There can be partial substitution of Si (IV) in the tetrahedral sheet by trivalent ions such as Al (III), which can cause negative charge in the clay structure. But in most of the cases (except mica) this substitution is quite small. Substitution of cations in octahedral sheets are more common. In dioctahedral sheets most common substitution is Mg (II) for Al (III) whereas in trioctahedral minerals Li (I) can replace Mg (II). Isomorphous

substitution of higher charge cations by lower charge cations (the most common occurrence) creates a net negative charge on the octahedral layers, leading to presence of charge compensating cations on the basal oxygen planes. Due to this clays generally have a high cation exchange capacity (CEC).

1.1.1.2. Clay groups and subgroups:

The major classification of clay minerals is by their layer type and charge. Clay minerals can be classified by two major predominate classes according to the ratio of tetrahedral and octahedral layers- 1:1 and 2:1. Clay structures formed by aligning one octahedral sheet to one tetrahedral sheet is referred to as a 1:1 clay. Whereas, if the unit clay sheet consists of one octahedral sheet sandwiched by two tetrahedral sheets that are oriented in opposite directions it is termed as 2:1 clay as shown in figure 1.1.2. The clays can be further classified by the inherent charge in their basal plane due to different substitutions in the octahedral and tetrahedral layers. The major clay groups with their compositions and most common examples are presented in table 1

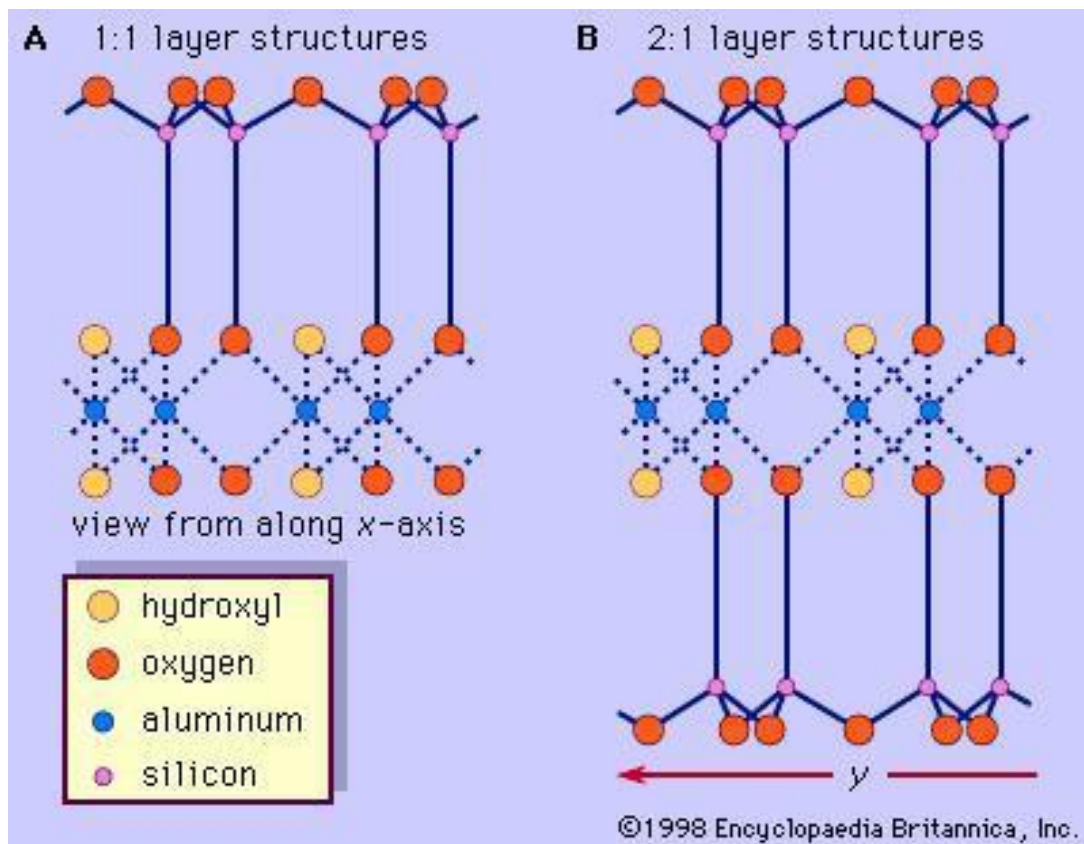


Figure 1.1.2. Schematic of 1:1 and 2:1 layered structures of clay. Adapted from ref (1).

Structure Type	Charge per unit cell	Group	Mineral examples	Ideal composition	Notes
1 : 1 (TO)	0	Kaolin-serpentine	Kaolinite, dickite, nacrite	$Al_4Si_4O_{10}(OH)_8$	Kaolin subgroup, dioctahedral, nonswelling
			Chrysotile, antigorite, lizardite	$Mg_6Si_4O_{10}(OH)_8$	Serpentine subgroup, trioctahedral, nonswelling
2 : 1 (TOT)	0	Pyrophyllite-talc	Pyrophyllite	$Al_4Si_8O_{20}(OH)_4$	Dioctahedral, nonswelling
			Talc	$Mg_6Si_8O_{20}(OH)_4$	Trioctahedral, nonswelling
	0.5-1.2	Smectite	Beidellite	$[(Al_4)(Si_{7.5-6.8}Al_{0.5-1.2})O_{20}(OH)_4]Ex_{0.5-1.2}$	Dioctahedral, swelling
			Montmorillonite	$[(Al_{3.5-2.8}Mg_{0.5-1.2})(Si_8)O_{20}(OH)_4]Ex_{0.5-1.2}$	
	1.2-1.8	Vermiculite	Saponite	$[(Mg_6)(Si_{7.5-6.8}Al_{0.5-1.2})O_{20}(OH)_4]Ex_{0.5-1.2}$	Trioctahedral, swelling
			Vermiculite	$[(Al_4)(Si_{6.8-6.2}Al_{1.2-1.8})O_{20}(OH)_4]Ex_{1.2-1.8}$	Dioctahedral, swelling
			Vermiculite	$[(Mg_6)(Si_{6.8-6.2}Al_{1.2-1.8})O_{20}(OH)_4]Ex_{1.2-1.8}$	Trioctahedral, swelling
			Illite	$[(Al_4)(Si_{7.5-6.5}Al_{0.5-1.5})O_{20}(OH)_4]K_{0.5-1.5}$	Dioctahedral, nonswelling
	2	Mica	Muscovite	$[(Al_4)(Si_6Al_2)O_{20}(OH,F)_4]K_2$	Dioctahedral, nonswelling
			Taenolite	$[(Li_2Mg_4)(Si_8)O_{20}(OH,F)_4]K_2$	Trioctahedral, lithium mica
4	Brittle mica	Margarite	$[(Al_4)(Si_4Al_4)O_{20}(OH,F)_4]Ca_2$	Dioctahedral, nonswelling	
		Palygorskite-sepiolite	Palygorskite	$[(Mg,Al)_4(Si_{7.5-7.75}Al_{0.5-0.25})O_{20}(OH)_2(OH_2)_4]Ex_{var}$	Dioctahedral, nonswelling
			Sepiolite	$[(Mg,M)_8(Si,M')_{12}O_{30}(OH)_4(OH)_2]_4]Ex_{var}$	Trioctahedral (M = Al, Fe(III); M = Fe(II), Fe(III), Mn(II))
2 : 1 channels or inverted ribbons	Variable				
2 : 1:1	Variable	Chlorite	Clinochlore		[TOT]O[TOT] structure

Table 1.1.1. Classification scheme of phyllosilicate clay minerals (T = Tetrahedral, O = Octahedral) Adapted from ref (2)

1.1.2. Aminoclay:

The emerging applications of clay in catalysis(2-4), separation(5, 6), nanocomposites (7-11), ferrofluids(6, 12), biomedicine(13) and for many other purposes(14-29) generated a great deal of interest in the design and synthesis of tailor made clays suitable for different applications. For example when the application of clay, the layered material requires a good dispersion in water(7, 27, 30, 31), poorly dispersible clays like smectite, kaolinite, and bentonites are of little use (32, 33). Many biological and catalytic applications necessitate the synthesis of functional clay which would be highly dispersible in water and interactable with desired molecules or substrates.

One such tailor made clay, magnesium (organo) phyllosilicate, having propylamine functionalities (henceforward referred to as aminoclay) (34-36) reported by Mann and co-workers shows high dispersity in water with interesting properties and structures.(37-48) It can be prepared by a room temperature, sol-gel process using magnesium chloride and organotrialkoxysilane as precursors.(35, 49, 50) Depending on the choice of organic group of the organotrialkoxysilane, clays with different organic pendant groups can also be prepared.(51) The interesting feature about aminoclay is its free and reversible exfoliation in water by protonation of amine groups. They can be reverted back to their stacked form by the addition of less polar solvents like ethanol. The exfoliated layers can further be sonicated to obtain nanosize, oligomeric clay units which can be assembled around biomolecules such as enzymes, DNA to produce functional hybrid materials.(38, 39, 43, 45) .

Aminopropyl-functionalized magnesium phyllosilicate can be prepared by co-condensation in an ethanolic solution containing magnesium chloride and 3-aminopropyltriethoxysilane. The high pH associated with APTES (ca. pH 10) helps in autocatalyzing the formation of aminoclay without the requirement of acid/base catalyst to form white precipitate at room temperature.(34-36) The aminoclay belongs to 2:1 trioctahedral smectite structure consisting of a central brucite sheet of octahedrally coordinated MgO/OH chains overlaid on both sides with an aminopropyl-functionalized silicate network to give an approximate unit cell composition of $[\text{H}_2\text{N}(\text{CH}_2)_3]_8\text{Si}_8\text{Mg}_6\text{O}_{16}(\text{OH})_4$ (44) (Figure 1.1.3a). The powder X-ray diffraction (PXRD) pattern of aminoclay shows a disordered, talc-like structure with a basal spacing consistent with the interdigitated organic aminopropyl pendants. The as-

synthesized aminoclay shows a low-angle reflection with a d_{001} interlayer spacing of 1.6 nm corresponding to the bilayer arrangement of propylamine groups (Figure 1.1.3b). The broad in-plane reflections at higher angles ($d_{020,110} = 0.41$ nm, $d_{130,200} = 0.238$ nm) and the characteristic (060) reflection at $2\theta = 59^\circ$ confirm the formation of 2:1 trioctahedral Mg-phyllsilicate clay with talc-like structure.(34, 36) The transmission electron microscope images of aminoclay showed a stacked lamellar structure having the lateral dimensions extending to micron regime (Figure 1.1.3b, inset).

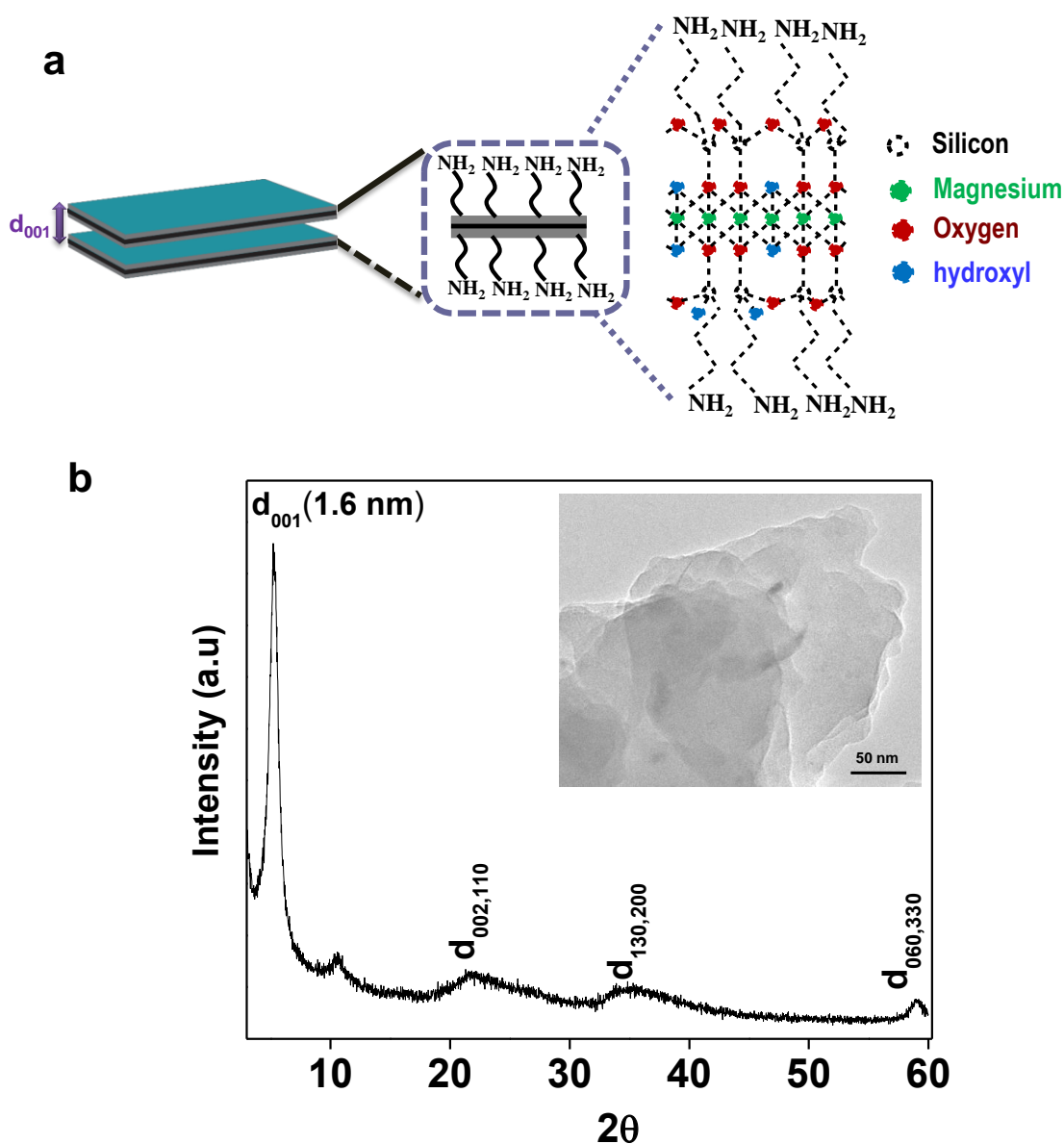


Figure 1.1.3. a) Two dimensional structural representation of amine functionalized magnesium phyllosilicate, b) XRD pattern of aminoclay, inset corresponding TEM image showing layered structure. Adapted from ref (52)

The important property of aminoclay is its switchable organization of the layered structure with respect to the polarity of the solvent (Figure 1.1.4). On addition of polar solvent like water to aminoclay, protonation of the amino groups results in the exfoliation of the organoclay layers forming a clear dispersion. The resulting delaminated layers would be having the lateral size of 30 to 150 nm and approximately 2-4 nm in thickness, corresponding to single or few layers stacking.(53) The extent of exfoliation can be controlled with the pH of the medium. The zeta potential of aminoclay at pH 9.6 (without any pH modification) showed +25 mV due to protonation of amines in the propylamine functional group.(54) Addition of low polar solvent like ethanol to the aqueous dispersion containing exfoliated clay layers induces stacking, leading to its precipitation due to the deprotonation. The switchable property of aminoclay helps the physical entrapment of various guest molecules,(43) while the amine groups aid in stabilizing metal nanoparticles and acidic components by chemical and electrostatic interaction.

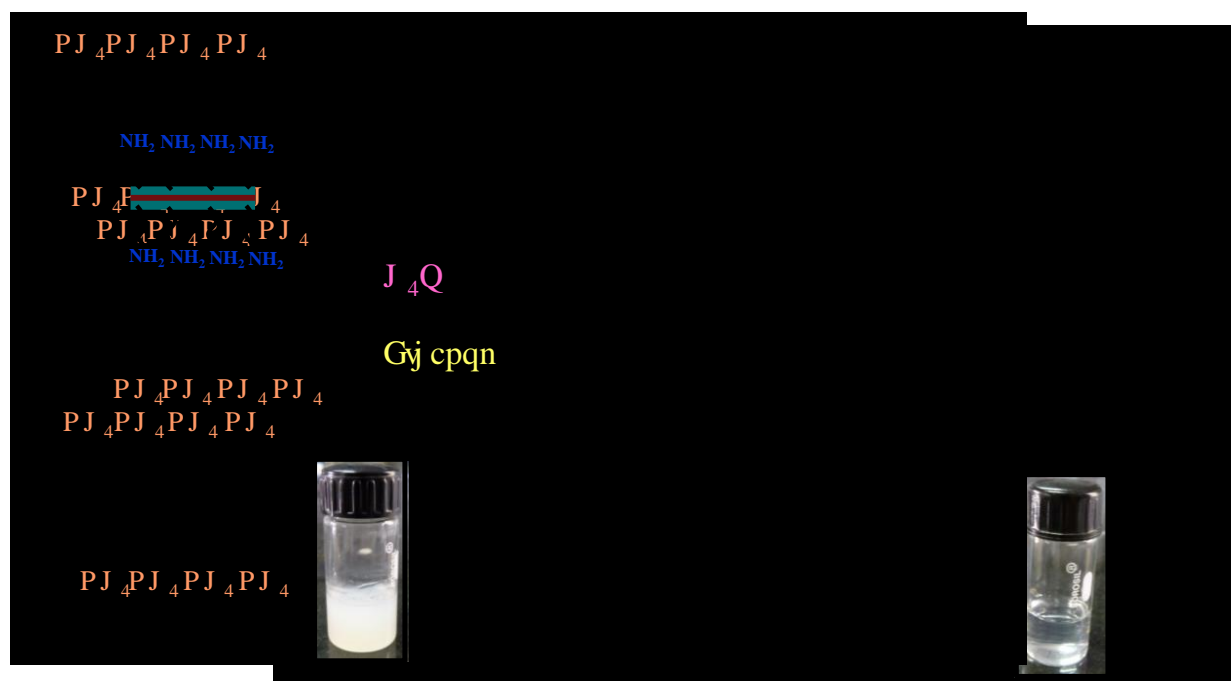


Figure 1.1.4. Top: Schematic showing disorder-order arrangement of aminoclay in ethanol and water respectively, bottom: corresponding optical images. Adapted from ref (52)

1.1.3. Laponite

Laponite is an entirely synthetic layered silicate developed by Laporte industries between 1965-1970. There are many advantages of making synthetic clays compared to naturally occurring clays, such as low cost, reduced impurities and controlled physical properties such as shape, size and charge of the particles. It has found widespread use as rheology modifier in many technological applications such as surface coatings, ceramic glasses, paints, household cleaners and personal care products.

The chemical formula of Laponite is given by $\text{Na}_{0.7}\text{Si}_8\text{Mg}_{5.5}\text{Li}_{0.3}\text{O}_{20}(\text{OH})_4$. It is structurally analogous to naturally occurring clay hectorite. In contrast to hectorite, Laponite particles have a relative uniform diameter of 25 ± 2 nm and a thickness of about 1 nm. Laponite has a 2:1 clay structure in which the octahedral layer is sandwiched between two tetrahedral silicate layers. (Figure 1.1.5a) The octahedral layer consists of a brucite $[\text{Mg}(\text{OH})_2]$ sheet in which few Mg (II) atoms are substituted by Li (I) as isomorphic substitution. This creates a deficiency of positive charge in the sheet. The excess negative charge is balanced by the presence of sodium ions in the interlayer galleries.

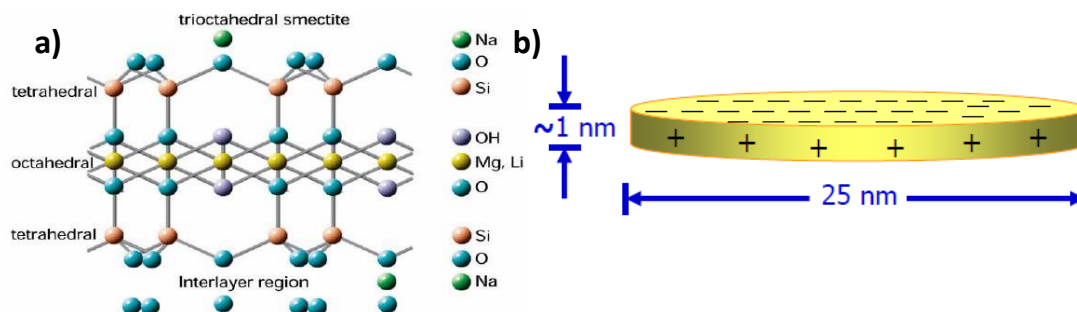


Figure 1.1.5. a) Structure of Laponite clay, b) Pictorial representation of single Laponite particle. (Adapted from Rockwood Ltd. Information brochure)

In aqueous dispersion the Na^+ ions dissociate creating a permanent negative charge to the face of Laponite sheets. The edge of Laponite particles, which predominantly contain MgOH from the dangling octahedral layer. In normal pH these OH groups are protonated (point of zero charge of the edges being pH 11) creating positive charge on the edges(55). This creates a very asymmetrical charge distribution in Laponite particles, with faces being negative and edges being positive. (Figure 1.1.5b)

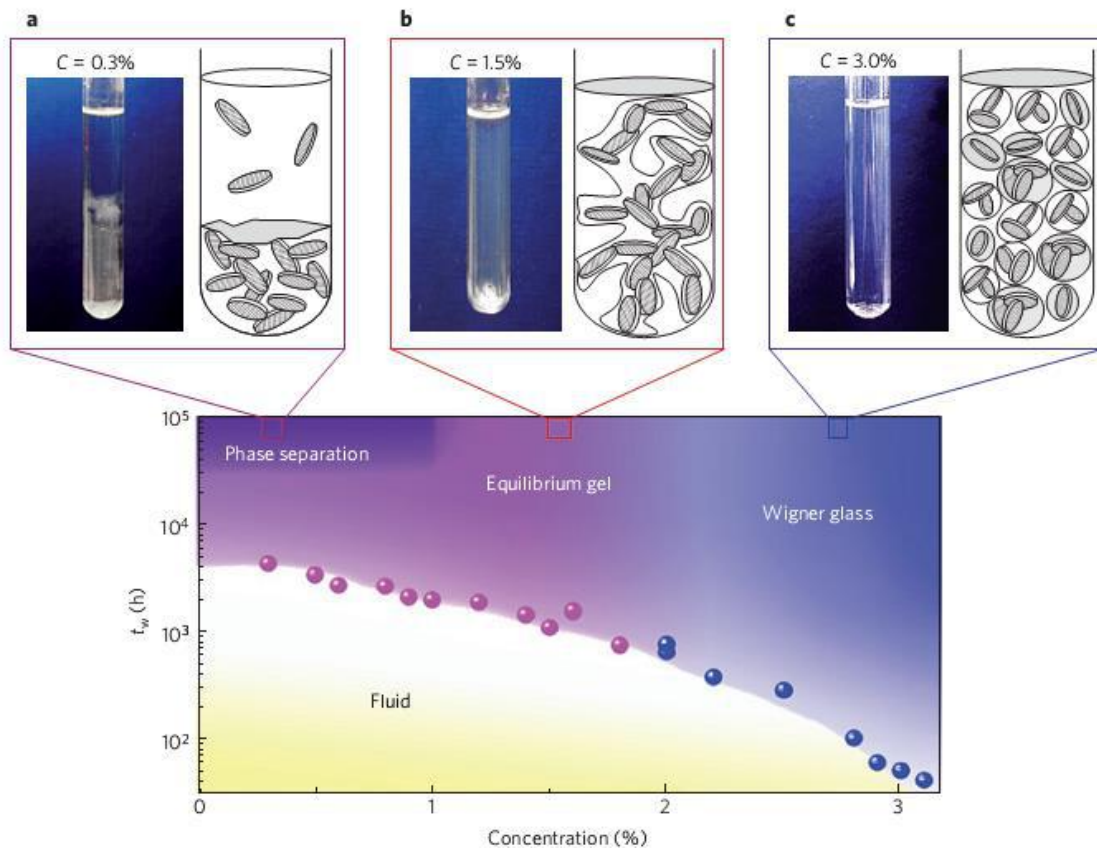


Figure 1.1.6. Top(a-c)- pictorial representation and pictures of Laponite solution at different stages of the phase diagram, bottom- Phase diagram of diluted Laponite suspensions, in the waiting-time-versus-concentration plane. Adapted from Ruzica et al.(56)

This asymmetric charge distribution in Laponite gives rise to unusual properties in solution which gives rise to a unique phase diagram(57). (Figure 1.1.6) There can be two kinds of Laponite-Laponite interactions. Firstly, there is the van der Waals interaction between Laponite particles which is isotropic in nature. In addition to that there also exists the electrostatic interaction, which can be either repulsive (face to face and rim to rim) or attractive (face to rim). Depending on the experimental conditions, any one of them can be dominant. However, van der Waals interaction only comes into picture where the particles are in close contact or when the electrostatic interaction has been nullified at high salt concentration. At low salt concentration and high Laponite concentration ($C_w > 2\%$) Laponite particles form an arrested gel (Wigner glass) by face to edge interaction, (Figure 1.1.7a) according to the phase diagram given below. This

gel formation can be modulated by changing the ionic strength of the medium. (Figure 1.1.7b)

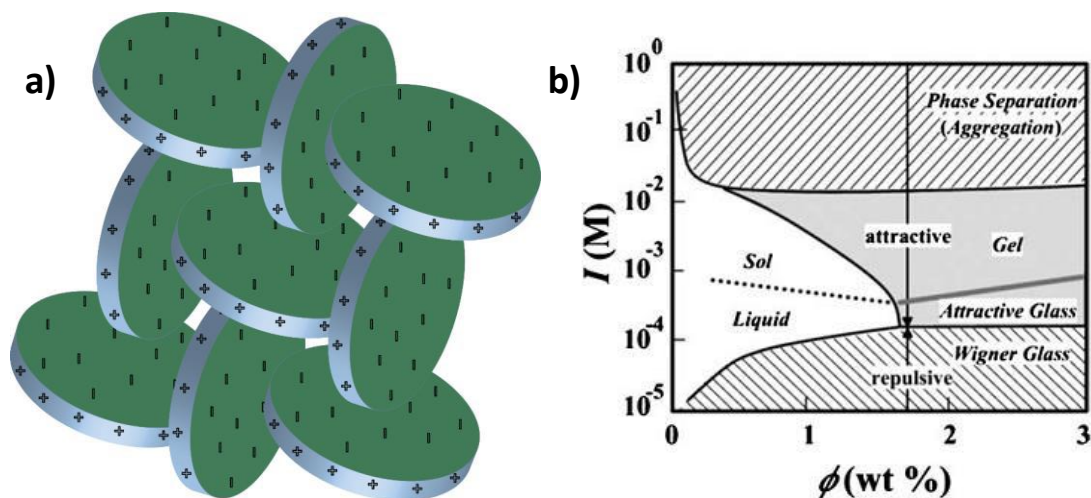


Figure 1.1.7. a) Schematic representation of Laponite particles forming house of cards formation in an arrested gel. b) The phase diagram of laponite solution with respect to weight % of clay in solution and ionic strength. Adapted from Tanaka et. al.(58).

1.1.4. Clay hybrids:

Due to their versatile application opportunity and abundance in earth crust a huge amount of research has been directed towards improving the properties of clays. Clay based hybrid materials have seen myriad of uses due to their versatility. Various recent reports present application of clay based hybrids in different prospects. These include polymer nanocomposites, organic catalysis. CO_2 photoreduction, ferrofluids and ferrogels, adsorbent for hydrophobic materials, optical, electrical and antimicrobial applications and many more.

The addition of clays to polymeric matrices enhances mechanical, physical (thermal and barrier) and chemical properties which are useful for packaging, tough polymer nanocomposites, etc. Moreover, the two dimensional nanospace and biocompatibility offered by the clays can also be useful for hosting various dyes and biomolecules. Some typical examples involving aminoclay and Laponite are given below.

1.1.4.1. Aminoclay-biomolecule hybrids

A striking feature of layered materials is their ability to accommodate a range of guest molecules within constrained interlayer regions.(13) Considerable interest has been

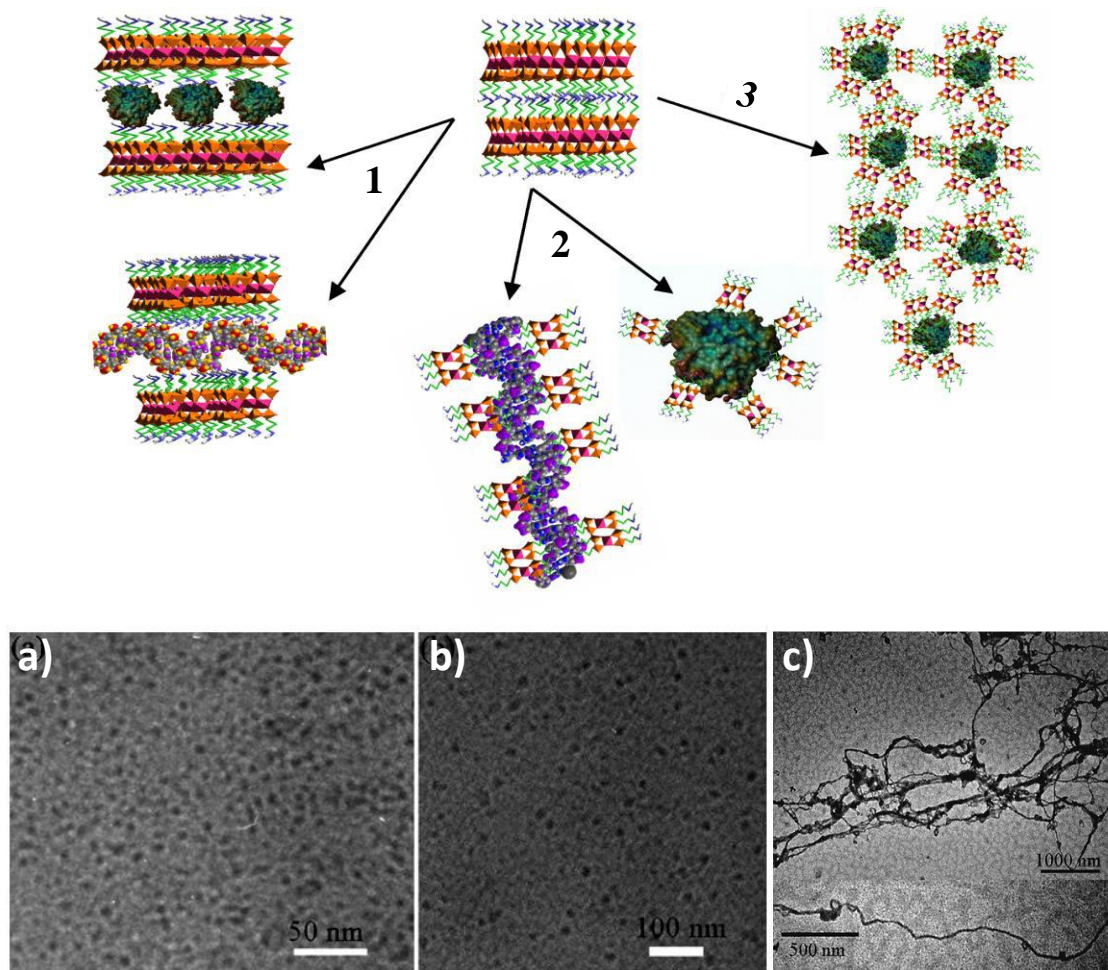


Figure 1.1.8. Top- Illustration showing protocols involving magnesium aminopropyl-functionalized phyllosilicate (top centre of figure) in the preparation of self-assembled bio-inorganic nanocomposite hybrids. (1) Formation of intercalated biofunctionalized nanocomposites with mesolamellar structure by protein- (top left) or DNA- (bottom left) induced assembly of exfoliated organoclay sheets. (2) Wrapping and encapsulation of single molecules of negatively charged proteins (bottom centre right) or DNA (bottom centre left) with low molecular weight cationic organoclay clusters to produce core-shell nanoparticles or nanowires, respectively. (3) Synthesis of partially ordered superstructures of organoclay-enveloped biomolecules by chemical modification of covalently linked organic groups attached to the phyllosilicate framework. Bottom- TEM images of oligomeric aminoclay wrapped a) myoglobin and b) haemoglobin; c) DNA templated aminoclay nanowire. Adapted from ref (52)

focused on the synthesis of organic- inorganic host-guest systems by insertion of drug and biomolecules(59, 60) within the clay galleries. The positively charged nature and the nanoscopic gap of the aminoclay in combination with negatively charged biomolecules has also been successfully utilized in the formation of intercalated, core-shell, nanowire type nanoarchitectures.(43)

Although there is a widespread interest in the biotechnological applications of various proteins and enzymes, very often their use in real world applications is hampered by the short term stability of these biomolecules in the process. In this regard, biomineralization methods can often enhance their stability for repetitive use. Negatively charged biomolecules such as myoglobin, haemoglobin, DNA and glucose oxidase were co-assembled in the presence of as synthesized aminoclay. The aminoclay-biomolecule hybrids showed retention of their secondary structure and enhanced biochemical activity. In another approach, cage like encapsulation of biomolecules has been achieved by using oligomeric aminoclay. This method produces individually wrapped biomolecules such as myoglobin, haemoglobin and glucose oxidase within ultrathin sheet of aminoclay. Such individually wrapped biomolecules retain their individual catalytic properties, and are even accessible to small gaseous molecules by diffusion through the defects. This approach of wrapping biomolecules with oligomeric clay sheets have also been adopted with DNA as a template to form clay wrapped DNA nanowires. The key factor in the spontaneous self-assembly of such mesolamellar nanocomposites is the coulombic interaction between the cationic exfoliated amino propyl groups and the negatively charged biomolecules. More on this topic can be found in the review by Mann et.al.(43)

1.1.4.2. Aminoclay-metal nanoparticles hybrids:

The chemical and physical properties associated with metal nanoparticles make them attractive candidates in the fields of catalysis, optics, storage and biology.(61-63) Thus for aqueous phase, heterogeneous catalysis, keeping in mind the prerequisites of recyclability and stable water dispersion, it is common to embed them in solid supports like porous metal oxides, carbons, zeolites and clays.(64, 65) However, for biphasic

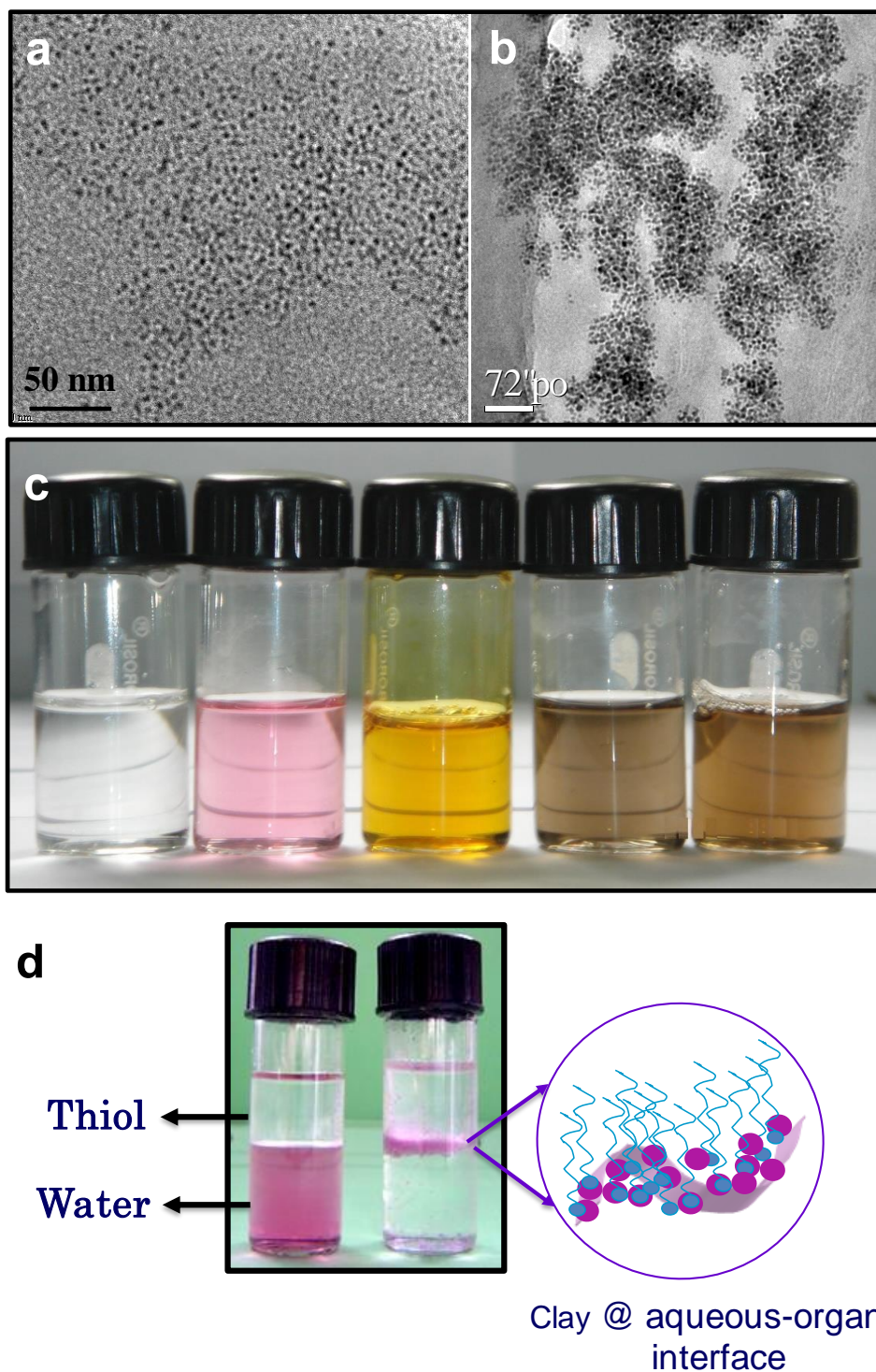
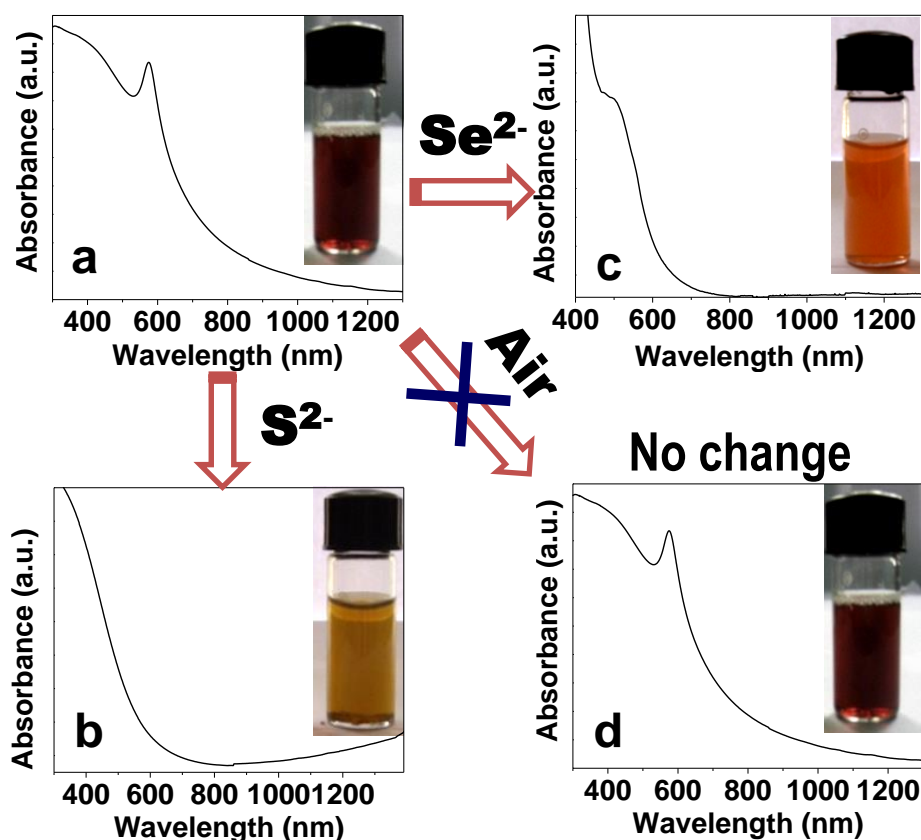


Figure 1.1.9. (a and b) TEM images of Au and Cu nanoparticles embedded in an aminoclay matrix respectively. (c) Optical images of aminoclay–metal nanoparticle hybrids forming transparent dispersions in water: (from left to right) aminoclay dispersion and aminoclay with Au, Ag, Pt and Pd nanoparticles and (d) aqueous Au–clay hybrid on addition of hexadecanethiol at the time of addition (left) and after 14 days (right). Adapted from ref (67, 68)

reactions their use is limited by their poor dispersibility in aqueous/organic medium. Therefore, it is essential to explore new solid-supports which could keep the catalyst at the oil-water interface for efficient catalysis.(66) The presence of amine groups and hence its high water dispersibility makes the aminoclay an attractive heterogeneous support for metal nanoparticles.(67, 68) TEM images show that the metal nanoparticles of size less than 10 nm (Figure 1.1.9a,b) can be effectively dispersed on aminoclay layers. Optical image of the hybrids containing aminoclay stabilized metal nanoparticles (Au, Ag, Pt and Pd) shown in Figure 1.1.9c are transparent in nature and highly dispersible in water. Furthermore, the interaction between the metal nanoparticles and clay is so strong that even hexadecanethiol, known to have very



strong interaction towards Au

Figure 1.1.10. UV-Vis spectra of (a) freshly prepared Cu-aminoclay solution, (b) Cu-aminoclay solution after the addition of Na_2S solution, (c) Cu-aminoclay solution after the addition of NaHSe solution, (d) Cu-aminoclay solution aged for 6 days in air. The inset shows the corresponding optical images. Adapted from ref (68)

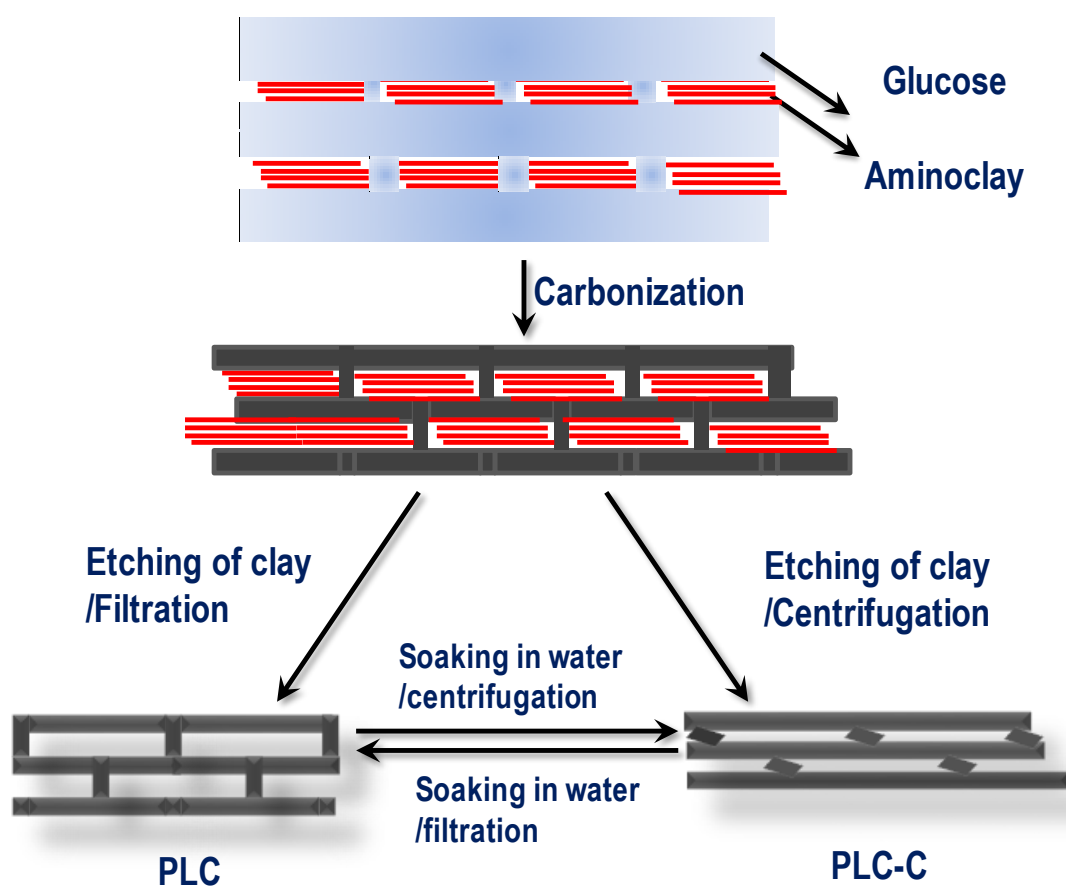
nanoparticle, cannot separate Au nanoparticles from aminoclay matrix (Figure 1.1.9d). Addition of hexadecanethiol (oil phase) to the aqueous dispersion brings the Au-aminoclay layers to the oil-water interface because at the interface the gold-bound hydrophobic hexadecanethiol and the hydrophilic clay layers can stabilize very well.

The gas barrier property of aminoclay layers is an added advantage in stabilizing oxophilic nanoparticles, such as copper. Copper nanoparticles are quite sensitive to air and form cuprous oxide and then cupric oxide upon exposure to ambient atmosphere.(69) Thus synthesis and storage of copper nanoparticles require stringent inert atmosphere.(70) The gas barrier property and the presence of reductive amine environment effectively prevent the oxidation of copper nanoparticles stabilized within the aminoclay layers even after prolonged exposure to air.(68) Furthermore, the permselective nature of aminoclay towards ionic species such as S^{2-} , Se^{2-} was evident by the formation of copper chalcogenides when respective anions (S^{2-} , Se^{2-}) were introduced in solution (Figure 1.1.10). The composites are inert to atmospheric oxygen even in dry form.

The metal nanoparticle grafted aminoclay was used for various catalytic hydrogenation applications.(68, 71-74) Pd nanoparticles dispersed on aminoclay has been effectively utilized as a recyclable catalyst for the hydrogenation of α,β -unsaturated carbonyl compounds and Suzuki coupling reactions in aqueous media.(71, 73) The basic nature of aminoclay has also been exploited in carrying out Suzuki reaction in the absence of external base.(73) The catalyst could be easily recovered and recycled three times without a significant loss of activity in hydrogenation and Suzuki cross coupling reactions. The Pd-aminoclay catalyst was also used for Mizoroki-Heck reaction between aryl halides and n-butyl acrylate or styrene under solvent free conditions.(71) Very recently, Cu-aminoclay nanocomposite has been employed as a catalyst for cycloaddition of aromatic azides with terminal alkynes to produce the corresponding 1,2,3-triazoles via Click reaction in good yields and selectivity.(74) Besides, Cu and Pt nanoparticles embedded aminoclay layers display high catalytic activity towards the reduction of the toxic pollutant, p-nitrophenol.(68, 72)

1.1.4.3. Aminoclay as a template for flexible porous layered carbon:

The making of intelligent host materials that are responsive to guests under appropriate conditions possessing integrated attributes of zeolite like regularity (ordering) and enzyme-like specificity is a challenging task for material scientists.(75) These structurally flexible porous inorganic materials could find enormous applications in sensors, sorption, catalysis, separation and gas storage owing to their unique properties and functions.(75) Introducing flexibility within the walls of porous carbon networks would be very advantageous for the size-selective separation of molecules or switching between different properties of the material itself. However, all the synthetic procedures (both hard and soft templating) to prepare porous carbons usually yield rigid pore



walls.(76, 77)

Figure 1.1.11. Stepwise formation of ordered and disordered layered flexible carbon materials. Adapted from ref (52)

Recently porous layered carbon (PLC) possessing switchable pores as a response to an applied mechanical force has been made using aminoclay as a soft-templating and

glucose as a carbon precursor (Figure 1.1.11).(78) The layer thickness of the PLC varies from 3-4 nm and the spacing between the layers varies from 2-4 nm. The layers are supported by soft, pillar-like, carbon nanoparticles of size around 3 nm. PLC possesses functional groups containing oxygen (15 %) and nitrogen (5 %) in addition to carbon. These functional groups play an important role in the loose connection of pillar-like structures within the layers. During centrifugation (or shear force) the layers slide over one another through buckling of the pillars (PLC- C) which results in the squeezing out of water between the layers. When there is no centrifugal force and the PLC is allowed to settle on its own in water, the layers would have a breathing space between them supported by the pillars and the water molecules in between. Similarly, when the PLC-C sample is soaked in water, the buckled, pillar-like carbon structures revert back to their original shape. Moreover, the variation of the pore size associated with the flexible carbon displayed size selective screening of dye molecules with different molecular sizes. The aminoclay has also been used as a template to synthesize layered carbon nitride from the cyanamide precursors.(79)

1.1.4.2. Laponite-dye hybrids

The usage of clay as a host material for the entrapment of dye molecules dates to prehistoric times.(80-82) Maya blue is one such organic-inorganic hybrid material has been known for 4000 years, combines the color of organic pigment (natural blue indigo) with inorganic palygorskite mineral.(81-83) There are several other examples where dye molecules entrapped in the clay matrix has been used for various applications. Recently laponite has been used for solubilizing the insoluble blue dye indigo.(84) On the other hand, efficient light harvesting needs special supramolecular organization of fluorescent donor and acceptor molecules.(85) Clay materials with their layered structure and water dispersibility are one of the most favorite candidates in this regard.

Laponite has been used as a host for dispersing water insoluble dye molecules in aqueous media. In a recent report Kynast et. al. utilized the excellent water solubility of Laponite particles to disperse Indigo, a water insoluble dye in water.(Figure 1.1.12) This approach has also been used to disperse Nile red(86) and phthalocyanine blue(87) in water. These Laponite dye hybrids are stable in water and can be used for myriad of application like transparent films, pigments, probe for biomedical imaging etc.

Laponite-Nile red hybrids also show unusual optical properties that are hard to achieve in aqueous media. For example, Nile red, forming h-aggregates are generally not fluorescent in aqueous media, whereas, this hybrid shows an enhanced fluorescence with a quantum yield of 0.35.

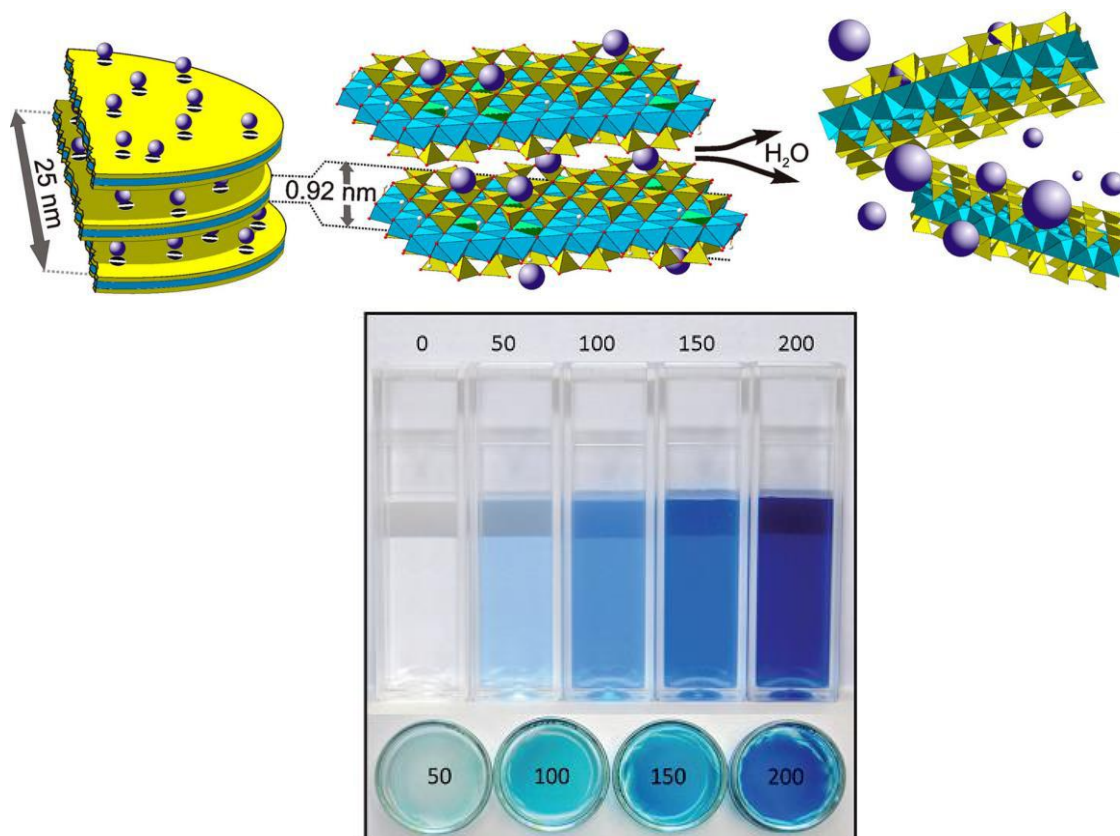


Figure 1.1.12. Top- Schematic representation of the structure of laponite disks with sodium cations (violet spheres) compensating the negative charges of $[LiO_6]$ – (green octahedra) in the octahedral $[MgO_6]$ sheets (blue). Dispersion in water yields disks with negatively charged nanoclay surfaces, which can encapsulate positively charged molecules like cationic dyes and neutral molecules like Nile Red and Phthalocyanine blue. Bottom- Photographic images of Laponite- Indigo solutions and films. Adapted from ref (84)

Laponite- dye hybrids have also been used to study unusual optical phenomenon such as nonlinear optical properties of dye molecules. Nonlinear optical properties are very demanding for use in device application, on the other hand, they also provide new techniques to study the properties of new materials. In particular, the second order processes are very useful because they are very sensitive to material properties. Laponite adsorbed methylene blue dye has been shown to demonstrate non-linear

optical properties, in particular second harmonic generation (88). The efficiency of the second harmonic generation can be increased up to 100 times compared to free dye molecules in presence of Laponite.

Laponite sheets also provide a good host platform to absorb various kinds of dye molecules showing different properties than their free state. In a paper, Whitten et. al. have demonstrated the superquenching of cyanine dyes on clay surface by a dipositive bipyridine quencher.(89)

1.1.5. Conclusion:

Clays are an attractive class of layered materials with remarkable properties and applications. Organically modified phyllosilicates are emerging as powerful candidates in the fields of chemistry, biology, materials, catalysis, etc. The exfoliation/restacking ability of organoclays in various solvents can be utilized in delivery of guest molecules and designing smart materials. The functional groups of organoclays can be utilized in stabilizing noble-metal nanostructures. This is advantageous because the coupling of size dependent optical, catalytic and electronic properties of nanoparticles with clay materials lead to the development of novel clay-nanoparticle hybrids. The nanoscopic voids provided by the clay layers could be used to prepare various layered nanostructures. On the other hand, the excellent water dispersibility of laponite clays have been employed to obtain stable aqueous dispersion of insoluble materials. Laponite-dye hybrids show interesting photophysical properties as well.

1.1.5. References:

1. "Clay Mineral", Encyclopædia Britannica Online. Retrieved from <http://www.britannica.com/science/clay-mineral>, (2016).
2. S. M. Auerbach, K. A. Carrado, P. K. Dutta, *Handbook of layered materials*. (CRC, 2004).

3. S. D. Miao *et al.*, Ru nanoparticles immobilized on montmorillonite by ionic liquids: A highly efficient heterogeneous catalyst for the hydrogenation of benzene. *Angew. Chem. Int. Ed.* **45**, 266-269 (2006).
4. G. M. Scheuermann, R. Thomann, R. Mulhaupt, Catalysts Based Upon Organoclay with Tunable Polarity and Dispersion Behavior: New Catalysts for Hydrogenation, C-C Coupling Reactions and Fluorous Biphasic Catalysis. *Catal. Lett.* **132**, 355-362 (2009).
5. X. L. Ding, S. M. Henrichs, Adsorption and desorption of proteins and polyamino acids by clay minerals and marine sediments. *Mar. Chem.* **77**, 225-237 (2002).
6. R. S. Hsu, W. H. Chang, J. J. Lin, Nanohybrids of Magnetic Iron-Oxide Particles in Hydrophobic Organoclays for Oil Recovery. *Acs Applied Materials & Interfaces* **2**, 1349-1354 (2010).
7. A. C. Balazs, T. Emrick, T. P. Russell, Nanoparticle polymer composites: Where two small worlds meet. *Science (New York, N.Y.)* **314**, 1107-1110 (2006).
8. L. J. Bonderer, A. R. Studart, L. J. Gauckler, Bioinspired design and assembly of platelet reinforced polymer films. *Science (New York, N.Y.)* **319**, 1069-1073 (2008).
9. E. Munch *et al.*, Tough, Bio-Inspired Hybrid Materials. *Science (New York, N.Y.)* **322**, 1516-1520 (2008).

10. P. Podsiadlo *et al.*, Ultrastrong and stiff layered polymer nanocomposites. *Science (New York, N.Y.)* **318**, 80-83 (2007).
11. M. A. Priolo, D. Gamboa, K. M. Holder, J. C. Grunlan, Super Gas Barrier of Transparent Polymer-Clay Multi layer Ultrathin Films. *Nano Lett.* **10**, 4970-4974 (2010).
12. V. Tzitzios *et al.*, Immobilization of magnetic iron oxide nanoparticles on laponite discs - an easy way to biocompatible ferrofluids and ferrogels. *J. Mater. Chem.* **20**, 5418-5428 (2010).
13. C. Viseras, P. Cerezo, R. Sanchez, I. Salcedo, C. Aguzzi, Current challenges in clay minerals for drug delivery. *Appl. Clay Sci.* **48**, 291-295 (2010).
14. T. Ebina, F. Mizukami, Flexible transparent clay films with heat-resistant and high gas-barrier properties. *Adv. Mater.* **19**, 2450-2453 (2007).
15. M. Eckle, G. Decher, Tuning the performance of layer-by-layer assembled organic light emitting diodes by controlling the position of isolating clay barrier sheets. *Nano Lett.* **1**, 45-49 (2001).
16. Y. Ide, N. Ochi, M. Ogawa, Effective and Selective Adsorption of Zn²⁺ from Seawater on a Layered Silicate. *Angew. Chem. Int. Ed.* **50**, 654-656 (2011).
17. M. Jaber, J. Mieke-Brendle, L. Michelin, L. Delmotte, Heavy metal retention by organoclays: Synthesis, applications, and retention mechanism. *Chem. Mater.* **17**, 5275-5281 (2005).
18. S. Jagtap, M. K. Yenkie, N. Labhsetwar, S. Rayalus, Fluoride in Drinking Water and Defluoridation of Water. *Chem. Rev.* **112**, 2454-2466 (2012).

19. J. J. Lin, C. C. Chu, M. L. Chiang, W. C. Tsai, Manipulating Assemblies of High-Aspect-Ratio Clays and Fatty Amine Salts to Form Surfaces Exhibiting a Lotus Effect. *Adv. Mater.* **18**, 3248-3252 (2006).
20. Y. M. Lvov, D. G. Shchukin, H. Mohwald, R. R. Price, Halloysite clay nanotubes for controlled release of protective agents. *ACS nano* **2**, 814-820 (2008).
21. M. W. Möller *et al.*, Barrier Properties of Synthetic Clay with a Kilo-Aspect Ratio. *Adv. Mater.* **22**, 5245-5249 (2010).
22. T. C. Pappas *et al.*, Nanoscale engineering of a cellular interface with semiconductor nanoparticle films for photoelectric stimulation of neurons. *Nano Lett.* **7**, 513-519 (2007).
23. S. S. Ray, Polylactide-Based Bionanocomposites: A Promising Class of Hybrid Materials. *Acc. Chem. Res.* **45**, 1710-1720 (2012).
24. E. Ruiz-Hitzky, P. Aranda, M. Darder, G. Rytwo, Hybrid materials based on clays for environmental and biomedical applications. *J. Mater. Chem.* **20**, 9306-9321 (2010).
25. E. R. Ruiz-Hitzky, M. Darder, P. Aranda, Functional biopolymer nanocomposites based on layered solids. *J. Mater. Chem.* **15**, 3650-3662 (2005).
26. H. B. Yao *et al.*, Gold Nanoparticle Functionalized Artificial Nacre: Facile in Situ Growth of Nanoparticles on Montmorillonite Nanosheets, Self-Assembly, and Their Multiple Properties. *ACS nano* **6**, 8250-8260 (2012).

27. W. J. Zhang, M. K. S. Li, P. L. Yue, P. Gao, Exfoliated Pt-clay/Nafion nanocomposite membrane for self-humidifying polymer electrolyte fuel cells. *Langmuir* **24**, 2663-2670 (2008).
28. C. H. Zhou, Z. F. Shen, L. H. Liu, S. M. Liu, Preparation and functionality of clay-containing films. *J. Mater. Chem.* **21**, 15132-15153 (2011).
29. A. Zhuk, R. Mirza, S. Sukhishvili, Multiresponsive Clay-Containing Layer-by-Layer Films. *ACS nano* **5**, 8790-8799 (2011).
30. F. F. Fang, H. J. Choi, J. Joo, Conducting polymer/clay nanocomposites and their applications. *J Nanosci Nanotechno* **8**, 1559-1581 (2008).
31. I. K. Tonle, T. Diaco, E. Ngameni, C. Detellier, Nanohybrid kaolinite-based materials obtained from the interlayer grafting of 3-aminopropyltriethoxysilane and their potential use as electrochemical sensors. *Chem. Mater.* **19**, 6629-6636 (2007).
32. L. B. de Paiva, A. R. Morales, F. R. V. Diaz, Organoclays: Properties, preparation and applications. *Appl. Clay Sci.* **42**, 8-24 (2008).
33. B. Lebeau *et al.*, One-step synthesis and solvent-induced exfoliation of hybrid organic-inorganic phyllosilicate-like materials. *J Nanosci Nanotechno* **6**, 352-359 (2006).
34. N. T. Whilton, S. L. Burkett, S. Mann, Hybrid lamellar nanocomposites based on organically functionalized magnesium phyllosilicate clays with interlayer reactivity. *J. Mater. Chem.* **8**, 1927-1932 (1998).

35. S. Mann *et al.*, Sol-gel synthesis of organized matter. *Chem. Mater.* **9**, 2300-2310 (1997).
36. S. L. Burkett, A. Press, S. Mann, Synthesis, characterization, and reactivity of layered inorganic-organic nanocomposites based on 2:1 trioctahedral phyllosilicates. *Chem. Mater.* **9**, 1071-& (1997).
37. K. M. Bromley, A. J. Patil, A. M. Seddon, P. Booth, S. Mann, Bio-functional mesolamellar nanocomposites based on inorganic/polymer intercalation in purple membrane (bacteriorhodopsin) films. *Adv. Mater.* **19**, 2433-2438 (2007).
38. A. J. Patil, S. Mann, in *Bio-inorganic Hybrid Nanomaterials*. (Wiley-VCH Verlag GmbH & Co. KGaA, 2008), pp. 239-270.
39. A. J. Patil, M. Li, E. Dujardin, S. Mann, Novel bioinorganic nanostructures based on mesolamellar intercalation or single-molecule wrapping of DNA using organoclay building blocks. *Nano Lett.* **7**, 2660-2665 (2007).
40. Y. C. Lee *et al.*, Optical Properties of Fluorescein-labeled Organoclay. *Photochem. Photobiol.* **86**, 520-527 (2010).
41. I. L. Lagadic, Schiff base chelate-functionalized organoclays. *Microporous Mesoporous Mater.* **95**, 226-233 (2006).
42. S. Mann, Self-assembly and transformation of hybrid nano-objects and nanostructures under equilibrium and non-equilibrium conditions. *Nature Materials* **8**, 781-792 (2009).
43. A. J. Patil, S. Mann, Self-assembly of bio-inorganic nanohybrids using organoclay building blocks. *J. Mater. Chem.* **18**, 4605-4615 (2008).

44. A. J. Patil, E. Muthusamy, S. Mann, Synthesis and self-assembly of organoclay-wrapped biomolecules. *Angew. Chem. Int. Ed.* **43**, 4928-4933 (2004).
45. A. J. Patil, E. Muthusamy, A. M. Seddon, S. Mann, Higher-order synthesis of organoclay pipes using self-assembled lipid templates. *Adv. Mater.* **15**, 1816-1819 (2003).
46. S. C. Holmstrom, A. J. Patil, M. Butler, S. Mann, Influence of polymer co-intercalation on guest release from aminopropyl-functionalized magnesium phyllosilicate mesolamellar nanocomposites. *J. Mater. Chem.* **17**, 3894-3900 (2007).
47. S. Sadasivan *et al.*, Novel protein-inorganic nanoparticles prepared by inorganic replication of self-assembled clathrin cages and triskelia. *Soft Matter* **4**, 2054-2058 (2008).
48. Y.-C. Lee, H.-J. Shin, J.-W. Yang, Self-Assembly of Aminoclay Template-Assisted J-aggregate Fibers. *Advanced Science Letters* **6**, 882-887 (2012).
49. Y. Fukushima, M. Tani, An Organic/Inorganic Hybrid Layered Polymer - Methacrylate Magnesium (Nickel) Phyllosilicate. *J. Chem. Soc. Chem. Commun.*, 241-242 (1995).
50. R. B. Ferreira, C. R. da Silva, H. O. Pastore, Aminopropyl-Modified Magnesium-Phyllosilicates: Layered Solids with Tailored Interlayer Access and Reactivity. *Langmuir* **24**, 14215-14221 (2008).

51. L. Ukrainczyk, R. A. Bellman, A. B. Anderson, Template synthesis and characterization of layered Al- and Mg-silsesquioxanes. *J. Phys. Chem. B* **101**, 531-539 (1997).
52. K. K. R. Datta, A. Achari, M. Eswaramoorthy, Aminoclay: a functional layered material with multifaceted applications. *J. Mater. Chem. A* **1**, 6707-6718 (2013).
53. A. J. Patil, E. Muthusamy, S. Mann, Fabrication of functional protein-organoclay lamellar nanocomposites by biomolecule-induced assembly of exfoliated aminopropyl-functionalized magnesium phyllosilicates. *J. Mater. Chem.* **15**, 3838-3843 (2005).
54. Y. C. Lee, E. J. Kim, D. A. Ko, J. W. Yang, Water-soluble organo-building blocks of aminoclay as a soil-flushing agent for heavy metal contaminated soil. *J. Hazard. Mater.* **196**, 101-108 (2011).
55. S. Jatav, Y. M. Joshi, Chemical stability of Laponite in aqueous media. *Appl. Clay Sci.* **97-98**, 72-77 (2014).
56. B. Ruzicka *et al.*, Observation of empty liquids and equilibrium gels in a colloidal clay. *Nat Mater* **10**, 56-60 (2011).
57. B. Ruzicka, E. Zaccarelli, A fresh look at the Laponite phase diagram. *Soft Matter* **7**, 1268-1286 (2011).
58. H. Tanaka, J. Meunier, D. Bonn, Nonergodic states of charged colloidal suspensions: Repulsive and attractive glasses and gels. *Physical Review E* **69**, 031404 (2004).

59. J.-H. Choy, S.-J. Choi, J.-M. Oh, T. Park, Clay minerals and layered double hydroxides for novel biological applications. *Appl. Clay Sci.* **36**, 122-132 (2007).
60. J.-H. Choy, S.-Y. Kwak, Y.-J. Jeong, J.-S. Park, Inorganic layered double hydroxides as nonviral vectors. *Angew. Chem.* **39**, 4041-4045 (2000).
61. C. Burda, X. B. Chen, R. Narayanan, M. A. El-Sayed, Chemistry and properties of nanocrystals of different shapes. *Chem. Rev.* **105**, 1025-1102 (2005).
62. V. H. Grassian, When Size Really Matters: Size-Dependent Properties and Surface Chemistry of Metal and Metal Oxide Nanoparticles in Gas and Liquid Phase Environments. *J. Phys. Chem. C* **112**, 18303-18313 (2008).
63. K. V. Rao, K. K. R. Datta, M. Eswaramoorthy, S. J. George, Highly Pure Solid-State White-Light Emission from Solution-Processable Soft-Hybrids. *Adv. Mater.*, doi: 10.1002/adma.201204407 (2013).
64. L. De Rogatis *et al.*, Embedded Phases: A Way to Active and Stable Catalysts. *Chemsuschem* **3**, 24-42 (2010).
65. M. Zahmakiran, S. Ozkar, Metal nanoparticles in liquid phase catalysis; from recent advances to future goals. *Nanoscale* **3**, 3462-3481 (2011).
66. A. Schmid *et al.*, Industrial biocatalysis today and tomorrow. *Nature* **409**, 258-268 (2001).
67. K. K. R. Datta, M. Eswaramoorthy, C. N. R. Rao, Water-solubilized aminoclay-metal nanoparticle composites and their novel properties. *J. Mater. Chem.* **17**, 613-615 (2007).

68. K. K. R. Datta, C. Kulkarni, M. Eswaramoorthy, Aminoclay: a permselective matrix to stabilize copper nanoparticles. *Chem. Commun.* **46**, 616-618 (2010).
69. J. H. Kim, S. H. Ehrman, T. A. Germer, Influence of particle oxide coating on light scattering by submicron metal particles on silicon wafers. *Appl. Phys. Lett.* **84**, 1278-1280 (2004).
70. P. Lignier, R. Bellabarba, R. P. Tooze, Scalable strategies for the synthesis of well-defined copper metal and oxide nanocrystals. *Chem. Soc. Rev.* **41**, 1708-1720 (2012).
71. H. Firouzabadi, N. Iranpoor, A. Ghaderi, M. Ghavami, S. J. Hoseini, Palladium Nanoparticles Supported on Aminopropyl-Functionalized Clay as Efficient Catalysts for Phosphine-Free C-C Bond Formation via Mizoroki-Heck and Suzuki-Miyaura Reactions. *Bull. Chem. Soc. Jpn.* **84**, 100-109 (2011).
72. S. J. Hoseini, M. Rashidi, M. Bahrami, Platinum nanostructures at the liquid-liquid interface: catalytic reduction of p-nitrophenol to p-aminophenol. *J. Mater. Chem.* **21**, 16170-16176 (2011).
73. A. S. Kumar *et al.*, Pd-Aminoclay Nanocomposite as an Efficient Recyclable Catalyst for Hydrogenation and Suzuki Cross Coupling Reactions. *J Nanosci Nanotechno* **12**, 2000-2007 (2012).
74. A. S. Kumar *et al.*, Aminoclay-Supported Copper Nanoparticles for 1,3-Dipolar Cycloaddition of Azides with Alkynes via Click Chemistry. *J Nanosci Nanotechno*, (2013, doi:10.1166/jnn.2013.7343).

75. S. Horike, S. Shimomura, S. Kitagawa, Soft porous crystals. *Nat Chem* **1**, 695-704 (2009).
76. M. Inagaki, H. Orikasa, T. Morishita, Morphology and pore control in carbon materials via templating. *R. Soc. Chem. Adv* **1**, 1620-1640 (2011).
77. E. Ruiz-Hitzky *et al.*, Supported Graphene from Natural Resources: Easy Preparation and Applications. *Adv. Mater.* **23**, 5250-5255 (2011).
78. K. K. R. Datta *et al.*, Observation of Pore-Switching Behavior in Porous Layered Carbon through a Mesoscale Order-Disorder Transformation. *Angew. Chem. Int. Ed.* **50**, 3929-3933 (2011).
79. B. V. V. S. P. Kumar, K. K. R. Datta, M. Eswaramoorthy, Tuning the Nitrogen Content and Porosity of Nanostructured Carbon Nitride Using Aminoclay as a Reactive Template. *Chem. Lett.* **40**, 1154-1156 (2011).
80. G. Fergus, G. N. Miguel, C. S. Carla, in *Encyclopedia of Surface and Colloid Science, Second Edition*. (Taylor & Francis, 2007), vol. null, pp. 389-410.
81. P. Gómez-Romero, C. Sanchez, in *Functional Hybrid Materials*. (Wiley-VCH Verlag GmbH & Co. KGaA, 2005), pp. 1-14.
82. G. Kickelbick, in *Hybrid Materials*. (Wiley-VCH Verlag GmbH & Co. KGaA, 2007), pp. 1-48.
83. C. Sanchez, P. Belleville, M. Popall, L. Nicole, Applications of advanced hybrid organic-inorganic nanomaterials: from laboratory to market. *Chem. Soc. Rev.* **40**, 696-753 (2011).

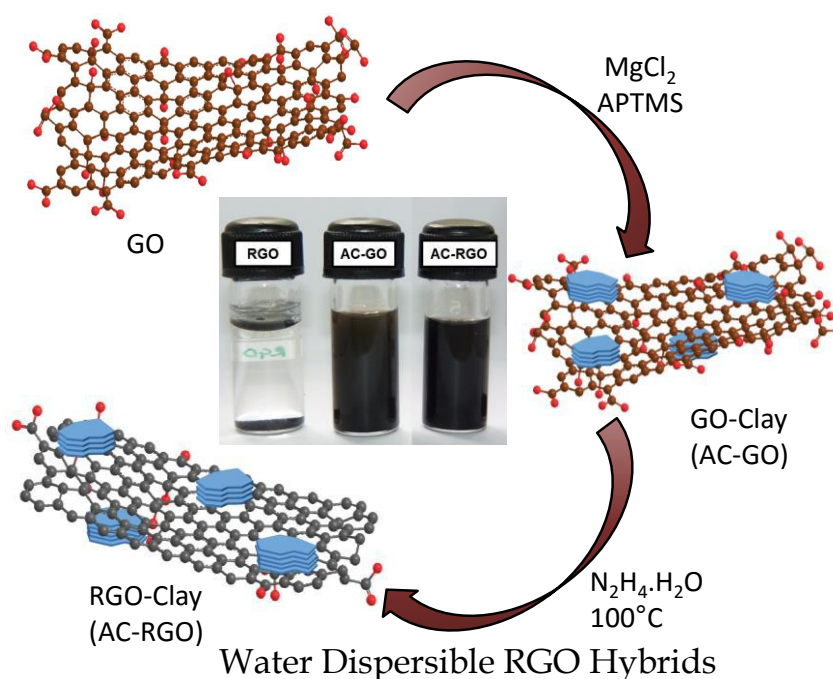
84. M. M. Lezhnina, T. Grewe, H. Stoehr, U. Kynast, Laponite Blue: Dissolving the Insoluble. *Angew. Chem. Int. Ed.* **51**, 10652-10655 (2012).
85. K. V. Rao, K. K. R. Datta, M. Eswaramoorthy, S. J. George, Light-Harvesting Hybrid Assemblies. *Chem. Eur. J.* **18**, 2184-2194 (2012).
86. T. Felbeck *et al.*, Nile-Red-Nanoclay Hybrids: Red Emissive Optical Probes for Use in Aqueous Dispersion. *Langmuir* **29**, 11489-11497 (2013).
87. M. C. Staniford *et al.*, Photophysical efficiency-boost of aqueous aluminium phthalocyanine by hybrid formation with nano-clays. *Chem. Commun.* **51**, 13534-13537 (2015).
88. C. Boutton *et al.*, Enhanced second-order optical nonlinearity of dye molecules adsorbed onto Laponite particles. *Clays Clay Miner.* **45**, 483-485 (1997).
89. L. Lu, R. M. Jones, D. McBranch, D. Whitten, Surface-Enhanced Superquenching of Cyanine Dyes as J-Aggregates on Laponite Clay Nanoparticles. *Langmuir* **18**, 7706-7713 (2002).

Chapter-1.2

Amphiphilic Aminoclay-RGO Hybrids: A Simple Strategy to Disperse High Concentration of RGO in Water

Summary

Aqueous dispersion of graphene or reduced graphene oxide (RGO) is very much important to realize the full potential of these materials in many fields. Herein we present a simple route to prepare highly water dispersible aminoclay-RGO (AC-RGO) hybrids by in-situ condensation of aminoclay over graphene oxide (GO) followed by reduction with hydrazine hydrate. The resultant hybrids are stable in aqueous medium even at concentrations up to 7.5 mg RGO/mL. To the best of our knowledge this is the highest concentration of aqueous dispersion of RGO. Significantly, the hybrids are amphiphilic in nature and show simultaneous adsorption of cytochrome C through hydrophobic interaction and DNA through electrostatic interaction. This strategy opens up new possibilities for the prospect of RGO in catalysis and biomedical applications.



1.2.1. Introduction:

Over the past few years graphene has created enormous interest as a layered material(1) with promising applications in microelectronic devices(2, 3), sensors(4, 5), polymer nanocomposites(6), catalysis(7), energy storage devices(8), biology(2, 9) etc. For many practical applications related to biology and catalysis, the reduced form of GO must be dispersed in aqueous medium which is quite challenging due to strong van der Waal interaction between the reduced sheets leading to aggregation. Surfactants(10, 11) and block co-polymers(12) were often used to reduce this interaction energy (Figure 1.2.1a)

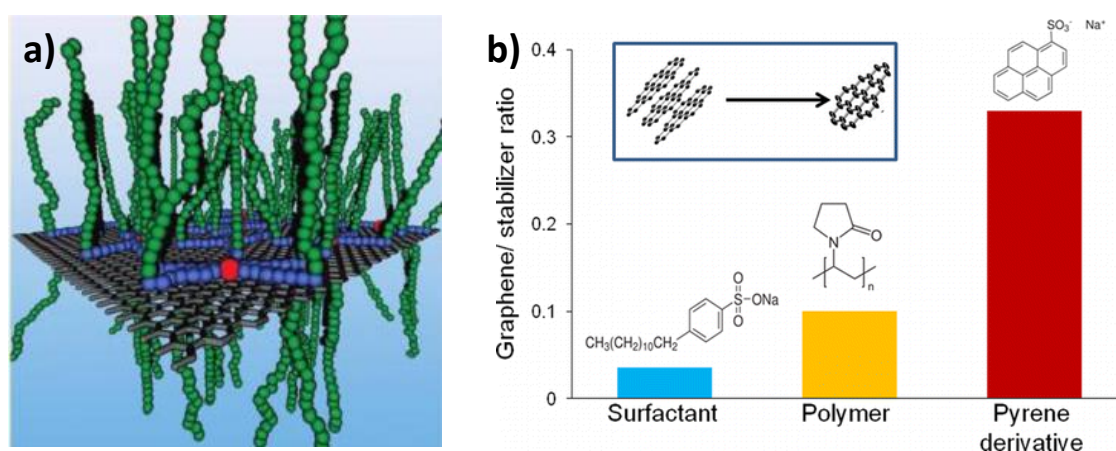


Figure 1.2.1. a) Schematic of interaction of graphene with block co-polymers. b) Comparison of relative amount of dispersant needed for dispersing graphene in water. Adapted from ref (12) and (15)

and hence increase the dispersion in polar solvents. Functionalization of graphene through covalent linkage(13) and π - π interactions(14) has also been explored to improve their aqueous dispersion. However, in most of the cases, especially for non-covalent functionalization the extent of dispersion of graphene/ RGO in water is quite low (<1 mg/mL).(15) On top of that, the amount of dispersant needed for dispersion of graphene is also quite high (Figure 1.2.1b). Considering the potential applications of the reduced form of GO in catalysis, adsorption and construction of novel hybrids it is essential to develop newer methods to disperse these hydrophobic layers in water efficiently.

1.2.2. Scope of present investigation

In this chapter we have used highly water dispersible aminoclay nanostructures for effective dispersion of RGO. The aminoclay used is a magnesium phyllosilicate with aminopropyl pendants covalently linked to the silicon(16-19). In water, the protonation of the amino groups favours the exfoliation of aminoclay layers by charge repulsion and enhance the solvation by polar water molecules. Although clays such as laponite(20), montmorillonite(21), bentonite(22) etc. have been used to prepare graphene clay composites, the limited water dispersibility of the clays makes the resulting composite poorly dispersible in water. The highly water dispersible aminoclay on the other hand with its strong interaction with RGO is able to disperse it well in water in large quantities. Moreover, the AC-RGO hybrid has the property of both aminoclay and RGO and show good uptake of both DNA and cytochrome C.

1.2.3. Experimental Procedure

1.2.3.1. Preparation of graphene oxide:

Graphene oxide (GO) was obtained from graphite by Hummer's method(23). In a typical procedure, 23 mL of concentrated H₂SO₄ was mixed with 1 g of graphite and 0.5 g NaNO₃ in a 250 mL round bottom flask and cooled in an ice bath at 0 °C. 3 g KMnO₄ was added slowly to the mixture in small portions with vigorous stirring. Temperature was maintained below 20 °C during this time. The ice bath was then removed and the reaction was brought to 30-35 °C, where it was maintained for 30 min. To this 46 mL water was added slowly causing violent effervescence and rise of temperature to 98 °C. The resultant brown coloured suspension was maintained at this temperature for 15 minutes. The suspension was then brought to room temperature and 140 ml water was added. The mixture was then treated with 1 mL of 30% H₂O₂ to reduce any unreacted permanganate. The bright yellow reaction mixture was then centrifuged at 5000 rpm, washed several times with distilled water until the pH turned neutral. The precipitate was dried at a 60 °C oven.

1.2.3.2. Preparation of RGO

RGO was prepared by the following method. First, 580 mg of GO was dispersed in 200 mL distilled water by sonication. To this suspension 5 mL of hydrazine hydrate was added and refluxed for 10 h. The solution turned clear and black cloudy precipitates of

RGO were seen floating. The precipitate was centrifuged at 5000 rpm, washed with distilled water until the pH turns neutral. Final product was dried overnight at 80 °C to get RGO.

1.2.3.3. Preparation of aminoclay

Typically, bulk aminopropyl-functionalized magnesium phyllosilicate clay was prepared at room temperature by drop wise addition of 1.0 mL (5.85 mmol) 3-aminopropyltrimethoxysilane to an aqueous solution of 0.84 g (3.62 mmol) magnesium chloride in water (25 mL) The solution was left stirring for 24 hours, dried at 60 °C, dispersed in water, reprecipitated from ethanol and dried. The yield of the product was 1.0 g.

1.2.3.4. Preparation of aminoclay-GO and aminoclay-RGO hybrids: (In-situ synthesis)

In this method, the aminoclay nanostructures were allowed to form over the surface of GO sheets dispersed in water. In a typical procedure, for preparation of AC-GO-25 (hybrid containing 25 wt% GO) 0.35 g of GO was dispersed in 25 mL water by sonication for 10 min. To the dispersion 0.84 g (3.62 mmol) magnesium chloride was added followed by drop wise addition of 1.0 mL (5.85 mmol) 3-aminopropyltrimethoxysilane. The solution was stirred for 48 hours to form a brown-black slurry, which was dried at 100 °C. The solid thus obtained was dispersed in water (20 mL) and precipitated from ethanol (100 mL). The precipitate was centrifuged and subsequently dried at 60 °C to get the aminoclay-GO hybrid (AC-GO-25).

For preparation of aminoclay-RGO hybrids (AC-RGO-25) 0.35 mL hydrazine hydrate was added to the AC-GO-25 slurry followed by drying at 100 °C. The resultant hybrid was dispersed in water and reprecipitated from ethanol followed by drying to get the aminoclay RGO hybrid. Thus prepared aminoclay GO and RGO hybrids are abbreviated as AC-GO and AC-RGO respectively followed by number which indicate the weight percent of GO or RGO with respect to clay. The amount of GO introduced was varied to get different compositions- AC-GO-7.5, 25, 35 and AC-RGO-7.5, 25, 35.

The hybrids were dispersed in water (0.1 g in 5 mL) by probe sonication for 5 min. For comparison 10 mg of RGO was also dispersed in 5 mL water by sonication. High

concentration water dispersion of RGO was prepared by sonicating 30 mg of AC-RGO 25 in 1 mL water.

1.2.3.5. Preparation of APTMS functionalized RGO:

To a 0.35 g GO dispersion in 20 mL distilled water 1 mL of APTMS was added. The reaction mixture was stirred for 48 h, 0.35 mL hydrazine hydrate was added to it and dried at 100 °C to get APTMS functionalized RGO.

1.2.3.6. Demineralization of clay from RGO-aminoclay hybrid:

The demineralization of a AC-RGO hybrid was done according to a previously reported procedure(24). In a typical method 0.25 g of AC-RGO 25 was stirred with 30 mL solution of 12% HCl and 13% HF for 12 h.

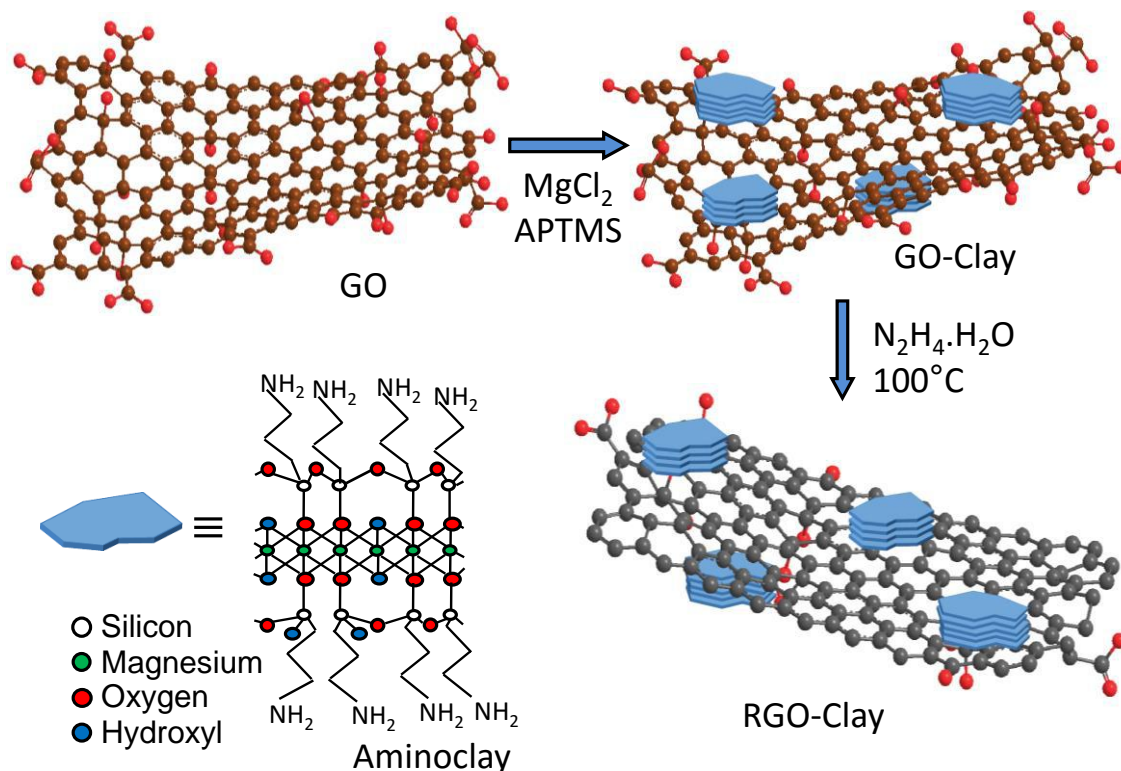
1.2.3.7. Adsorption of biomolecules on AC-GO and AC-RGO hybrids

Adsorption studies with biomolecules (cytochrome C and DNA) were done at pH 10.3. The reason for choosing these biomolecules is that their sores bands are quite apart (260 nm for DNA and 410 nm for cytochrome C) and don't interfere with one another. Stock solution (1g/L) of both the biomolecules (DNA and cytochrome C) were prepared by dissolving them in tris buffer (0.1M) solution (pH 10.3). For each experiment 20 mg of each hybrid (AC-RGO 7.5, 25, 35) was dispersed in 4 mL of the stock solutions. 20 mg of aminoclay and 8 mg of RGO were also suspended in 4 mL of the stock solutions as references. For combined adsorption studies a stock solution containing 1 g/L of DNA and cytochrome C was used. These solutions were allowed to stand for 24 h at 25 °C to attain the equilibrium. After ageing of the solutions they were centrifuged at 10000 rpm and the supernatant liquid was taken for UV-Vis absorption studies to quantify the remaining biomolecule concentration.

For adsorption measurements at pH 5.8 and 7 phosphate buffer solution of pH 7 was prepared and the pH was adjusted by addition of acid as required.

1.2.4. Results and discussion:

The schematic of in-situ formation of AC-GO and their subsequent reduction to AC-RGO hybrid is shown in Scheme 1.2.1. Hybrids with different RGO content were



denoted

Scheme 1.2.1. In-situ preparation of AC-GO and AC-RGO hybrids. The blue platelets depict aminoclay, the brown and grey sheets depict GO and RGO respectively. Inset: structure of aminoclay.

as AC-RGO-7.5, AC-RGO-25 and AC-RGO-35 where the numbers indicate the wt% of RGO in the hybrids. The synthesis of aminoclay in presence of GO facilitates its formation in the form of nanostructures on the surfaces of GO. On the other hand, bulk aminoclay synthesis (in absence of GO) leads to larger aminoclay layers. The negatively charged GO surfaces act as nucleation centers for the condensation of clay nanostructures from its precursors. The as synthesized clay-GO hybrids have been converted to clay-RGO hybrids by reducing them in presence of hydrazine hydrate. The binding of aminoclay nanostructures with RGO is so strong that the clay does not come out in water even after sonication of AC-RGO hybrids followed by filtration. The filtrate does not show any precipitation for clay upon addition of ethanol. This strong

binding indicates that in addition to the electrostatic interaction between aminoclay and GO (which greatly reduces upon reduction) the chemical linkage formed by the ring opening reaction of the epoxy groups by amine(25, 26) in the reaction condition play a significant role in holding the aminoclay nanoparticles over the RGO sheets. This is in contrast to the phase separation of clay from AC-RGO hybrids (in water) prepared by mixing preformed aminoclay with GO followed by reduction (Figure 1.2.2). Similarly, the APTMS functionalized RGO and the demineralized AC-RGO hybrid precipitated immediately in water (Figure 1.2.2)

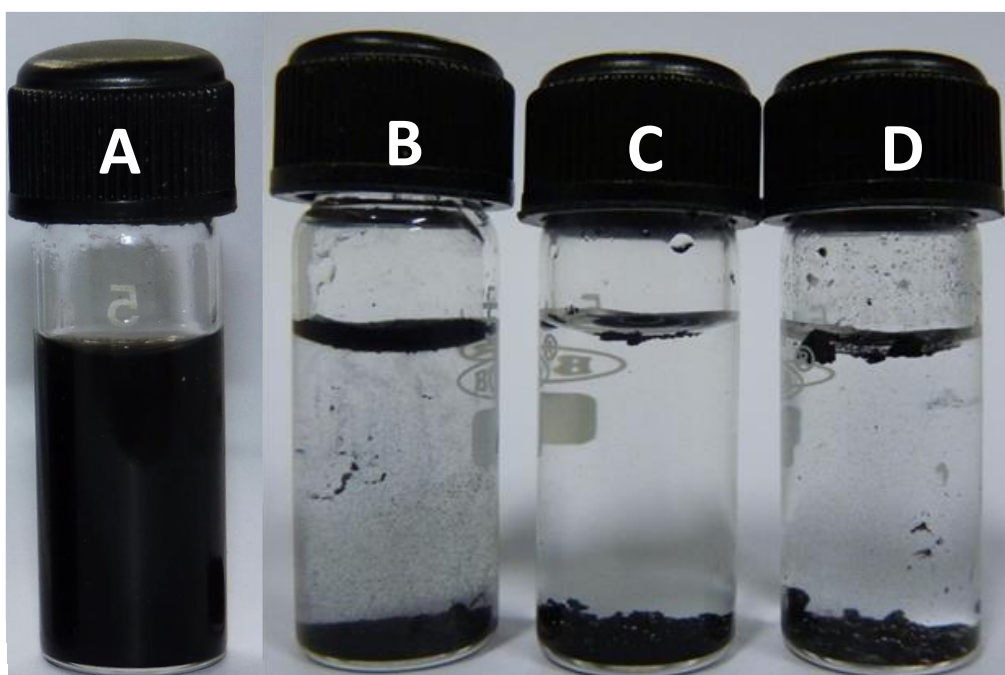


Figure 1.2.2. A) AC-RGO-25 hybrid dispersed in water. B) Reduced form of preformed aminoclay-GO hybrid. C) APTMS functionalized RGO. D) Resultant RGO upon removal of clay from AC-RGO hybrid by demineralization.

This strongly suggests that the in-situ preparation method is essential to avoid phase separation and get highly water dispersible aminoclay-RGO hybrids.

Transmission electron microscopy (TEM) images show presence of clay nanoparticles on RGO surface (Figure 1.2.3 a). Higher magnification image show clay nanoparticles of size ranging from 5 to 50 nm distributed on the RGO sheet (Figure 1.2.3 b).

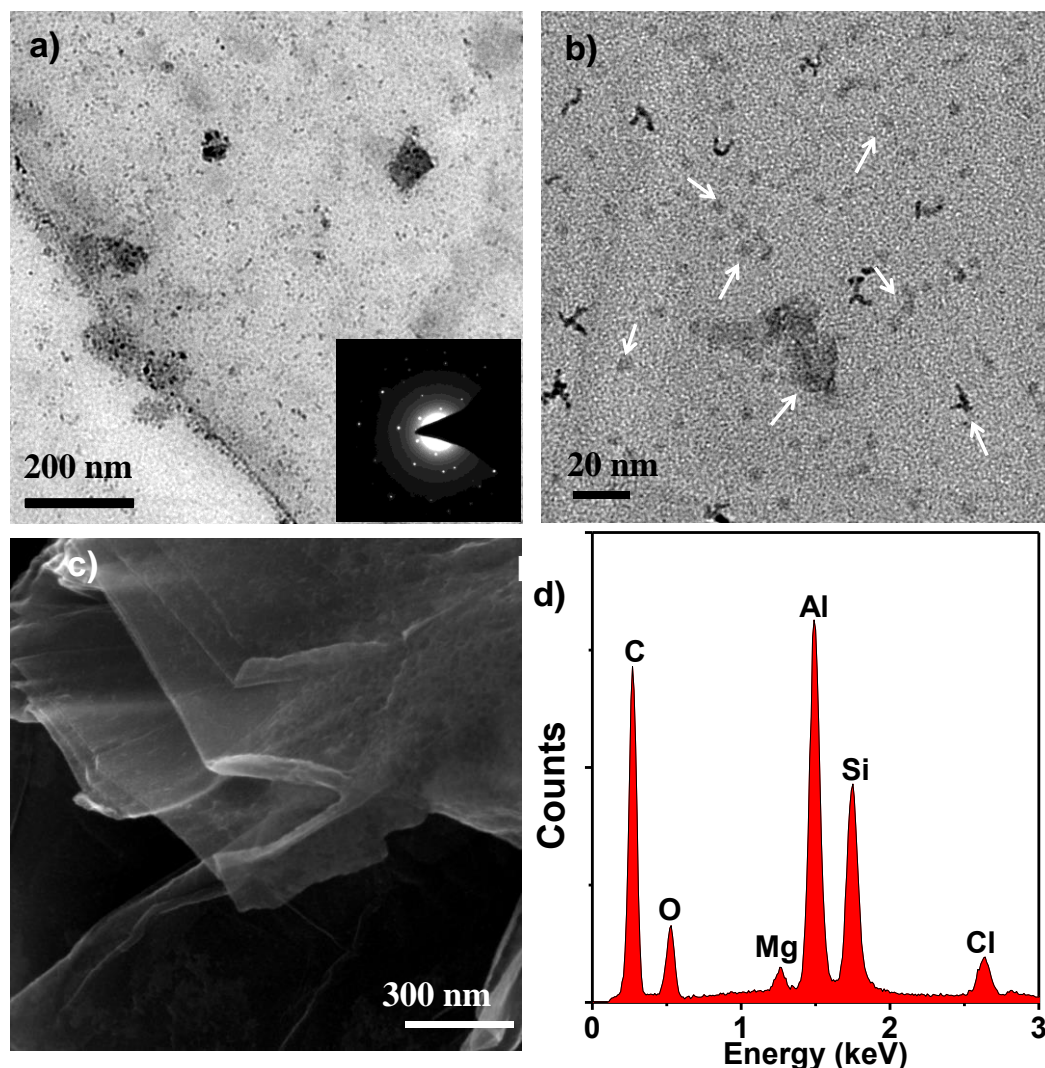


Figure 1.2.3. a) TEM image of the hybrid where clay is dispersed on RGO matrix. Inset shows ED pattern of RGO. b) High magnification TEM image show clay nanoparticles of size 5-50 nm c) FESEM image of the hybrids showing clay nanoparticles deposited on RGO. Distribution of clay nanoparticles is not very uniform. d) EDAX analysis of the composite showing presence of Mg, Cl and Si along with carbon, which confirms presence of clay in the hybrid.

Field emission scanning electron microscopy (FESEM) images of the AC-RGO-25 hybrid at low magnification show sheet like structures of RGO decorated with aminoclay nanoparticles (Figure 1.2.3 c). EDAX analysis show presence of Mg, Si and Cl associated with aminoclay (Figure 1.2.3 d). Elemental mapping also shows co-existence of clay and RGO in the hybrid (Figure 1.2.4). The powder XRD patterns (Figure 1.2.5 a) show the characteristic (d_{060}) diffraction peak around $2\theta = 60^\circ$

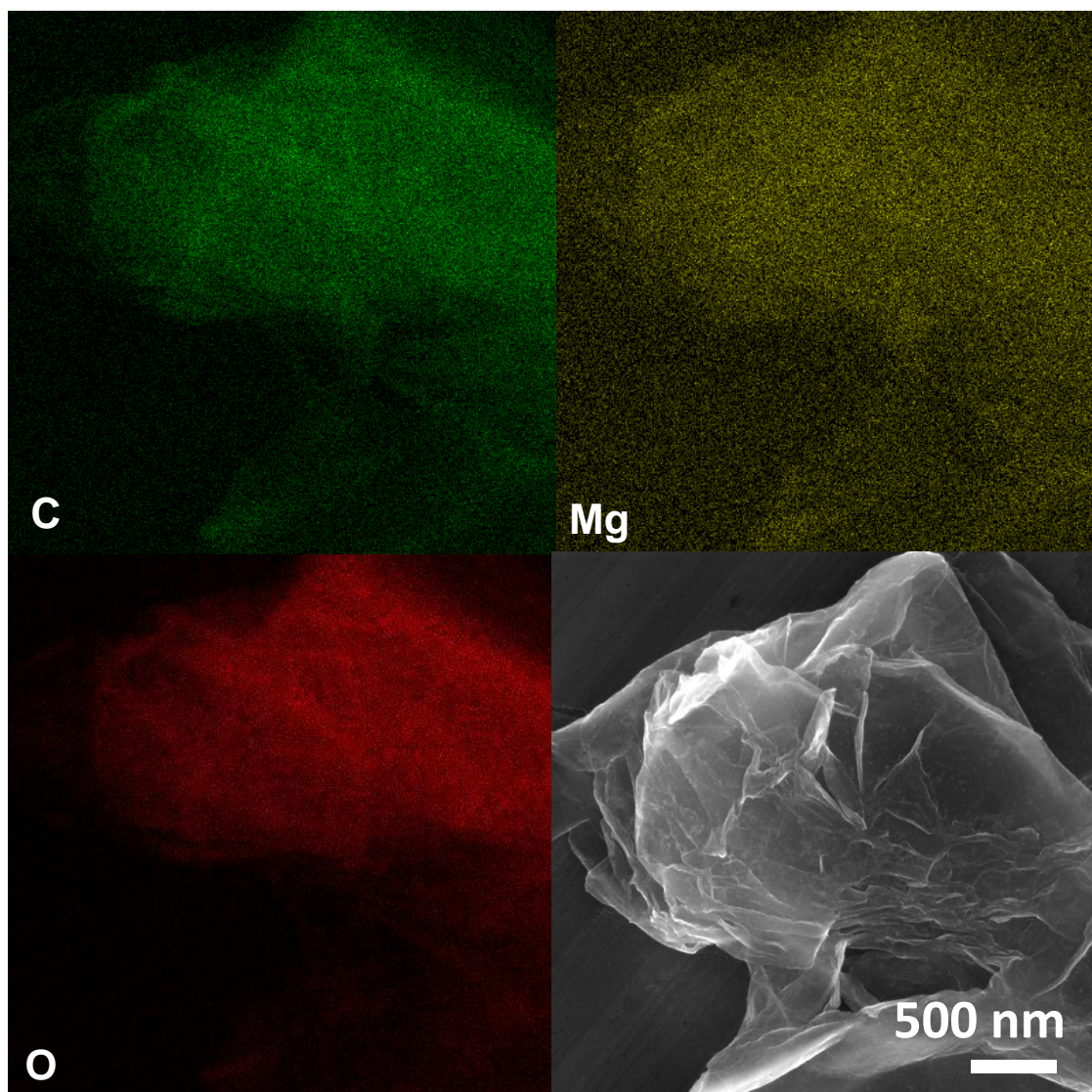


Figure 1.2.4. Elemental mapping of the composite showing distribution of aminoclay (Mg, O) on RGO (C, O)

corresponding to the 2:1 trioctahedral smectite clay for all the AC-RGO hybrids. However, the low angle peak observed for aminoclay interlayer spacing at $2\theta = 5.4^\circ$ (16, 17) gets broadened and weakened with increasing amount of RGO (AC-RGO-25 and AC-RGO-35). This clearly suggests the existence of aminoclay in the form of nanostructures over the RGO sheets. The peaks corresponding to RGO at 23° and 42° were visible for the hybrids with higher RGO content (AC-RGO-25 & 35). Raman spectra (Figure 1.2.5 b) on AC-RGO-25 shows the characteristic 2D band at 2650 cm^{-1} associated with reduced graphene oxide in addition to the D and G bands at 1325 cm^{-1} and 1580 cm^{-1} respectively.

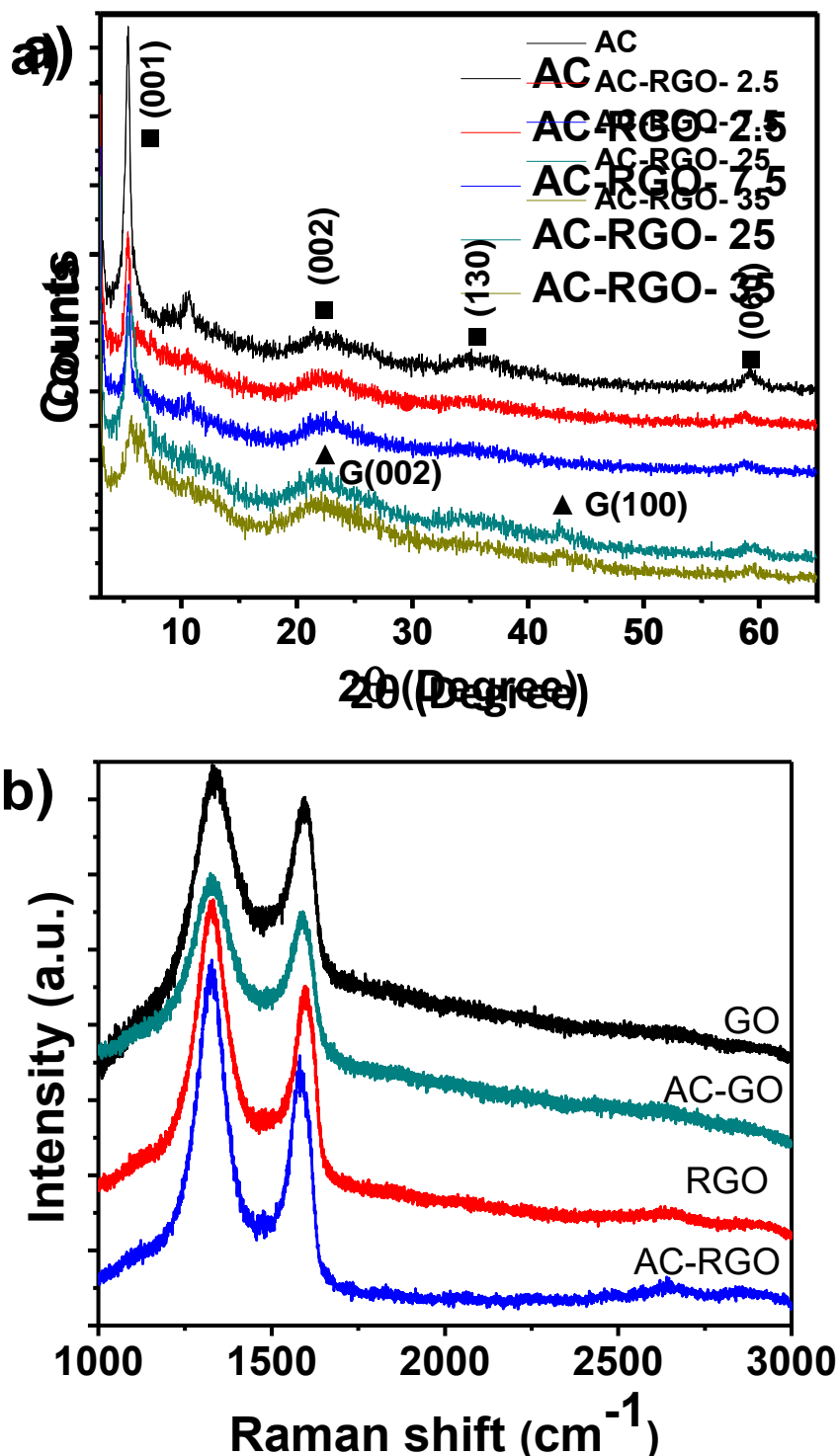


Figure 1.2.5. a) PXRD pattern of aminoclay and different aminoclay- RGO hybrids. ■ and ▲ represents aminoclay and RGO peaks respectively. b) Raman spectra (green laser) of GO, RGO and their clay hybrids. Appearance of 2D band (2750 cm⁻¹) is evident in both RGO and AC-RGO.

The appearance of 2D band at 2650 cm^{-1} in AC-RGO-25 supports the conversion of GO to RGO on reduction of AC-GO-25. Furthermore, the anchored clay nanostructures prevent the aggregation of RGO layers, as evident from the shift in the G band from 1593 cm^{-1} for the bulk RGO to 1580 cm^{-1} for AC-RGO-25(27).

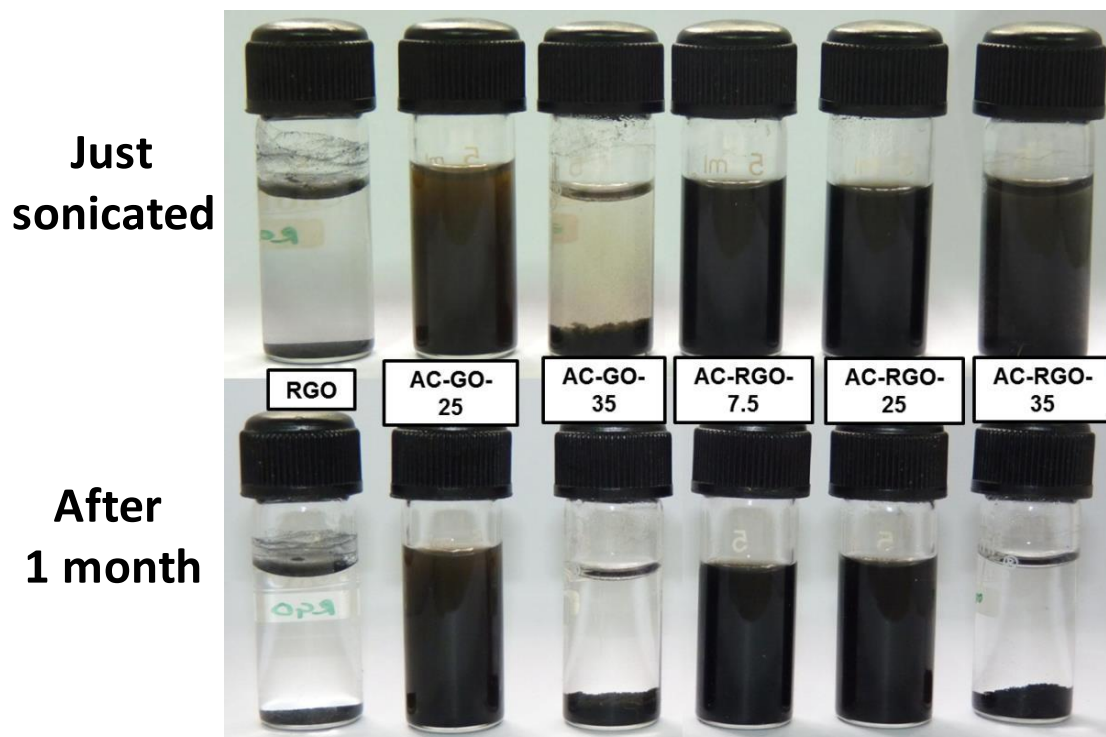


Figure 1.2.6. Picture of aqueous dispersion of RGO, aminoclay–RGO and aminoclay–GO hybrids. Top panel- as prepared, 2 min after sonication, bottom panel- same samples left for 30 days.

Figure 1.2.6 shows the optical images of the aqueous dispersions of AC-GO and AC-RGO hybrids kept for one month along with the freshly prepared dispersions. Aqueous dispersion of RGO is also shown for comparison. As expected, the strong hydrophobic interaction between the layers facilitates the immediate precipitation of RGO in water. The AC-GO-25 hybrid, which contains 25 wt % of GO, dispersed well in water and the dispersion was stable for more than a month. However, hybrid containing 35 wt% GO precipitates immediately, most probably by the neutralization of positive charges in the aminoclay by negatively charged GO. Indeed, zeta potential analysis shows that the highly positive zeta potential observed for the hybrids decrease as the GO content in the AC-GO hybrids increases. (Figure 1.2.7) For example, AC-GO-7.5 (containing 7.5% GO) shows the zeta potential of +28 mV which decrease to +22 mV for AC-GO-25

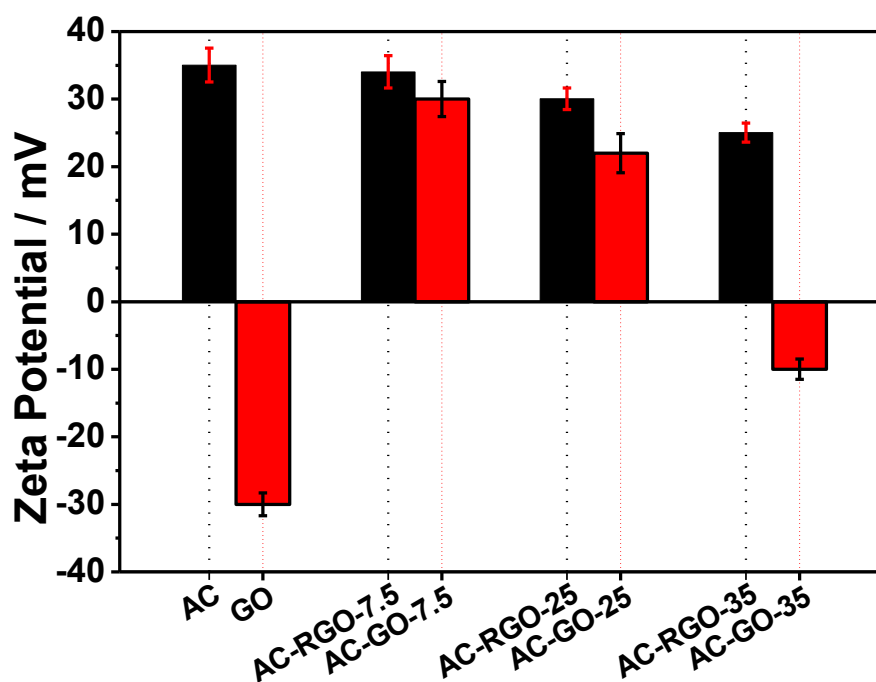


Figure 1.2.7. Zeta potential of aqueous dispersions of aminoclay-GO and aminoclay – RGO hybrids, along with aminoclay and GO.

(containing 25% GO). Further increase in the GO content to 35% (AC-GO-35) neutralizes the positive charges and reverses the zeta potential to slightly negative value (Figure 1.2.7). Reduction of AC-GO-25 hybrid by hydrazine hydrate increases the zeta potential to more positive value probably due to the removal of oxygen functional groups from GO. The charge repulsion from the excess positively charged amine groups of the clay, coated on the RGO layers prevents their aggregation and keeps the dispersion stable for more than a month. It is also interesting to note that AC-GO-35 dispersion which precipitates out immediately becomes stable for about 12 h when it is in reduced form (AC-RGO-35). The relative dispersion stability can be explained from the increase in zeta potential from -10 mV in AC-GO-35 to +20 mV in AC-RGO-35. But the dispersion stability of AC-RGO-35 is not as high as that of other hybrids containing lesser amount of RGO. This is because in high RGO content, the hydrophobic interaction becomes dominant than electrostatic repulsion.

The highest concentration of stable dispersion is achieved by dispersing 30 mg of AC-RGO-25 in 1 mL water, which makes RGO dispersion concentration 7.5 mg/mL. To

the best of our knowledge this is the highest concentration of aqueous dispersion of RGO achieved.

Adsorption of biomolecules on inorganic substrate is highly beneficial and finds its application in many fields. For example, adsorption of proteins or enzymes on inorganic supports increase their temperature stability(28), layered materials are highly useful for gene encapsulation and delivery,(29) simultaneous adsorption of DNA and proteins on a surface helps to uncover many aspects of DNA protein interaction which are useful for structural biology and proteomics.(30) These applications preferably require a hydrophobic surface. Protein adsorption on hydrophobic surface is well known.(31) In case of DNA, though the interaction is electrostatic, hydrophobic moieties enhance the adsorption.(32) Another prerequisite for adsorption of biomolecule is water dispersibility of the moieties, which increases the interaction with solvated biomolecules and enhances the adsorption. In this regard, the AC-RGO hybrids which can be dispersed in aqueous medium in high concentrations and contain hydrophobic and hydrophilic domains can find huge application. Adsorption of DNA and Cytochrome C is performed as a proof of concept study to demonstrate the amphiphilic character of these hybrids. Figure 1.2.8 a shows the adsorption of DNA over the RGO, aminoclay, and AC-RGO hybrids containing different amounts of RGO. As expected, the positively charged aminoclay has a strong affinity for the negatively charged DNA at pH 10.3. RGO on the other hand did not show any significant uptake. Poor aqueous dispersibility and the negative charge on RGO hinder the effective interaction with DNA. Interestingly AC-RGO-7.5 and AC-RGO-25 show higher amount of DNA uptake than aminoclay itself. This suggests that though the nature of interaction between DNA and aminoclay hybrids are mostly electrostatic, hydrophobicity of RGO also contribute to the uptake. Hydrophobic domains in the dispersed AC-RGO hybrids interact with the hydrophobic nucleobases of DNA and hence increase its adsorption. Though the amount of interaction in double stranded DNA is very less compared to single stranded DNA because of the pairing of nucleobases it still plays a part.(32) The increased uptake also hints the exposure of individual RGO sheets to the solution as a result of hybridization with aminoclay. As the RGO content increases to 35 wt% in the hybrids the uptake of DNA decreases which is in commensurate with its poor dispersibility in water. The amount of DNA uptake was more than that observed in mesoporous silica materials ($\sim 6 \mu\text{g}/\text{mg}$). (33, 34)

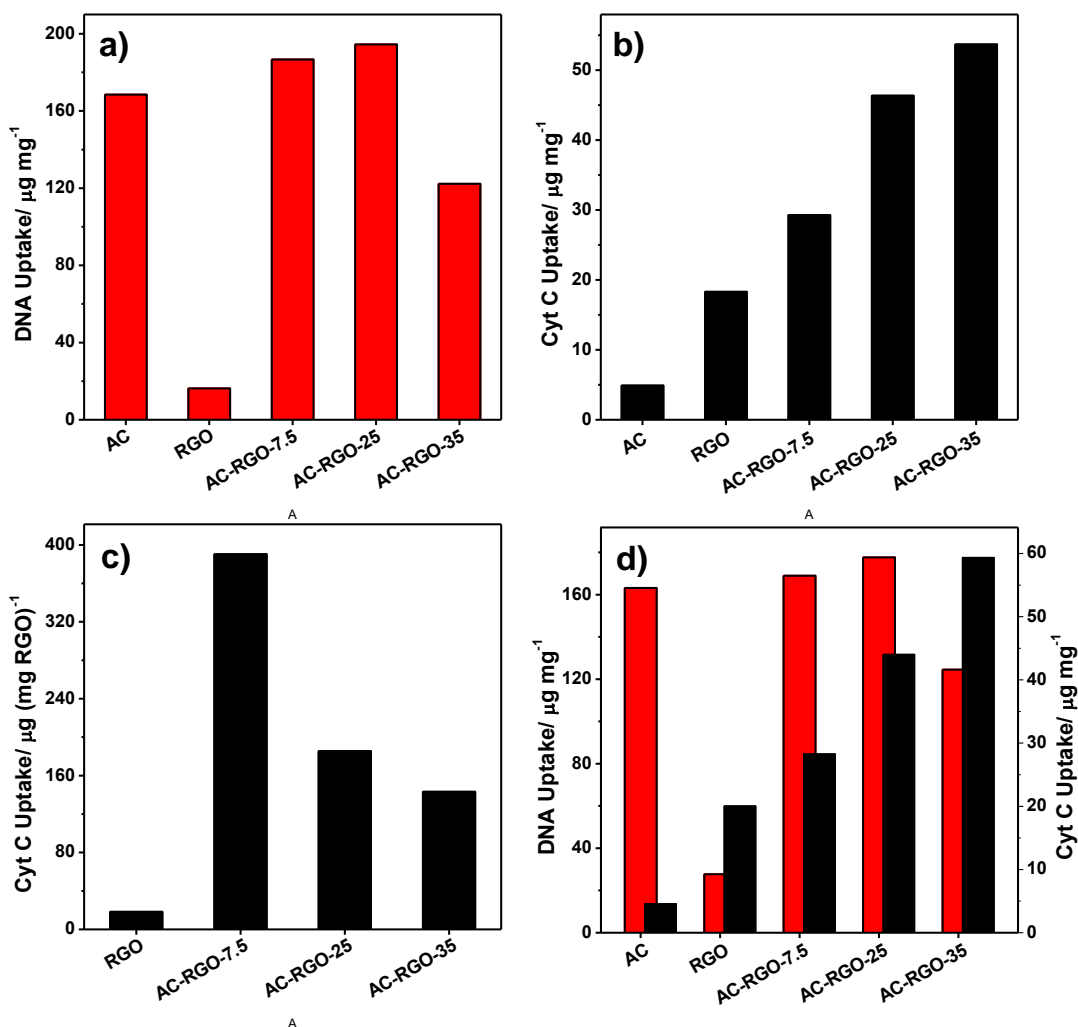


Figure 1.2.8. Bar diagram for uptake of DNA and cytochrome C (Cyt C) in AC, RGO and different AC-RGO hybrids at pH 10.3. a) Uptake of DNA, b) Uptake of Cyt C, c) Estimated uptake of Cyt C per mg of RGO in the AC-RGO hybrids and in RGO, d) Simultaneous uptake of DNA and Cyt C over AC, RGO and AC-RGO hybrids.

The adsorption of Cytochrome C (Cyt C) was studied at its isoelectric point (pH 10.3) and the results are shown in Figure 1.2.8b. Cyt C being neutral at its isoelectric point did not show any significant uptake either with pure aminoclay or with RGO whereas, the hybrids show considerable uptake of Cyt C. The amount of uptake increases with increased amount of RGO in the hybrid. Since the electrostatic interaction is unlikely to influence the adsorption at the isoelectric pH, where Cyt C is neutral, it is evident that hydrophobic interaction plays a dominant role in higher amount of adsorption in the

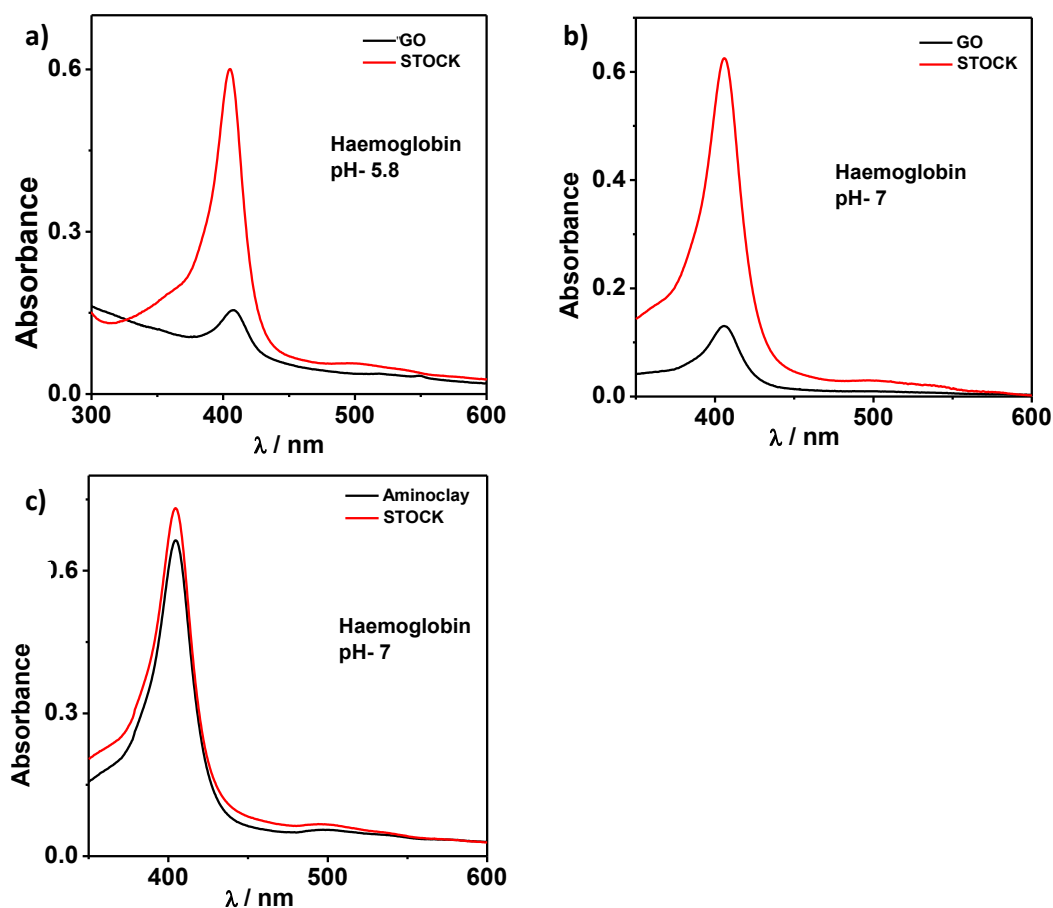


Figure 1.2.9. Adsorption profiles of a) Haemoglobin on GO at pH 5.8, where Haemoglobin is positively charged, b) Haemoglobin on GO at pH 7, where the protein is almost neutral, c) Adsorption of haemoglobin on AC at pH 7.

hybrids. In case of RGO, the strong interlayer interaction resulted in settling of the sheets in water and reduces the Cyt C uptake. In the hybrids, the aminoclay nanoparticles play a pivotal role in blocking the interlayer interaction between the RGO layers and hence large hydrophobic regions of RGO are accessible to Cyt C. This is reflected in increase in uptake of protein in the hybrids. Indeed, the hydrophobic interaction play a strong role is confirmed by carrying out the adsorption of haemoglobin on graphene oxide at pH 5.8 when both of them are oppositely charged (Figure 1.2.9 a). The uptake of haemoglobin in GO is high and comparable to the uptake of the protein at pH 7 where it is almost neutral (Figure 1.2.9 b). Again, the contribution of aminoclay to the adsorption can be ruled out as it adsorbs neither Cyt C nor haemoglobin (Figure 1.2.9 c) at their respective isoelectric points.

This strongly indicates that unlike DNA adsorption, where the electrostatic forces are crucial, protein uptake is strongly influenced by the hydrophobic interaction. The discontinuous sp^2 hybridized patches present in GO(35) interacts with the hydrophobic amino acid side chains of the protein making the adsorption possible. Interestingly, when the amount of Cyt C uptake plotted against per mg of RGO in hybrids it was found that AC-RGO-7.5 has maximum protein adsorption (Figure 1.2.8c). This is quite understandable that at low amount of RGO in the hybrids, all the RGO layers are highly exfoliated by the large amount of positively charged aminoclay nanoparticles. As the RGO content increases amount of aminoclay nanoparticles available per sheet decreases and the RGO sheets are not as exfoliated as those with low loading. Hence the available amount of RGO surface interacting with the protein decreases which explains the lower uptake in AC-RGO-35. Indeed, we observe an increase in uptake by RGO in the AC-RGO hybrids by more than 20 times in the hybrid than RGO itself.

For simultaneous adsorption of these biomolecules the hybrids were allowed to stand with a solution containing 1 mg/mL of both cytochrome C and DNA in 0.1M tris buffer as before. The hybrids simultaneously adsorb both the biomolecules and the adsorption does not differ significantly from the individual adsorption profiles (Figure 1.2.8 d). This similarity indicates that there are hydrophilic pockets (aminoclay nanoparticles) where DNA gets adsorbed and hydrophobic pockets (uncoated RGO sheet segments) where adsorption of Cyt C happens, making the adsorption of one biomolecule independent of the presence of other.

1.2.5. Conclusion

In conclusion, aminoclay-RGO hybrids with high water dispersibility were prepared in a simple method. Highest concentration of RGO (7.5 mg/mL) could be dispersible in aqueous media for the first time in the form of AC-RGO hybrids. The dispersion stability of the hybrids is a tradeoff between electrostatic repulsion between positively charged aminoclay nanoparticles and hydrophobic interaction between RGO sheets. The ambiphilic nature of these hybrids is utilized for the simultaneous sorption of cytochrome C and DNA – two different kinds of biomolecules. Furthermore, we believe that the amine groups from the clay would give the flexibility to modify the surface of the GO and RGO with various biomolecule receptors to improve the

selectivity in sensing applications. Besides, these hybrids can also be used as catalytic support which could provide localized interfaces to carry out biphasic reactions.

1.2.6. References

1. K. S. Novoselov *et al.*, A roadmap for graphene. *Nature* **490**, 192-200 (2012).
2. C. Wang *et al.*, Gold Nanoclusters and Graphene Nanocomposites for Drug Delivery and Imaging of Cancer Cells. *Angew. Chem. Int. Ed.* **50**, 11644-11648 (2011).
3. S. Seo *et al.*, Solution-Processed Reduced Graphene Oxide Films as Electronic Contacts for Molecular Monolayer Junctions. *Angew. Chem. Int. Ed.* **51**, 108-112 (2012).
4. J. T. Robinson, F. K. Perkins, E. S. Snow, Z. Wei, P. E. Sheehan, Reduced graphene oxide molecular sensors. *Nano Lett.* **8**, 3137-6277 (2008).
5. P. A. Russo *et al.*, Room-Temperature Hydrogen Sensing with Heteronanostructures Based on Reduced Graphene Oxide and Tin Oxide. *Angew. Chem. Int. Ed.* **51**, 11053-11057 (2012).
6. J. R. Potts, D. R. Dreyer, C. W. Bielawski, R. S. Ruoff, Graphene-based polymer nanocomposites. *Polymer* **52**, 5-30 (2011).
7. D. R. Dreyer, C. W. Bielawski, Carbocatalysis: Heterogeneous carbons finding utility in synthetic chemistry. *Chem. Sci.* **2**, 1233-2473 (2011).
8. W. Gao *et al.*, Direct laser writing of micro-supercapacitors on hydrated graphite oxide films. *Nat. Nanotechnol.* **6**, 496-996 (2011).
9. X. Sun *et al.*, Nano-Graphene Oxide for Cellular Imaging and Drug Delivery. *Nano Res.* **1**, 203-415 (2008).

10. Y. Si, E. Samulski, Synthesis of water soluble graphene. *Nano Lett.* **8**, 1679-1682 (2008).
11. M. Lotya, P. King, U. Khan, S. De, J. Coleman, High-concentration, surfactant-stabilized graphene dispersions. *ACS Nano* **4**, 3155-3217 (2010).
12. J.-W. T. Seo, A. A. Green, A. L. Antaris, M. C. Hersam, High-Concentration Aqueous Dispersions of Graphene Using Nonionic, Biocompatible Block Copolymers. *J. Phys. Chem. Lett.* **2**, 1004-1008 (2011).
13. V. Georgakilas *et al.*, Organic functionalisation of graphenes. *Chem. Commun.* **46**, 1766-1774 (2010).
14. Y. Xu, H. Bai, G. Lu, C. Li, G. Shi, Flexible graphene films via the filtration of water-soluble noncovalent functionalized graphene sheets. *J. Am. Chem. Soc.* **130**, 5856–5857 (2008).
15. D. Parviz *et al.*, Dispersions of Non-Covalently Functionalized Graphene with Minimal Stabilizer. *ACS Nano* **6**, 8857-8867 (2012).
16. E. Muthusamy, D. Walsh, S. Mann, Morphosynthesis of Organoclay Microspheres with Sponge-like or Hollow Interiors. *Adv. Mater.* **14**, 969-972 (2002).
17. S. L. Burkett, A. Press, S. Mann, Synthesis, Characterization, and Reactivity of Layered Inorganic–Organic Nanocomposites Based on 2:1 Trioctahedral Phyllosilicates. *Chem. Mater.* **9**, 1071-1073 (1997).
18. L. Ukrainczyk, R. A. Bellman, A. B. Anderson, Template Synthesis and Characterization of Layered Al– and Mg–Silsesquioxanes. *J. Phys. Chem. B* **101**, 531-539 (1997).

19. Y. Fukushima, M. Tani, An organic/inorganic hybrid layered polymer: methacrylate-magnesium(nickel) phyllosilicate. *J. Chem. Soc., Chem. Commun.*, 241-242 (1995).
20. S. M. Alhassan, S. Qutubuddin, D. A. Schiraldi, Graphene Arrested in Laponite-Water Colloidal Glass. *Langmuir* **28**, 4009-4015 (2012).
21. C. Zhang *et al.*, Aqueous stabilization of graphene sheets using exfoliated montmorillonite nanoplatelets for multifunctional free-standing hybrid films via vacuum-assisted self-assembly. *J. Mater. Chem.* **21**, 18011-18017 (2011).
22. C. Nethravathi, B. Viswanath, C. Shivakumara, N. Mahadevaiah, M. Rajamathi, The production of smectite clay/graphene composites through delamination and co-stacking. *Carbon* **46**, 1773-1781 (2008).
23. W. S. Hummers Jr, R. E. Offeman, Preparation of graphitic oxide. *J. Am. Chem. Soc.* **80**, 1339-2678 (1958).
24. K. K. R. Datta *et al.*, Observation of Pore-Switching Behavior in Porous Layered Carbon through a Mesoscale Order–Disorder Transformation. *Angew. Chem.* **123**, 4015-4019 (2011).
25. O. C. Compton, D. A. Dikin, K. W. Putz, L. C. Brinson, S. T. Nguyen, Electrically Conductive “Alkylated” Graphene Paper via Chemical Reduction of Amine-Functionalized Graphene Oxide Paper. *Adv. Mater.* **22**, 892-896 (2010).
26. J. Oh *et al.*, Graphene oxide porous paper from amine-functionalized poly(glycidyl methacrylate)/graphene oxide core-shell microspheres. *J. Mater. Chem.* **20**, 9200-9204 (2010).
27. A. M. Rao *et al.*, Effect of van der Waals Interactions on the Raman Modes in Single Walled Carbon Nanotubes. *Phys. Rev. Lett.* **86**, 3895-3898 (2001).

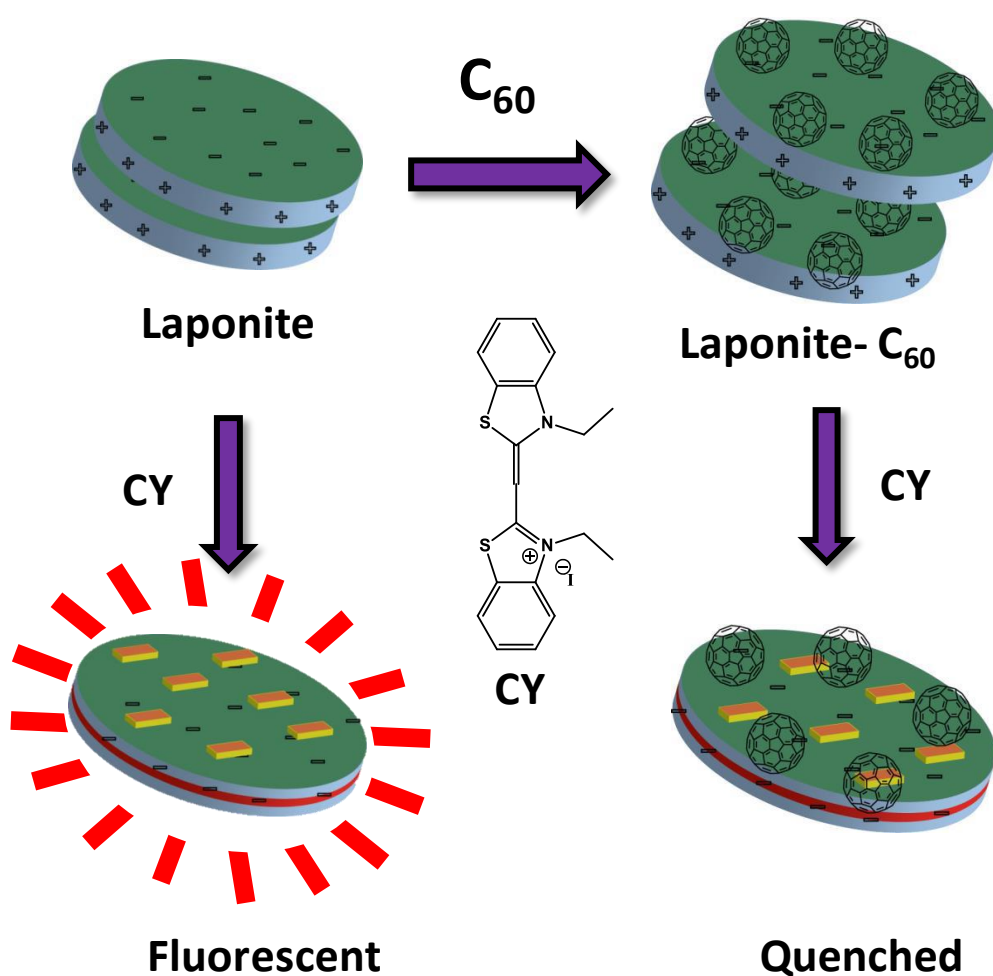
28. A. J. Patil, E. Muthusamy, S. Mann, Synthesis and Self-Assembly of Organoclay-Wrapped Biomolecules. *Angew. Chem.* **116**, 5036-5041 (2004).
29. J.-H. Choy, S.-Y. Kwak, Y.-J. Jeong, J.-S. Park, Inorganic Layered Double Hydroxides as Nonviral Vectors. *Angew. Chem. Int. Ed.* **39**, 4041-4045 (2000).
30. E. M. Boon, J. E. Salas, J. K. Barton, An electrical probe of protein-DNA interactions on DNA-modified surfaces. *Nat. Biotechnol.* **20**, 282-286 (2002).
31. A. Vinu, C. Streb, V. Murugesan, M. Hartmann, Adsorption of Cytochrome C on New Mesoporous Carbon Molecular Sieves. *J. Phys. Chem. B* **107**, 8297-8299 (2003).
32. A. J. Patil, J. L. Vickery, T. B. Scott, S. Mann, Aqueous Stabilization and Self-Assembly of Graphene Sheets into Layered Bio-Nanocomposites using DNA. *Adv. Mater.* **21**, 3159-3164 (2009).
33. F. Gao, P. Botella, A. Corma, J. Blesa, L. Dong, Monodispersed Mesoporous Silica Nanoparticles with Very Large Pores for Enhanced Adsorption and Release of DNA. *J. Phys. Chem. B* **113**, 1796-1804 (2009).
34. S. M. Solberg, C. C. Landry, Adsorption of DNA into Mesoporous Silica. *J. Phys. Chem. B* **110**, 15261-15268 (2006).
35. J. Kim, L. J. Cote, J. Huang, Two Dimensional Soft Material: New Faces of Graphene Oxide. *Acc. Chem. Res.* **45**, 1356-1364 (2012).

Chapter- 1.3

Highly water dispersible clay- Fullerene hybrids: Surface mediated quenching of cyanine dyes

Summary:

Very low water solubility of fullerene C_{60} prevents its use in many areas such as catalysis and biomedical applications. We have demonstrated a cheap and easy way to disperse fullerene in aqueous media by immobilization onto laponite surface. These laponite- C_{60} hybrids show high water dispersibility and fullerene concentration of up to 3×10^{-4} M was achieved. We have also demonstrated the surface mediated quenching of 3,3' dithiacyanine molecules in aqueous solution.



1.3.1. Introduction:

Ever since the discovery by Kroto et. al.(1) and the first large scale synthesis by Huffman and co-workers(2), fullerenes have caught everyone's imagination as the next highly functional material due to its exciting electronic (3) and catalytic (4-6) properties as well as its importance in biological applications (7, 8). One of the main reasons for not achieving its full potential of C₆₀ fullerene in many areas is its insolubility in aqueous media. A list of solubility of fullerene in different media is given in the table below. The solubility of C₆₀ in water is in the order of 10⁻²⁴ moles/litre (9). Hence, water solution of fullerene is of no value for many applications.

Solvent	Solubility (mol/L)
1-chloronaphthalene	7×10 ⁻²
1,2-dichlorobenzene	4×10 ⁻²
carbon disulphide	1×10 ⁻²
Chlorobenzene	1×10 ⁻²
Toluene	4×10 ⁻³
Benzene	2×10 ⁻³
Decane	1×10 ⁻³
Acetone	1×10 ⁻⁶
Water	2×10 ⁻²⁴

Table 1.3.1. Solubility of C₆₀ fullerene in different solvents.

Many methods have been developed to overcome this problem, such as functionalization of fullerene with hydrophilic counterparts (10-12) immobilizations in cyclodextrin moiety etc. have been explored to improve their solubility in water (13). However, most of the organic functionalization methods have serious drawback of not being regio-specific, having over functionalized or giving low yield which lower their scope to produce materials with much practical value. Keeping the fullerene dispersed in water with its structure and functionality intact would widen the scope of application of fullerene beyond organic media.

1.3.2. Scope of the present investigation:

Herein we present a very interesting clay based strategy to enhance the application of fullerene in aqueous medium. Clays have been used as hosts to organic moieties for a long time since mayan civilization, more recent examples include use of laponite as a hydrophilic matrix to solubilize indigo and red dyes(14, 15). Very few reports exist in literature that deals with incorporation of fullerenes into clay(16) or LDH matrix(17), but none of them show the high water dispersibility we have seen here.

In this report we show C₆₀ fullerene, otherwise insoluble in aqueous phase, while being immobilized in an inorganic clay matrix (Laponite) can be dispersed in aqueous phase. Furthermore, we have demonstrated that the laponite- fullerene hybrids can quench dithiacyanine dyes embedded on the clay surface.

1.3.3. Experimental Procedure:

1.3.3.1 Materials and characterization techniques:

Laponite XLG clay was obtained from Rockwood Additives Pvt. Ltd., Sodium polyacrylate (Sigma), 3,3'-diethylthiacyanine iodide, (Sigma) C₆₀ (Alfa- Aesar) were used without any further purification. Toluene and Acetonitrile (AR grade, Merck) were used as solvents.

Powder X-ray diffraction (PXRD) patterns were recorded using Rigaku diffractometer using Cu K α radiation, ($\lambda=1.54 \text{ \AA}$). Electronic absorption spectra were recorded on a Perkin Elmer Lambda 750 UV-Vis-NIR Spectrometer. 1 cm path length cuvette was used for recording the spectra. Zeta potential studies were performed with Malvern Zetasizer nano ZS with a green laser at 173° backscattering detector. Photoluminescence spectra were recorded on Perkin Elmer Ls 55 luminescence spectrometer.

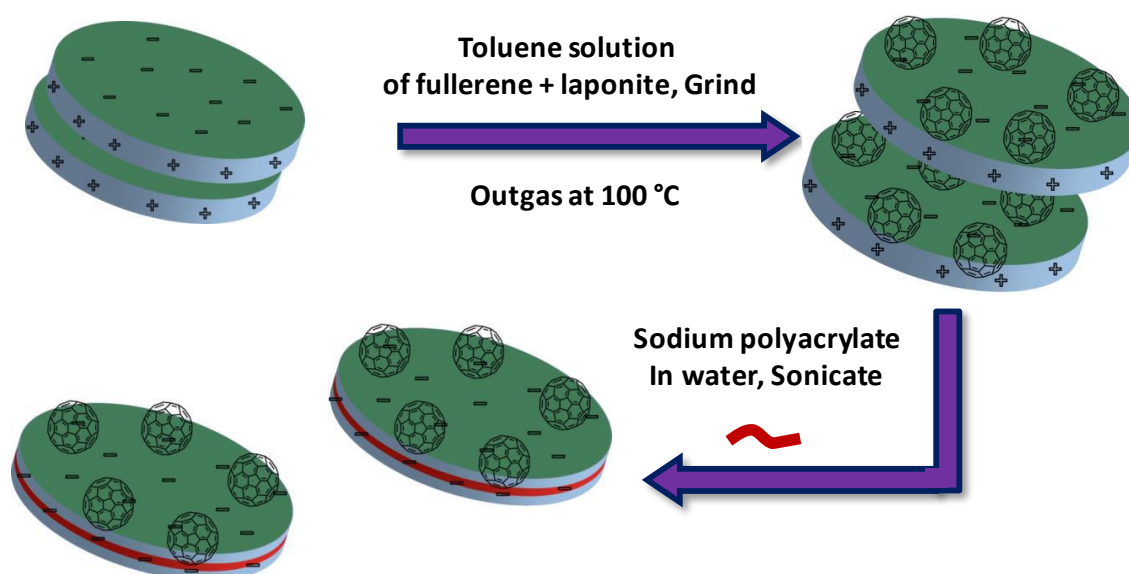
1.3.3.2. Preparation of laponite C₆₀ hybrids (LPC₆₀):

Laponite –fullerene hybrids were prepared as follows. First the desired amount of fullerene was dissolved in 10-15 mL of toluene. 100 mg of laponite was taken in a mortar. The fullerene solution was added dropwise with continuous grinding until toluene evaporated. The obtained solid was outgassed at 100 °C under vacuum to

remove excess toluene and water. Scheme 1.3.1 shows synthetic scheme. Different compositions of hybrids were prepared by this method with fullerene content of 1.0, 1.5 and 2.3 wt% which are denoted by LPC_{60-x} where x is the weight % of C_{60} in the hybrid.

1.3.3.3. Dispersion of Laponite fullerene hybrids in water:

The required amount of LPC_{60} hybrids were added to Millipore water under sonication. The suspension was sonicated for 30 min to obtain a clear dispersion. The LPC_{60} hybrids form Wigner glass type arrested gel over time, to overcome this a stabilizing agent, sodium polyacrylate was added to the solution (4 mg/ 20 mg of hybrid) prior to the addition of LPC_{60} .



Scheme 1.3.1. Schematics of preparation of LPC_{60} from Laponite and fullerene and their dispersion in water.

1.3.3.4. UV-vis and PL studies:

20 mg/mL Laponite and LP loaded with 1.5 wt% C_{60} stock solution was prepared with 4mg/mL poly sodium acrylate solution. 10^{-4} M 3,3'-Diethylthiacyanine iodide solution was used as stock solution. The UV-vis studies were performed with fixed concentration of dithiacyanine at 10^{-5} M while varying the Laponite and LPC_{60} concentration as required in a 1 cm quartz cuvette as required. Steady state PL studies were performed with similar solutions in a 2 mm quartz cuvette in a front facing geometry.

1.3.3.5. Time correlated single photon counting (TCSPC) studies:

The lifetime measurements were carried out with an EPLED-380 ($\lambda_{\text{ex}} = 404 \text{ nm}$) pico second pulsed light emitting diode.

1.3.4. Results and discussion:

Laponite was used here as an inorganic matrix to immobilize C_{60} fullerene. Laponite is a synthetic clay belonging to the family of smectites with a chemical composition $\text{Na}_{0.7}[\text{Mg}_{5.5}\text{Li}_{0.3}\text{Si}_8\text{O}_{20}(\text{OH})_4](\text{H}_2\text{O})_n$. It consists layers of octahedral Mg^{+2} sandwiched between tetrahedral SiO_4 layers. Partial substitution of Mg^{+2} in O_h sheets with Li^+ gives negative charge to the clay faces, while protonation of the dangling Si-OH and Mg-OH hydroxyl groups in the edges can bring positive charge in aqueous medium. Physically, laponite sheets have diameter of around 25 nm with thickness less than 1 nm (Figure 1.3.1). Due to its high charge and small size, this clay is highly water dispersible and hence a suitable host material for water insoluble molecules.

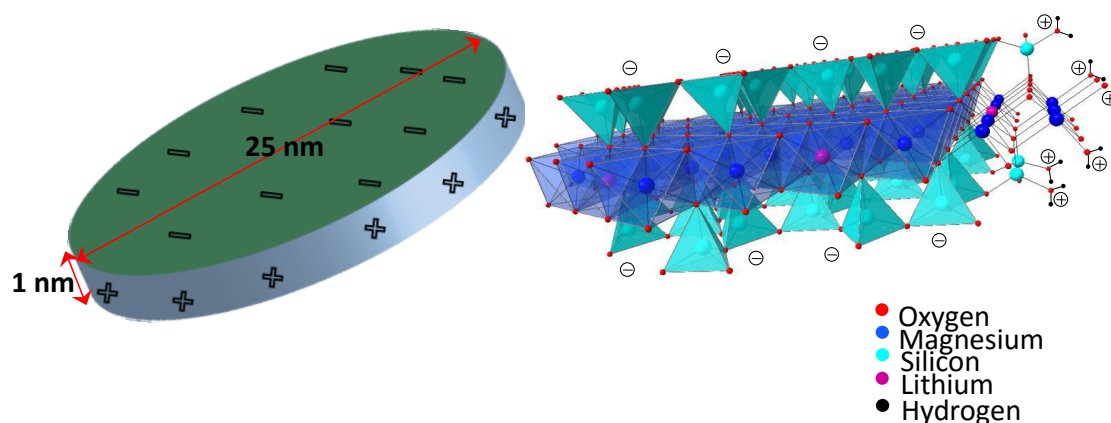


Figure 1.3.1. Structure of laponite- left: a laponite sheet, the diameter of which is about 25 nm, with a thickness of about 1 nm. Right- structure of the sheet consisting of Mg^{+2} octahedra (blue) sandwiched between tetrahedral Si^{+4} layers. The corner atoms of both octahedral and tetrahedral layer are oxygen (red). Partial substitution of Mg^{+2} with Li^{+1} gives the faces negative charge, while protonation of the edge hydroxyl groups (Si-OH and Mg-OH) gives the edges positive charge.

Scheme 1.3.1 shows the synthetic scheme of laponite- fullerene hybrids (LPC_{60}). Continuous grinding while mixing the fullerene in toluene is necessary to prevent the crystallization of fullerene molecules separately. The removal of water molecules from

laponite surface during degassing step allows fullerene molecules rearrange themselves on this surface rendering the interaction stronger.

We prepared laponite fullerene hybrids with different fullerene loadings of 1.0, 1.5 and 2.3 weight%. The amount of C₆₀ loading on laponite determined by TGA analysis, from the difference in weight loss between LP and LP loaded with different amounts of C₆₀ in the temperature range 250 °C to 500 °C. (Figure 1.3.2.a) Laponite fullerene hybrids with different amount of loading of C₆₀ fullerene were tested for their water solubility at concentration 10 mg/mL. While LP loaded with 1.0 wt% C₆₀ formed a transparent brown solution at 10 mg/mL, LP loaded with 1.5 wt% C₆₀ formed a dark brown solution, but both of them were fully dispersible in water. On the other hand, at higher fullerene loading, LP with 2.3 wt% C₆₀ formed a turbid dispersion (Figure 1.3.2.b). This can be explained from the fact that with increase in fullerene loading the hydrophobicity of the hybrids increase making their water dispersion more difficult. LP loaded with 1.5 wt% C₆₀ was taken up for further studies and is referred henceforth as LPC₆₀.

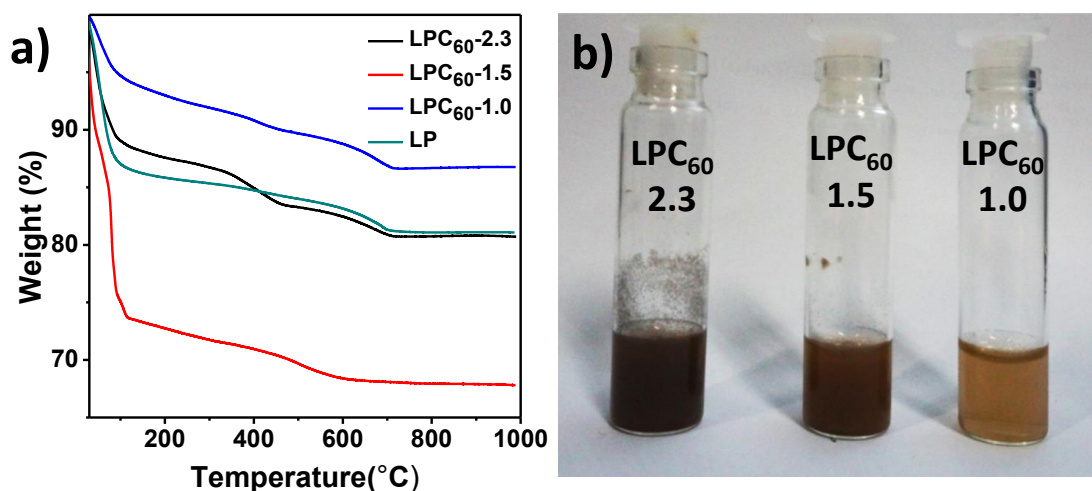


Figure 1.3.2. a) TGA profiles of Laponite fullerene hybrids with different amount of fullerene loading of 1.0, 1.5 and 2.3 weight%. b) Picture of water dispersions of different laponite-fullerene hybrids at 10 mg/mL.

Figure 1.3.3a inset shows the dispersion of LP and LPC₆₀ in water. While laponite dispersion is colourless, LPC₆₀ shows a deep brown colour due to incorporation of fullerene. UV- Vis spectra of LPC₆₀ (Figure 1.3.3.a) shows features identical to fullerene, including its characteristic absorption peak at 360 nm and a high intensity absorption peak at 240 nm assigned to $3^1T_{1u} \leftarrow 1^1A_g$, and $6^1T_{1u} \leftarrow 1^1A_g$ transitions. At

high concentration dispersion (10 mg/ mL) we also observe a weak and broad peak around 540 nm, which can be attributed to the vibronic transitions.(18)

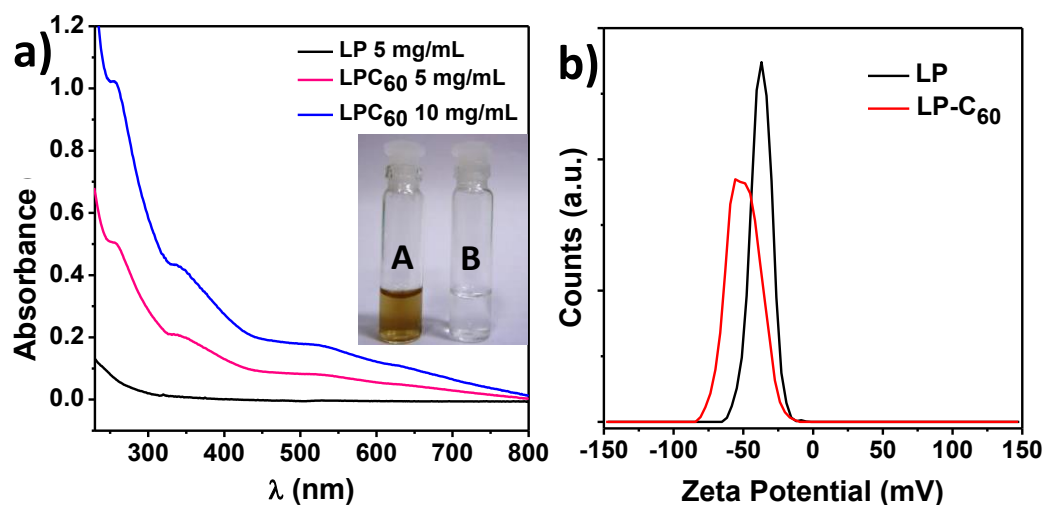


Figure 1.3.3. a) UV-vis spectra of laponite and LPC_{60} hybrids at different concentration. LPC_{60} hybrids show typical fullerene absorption peaks at 350 nm and 260 nm with a broad low intensity peak at 540 nm. Inset shows optical images of LPC_{60} (A) and LP (B) dispersion in water (5 mg/mL). b) Zeta potential distribution of laponite and LPC_{60} in water.

Zeta potential measurements (Figure 1.3.3.b) show that laponite immobilized fullerenes (LPC_{60}) possess higher negative zeta potential (-51.7 mV) compared to laponite (-37.2 mV). This could be attributed to acquisition of negative charge by fullerene molecules in aqueous media as a form of charge transfer from the water molecules due to its superior electron affinity(19).

At lower concentration (< 20 mg/mL), the LPC_{60} forms transparent solution, however, at higher concentration it forms gel due to the electrostatic interaction between the positively charged edges and negatively charged faces (the house of cards arrangement) (Figure 1.3.4a and c). The highest concentration of fullerene that can be achieved without gel formation was 3×10^{-4} M (without addition of polyanion), which is around 18 orders higher than solubility of fullerene in water. The gel formation can be prevented to some extent by coating the positively charged edges of laponite with a negatively charged polymer like sodium polyacrylate (Figure 1.3.4b and d), however, excess of this polymer increases the ionic strength of the solution, thus resulting lower solubility. It is clearly shown that the dispersion capacity of fullerene in aqueous phase

is only limited by the water dispersibility and gel formation by laponite itself.

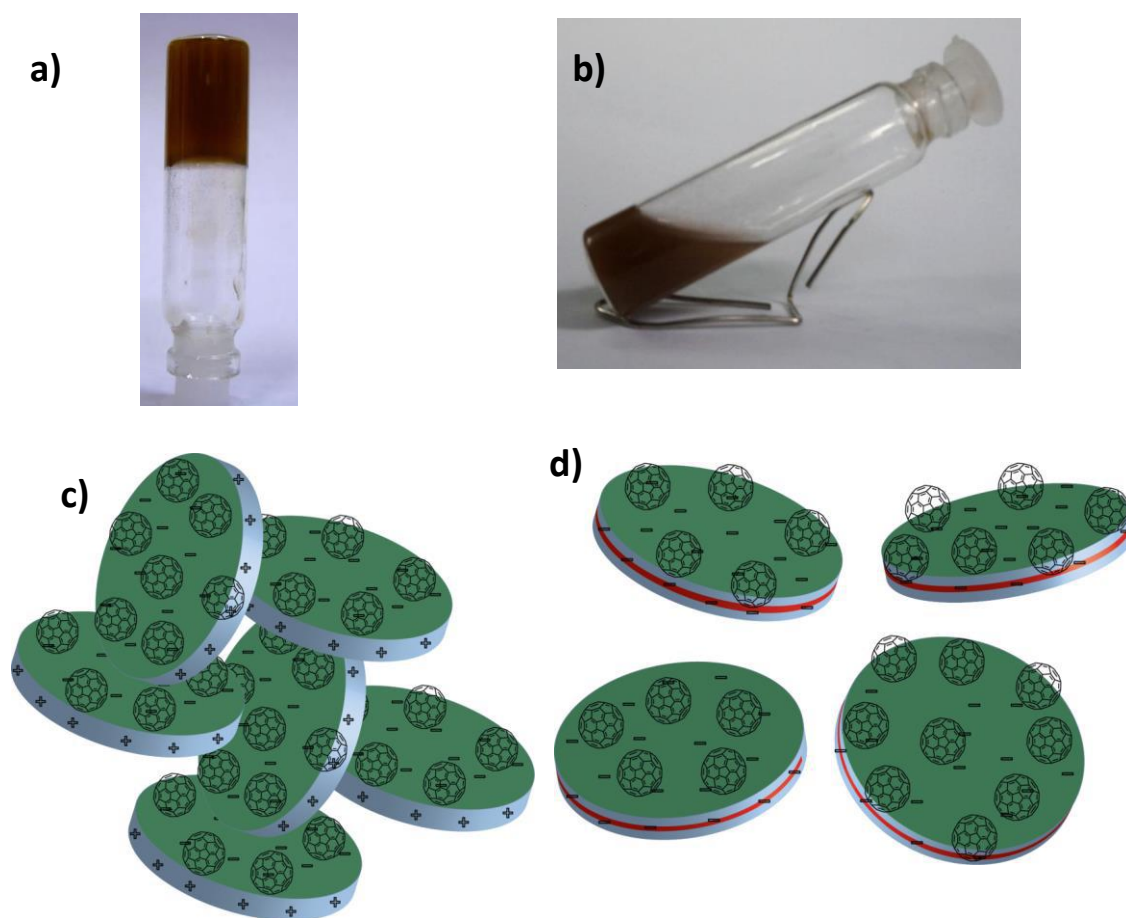


Figure 1.3.4. *a) and b) Images of high concentration (20 mg/mL) LPC_{60} hybrids in absence and presence of sodium polyacrylate. c) and d) represents the schematic of LPC_{60} hybrids in gel formation and in presence of sodium polyacrylate (red)*

The powder X-ray diffraction pattern of laponite show a low angle peak at $2\theta = 5.9^\circ$ ($d=1.5$ nm) corresponding to interlayer distance between laponite sheets (Figure 1.3.5). The higher angle peaks correspond to in-plane lattices of laponite, all the peaks are broad and have shark fin like feature, characteristic of turbostratic effect, commonly observed in clay minerals. After immobilization of fullerene, the pattern remains more or less same, depicting no loss of ordering of laponite. The unchanged nature of low angle peak of the laponite-fullerene hybrid is in accordance with immobilisation of uncharged species(14), which do not affect the d - spacing the way intercalation of charged molecules do. At high loading characteristic XRD peaks of fullerene crystal start appearing at $2\theta = 10.5^\circ$ and 17° (20).

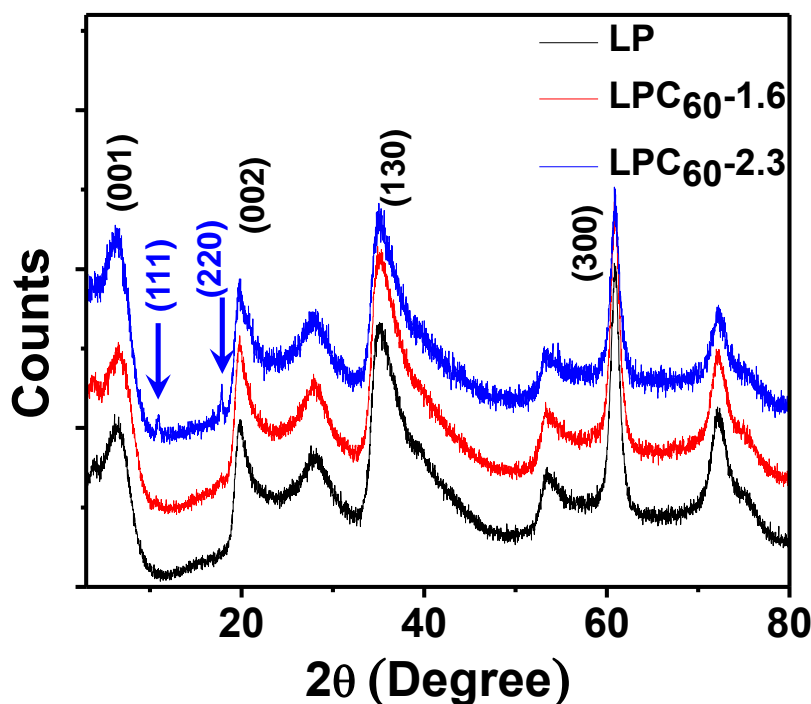


Figure 1.3.5. XRD profile of LPC_{60} in comparison with laponite. At high fullerene content the peaks due to fullerene are visible (blue arrows)

The dye used to study the quenching properties of such LPC_{60} hybrids, is 3,3'-Diethylthiacyanine iodide (CY). This dye was chosen for two main reasons. Firstly, it is a donor molecule. Secondly and most importantly, it is a positively charged molecule. The negative charges on laponite sheets can effectively attract it electrostatically, making it sit on the laponite surface. In addition to this, cyanine dyes are very useful in photovoltaics because of their high extinction coefficients, the ease of solution processing as well as their advantageous electrochemical properties.

Cyanine dyes are known for forming H-aggregates in the literature.⁽²¹⁾ 10^{-4} M solution of the dye in aqueous solution forms H-aggregate, as evident from the appearance of an absorbance shoulder at lower wavelength region (402 nm). The 10^{-5} M solution is rather molecularly dissolved (Figure 1.3.6a).

To determine the effect of laponite on CY, 10^{-5} M solution of CY was titrated spectroscopically with laponite solution (20 mg/mL). With increase in laponite

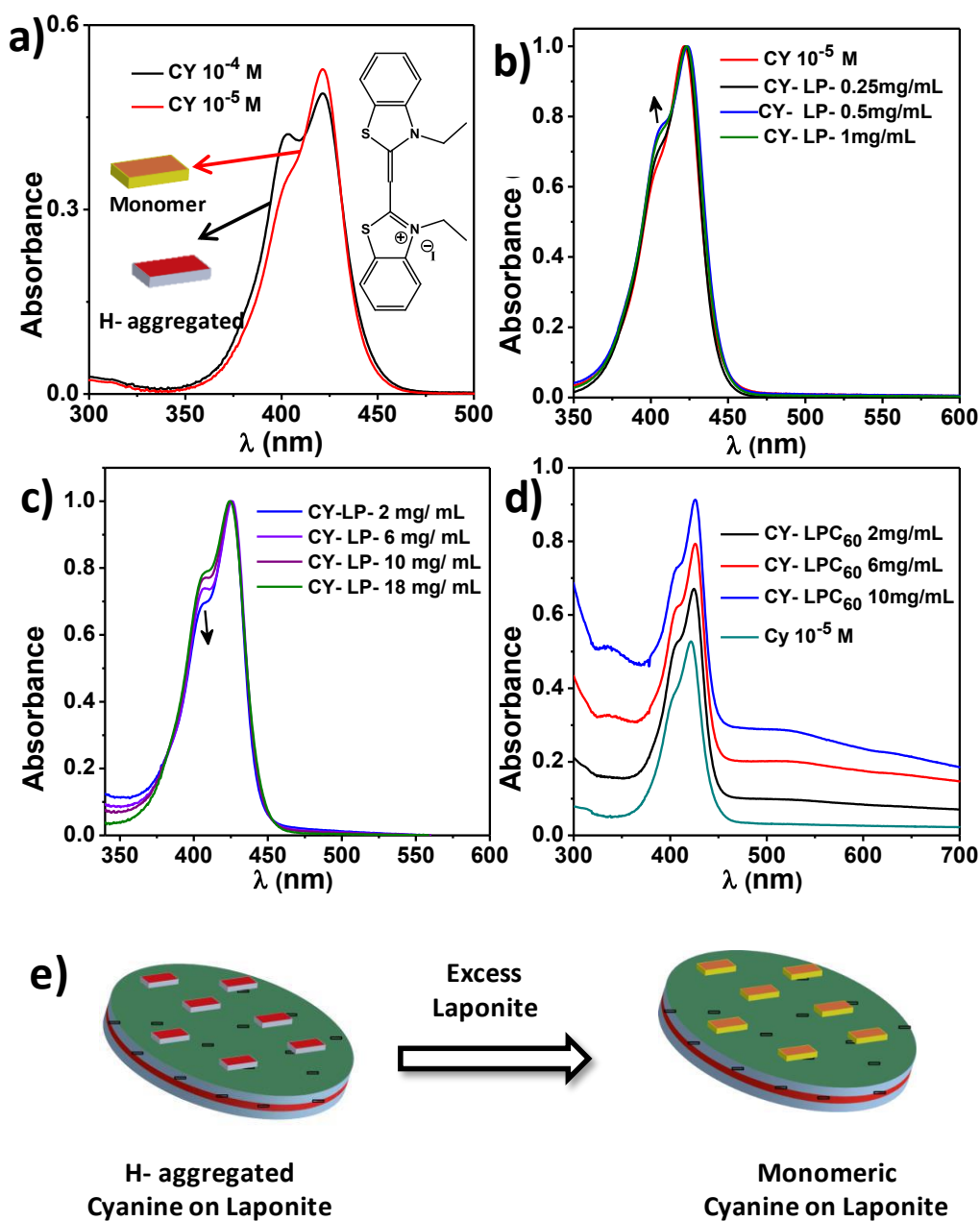


Figure 1.3.6. a) Monomeric (10^{-5} M) and h-aggregated (10^{-4} M) forms of CY in water. Inset- structure of CY, b) initial increase of H- aggregate band on titration of 10^{-5} M CY with laponite, c) decrease of aggregated form and return of the monomeric state at higher concentration of Laponite, d) Titration of 10^{-5} M CY with LPC_{60} e) Schematic representation of conversion of h-aggregated CY on laponite to monomeric form upon addition of excess laponite.

concentration, up to 2 mg/mL, formation of H-aggregates of CY on laponite sheets was evident, as observed from the strong aggregate band (402 nm) (Figure 1.3.6.b, c, e).

Further increase in laponite concentration (> 2 mg/mL in solution) reduces the aggregate band intensity (Figure 3e), bringing it closer to molecularly dissolved state. This suggests that as the concentration of laponite increase, the preformed H-aggregates on the clay matrix gets more room to reorganize. Thus the dynamic H-aggregate breaks down to individual molecular state. The same trend is observed in LPC_{60} hybrids as well (Figure 1.3.6.d). These studies are similar to the report by Whitten et. al.(22), However in this study, instead of J aggregate, formation of H-aggregates was observed possibly due to the structural difference of the dye molecules.

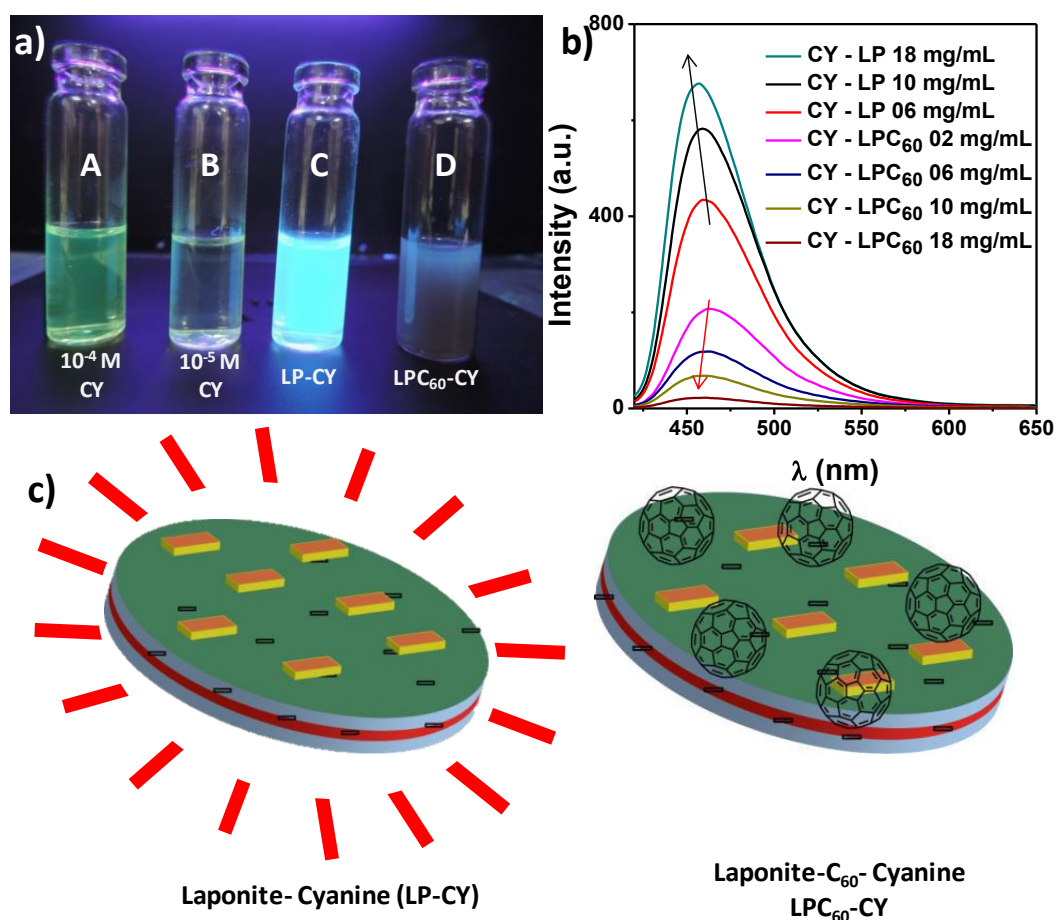


Figure 1.3.7. a) Optical image of A- aggregated (10^{-4} M) and B- monomeric (10^{-5} M) CY solutions, C- LP added to CY and D- LPC_{60} added to CY under UV light. b) PL spectra of LP and LPC_{60} added to 10^{-5} M CY solution, $\lambda_{exc}=360$ nm. c) schematic representation of fluorescent LP-CY and non-fluorescent LPC_{60} -CY

The PL spectra of CY on addition of laponite show enormous increase in fluorescence intensity (Figure 1.3.7a, b). Solution of CY in molecularly dissolved state (10^{-5} M) and

H-aggregated state (10^{-4} M) are not fluorescent at all (Figure 1.3.7a). The reason of the monomeric state not being fluorescent is the free rotational degrees of freedom of the molecule around the C-C bond hindering the conjugation. On the other hand, in H-aggregated form, the aggregates quench.

On addition of laponite to the 10^{-5} M CY solution, CY molecules get bound to the laponite surface and lose their degree of freedom. Corresponding increase in fluorescence intensity is observed (Figure 1.3.7.b, c). Again, the monomeric CY on laponite being more fluorescent than the aggregated form, with addition of laponite, fluorescence intensity increases (as the H-aggregated form shifts towards monomeric form of CY). The excitation spectra of 10^{-5} M CY titrated against laponite show features same as the UV vis spectra, with the monomer emission band being the most intense (Figure 1.3.8). From these studies we can confirm that monomeric CY molecules embedded on laponite surface lose their rotational freedom and show intense fluorescence.

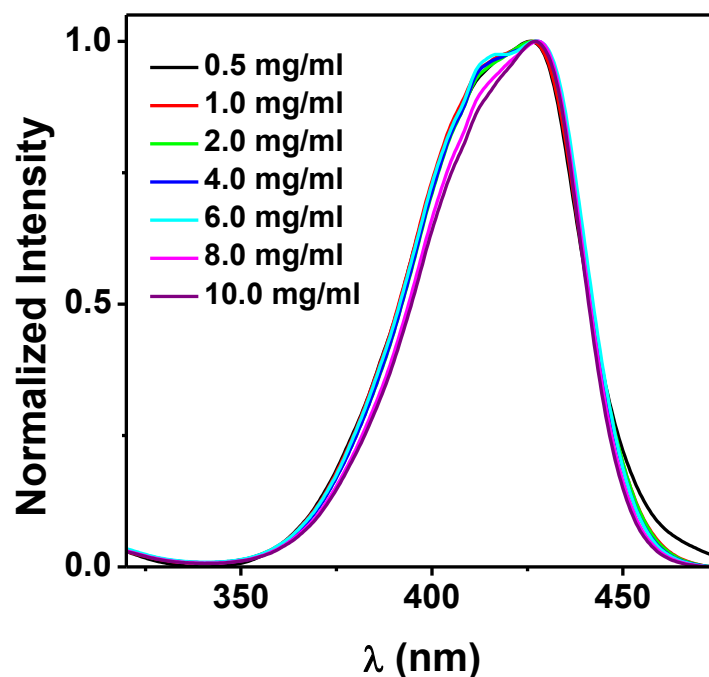
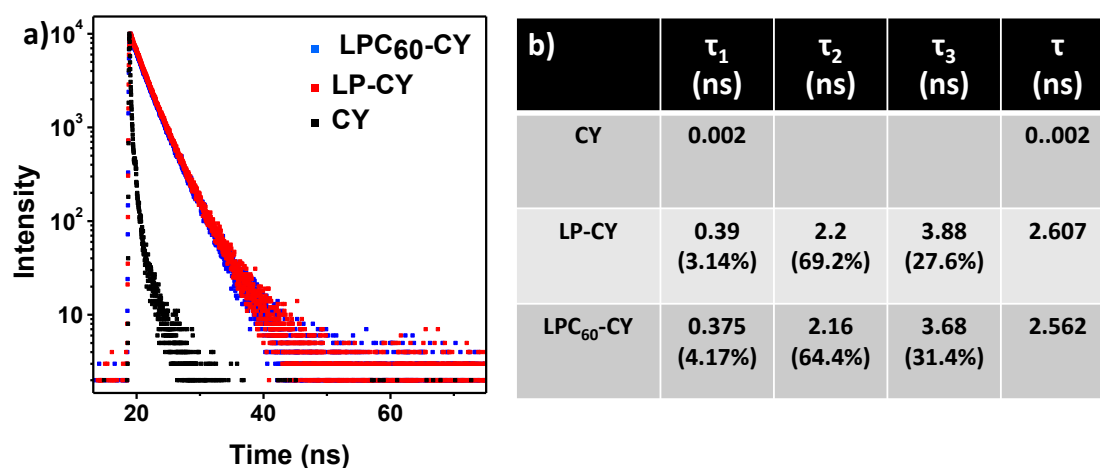


Figure 1.3.8. Normalized excitation spectra ($\lambda_{mon} = 510$ nm, $l = 2$ mm) of 10^{-5} M CY solution with increase in laponite concentration.

On the other hand, increase in the concentration of LPC_{60} in 10^{-5} M CY solution

(Figure 1.3.7b, c) we see a gradual decrease in fluorescence intensity. At the concentration of 18 mg/ mL of LPC_{60} the fluorescence almost completely quenches. On increasing concentration of LPC_{60} , as the amount of fullerene increase with respect to the CY monomers present, more quenching occurs.

The mechanism of the quenching was investigated by different methods. Lifetime measurements were done by time correlated single photon counting (TCSPC) method. (Figure 1.3.8a, b) The results show very low lifetime for 10^{-5} M CY of 2 ps, establishing their non-fluorescent nature in a molecularly dissolved state. On the other hand, lifetime of the dye dramatically increased to 2.6 ns after addition of laponite,



showing increase

Figure 1.3.8. a-TCSPC spectra of 10^{-5} M CY in comparison with 10^{-5} M CY added to 2.0 mg/ mL of laponite and LPC_{60} hybrids $\lambda_{mon} = 480$ nm and $\lambda_{ex} = 404$ nm. b-Table representing the lifetime of each of the species, through multiexponential fit. The numbers in parenthesis represent the composition of the species.

of fluorescence of the dye molecules embedded on the clay particles. We observed no decrease in lifetime of CY on LPC_{60} hybrids, which suggests the quenching of the CY molecules does not occur in the excited state. This rules out any possibility of this quenching being any kind of energy transfer or photo induced electron transfer processes. Although PET processes are very common with fullerene where fullerene acts as an acceptor, they are mainly limited to dyad kind of systems.(23)

The solution state quenching behaviour of the molecules were studied in 80:20 toluene-acetonitrile mixture. This also helps us investigate the contribution of ground state

charge transfer between the molecules in molecularly dissolved state. The spectroscopic titration of 10^{-5} M CY with fullerene solution do not show presence of any charge transfer band even in 1:1 concentration (Figure 1.3.9a). PL studies show that though the fluorescence is low, there is no decrease in CY fluorescence on addition of fullerene (Figure 1.3.9b). These studies confirm that in molecularly dissolved state in solution, these molecules do not show any interaction in ground state.

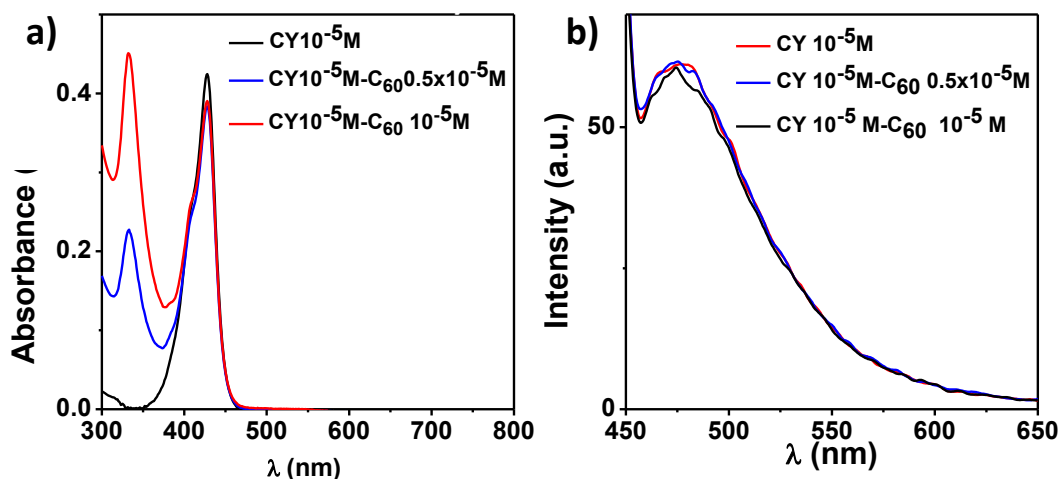


Figure 1.3.9. a) UV-Vis absorption spectra of 10^{-5} M CY with varying amounts of fullerene solution in toluene: acetonitrile (80:20) mixture. b) PL spectra of the same, $\lambda_{exc} = 430$ nm, $l = 10$ mm

To further investigate effect of fullerene on laponite embedded CY molecule, cyclic voltammetry studies were carried out as shown in figure 1.3.10. CY molecules on laponite sheet show distinct oxidation peak at 1.36 eV ($E_{onset} = 1.16$ eV) and reduction peak at -0.67 eV ($E_{onset} = -0.52$ eV). The calculated HOMO and LUMO levels for CY are at -5.5 eV and -3.9 eV. These values match well with HOMO and LUMO energy values of CY molecules reported previously. On the other hand, CY molecules embedded on LPC₆₀ hybrids show a definitive shift in HOMO and LUMO levels, suggesting charge transfer or hybridization of CY and fullerene molecules.

These studies show that though C₆₀ and CY do not interact with each other in a molecularly dissolved state, upon being embedded on clay surface, because of the proximity to each other successful charge transfer occurs, which results in quenching of fluorescence of the CY molecules. However, we did not observe any charge transfer band in the absorbance studies, possibly due to very weak nature of the interaction.

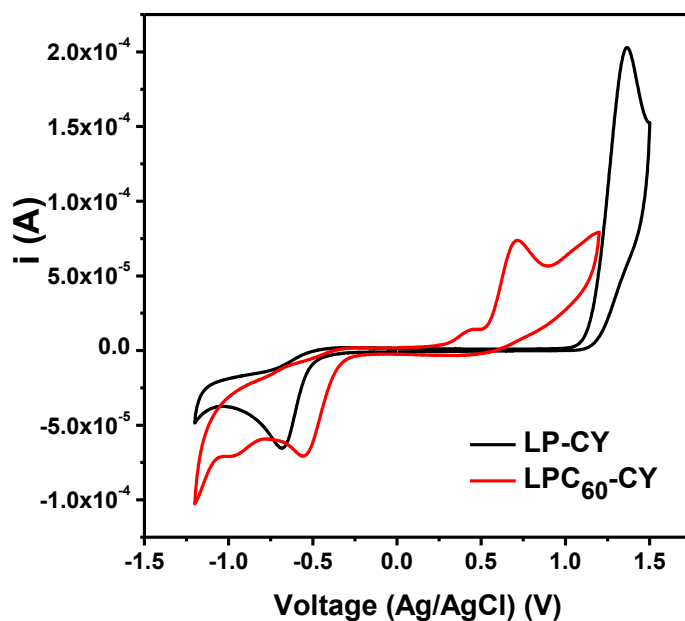
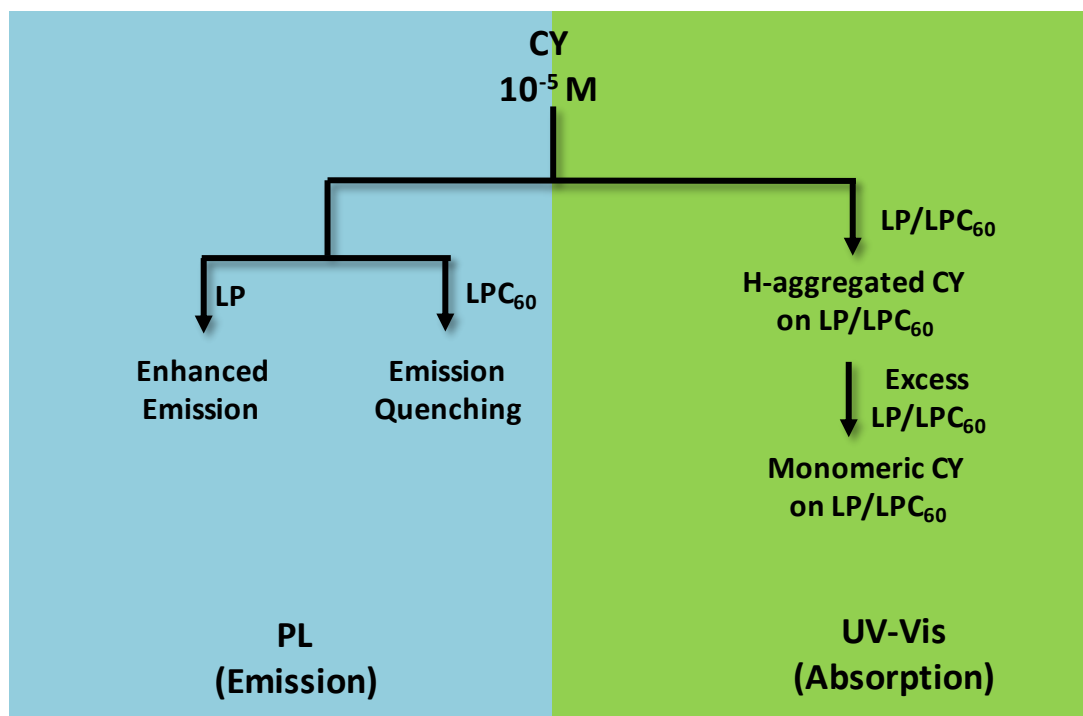


Figure 1.3.10. Cyclic voltammograms of CY molecules embedded on laponite and LPC_{60} hybrids

The whole process is explained schematically in scheme 1.3.2



Scheme 1.3.2. Interaction of CY with LP and LPC_{60}

1.3.5. Conclusion:

In conclusion, in this report we have presented a facile and easy method to disperse fullerene molecules in water by the assistance of clay nanoparticles. Highest concentration of fullerene in water achieved was 7×10^{-5} M, 17 orders of magnitude higher than the nascent fullerene molecules. We have also shown surface mediated quenching of 3,3'-dithiacyanine dye on Laponite fullerene hybrids.

1.3.6. References

1. H. W. Kroto, J. R. Heath, S. C. O'Brien, R. F. Curl, R. E. Smalley, C₆₀: Buckminsterfullerene. *Nature* **318**, 162-163 (1985).
2. W. Krätschmer, K. Fostiropoulos, D. R. Huffman, The infrared and ultraviolet absorption spectra of laboratory-produced carbon dust: evidence for the presence of the C₆₀ molecule. *Chem. Phys. Lett.* **170**, 167-170 (1990).
3. G. Yu, J. Gao, J. C. Hummelen, F. Wudl, A. J. Heeger, Polymer Photovoltaic Cells: Enhanced Efficiencies via a Network of Internal Donor-Acceptor Heterojunctions. *Science* **270**, 1789-1791 (1995).
4. T. Braun *et al.*, Fullerene-based ruthenium catalysts: a novel approach for anchoring metal to carbonaceous supports. I. Structure. *Catal. Lett.* **43**, 167-173 (1997).
5. B. Coq, J. Marc Planeix, V. Brotons, Fullerene-based materials as new support media in heterogeneous catalysis by metals. *Applied Catalysis A: General* **173**, 175-183 (1998).
6. A. W. Jensen, C. Daniels, Fullerene-Coated Beads as Reusable Catalysts. *J. Org. Chem.* **68**, 207-210 (2002).
7. R. Sijbesma *et al.*, Synthesis of a fullerene derivative for the inhibition of HIV enzymes. *J. Am. Chem. Soc.* **115**, 6510-6512 (1993).

8. H. Tokuyama, S. Yamago, E. Nakamura, T. Shiraki, Y. Sugiura, Photoinduced biochemical activity of fullerene carboxylic acid. *J. Am. Chem. Soc.* **115**, 7918-7919 (1993).
9. M. V. Korobov, A. L. Smith, Solubility of the fullerenes. in *Fullerenes: Chemistry, physics, and technology*, 53-90 (2000).
10. Y. Iwamoto, Y. Yamakoshi, A highly water-soluble C₆₀-NVP copolymer: a potential material for photodynamic therapy. *Chem. Commun.*, 4805-4807 (2006).
11. O. A. Troshina, P. A. Troshin, A. S. Peregudov, V. I. Kozlovski, R. N. Lyubovskaya, Photoaddition of N-Substituted Piperazines to C₆₀: An Efficient Approach to the Synthesis of Water-Soluble Fullerene Derivatives. *Chem. Eur. J.* **12**, 5569-5577 (2006).
12. E. Nakamura, H. Isobe, Functionalized Fullerenes in Water. The First 10 Years of Their Chemistry, Biology, and Nanoscience. *Acc. Chem. Res.* **36**, 807-815 (2003).
13. T. Andersson, K. Nilsson, M. Sundahl, G. Westman, O. Wennerstrom, C₆₀ embedded in [gamma]-cyclodextrin: a water-soluble fullerene. *J. Chem. Soc., Chem. Commun.*, 604-606 (1992).
14. M. M. Lezhnina, T. Grewe, H. Stoehr, U. Kynast, Inside Back Cover: Laponite Blue: Dissolving the Insoluble. *Angew. Chem. Int. Ed.* **51**, 10671-10671 (2012).
15. T. Felbeck *et al.*, Nile-Red–Nanoclay Hybrids: Red Emissive Optical Probes for Use in Aqueous Dispersion. *Langmuir* **29**, 11489-11497 (2013).
16. D. Gournis *et al.*, Incorporation of Fullerene Derivatives into Smectite Clays: A New Family of Organic–Inorganic Nanocomposites. *J. Am. Chem. Soc.* **126**, 8561-8568 (2004).

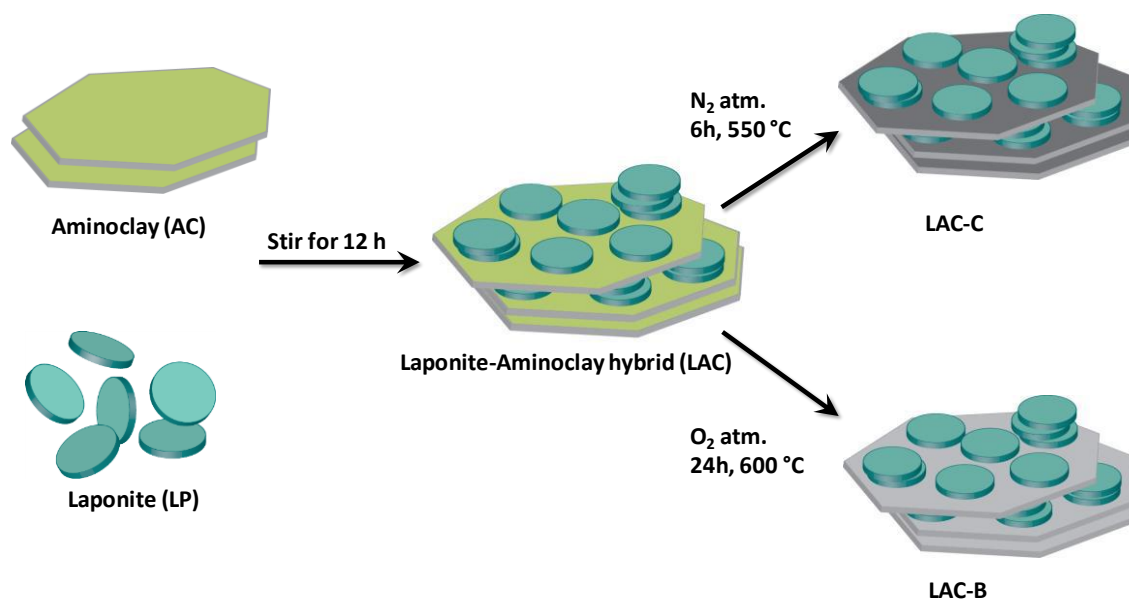
17. T. Tsoufis *et al.*, Incorporation of Pure Fullerene into Organoclays: Towards C₆₀-Pillared Clay Structures. *Chem. Eur. J.* **19**, 7937-7943 (2013).
18. S. Leach *et al.*, Electronic spectra and transitions of the fullerene C₆₀. *Chem. Phys.* **160**, 451-466 (1992).
19. S. Banerjee, Molecular dynamics study of self-agglomeration of charged fullerenes in solvents. *J. Chem. Phys.* **138**, - (2013).
20. J. C. Scanlon, L. B. Ebert, X-ray diffraction study of fullerene soot. *J. Phys. Chem.* **97**, 7138-7140 (1993).
21. H. Yao, K. Ashiba, Highly fluorescent organic nanoparticles of thiocyanine dye: A synergetic effect of intermolecular H-aggregation and restricted intramolecular rotation. *R. Soc. Chem. Adv* **1**, 834-838 (2011).
22. L. Lu, R. M. Jones, D. McBranch, D. Whitten, Surface-Enhanced Superquenching of Cyanine Dyes as J-Aggregates on Laponite Clay Nanoparticles. *Langmuir* **18**, 7706-7713 (2002).
23. J. Baffreau *et al.*, Superabsorbing Fullerenes: Spectral and Kinetic Characterization of Photoinduced Interactions in Perylenediimide–Fullerene-C₆₀ Dyads. *J. Phys. Chem. A* **110**, 13123-13125 (2006).

Chapter 1.4.

Clay- Carbon hybrid materials for CO₂ capture.

Summary:

Carbon capture and sequestration presents a huge challenge in today's world due to the increased emission of greenhouse gases, especially CO₂. Among present technologies to reduce CO₂ from earth atmosphere, research in adsorbent based capture of CO₂ promises a cheap and formidable solution. Carbon based materials are known for their high surface area and excellent adsorption capacity. In this work we present a cheap and easy preparation of clay-carbon composite for CO₂ capture.



1.4.1. Introduction:

In modern world, in view of the pollution and global warming concerns, capture and sequestration of greenhouse gases is highly important. CO₂ is a major contributor of greenhouse gas and the escalating levels of CO₂ are one of the most pressing concerns for humankind.(1)

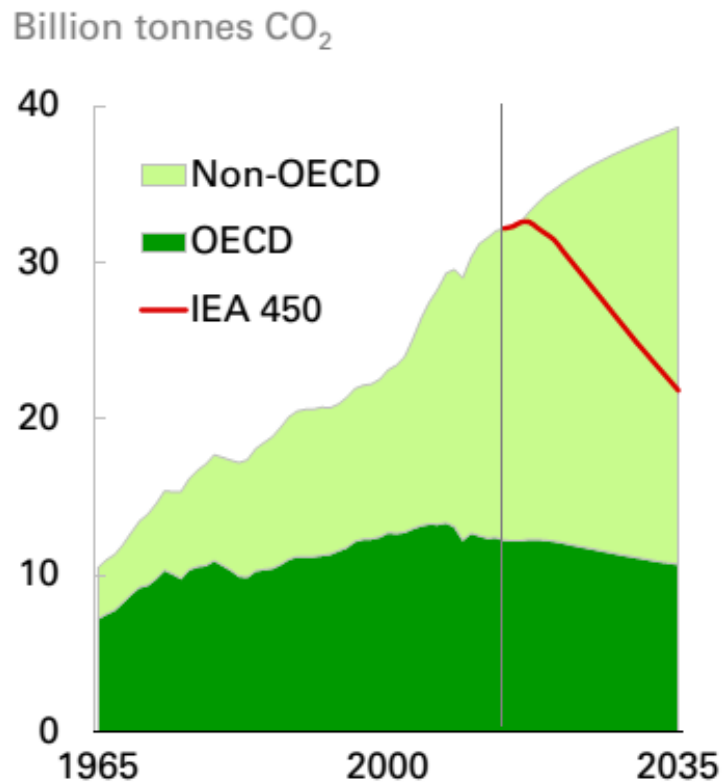


Figure 1.4.1. Predicted trend of increase in global CO₂ emission from 1965 to 2035. OECD-Organisation for Economic Co-operation and Development, IEA – International Energy Agency. Adapted from BP energy outlook 2016.

In worldwide CO₂ production of 19.4 giga tons in 2008, according to IEA, a third of it is from power generation and another one third is from transport.(2) Mckinsky and company submitted a highly cited study of most economically attractive and least expensive ways to cut the CO₂ emission of USA by half.(3) They concluded that reducing the emission of CO₂ by that extent was not possible without carbon capture and storage (CCS) from large power sources such as power plants. The existing strategy for such carbon capture and storage has been dependent on the use of amine absorbents and scrubbers.

There has been a lot of research going on to find cheap and efficient alternatives for efficient CCS during pre or post combustion processes. The prerequisites for such a material are energy efficient regeneration of the material and chemical robustness. Past reports include a variety of different materials. The majority of them can be classified into the following groups:

- Physisorbates, such as zeolites, activated charcoal etc.
- Chemisorbants such as oxides of sodium, potassium, calcium, cesium, tantalum, rhodium, aluminium etc., lithium silicates and zirconates, and hydrotalcites.
- Organic and organic-inorganic hybrids such as amines physically or chemically adsorbed on solid supports such as oxides or mesoporous silica, amines supported on solid organic supports and metal organic frameworks (MOFs).

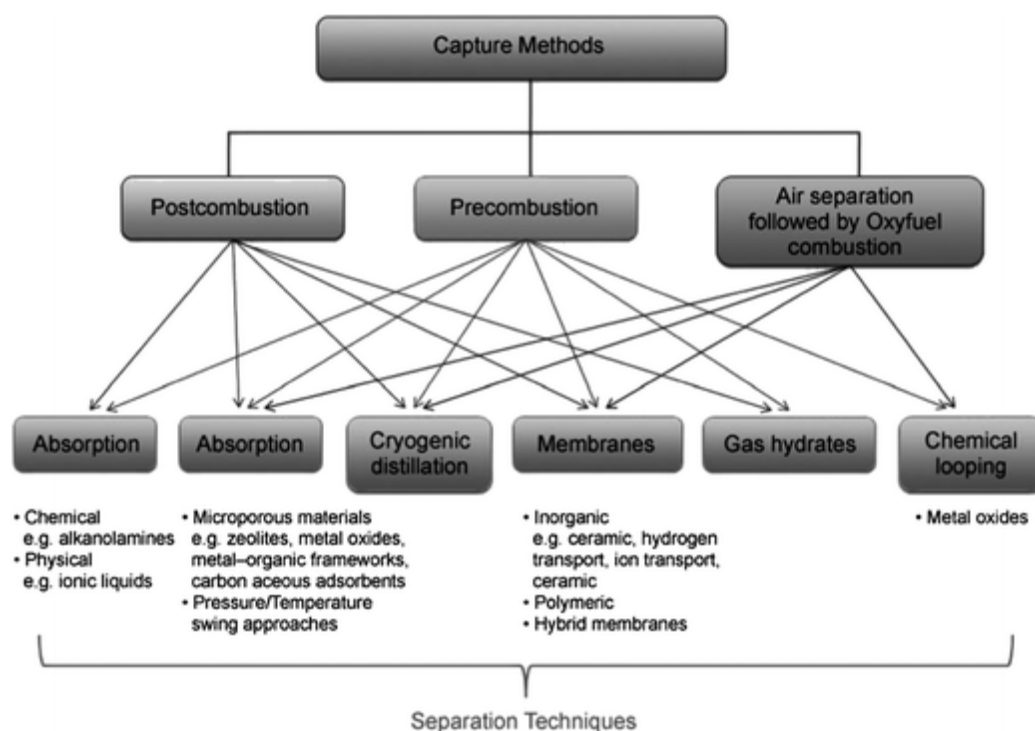


Figure 1.4.2. Materials for CO₂ capture in the context of postcombustion, precombustion, and oxyfuel processes. Adapted from ref (4)

While the maximum CO₂ adsorption for zeolites is about 5.6 mmol of CO₂/ g of adsorbate (hereon referred to as mmol/g),(5) that for functionalized mesoporous silica is about 5.5 mmol/g for tetraethylene pentamine/ polyethyleneamine impregnated MCM-41. Among various MOFs MIL type Al, Zn and Cr coordinated metal oxide

frameworks show high CO₂ adsorption at low as well as room temperature.(6) Oxide and hydrotalcite based adsorbents' adsorption capacity rarely exceed 1 mmol/g whereas activated carbons are shown to be highly active (~3.3 mmol/g at 1 atm, 298 K).(5)

1.4.2. Scope of the present investigation:

All of these previously mentioned adsorbates either have high regeneration energy requirement, are costly to prepare or are not very robust. Hence we synthesized a clay carbon composite by carbonizing a synthetic organo-clay (aminoclay) and laponite together. As we know clay materials are very cheap and easily available, they are chemically robust too. Moreover, carbon being the CO₂ adsorbent, as carbon and CO₂ are weakly bound, regeneration of the adsorbate is also easy. The composite of two different clays give us a hierarchical structure, making it more effective for adsorption purposes.

1.4.3. Experimental Procedures:

1.4.3.1. Materials used

A synthetic laponite XLG clay with empirical composition of $\text{Na}^+_{0.7}[(\text{Si}_8\text{Mg}_{5.5}\text{Li}_{0.3})\text{O}_{20}(\text{OH})_4]^{-0.7} \cdot x\text{H}_2\text{O}$ (Rockwood Additives) was used, MgCl_2 (Merck, India), 3-aminopropyltriethoxysilane (Aldrich), ethanol (HPLC grade) were used for synthesis of aminoclay.

1.4.3.2. Preparation of aminoclay:

Typically, bulk aminopropyl-functionalized magnesiumphyllosilicate clay was prepared at room temperature by drop wise addition of 1.0 mL (5.85 mmol) 3-aminopropyltrimethoxysilane to an aqueous solution of 0.84 g (3.62 mmol) magnesium chloride in water (25 mL) The solution was left stirring for 24 hours, dried at 60 °C, dispersed in water, reprecipitated from ethanol and dried. The yield of the product was 1.0 g.(7)

1.4.3.3. Preparation of aminoclay and laponite composite:

The composite was prepared in the following manner. Firstly, laponite was exfoliated by dispersing 100 mg of sample in 10 mL of water by sonication (for 10 min). Aminoclay was separately exfoliated in water by dispersing 100 mg sample in 10 mL

of water by sonication (for 10 min). The laponite suspension was then added drop wise to aminoclay suspension while continued stirring. The clear solution of aminoclay gradually turned white slurry during the addition of laponite solution. The suspension was stirred for 1 h and allowed to stand for 24 h, followed by filtration and washing with water, finally the precipitate was then dried at 50 °C for 48 h. Following the same procedure, composites with different weight ratios of aminoclay and laponite (5:1; 3:1; 1:1; 1:3; 1:5) were prepared.

1.4.3.4. Carbonization of composite:

The composite was carbonized at 600 °C for 6 h under N₂ atmosphere at a step rate of 1.5 °C. To remove clay residue from carbonized composite, the carbonized composite was dispersed first in 3 M Sodium Hydroxide solution, stirred for 24 h, centrifuged, collected the precipitate and redispersed in 12 % Hydrochloric acid, followed by stirring for another 24 h, then centrifuged, washed two times with water and one time with ethanol. The carbonized composite was allowed to dry at 80 °C for 24 h. On the other hand, the composite was burnt under O₂ atmosphere at 600 °C for 24 h in order to remove all carbon content. Same procedures were followed for carbonization and burning of aminoclay and laponite.

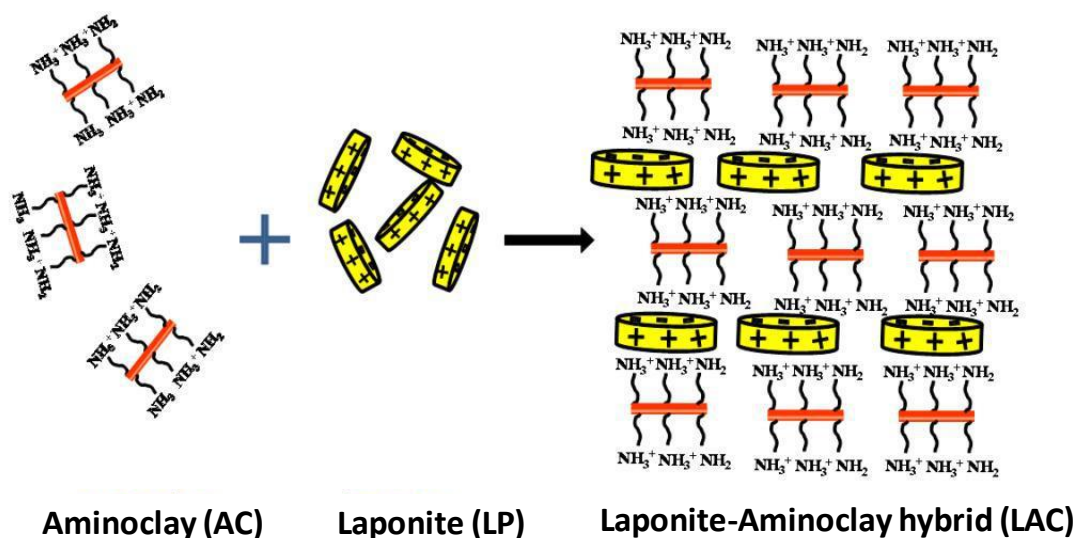
1.4.3.5. General characterization and equipments.

Powder XRD patterns were recorded using Bruker-D8 diffractometer using Cu K α radiation, ($\lambda=1.54$ Å, Step size: 0.02, Current: 30 mA and Voltage: 40 kV). The N₂ sorption studies at 77K, CO₂ sorption studies at 195K and 273K were performed on a Autosorb-1C (Quantachrome corp.). The samples were outgassed at 100 °C for 12 h under high vacuum before the analysis. The specific surface areas (SSA) were calculated according to the BET method using the Quantachrome software (ASiQwin). Ultrahigh purity gases (99.9995%) were used for all experiments. Thermogravimetric analysis experiments were performed using Mettler Toledo 850 from 30 °C to 900 °C in oxygen stream with a heating rate of 10 °C/min. FT-IR spectra were recorded on a Bruker IFS 66v/S spectrometer. FESEM images were obtained by means of Nova-Nano SEM-600 (FEI, Netherlands). Electronic absorption spectra were recorded on a Perkin Elmer Lambda 900 UV-Vis-NIR spectrometer.

1.4.4. Results and discussion:

Intercalation of two different layered structures to get a new three dimensional structure has picked up immense interest recently for their ample demand in semiconductor and electronics.(8) On the other hand, clay based porous heterostructures are well known and used for different applications.(9-11) Lately, two different types of clays- hydrotalcite and montmorillonite also have been assembled periodically in search of new properties.(12) The clays used in this work are aminoclay and laponite.

Aminoclay is a synthetic 2:1 smectite type of clay with aminopropyl pendant groups. In aqueous solution protonation of the amine groups makes the clay positive and helps its exfoliation.(13) On the other hand, laponite has unique disk like shape of around 25 nm diameter; while the faces of the disks are negatively charged, the edges are positive.



Scheme 1.4.1. Self-assembly of aminoclay and laponite in aqueous media.

The laponite particles assume an overall negative charge. In aqueous solution, the positively charged aminoclay and negatively charged laponite nanoparticles self-assemble to form a hierarchical network, (Scheme 1.4.1) which is evident from the fact that the solution turns cloudy when these two clear clay dispersions are mixed together. Zeta potential measurements also support the fact, as the charge of the resultant composite turns neutral (Figure 1.4.3a). IR spectra of aminoclay show peaks for the aminopropyl chain (C-H stretch at 3040 cm^{-1} , H-C-H bend at 1502 cm^{-1} , H-N-H bend at 1617 cm^{-1} , and a peak for NH_3^+ at 2001 cm^{-1}) as well as the inorganic framework (Si-O stretch at 1022 cm^{-1} , and Mg-O stretch at 560 cm^{-1}).(14) In the spectra of laponite, the bands corresponding to organic counterparts are missing. The composite shows the

combined spectra of aminoclay and laponite, though the relative intensities of organic moieties are less compared to pure aminoclay. (Figure 1.4.3b) Moreover, the peak corresponding to NH_3^+ is shifted to higher wavenumber, which proves that the clays interact electrostatically and that interaction is present even in dried state. Composites with different weight ratios of aminoclay and laponite were prepared. Figure shows the respective XRD spectra. Both laponite and aminoclay have a low angle peak at 5.5° ,

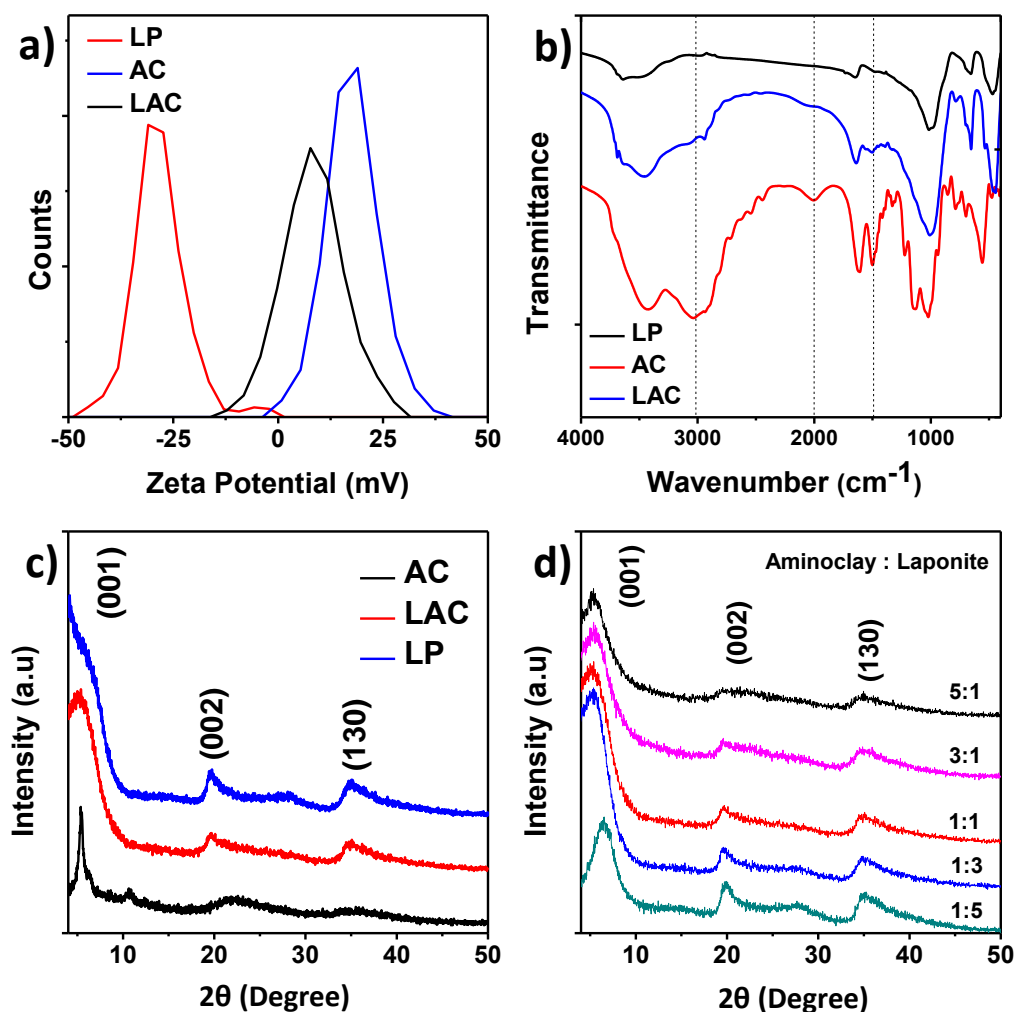
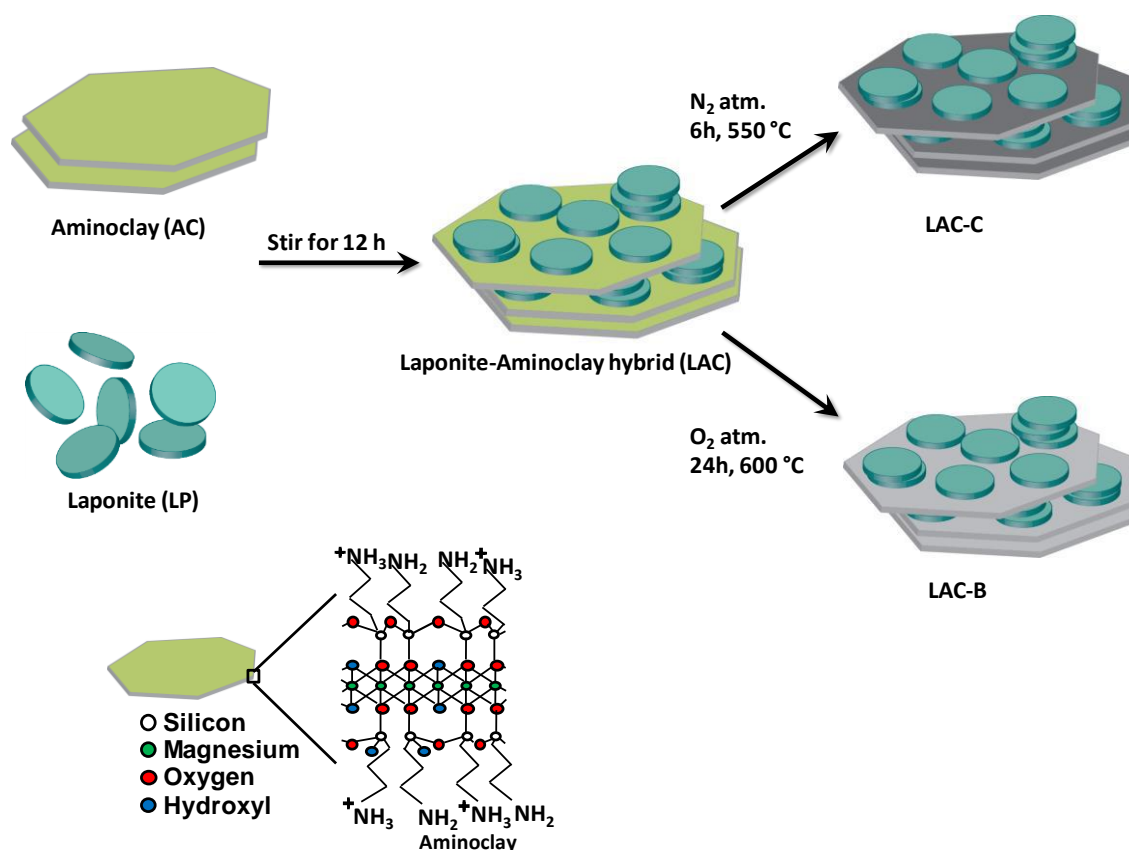


Figure 1.4.3. a) Zeta potential of laponite (LP), aminoclay (AC) and Laponite-aminoclay composite (LAC). b) IR spectra of LAC in comparison to LP and AC. c) XRD spectra of LP, AC and LAC and d) XRD profile of different composites with varying aminoclay:laponite composition.

corresponding to the interlayer spacing. While aminoclay has a strong and well defined low angle peak, that of laponite is broad, probably because of its small size and low

structural ordering. Higher order peaks of both the clays are broad and have asymmetric, shark fin like structure due to turbostratic disorder so commonly observed in clay minerals. The XRD of the composite has a broad, but intense low angle peak and the spectrum is more similar to laponite than aminoclay. (Figure 1.4.3c) Composites with different weight ratios of laponite and aminoclay do not show much difference structurally according to their XRD. (Figure 1.4.3d) Hence, rest of this work has been carried with 1:1 aminoclay-laponite composite.

Individual materials and the composites were heated under two different conditions. Heating under inert condition (N_2) produces carbonized materials, whereas, heating under O_2 burns all the carbon as CO_2 . The XRD of the burnt, carbonized and as synthesized composites suggests that the low angle ordering is almost invariably lost after heating in all the materials. (Scheme 1.4.2)



Scheme 1.4.2. Formation of carbonized (LAC-C) and burnt (LAC-B) hybrids from laponite-aminoclay hybrids.

The amount of carbon in the carbonized materials can be assessed from the weight loss in between $200\text{ }^\circ\text{C}$ to $600\text{ }^\circ\text{C}$ in TGA profile (Figure 1.4.4a). Pure laponite shows

minimal weight loss (about 1%) in this temperature window, whereas as-prepared LAC has weight loss of almost 10-15% due to the aminopropyl groups. The carbonized composite has carbon content of 2%, whereas the burnt composite has almost no weight loss. Laponite loses some structural water molecules in this temperature range, accounting for its low weight loss, but as the burnt and carbonized composites are pre heated up to 550 or 600 C the weight loss directly corresponds to their carbon content.

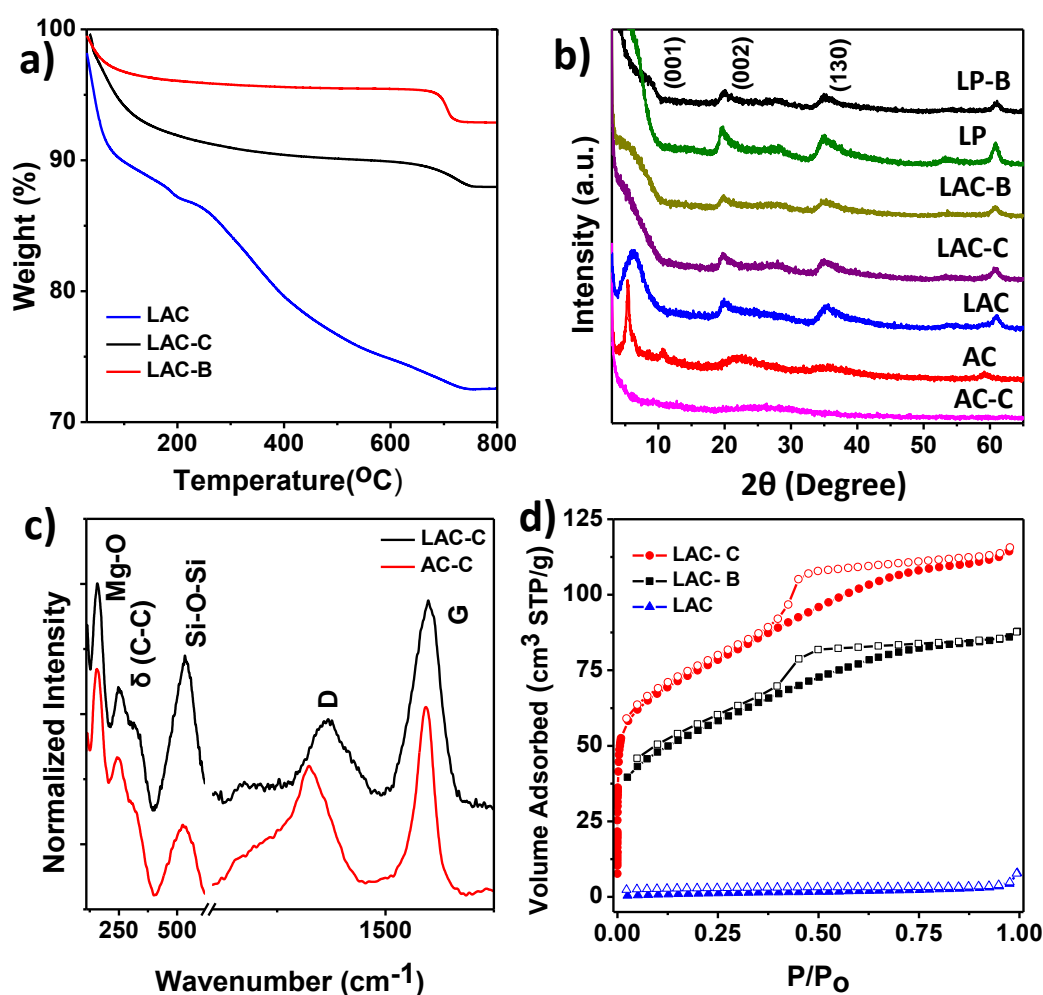


Figure 1.4.4. a) TGA profile of as-prepared laponite-aminoclay hybrid in comparison to carbonized (LAC-C) and burnt (LAC-B) hybrids. The amount of carbon was determined from the weight loss from 200 °C to 600 °C. b) XRD profiles of aminoclay, laponite, laponite-aminoclay hybrids and their burnt and carbonized counterparts. c) Raman spectra of carbonized aminoclay in comparison with carbonized hybrid. d) N₂ adsorption isotherms of as-prepared laponite-aminoclay hybrids along with burnt and carbonized hybrids.

The XRD profiles of as-prepared, carbonized and burnt hybrids do not show any loss of structure after heating (Figure 1.4.4b). On the other hand, aminoclay after carbonization loses its structure while laponite retains its structure even after heating. The Raman spectra of carbonized hybrid and carbonized aminoclay show graphitic nature, where the D band is much less intense than the G band. The peaks for Mg-O, Si-O-Si and C-C are also present. (Figure 1.4.4.c)

The surface area of the as- prepared, burnt and carbonized hybrids were studied by Nitrogen adsorption measurements at 77 K. The isotherms are (Type-I) fully reversible in nature. The as-prepared hybrid shows a very less uptake of Nitrogen. On the other hand, carbonized hybrid and burnt hybrid isotherms show a rapid uptake at low pressure (0 – 0.1 bar) indicating a paramount microporous nature. (Figure 1.4.4.d) Applying the Brunauer – Emmett - Teller (BET) model in the pressure 0 - 1 bar resulted in apparent surface areas of 4.51 m²/g (LAC), 257 m²/g (LAC-C), 197 m²/g (LAC-B). The excess uptake by LAC-C can be attributed to the microporous carbon formed on the clay surface.

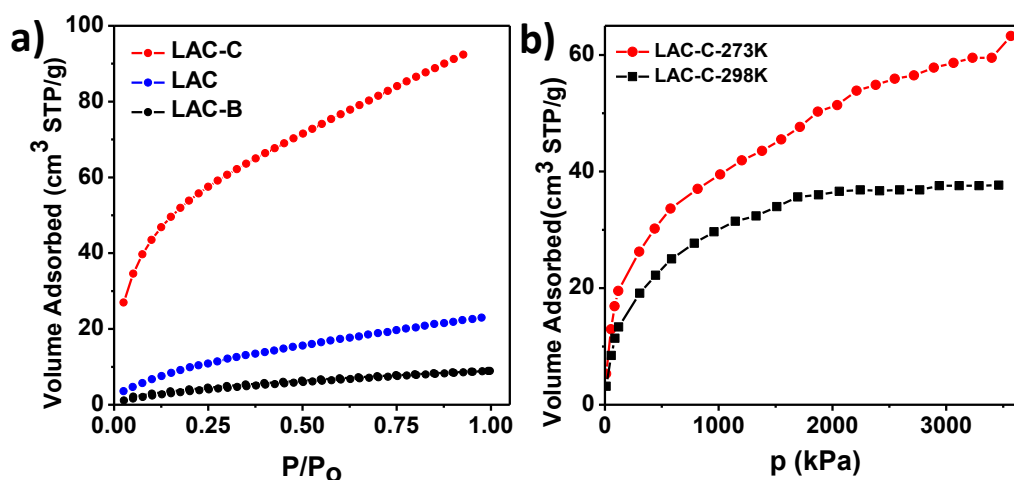


Figure 1.4.5. a) CO₂ uptake by the composites at 195K and b) CO₂ uptake by the composites at 273K and 298K under high pressure.

CO₂ uptake studies at 195K show remarkable uptake for the carbonized hybrid. (Figure 1.4.5.a) Uptake by the burnt hybrid is negligible whereas as-prepared hybrids show little uptake probably due to the presence of amine functional groups. The carbonized composite shows an uptake of 18.7 wt% (4.25 mmol/g), the uptake of as-synthesized hybrid was 4.5 wt% (1.05 mmol/g), for burnt hybrids the uptake was 1.7 wt% (0.38 mmol/g). If we consider the uptake for carbon alone, the uptake is much higher (193.5

mmol/g) compared to other previously reported porous carbons. We believe this increase is due to the hierarchical structure of the hybrids which helps to reduce diffusion length and increase in uptake of the gas molecules.

S.No.	Activated carbon	CO ₂ capture capacity (mmols/g)	Pressure (bar)	Temperature (K)	Reference
1	NORIT R1 Extra	10.2	40	298	(15)
2	MAXSORB	0.5	1	298	(16, 17)
		25	30	298	
3	BPL Carbon	0.4	1	298	(16, 18)
		4	10	298	
4	Activated Charcoal	16.5	8	298	(19)
5	BCN	22.7	1	195	(20)
6	LAC-C	4.25	1	195	
		2.8	35	273	
7	LAC-C*	193.5	1	195	
		90	35	273	

Table 1.4.1. Comparison of CO₂ capture performance of different porous carbon adsorbents. LAC-C represents the results obtained in this work. LAC-C* represent CO₂ adsorbed by carbon alone. Data was obtained by substituting adsorption of LAC-B from LAC-C and accounting for 2 wt% of carbon in LAC-C.

The hybrids show high CO₂ uptake even at high temperature. (Figure 1.4.5.d) Amount was 7.4 wt% at 35 atm. A comparison of CO₂ uptake capacities of different activated hybrids is shown in the table above.

1.4.5. Conclusion

In conclusion, clay hybrid materials were prepared by self-assembly of two types of clays: aminoclay and laponite. The differently charged clay sheets dispersed in water attract each other electrostatically to form a cloudy precipitate. Carbonization of the hybrids was achieved by heating them under inert atmosphere at 550 °C. The carbonization produces microporous carbon on the surface of the clay sheets. Aminopropyl functional groups of the aminoclay serve as carbon source for the hybrids. The clay-carbon hybrids show high surface area and high uptake of CO₂ due to their microporous nature and low diffusion length for gas molecules due to the pillared architectures. The CO₂ capture efficiency of the hybrids were on par with traditional porous carbons, and much higher if estimated based on the available carbon in the hybrids.

1.4.6. References:

1. H. Yang *et al.*, Progress in carbon dioxide separation and capture: A review. *J. Environ. Sci.* **20**, 14-27 (2008).
2. S. Solomon, *Climate change 2007-the physical science basis: Working group I contribution to the fourth assessment report of the IPCC.* (Cambridge University Press, 2007), vol. 4.
3. P. Enkvist, T. Nauc ler, J. Rosander, A cost curve for greenhouse gas reduction. *McKinsey Quarterly* **1**, 34 (2007).
4. D. M. D'Alessandro, B. Smit, J. R. Long, Carbon Dioxide Capture: Prospects for New Materials. *Angew. Chem. Int. Ed.* **49**, 6058-6082 (2010).
5. S. Choi, J. H. Drese, C. W. Jones, Adsorbent Materials for Carbon Dioxide Capture from Large Anthropogenic Point Sources. *ChemSusChem* **2**, 796-854 (2009).
6. K. Sumida *et al.*, Carbon Dioxide Capture in Metal–Organic Frameworks. *Chem. Rev.* **112**, 724-781 (2012).

7. K. K. R. Datta, M. Eswaramoorthy, C. N. R. Rao, Water-solubilized aminoclay-metal nanoparticle composites and their novel properties. *J. Mater. Chem.* **17**, 613-615 (2007).
8. A. K. Geim, I. V. Grigorieva, Van der Waals heterostructures. *Nature* **499**, 419-425 (2013).
9. J. A. Cecilia, C. García-Sancho, F. Franco, Montmorillonite based porous clay heterostructures: Influence of Zr in the structure and acidic properties. *Microporous Mesoporous Mater.* **176**, 95-102 (2013).
10. A. Galarneau, A. Barodawalla, T. J. Pinnavaia, Porous clay heterostructures formed by gallery-templated synthesis. *Nature* **374**, 529-531 (1995).
11. A. C. Perdigon *et al.*, Synthesis of porous clay heterostructures from high charge mica-type aluminosilicates. *J. Mater. Chem. A* **1**, 1213-1219 (2013).
12. R. Chalasani, A. Gupta, S. Vasudevan, Engineering New Layered Solids from Exfoliated Inorganics: a Periodically Alternating Hydrotalcite – Montmorillonite Layered Hybrid. *Scientific Reports* **3**, 3498 (2013).
13. K. K. R. Datta, A. Achari, M. Eswaramoorthy, Aminoclay: a functional layered material with multifaceted applications. *J. Mater. Chem. A* **1**, 6707-6718 (2013).
14. J. E. Martin, A. J. Patil, M. F. Butler, S. Mann, Guest-Molecule-Directed Assembly of Mesostructured Nanocomposite Polymer/Organoclay Hydrogels. *Adv. Funct. Mater.* **21**, 674-681 (2011).
15. S. Himeno, T. Komatsu, S. Fujita, High-pressure adsorption equilibria of methane and carbon dioxide on several activated carbons. *Journal of Chemical & Engineering Data* **50**, 369-376 (2005).

16. K. B. Lee, M. G. Beaver, H. S. Caram, S. Sircar, Reversible Chemisorbents for Carbon Dioxide and Their Potential Applications. *Industrial & Engineering Chemistry Research* **47**, 8048-8062 (2008).
17. F. Dreisbach, R. Staudt, J. Keller, High pressure adsorption data of methane, nitrogen, carbon dioxide and their binary and ternary mixtures on activated carbon. *Adsorption* **5**, 215-227 (1999).
18. A. Phan *et al.*, Synthesis, Structure, and Carbon Dioxide Capture Properties of Zeolitic Imidazolate Frameworks. *Acc. Chem. Res.* **43**, 58-67 (2010).
19. Q. Wang, J. Luo, Z. Zhong, A. Borgna, CO₂ capture by solid adsorbents and their applications: current status and new trends. *Energy Environ. Sci.* **4**, 42-55 (2011).
20. K. Raidongia *et al.*, BCN: A Graphene Analogue with Remarkable Adsorptive Properties. *Chem.Eur. J.* **16**, 149-157 (2010).

PART-2

Chapter 2.1. *Introduction to gas permeation and separation through membranes.*

Chapter 2.2. *Casting molecular channels through graphene oxide surface: Effect of domain formation on gas permeation of Graphene oxide membranes.*

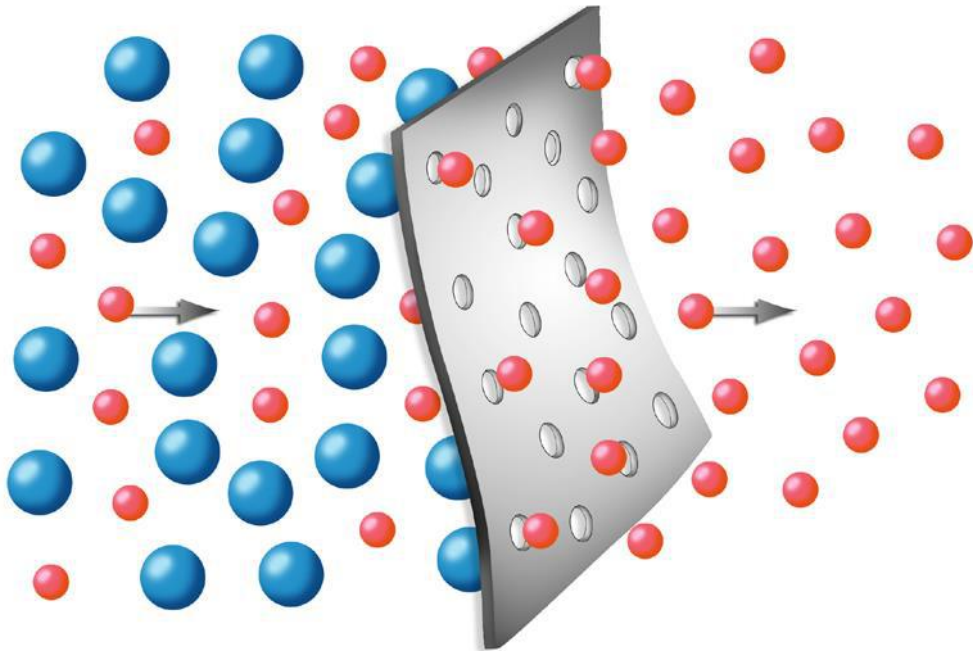
Chapter 2.3. *High performance MoS₂ membranes: Effect of thermally driven phase transition on CO₂ separation efficiency.*

Chapter-2.1

Introduction to gas permeation and separation through membranes

Summary:

Membrane based gas separation methods provide an easy, cheap and energy efficient solution compared to other traditional techniques. In this chapter, we have briefly introduced the history and development of membrane based gas separation processes, and basic theory of gas permeation through different membranes. Few examples of separation of H_2 from CO_2 by porous membranes such as silica, zeolite metal organic framework and carbon molecular sieve are presented.



2.1.1. Introduction:

Separation processes are an integral part of industrial processes for separation, purification and recovery of substances. Membrane based separation methods are highly efficient which could reduce capital investment, application cost and safety. Separation of gas mixtures is an important part of many industries to recover gases and enable pollution control. Common practices involved for separation gases are cryogenic distillation, adsorption on solid surfaces and solvent absorption. Recently membranes are increasingly finding applications in gas separation and have shown a huge potential. Industrial scale membrane separations have already been employed in industrial sectors in united states and some European countries. Membrane technology can complement conventional techniques for efficient separation of gases. Few inherent advantages of membrane gas separation are as follows.

- Cost effective operation.
- Less energy consumption.
- Lower environmental footprint, no corrosive or harmful chemicals required.
- Operates at ambient temperature and pressure unlike other separation processes like cryogenic distillation, which require extreme condition.
- Membrane based separation processes are very efficient because they can operate in continuous mode with complete or partial recycling of permeate/retentate.
- Can be integrated to other separation processes seamlessly for better separation performance.
- Different membranes can be synthesized according to the specific need for the situation.

2.1.2. History of membrane based gas separation:

The history of membrane based gas separation can be dated back to two centuries. In 1900s a Scottish chemist named Thomas Graham first proposed the laws of diffusion of gases and liquids through various medium. He discovered that certain substances such as gelatin and glue pass very easily through a barrier compared to other substances such as inorganic salts, thus establishing a distinction between two types of materials. In 1885 Fick first studied the laws of diffusion of gas permeation through cellulose nitrate

membranes and established the concept of diffusion which is known as Fick's law. Only in the last 30 years membranes were applied on an industrial scale for gas separation, since the first industrial installation of PRISM membranes by Perma for hydrogen separation from purge gas for ammonia synthesis.

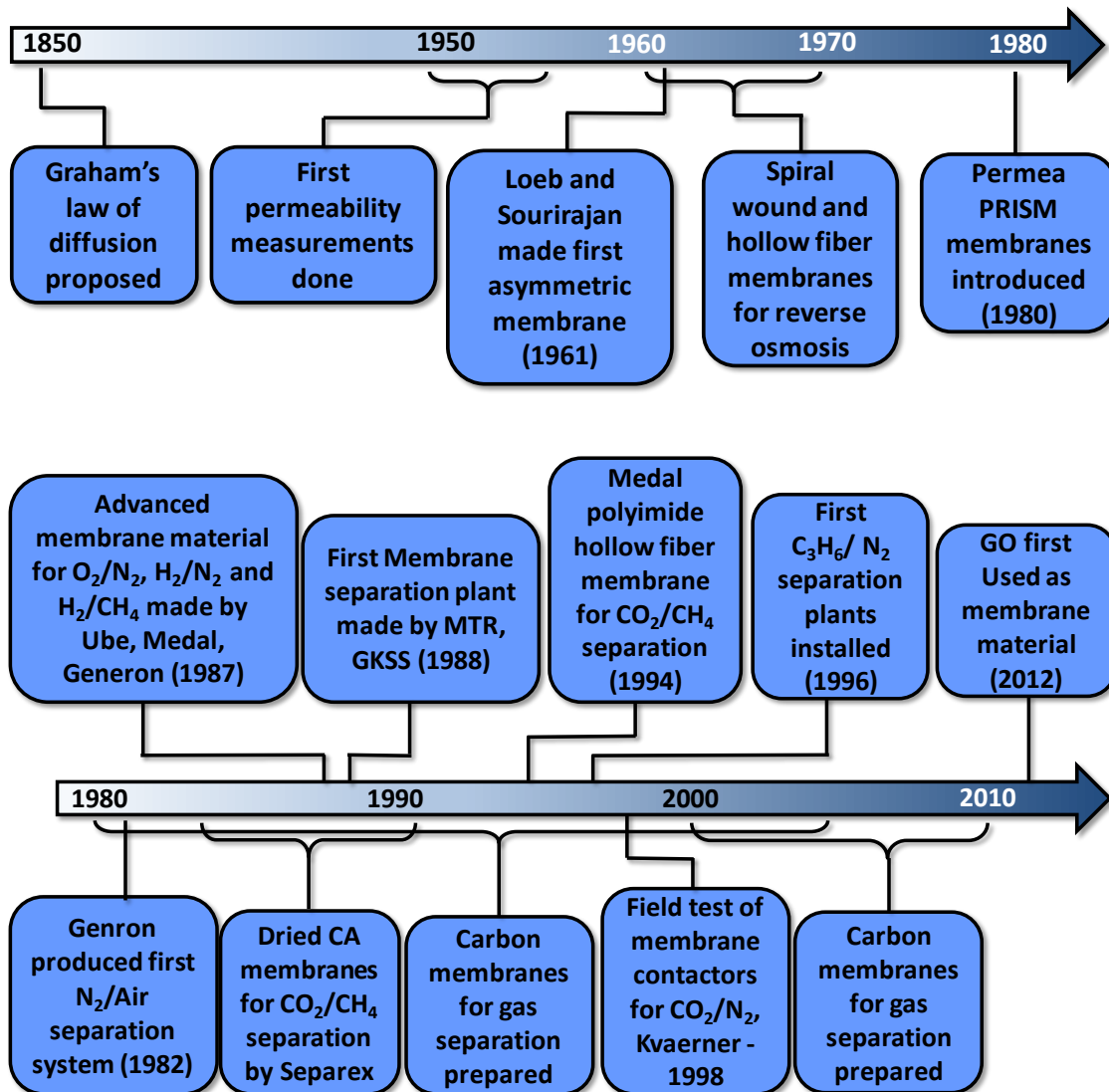


Figure 2.1.1: Milestones in the application of membranes for gas separation.

A more detailed description of notable events in development of membrane technology is given below:

Scientist (year) (Ref)	Events
Nollet (1752) (1)	Discovered that a pig's bladder passes preferentially ethanol when it was brought in contact on one side with a water-ethanol mixture and on the other side with pure water. This was the first recorded study of membrane phenomena and the discovery of osmosis phenomena
Graham (1829) (2)	Performed the first recorded experiment on the transport of gases and vapors in polymeric membranes
Fick (1855) (3)	Proposed a quantitative description of material transport through boundary layers
Graham (1866) (2)	Systematically studied on mass transport in semipermeable membranes during diffusion of gases through different media and reported that the natural rubber exhibits different permeabilities to different gases. Graham's Law of Mass Diffusion was proposed
Lord Rayleigh (1900) (4)	Determined relative permeabilities of oxygen, argon, and nitrogen in rubber
Benchold (1907) (5)	Prepared nitrocellulose membranes with graded pore size structure. Defined the relationship between bubble point and temperature, surface tension, and pore radius
Knudsen (1908) (6)	Defined Knudsen diffusion
Shakespear (1917- 1920) (7-9)	Found temperature dependency of gas permeability that is independent of partial pressure difference across membranes
Dayn Daynes (1920) (10)	Developed time lag method to determine diffusion and solubility coefficient

Scientist (year) (ref)	Events
Barrer (1939) (11)	Applied Arrhenius equation for permeabilities and diffusivities
Barrer and Strachan (1955) (12)	Studied the diffusion and the adsorption of permanent gases through compressed carbon powders
Loeb and Sourirajan (1962, 1964) (13, 14)	Developed RO membrane based on cellulose acetate, which provided high fluxes at moderate hydrostatic pressures. Found dried RO membrane can be used for gas separation
Vieth and Sladek (1965) (15)	Proposed models for sorption and diffusion in glassy polymers
Stern et al. (1969) (16)	First to systematically study the transport of gases in high polymers at elevated temperatures
Cynara and Separex Company (1982–1983) (17)	Developed cellulose acetate membranes for the separation of CO ₂
Henis and Tripodi (1980) (Monsanto, Inc.) (18)	The first major product Monsanto Prism A [®] membrane for hydrogen separation
Gies (1986) (19)	All-silica zeolite deca-dodecasil 3R (DD3R)
Paul and Kemp (1973) (20)	First reported MMMs for gas separation
Permea PRISM membrane (1980)	First commercialized gas separation membrane
Kulprathipanja et al. (1988) (21)	Mixed matrix systems of polymer/adsorbent might yield superior separation performance to that of pure polymeric system

Scientist (year) (Ref)	Events
Robeson (1991) (22)	Proposed upper bound between gas permeability and selectivity
Iijima (1991) (23)	Discovery of carbon nanotubes (CNTs)
Suda and Haraya (1997) (24)	Prepared carbon molecular sieve (CMS) membrane, prepared from pyrolyzation of polyimide, and permeabilities of different gases were studied ($H_2 > He > CO_2 > O_2 > N_2$)
McKeown (1998) (25)	Polymers of intrinsic microporosity (PIMS)
Yang et al. (1999) (26)	Proposed gas separation by zeolite membranes on the basis of different adsorption properties
Caro et al. (2000) (27)	Proposed gas separation by zeolite membranes on the basis of differences in the molecular size and shape
Mahajan and Koros (2002) (28-30)	Application of 4A zeolite in polymers for MMMs membrane preparation
Skoulidas et al. (2002) (31)	Made simulations for both self- and transport diffusivities of light gases such as H_2 and CH_4 in carbon nanotubes and zeolite
Ackerman et al. (2003) (31, 32)	Made simulations for Ar and Ne transport through CNTs
Hinds et al. (2004) (33)	Tried to incorporate aligned CNTs into the polymer matrix and proposed the potential of the nanotubes' inner cores to act as a channel for gas transport
McKeown et al. (2005) (34)	PIMS are excellent performers for gas separation
Chen and Sholl	Predicted selectivity and flux of $CH_4 - H_2$ separation using

(2006) (35)	single- walled carbon nanotubes as membranes
Scientist (year) (Ref)	Events
Gonzo et al. (2006) (36)	Applied Maxwell equation to the performance of mixed matrix membranes (MMMs)
Cong et al. (2007) (37)	Used BPPO dpmembranes using both pristine single-wall CNTs (SWNTs) and multi-wall CNTs (MWNTs). Composite membranes increased in CO ₂ permeability compared to the corresponding pure-polymer membrane
Husain and Koros (2007) (38)	Increased hydrophobicity of the zeolite surface by capping surface hydroxyls with hydrophobic organic chains via Grignard type reactions (MMMs preparation)
Himeno et al. (2007) (39)	α -alumina surface coated with DDR zeolite for gas separation
Bergh et al. (2008) (40)	Separation and permeation characteristics of a DDR zeolite membrane (gas separation)
Yoo, Lai, and Jeong group (2009) (41)	The first MOF membranes were reported
Li et al. (2010) (42)	SAPO-34 zeolite membranes for CO ₂ -CH ₄ separation
Betard et al. (2012) (43)	Metal-organic framework (MOF) membrane by stepwise deposition of reactants
Nair et. al. (2012) (44)	GO first used as membrane material
Kim et. al. and Li et. al. (2013) (45, 46)	Molecular sieving properties of GO membranes discovered.

Table 2.1.1. Events in development of gas separation membranes. Adapted from ref (47)

2.1.3. Theory of gas permeation:

The driving force for gas separation is partial pressure gradient which is the product of total pressure and mole fraction. Both dense and porous membranes are used for gas separation. Before going into the detail of gas separation, some useful terminologies to know are given below.

Permeance: Permeability of a membrane can be described as the state or quality of a material or membrane that causes it to allow liquids or gases to pass through it. The productivity of a gas separation membrane is expressed in terms of its permeance, the amount of permeate that passes through a certain membrane area in a given time for a particular pressure difference. Values of permeance are often quoted in units of GPU [1 GPU = 10^{-6} cm³ (STP) cm⁻² s⁻¹ cmHg⁻¹].

Permeability: Permeance multiplied by the thickness of the membrane gives permeability P (sometimes called permeability coefficient). It is a characteristic of the material. In principle, permeability is independent of membrane thickness for a homogeneous membrane, but in practice values can depend both on thickness of the membrane and on its history. Permeability is defined as:

$$P = \frac{q \cdot t}{A \cdot \Delta p}$$

where q is the mass flux of gas through a membrane of area A and thickness t , under a partial pressure gradient Δp across the membrane.

Values of permeability are often quoted in units of Barrer [1 Barrer = 10^{-10} cm³ (STP) cm cm⁻² s⁻¹ cmHg⁻¹ = 3.35×10^{-16} mol m m⁻² s⁻¹ Pa⁻¹]

Separation factor or selectivity: Another key characteristic of membranes is their selectivity in gas separation. There are several definitions of this property. If permeation of different gases proceeds independently, that is, the permeability of one gas is not sensitive to the presence of other permeating gases, then the ideal separation factors defined as:

$$\alpha_{AB} = \frac{P_A}{P_B}$$

Here P_A and P_B are the permeability coefficients of gases A and B measured in runs with individual permeation. Commonly, a ‘fast’ gas is taken as A, that is, $\alpha_{AB} > 1$

Upper bound relationship: Both high permeability coefficients and high selectivities of membrane are desirable for increasing process capacity and purity of product; however, there is an inherent trade-off between permeability and selectivity, whereby polymers with high permeability typically have low selectivity, and vice versa. This well-known trend was analysed in detail by Robeson, who empirically deduced the concept of an upper bound for a variety of gas separations.(22, 48) The upper bound represents the most favourable combinations of permeability and selectivity characteristics of polymer membranes reported in the literature, and are described by the following equation:

$$P_A = k\alpha_{AB}^n$$

Where P_A is the permeability of the more permeable gas, α is the separation factor of gases A and B (P_A/P_B), k and n are empirical constants for particular set of gases. An example of upper bound plot is given below:

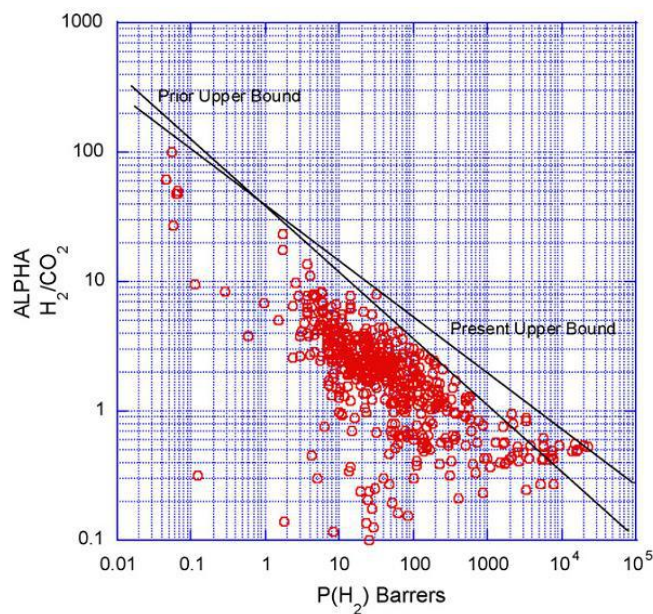


Figure 2.1.2. Upper bound relationship of H_2 and CO_2 . The previous upper bound refers to upper bound in 1991 whereas the present upper bound reflects to the data collected till 2008. Adapted from ref (48)

2.1.3.1. Gas permeation through a non-porous membrane:

Gas permeation through dense non-porous membranes occur through a solution-diffusion pathway. The partial pressure difference between the two sides of the membrane creates a concentration gradient between the faces through which gas molecule passes through following Fick's law as depicted in figure 4.2. Let us consider a steady state isothermal flux through a homogeneous (uniform) polymer film with thickness that separates two gas phases containing a single gas with pressure $p_2 > p_1$ (Fig. 2.1.3). According to Fick's first law applied to the polymer-sorbed gas system, the flux can be represented as:

$$J = -D \frac{dc}{dx}$$

where c is concentration, x is the coordinate across the film and the diffusion coefficient D . This equation predicts a linear concentration profile within the membrane.

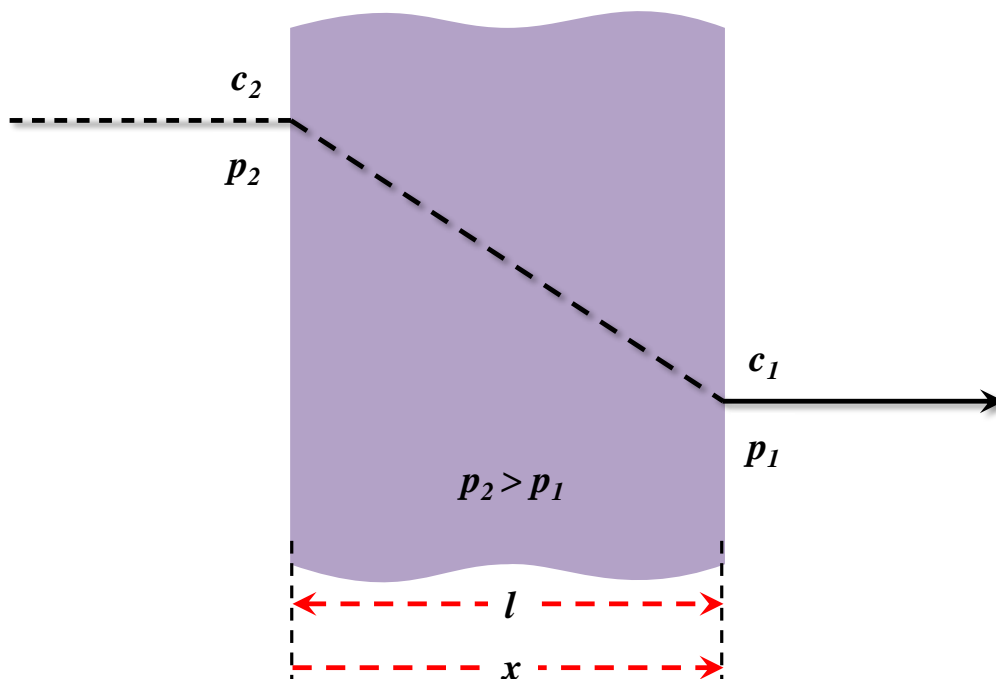


Figure 2.1.3. Schematic of gas permeation through a non-porous membrane.

Two theoretical approaches are employed to explain and describe diffusion and permeation of gases in polymers. The first one, the transition state theory (49) is based on the concept that diffusion in condensed media is an activated process like the rate of chemical reactions. Hence, the Arrhenius equation is applicable to the temperature dependence of the diffusion coefficients:

$$D = D_0 e^{(-E_D/RT)}$$

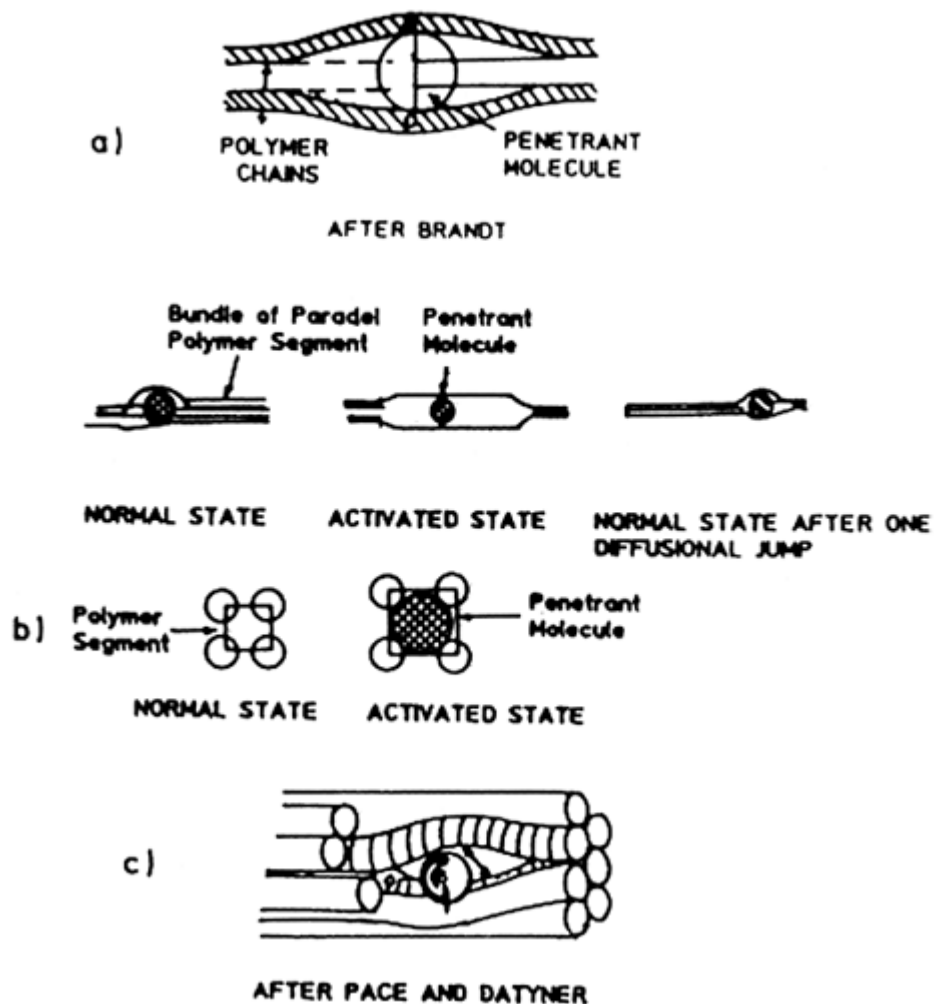
Although this approach is mainly qualitative, because no straightforward method has been proposed for prediction of activation energy of diffusion E_D and, especially the pre-exponential term D_0 , its application can be very useful, for example for description of permeability–permselectivity diagrams.(50) An advanced development of the activated diffusion approach(51) is extensively used in contemporary simulations of mass transfer in polymers.

Another approach, the free volume theory is based on the concept that all condensed (amorphous) media contain a free volume (holes, microcavities) that is either fluctuating in nature (liquid, rubbers) or is embedded in a rigid matrix (inorganic glasses, glassy polymers). The presence, size and/or mobility of these microcavities is a prerequisite for diffusion of small particles in the medium. The concept of free volume was introduced long ago, (52) but in these works free volume was considered as an abstract notion. Today, free volume theory is the leading approach for understanding and description of nanostructure in polymers. It is very helpful that several direct methods are now available for estimation of free volume in polymers (53, 54) and in numerous works free volume (its size and size distribution) is related to the observed values of D and P .

Figure 2.1.4 illustrates a schematic representation of the various models proposed for polymer microstructure for the transport of small permeant molecules through the matrix.

- Figure 2.1.4a illustrates a bundle of parallel polymer chains and inclusion of gas molecules. In order to move into the polymer matrix, the gas molecule pushes the polymer chain and jumps into a new position.
- Figure 2.1.4b shows that the polymer segments are in a normal and an activated state. In the activated state the polymer chain accommodates a diffusing molecule, allows it to diffuse, and then returns to the normal configuration after the jump of the molecule. It also shows the normal and activated states of the polymer segments.
- Figure 2.1.4c shows the model proposed by Pace and Datyner (55). The model accounts for the structure of the polymer contributing to gas diffusions and incorporates some of the features of models Fig. 4.4a, b.

In the model illustrated in Fig. 4.4c, it is assumed that non-crystalline polymer regions possess an appropriate semi-crystalline order with chain bundles. These bundles are parallel along distances of several nanometers and can be considered as tubules. The tubules, consisting of parallel chains, facilitate the movement of the permeant, and the transport occurs by leaps between these tubules. These jumps occur when the thermal



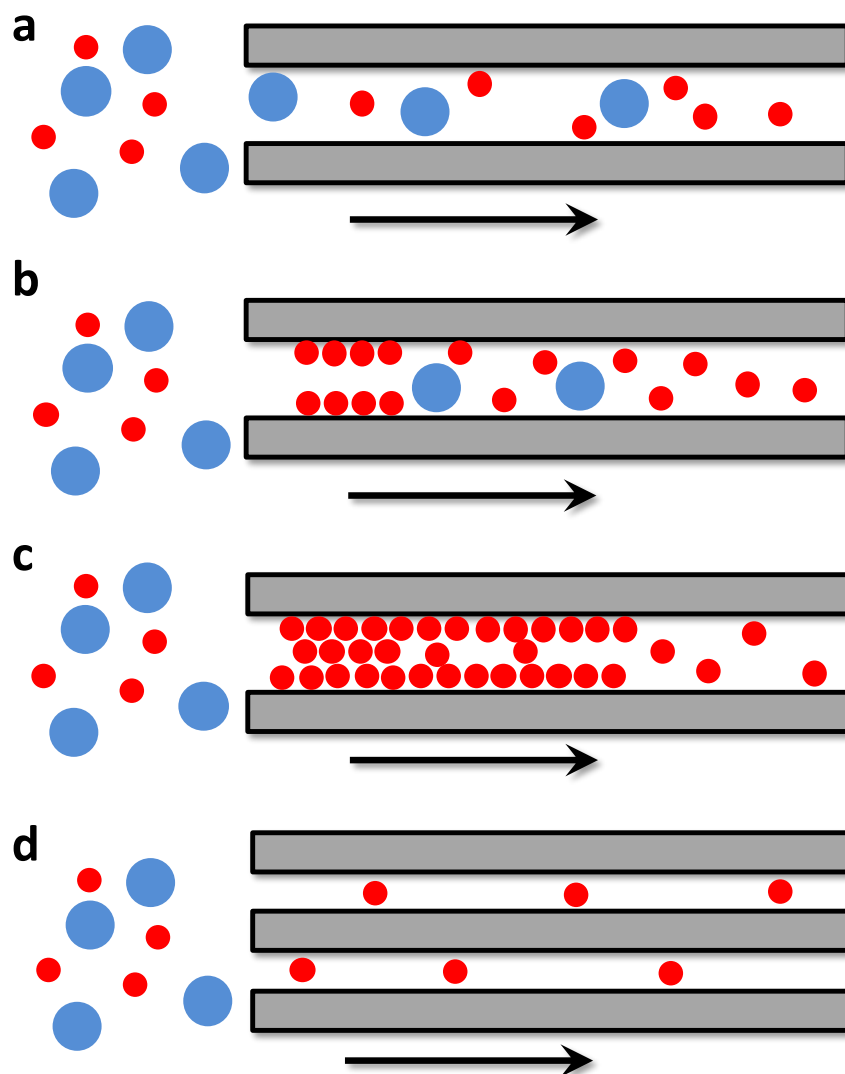
motions of local segments of the polymer chain open up a sufficiently large channel to a neighbouring gap. The gas molecule/particles can then diffuse through this channel. Once the channel closes, the jump is successfully concluded. According to this model, the selectivity of a membrane material depends on the control of these leap channels. Large

Figure 2.1.4. Schematic representation of the various models proposed for transport of small molecule through a polymer membrane. Adapted from reference (56)

openings or high flexibilities cause large diffusion coefficients and low apparent energies of activation for diffusion, whereas more limited motions permit the passage of smaller species much more readily than the large particles.

2.1.3.2. Gas permeation through a porous membrane:

A porous membrane is a rigid, highly voided structure with randomly distributed interconnected pores. The separation of materials by porous membrane is mainly a function of the permeant character and membrane properties, such as the molecular size



of the membrane polymer, pore size, and pore size distribution. A porous membrane is

Figure 2.1.5. *Four types of diffusion mechanisms through a porous membrane. a) Knudsen diffusion, b) surface diffusion, c) capillary condensation and d) molecular sieving*

very similar in its structure and function to a conventional filter. In general, only those molecules that differ considerably in size can be separated effectively by microporous membranes. Porous membranes for gas separation do exhibit very high levels of flux but inherit low selectivity values. Microporous membranes are characterized by the average pore diameter d , the membrane porosity, and tortuosity of the membrane. Porous membranes can be utilized for gas separation. The pore diameter must be smaller than the mean free path of gas molecules. Under normal condition (100 kPa, 300 K) diameter is about 50 nm. The gas flux through the pore is proportional to the molecule's velocity, i.e., inversely proportional to the square root of the molecule mass (Knudsen diffusion). Flux through a porous membrane is much higher than through a nonporous one, 3–5 orders of magnitude. Separation efficiency is moderate—hydrogen passes four times faster than oxygen.

Four types of diffusion mechanism can be utilized to effect separation by porous membranes (see Figure 2.1.5).⁽⁵⁷⁾ The four diffusion mechanisms above are:

1. Knudsen (or free molecule) diffusion: In Knudsen diffusion, a gas molecule will experience more collisions with the pore walls than with other gas molecules. The Knudsen selectivity depends on the ratio of molecular weight of the molecules.

Let us consider the effusion of a gas mixture through a long channel with circular cross section. The nature of the flow depends on the comparative magnitude of the mean free path λ and the radius r of the opening. When the opening is large ($r \gg \lambda$), there is a continual momentum transfer from the lighter and faster molecules to the heavier and larger molecules in the gas mixture by collision. Since both the molecules pass through the orifice with same drift velocity, the flow is ideally non separative. In this region the flow is ideally governed by Poiseuille equation.

In the other limiting case ($r \ll \lambda$), a molecule going through the orifice have very little chance to collide with another molecule in the vicinity of the orifice. The molecules travel through the channels independently with a velocity component to the mean speed \bar{v} of thermal agitation and inversely proportional to the square root of its molecular mass ($m^{-1/2}$). The flow in this limit is separating. In this limit the flow is governed by the well-known Knudsen formula.

$$\bar{F} = -\frac{16r}{3\pi m \bar{v}} \frac{dp}{dx}$$

Where \bar{F} denotes the mean flow of molecules per unit area per unit time in the x direction across a pressure gradient dp . This formula has been confirmed by Knudsen and Adzumi in experiments with bundles of capillary tubes at very low pressure. This equation is only valid when $\lambda \gg r$.

The Knudsen number (K_n) is defined as the ratio of the mean free path of the gas molecules (λ) and a representative physical length scale (e.g., the pore radius), (r)

$$K_n = \frac{\lambda}{r}$$

Gas Pair	Separation factor $\sqrt{(m_2/m_1)}$
H ₂ /CH ₄	2.82
H ₂ /N ₂	3.74
H ₂ /CO	3.74
H ₂ /O ₂	4.0
H ₂ /CO ₂	4.69

N ₂ /O ₂	1.07	Knudsen separation ratio
O ₂ /CO ₂	1.17	

n can be achieved with membranes having pore sizes smaller than the mean free path of gas molecules. Table 4.2 presents the ideal separation factors of various pairs of gases based on Knudsen flow.

Table 2.1.2. *Calculated separation factors based on Knudsen flow of selected binary gas mixtures.*

Momentum transfer theory: Let us consider first the changes that take place in the character of the flow as λ decreases from an initially large value. In a long tube of length $L \gg r$ there will be no intermolecular collisions so long as $\lambda \gg r$. If $L \gg \lambda \gg r$, a molecule will make many intermolecular collisions before reaching the outlet, but for every collision that a molecule makes with another molecule, it will make many collisions with the wall. Now the flow is ideally separative as long as intermolecular collisions can be neglected; when these occur momentum is transferred on the average from the lighter to the heavier gas so that the flow rates tend to equalize. If $\lambda \gg r$, the effect of a momentum transfer in an intermolecular collision is effaced during the many subsequent collisions with the wall which precede another intermolecular collision, and in which the molecule comes into equilibrium with the molecules of the wall. Thus the flow remains ideally separative Knudsen flow until the mean free path λ becomes comparable to the diameter of the tube. When $\lambda \sim r$ the effect of an intermolecular collision persists until the next intermolecular collision, and the cumulative effect of collisions between unlike molecules is to equalize the flow rates and diminish the separation efficiency.

2. Surface diffusion: Surface diffusion can occur in parallel with Knudsen diffusion. Gas molecules are adsorbed on the pore walls of the membrane and migrate along the surface. Surface diffusion increases the permeability of the components adsorbing more strongly to the membrane pores. At the same time, the effective pore diameter is reduced. Consequently, transport of non-adsorbing components is reduced and

selectivity is increased. This positive contribution of surface diffusion only works for certain temperature ranges and pore diameters.

3. Capillary condensation: Capillary condensation occurs if a condensed phase (partially) fills the membrane pores. If the pores are completely filled with condensed phase, only the species soluble in the condensed phase can permeate through the membrane. Fluxes and selectivities are generally high for capillary condensation. The appearance of capillary condensation, however, strongly depends on gas composition, pore size, and uniformity of pore sizes.

4. Molecular sieving: Molecular sieving occurs when pore sizes become sufficiently small (3.0–5.2 Å), leading to the separation of molecules that differ in kinetic diameter. The pore size becomes so small, that only the smaller gas molecules can permeate through the membrane. Typical examples of molecular sieving membranes include zeolites and Metal organic frameworks. A table of different gas molecules and their kinetic diameters is given below in table 2.1.3.

Gas molecule	Mol. Wt.	Kinetic diameter (Å)
H ₂	2	2.89
He	4	2.6
CH ₄	16	3.8
N ₂	28	3.64
O ₂	32	3.46
CO ₂	44	3.3

Table 2.1.3. Molecular weight and kinetic diameter of gases.

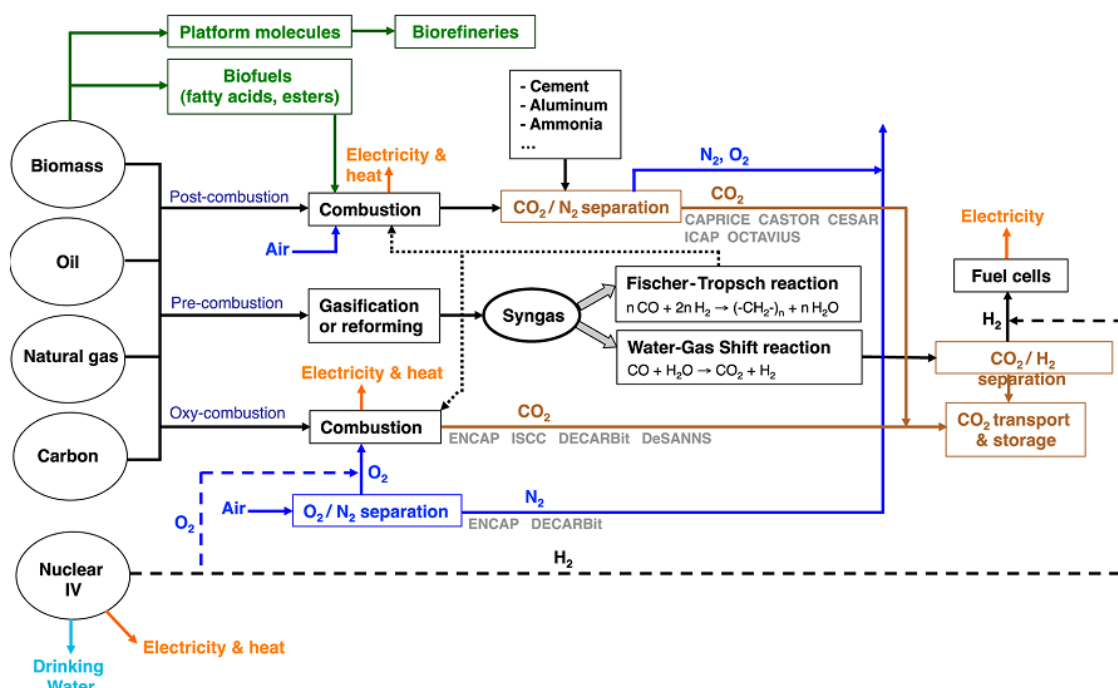
In some cases, molecules can move through the membranes by more than one mechanism. Knudsen diffusion gives relatively low separation selectivity compared to surface diffusion and capillary condensation. Shape selective separation or molecular sieving can yield high selectivities. The separation factor of these mechanisms depends

strongly on the pore size distribution, temperature, pressure and interaction between gases being separated, and the membrane surfaces.

2.1.4. Separation of H₂ from CO₂ by porous inorganic membranes:

In today's world, scientific community is concerned by the rising levels of CO₂ in the atmosphere as a greenhouse gas due to the increase in consumption of fossil fuel, industrial processes, deforestation, and use of fertilizers. CO₂ is considered to play a major part in global rising of temperatures. CO₂ emissions account for 70% of global emission of greenhouse gases followed by CH₄ and N₂O. Since the industrial revolution global CO₂ levels have increased dramatically from 280 ppmv at 1975 to >380 ppmv at present with an annual increase of 1ppm. This increase in CO₂ levels have led to increase in global temperatures 0.6 to 0.7 C. During the period (2000-2004) global temperature have risen by more than 0.3%. on current trends, the Intergovernmental Panel on Climate Change (IPCC) projects 1.8-4.0 C increase in temperature by the end of the century, leading to irreversible consequences (like increase in sea levels) to mankind and ecosystem. In this context, according to a number of technical reports and papers, CO₂ capture, transport and storage (CCS) is considered one of the most viable strategies to control the levels of atmospheric CO₂.

Among the steps involved in CCS chain, CO₂ capture is by far the most important and challenging one. This step can account for about 50%-90% of the total cost of the whole process depending on the source of CO₂ emission. Among the existing technologies, chemical adsorption of CO₂ by alkanolamines and variants is the most adopted one in capturing CO₂ from flue gas streams in large quantities.(58) One of the major disadvantage of this process is that it cannot be operated in a continuous mode.



For regeneration of the adsorbents, adsorbed CO₂ must be released in a separate chamber by decreasing pressure or increasing temperature. Also the stability of the adsorbent in the presence of O₂ or SO₂ remains a challenge. A schematic depicting capture strategies as a function of the combustion type, and implementation is presented in figure 2.1.6.

Figure 2.1.6. CO₂ capture strategies as a function of the combustion type, implementation in the overall strategy for energy production and CO₂ capture/storage, strategic target separations, and relevant FP6 and FP7 European projects recently accomplished. Adapted from reference(59).

In this chapter we focus only on porous inorganic membranes (PIMs) as alternative candidates to chemical absorption and other prospective technologies for CO₂ capture in different pre and post combustion scenarios as depicted in figure 4.7. Although some studies point out the advantages of chemical absorption over membrane technologies for CO₂ capture,(60) most of these statements focus on nonoptimized membrane materials (e.g., resistant to water and acids, manufacture of thin layers, reproducibility of synthesis protocols), offering a biased view of the field.

In term of membrane technologies, PIMs for gas separation are still in early stage of development, yet they show tremendous potential for pre and post combustion CO₂ capture for different reasons.

- PIMs show higher thermal, chemical, and mechanical stability than polymers and are therefore more robust and offer potentially longer life and reduced maintenance costs.
- PIMs offer higher permeability than polymeric membranes, allowing smaller layouts and lower investment costs.
- Unlike adsorbents PIMs can function in continuous mode.

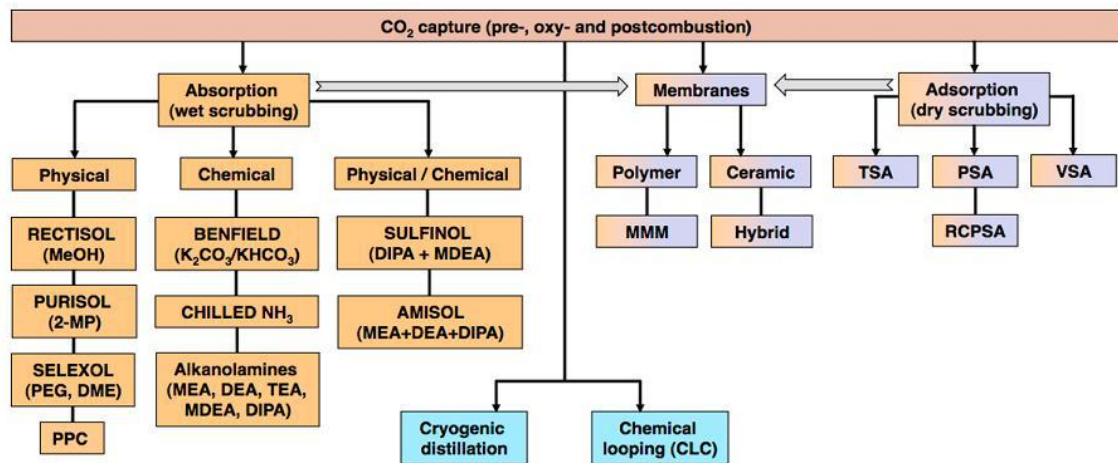


Figure 2.1.7. Summary of technologies for CO₂ capture stressing the intimate synergy between absorption and adsorption concepts for membrane design (violet, precombustion; blue, oxy-combustion; orange, postcombustion). Adapted from reference(59).

Up to now, a range of inorganic materials have been applied to the separation of hydrogen, including silica, zeolite, MOFs, carbon and amorphous metal oxides. These materials have well-defined or amorphous pore structures and can selectively separate hydrogen mainly based either on size-exclusion, i.e., the so-called molecular sieving or selective. Since weak adsorption is generally observed for H₂ on these membrane materials, surface treatment seems not an effective method to improve hydrogen

selectivity.

Membrane type		Membrane material	Driving force	Selectivity	Permeation	Features
POLYMER		Glassy & Rubbery	Solution/ Diffusion	High selective CO ₂ or H ₂	Low	Low resistance
		Mixed Matrix			Moderate	
Metal & ceramic DENSE	Metal	Metal (Pd, Pd(Ag), Ni...)	Solution/ Diffusion	High selective H ₂	Low / Moderate	High T Moderate resistance
	Ceramic	Molten carbonates M ₂ (CO ₃) _x	Solution/ Diffusion	High selective CO ₂		Moderate resistance
		Metal, ceramic with impregnated / immobilized liquids	Chemical reaction	Selective CO ₂	Moderate resistance	
		Composite: • Metal-glass • Metal-ceramic • Metal-metal (metal = Pd, Pd(Ag)...))	Solution/ Diffusion	High selective H ₂	Moderate resistance	
Inorganic POROUS	Meso (2-50 nm)	Amine-grafted silicas	Adsorption/ Diffusion	Selective CO ₂	Low / Moderate	Moderate resistance
	Micro (<2 nm)	Amine-functionalized silicas	Adsorption/ Diffusion	Selective CO ₂	High	Moderate resistance
		Stabilized silicas	Molecular sieving / Activated Diffusion	Selective H ₂	High	High T Low/moderate resistance
		Zeolites	Adsorption/ Diffusion	Selective CO ₂ or H ₂	High	High resistance
		MOFs / ZIFs	Adsorption/ Diffusion	Selective CO ₂ or H ₂	Moderate / High	Moderate resistance

Table 2.1.4. Classification and characteristics of membranes for pre- and post-combustion CO₂ capture. Adapted from reference(59).

2.1.4.1. Microporous silica membranes:

Microporous silica membranes show promising potential in two separations: (1) H₂ separation from H₂/CO₂ mixtures at high temperatures (>473 K) driven by preferential H₂ diffusion and a molecular sieving effect, and (2) near-room temperature CO₂ separation from CO₂/N₂ and CO₂/H₂ mixtures based on preferential CO₂ adsorption (amine-functionalized silicas). In this report, we shall focus on H₂ selective silica membranes only.

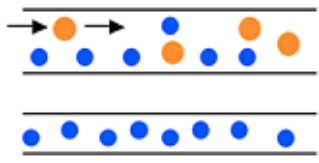
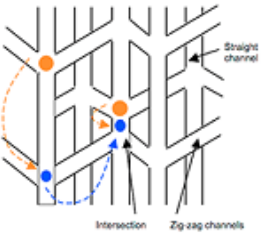

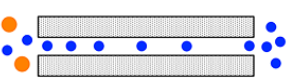
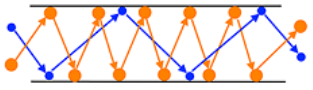
Pore nature	Diffusion mechanism	Scheme	Framework	Membrane separations
Microporous	Single-file diffusion in channels		MOR	Slowing down of faster molecules
	Diffusion within intersecting channels		MFI, BEA	CO ₂ /H ₂ at T↓ CO ₂ /N ₂ at T↓
	Diffusion between cages separated by windows		CHA, DDR, LTA, ITQ-29, ZIFs, ZMOFs	CO ₂ /N ₂ at T↓ CO ₂ /CH ₄ at T↓ CO ₂ /H ₂ at T↓ H ₂ /CO ₂ at T↓ (ZIF)
	Diffusion within intercrystalline domains		Microporous silica	H ₂ /CO ₂ at T↑
Mesoporous			Mesoporous silica, COF	N ₂ /CO ₂ at T↓

Table 2.1.5. Summary of the Structural Features of Silicas, Zeolites, and MOFs with Potential for Membrane Design for CO₂ Capture. Adapted from reference(59).

Silica membranes show a huge promise in H₂ separation due to their high permeability of $10^{-8} - 10^{-7}$ mol/(m²s Pa) and a varying separation factor (10-1500). The main method for preparing such membrane is either sol-gel approach or CVD.

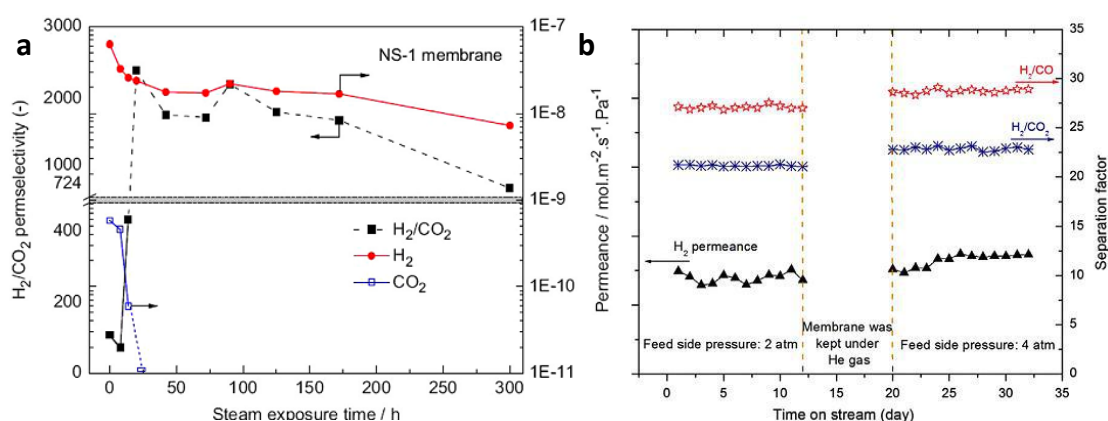
One main drawback of silica membranes is their low hydrothermal stability. Recent research in this area has led to the development of hybrid structure silica membranes, which in addition to providing hydrothermal stability also provide other interesting properties. For example, metal doping of silica membranes can offer a reasonable H₂/CO₂ selectivity up to a several thousand, which is quite high and was not achievable

with bare silica membranes due to preferential adsorption based transport of CO_2 and a small difference in kinetic diameter between H_2 and CO_2 . (61-64)

The incorporation of Nb in microporous silica membrane can create new Bronsted and Lewis acid sites which improves H_2 selectivity of the membranes. On the other hand the increase in stability of the doped membranes with niobium(61), cobalt (63) or Ag (65) was also reported. Figure 2.1.8a shows the long term stability of Nb doped silica membranes up to 300 h at the presence of steam at a pressure of 150 kPa while retaining the H_2/CO_2 selectivity.

2.1.4.2 Zeolite membranes:

Because of its small pore structure, zeolite membranes can separate gas molecules based on their size. The molecular sieving nature of zeolite membranes have led to its



application in various gas separations.

Figure 2.1.8. a) Hydrothermal stability test of NS-1 membrane. Shown are the H_2 and CO_2 gas permeance at 200°C and the calculated single gas H_2/CO_2 selectivity as a function of the time of exposure to 150 kPa steam. Adapted from reference(61). b) Long-term stability of the modified silicate/ ZSM-5 bilayer membrane under water gas shift reaction conditions (gas composition on feed side: $\text{H}_2:\text{CO}_2:\text{H}_2\text{O}:\text{CO} = 1:1:1:1$, with the presence of 400 ppm H_2S at 500°C , total gas flow rate: 80 ml/min (STP), sweeping helium gas flow rate: 20 ml/min (STP), permeate side pressure: 1 atm. Adapted from reference(66)

In the last decade zeolite membranes have received increased interest in the field of H₂ separation as H₂ permeance was increased by one order (10⁻⁸ to 10⁻⁷ mol/(m² s Pa)) without affecting the selectivity. This enhancement was achieved by deposition of silica species in the zeolitic channels via thermal cracking of methyl diethoxysilane(67), methyldiethoxysilane (MDES).(68, 69) The modified zeolite membranes also show promise to improve hydrothermal stability under WGS conditions.(68) An alternative approach to improve the hydrogen flux is to prepare a thin and high quality zeolite functional layer on a thick silicalite bottom layer, i.e., the so-called bilayer zeolite membranes.(66) It is remarkable that the bilayer membranes demonstrated a long-term stability of at least 24 days under WGS conditions in the presence of 400 ppm H₂S at 773 K, as shown in figure 2.1.8b.

2.1.4.3. Metal organic framework (MOF) membranes:

In recent years metal organic framework (MOF) membranes have emerged as a new material for H₂/CO₂ separation. Metal organic frameworks consist of metal ion centre linked with organic linkers thus forming a 2D or 3D crystalline nanoporous architecture. MOFs offer a various functionality with a huge range of pore diameter. This chemical and physical properties can also be customized with proper choice of organic linkers and metal sites for specific applications. (70, 71) In addition to these, MOFs offer the advantages of uniform pore size, strong adsorption sites and high porosity making them very applicable for gas separation applications.

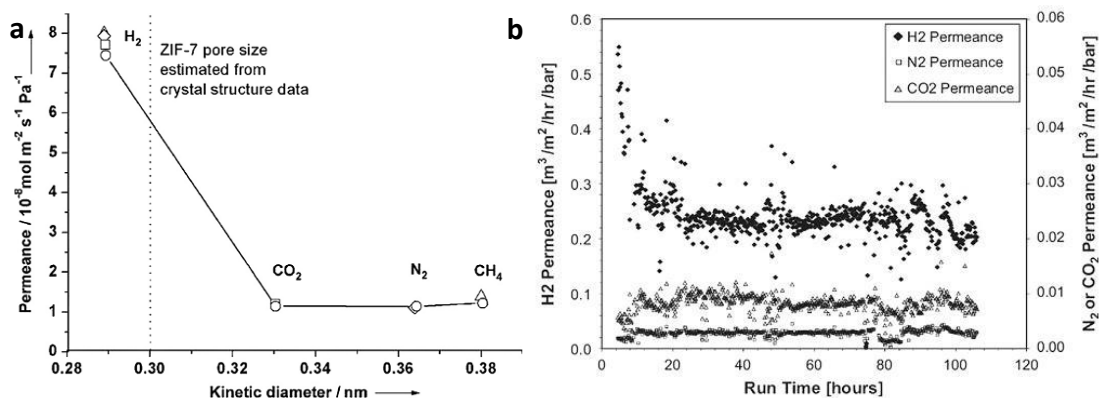


Figure 2.1.9. a) Permeances of single gases (circles) and from 1:1 mixtures (squares: H₂/CO₂ mixture, rhombuses: H₂/N₂ mixture, triangles: H₂/CH₄ mixture) of the ZIF-7 membrane at 200 °C as a function of molecular kinetic diameters. Adapted from

reference(72) and b) Permeance of H₂, N₂ and CO₂ through a carbon molecular sieve hollow fiber membrane for several hours. Adapted from reference(73).

Extensive research has been dedicated towards synthesis and fabrication of MOF membranes for H₂ separation. H₂ permeance of the order of 10⁻⁶ mol/(m²sPa) was reported for MOF membranes which is an order of magnitude higher than other microporous membranes such as carbon molecular sieve, silica and zeolite. Two main mechanism exists for selective separation of H₂ from gas mixture: (1) Preferential adsorption and (2) size selective permeation (molecular sieving). In preferential adsorption, the permeation depends on the interaction of the gas molecule with the pore wall and the diffusion properties. Though the interaction of H₂ is with the pore walls is less in comparison to molecules such as CO₂ or CH₄, the faster diffusion of H₂ makes its separation much easier. For example, HKUST-1 membrane, which shows weak interaction towards H₂ reaches H₂/CO₂ selectivity of 3-10. Caro et. al, Li et. al. and Huang et. al.(72, 74-76) have developed ZIF membranes in which pore size is close to the kinetic diameter of H₂ thus showing molecular sieving effect and efficient separation of H₂ and CO₂ (as shown in figure 2.1.9a) with separation factor in the range of 4-64.

Latest discovery in MOF molecular sieving membranes include fabrication of ultrathin 2D MOF membranes for separation of H₂ and CO₂ by prof. Huang and co-workers.(77) The membranes show a hydrogen selectivity of 200 with excellent hydrothermal stability of up to 400h. Interestingly, they observed a simultaneous increase of both permeance and selectivity by suppressing lamellar stacking of the nanosheets. This discovery may create new opportunities for MOF based molecular sieving membranes for H₂/CO₂ separation.

2.1.4.4. Carbon Molecular sieve membranes:

Carbon molecular sieve membranes are made of microporous carbons in the form of hollow fibres or tubes. They are made from pyrolysis of various polymer precursors such as phenolic resin, cellulose acetate or polymeric hollow fibres or films.(78, 79)

Based on the size of the pores, CMS membranes can be classified into two types- molecular sieving (pore size < 4Å) and adsorption selective carbon membranes (pore

size 5-7Å). CMS membranes can separate gases based on their molecular diameter.(80) However, the H₂ permeance of these membranes turn out to be lower than MOF, silica or zeolite membranes.

Recently great effort has been devoted towards improving hydrothermal stability of CMS membranes. These membranes perform well under flue gas atmosphere containing acid gases such as SO₂ or NO_x. Their performance for water gas shift reaction under industrial condition show high stability for several hundred hours, as depicted in figure 2.1.9b.

In addition to these membranes several other kinds of porous membranes exist e.g. amorphous metal oxide or covalent organic framework (COF) membranes. But they are still in the early stage of development to be commented upon.

Very recently layered materials, especially graphene and graphene oxide have come to the forefront of research as membrane materials for gas separation. Nair et. al.(44) first demonstrated the excellent barrier properties of freestanding membranes. Two very recent studies by Joshi et al.,(81) Li et. al.(46) and Kim et al.(45) reported small molecule and gas permeation properties through GO. Kim et al. and Li et. al. reported highly permeable and selective GO membranes with molecular sieving properties for separating mixtures of gases of industrial relevance. The next two chapters will be focused on gas permeation and separation properties of graphene oxide and MoS₂ membranes.

2.1.5. References:

1. J. Nollet, Recherches sur les Causes du Bouillonnement des Liquides. *Histoire de l'Academie Royale des Sciences, Paris Annee 1748*, 1752 (1752).
2. T. Graham, XXII.-On the absorption and dialytic separation of gases by colloid septa. *J. Chem. Soc.* **20**, 235-288 (1867).
3. A. Fick, Ueber Diffusion. *Ann. d. Physik* **170**, 59-86 (1855).

4. L. Rayleigh, Reviews-On the passage of argon through thin films of india-rubber. *The Journal of Physical Chemistry* **5**, 82-82 (1900).
5. B. H, Ultrafiltration. *Biochem Z* **6**, 379 (1907).
6. M. Knudsen, The laws of molecular flow and the internal viscous streaming of gases through tubes. *Ann Phys* **28**, 75 (1908).
7. S. GA, On the permeability of films and of proofed fabrics. . *Adv. Comm. for Aeronautics Report T1164*, (1918).
8. S. GA, *Adv. Comm. for Aeronautics Report 317 and 516* (1917).
9. D. H. Shakespear GA, The theory of the Kathrometer. *Proc R Soc* **97A**, 273 (1920).
10. H. A. Daynes, The Process of Diffusion through a Rubber Membrane. *Proceedings of the Royal Society of London A: Mathematical, Physical and Engineering Sciences* **97**, 286-307 (1920).
11. R. M. Barrer, E. K. Rideal, Permeation, diffusion and solution of gases in organic polymers. *Transactions of the Faraday Society* **35**, 628-643 (1939).
12. R. M. Barrer, E. Strachan, Sorption and Surface Diffusion in Microporous Carbon Cylinders. *Proceedings of the Royal Society of London A: Mathematical, Physical and Engineering Sciences* **231**, 52-74 (1955).
13. S. Loeb, *Sea Water Demineralization by Means of a Semipermeable Membrane: Progress Report July 1, 1962-December 31, 1962*. (Department of Engineering, University of California, 1963).

14. Loeb S, S. Sourirajan Srinivasa, in 3133132. (United States, 1964).
15. W. Vieth, K. Sladek, A model for diffusion in a glassy polymer. *Journal of Colloid Science* **20**, 1014-1033 (1965).
16. S. A. Stern, J. T. Mullhaupt, P. J. Gareis, The effect of pressure on the permeation of gases and vapors through polyethylene. Usefulness of the corresponding states principle. *AIChE J.* **15**, 64-73 (1969).
17. R. W. Baker, Future Directions of Membrane Gas Separation Technology. *Industrial & Engineering Chemistry Research* **41**, 1393-1411 (2002).
18. J. M. Henis, M. K. Tripodi, A novel approach to gas separations using composite hollow fiber membranes. *Sep. Sci. Technol.* **15**, 1059-1068 (1980).
19. G. H., in *Zeitschrift für Kristallographie - Crystalline Materials*. (1986), vol. 175, pp. 93.
20. D. R. Paul, D. R. Kemp, The diffusion time lag in polymer membranes containing adsorptive fillers. *Journal of Polymer Science: Polymer Symposia* **41**, 79-93 (1973).
21. S. Kulprathipanja, R. W. Neuzil, N. N. Li, U. Patents, Ed. (1988), chap. US 4740219 A.
22. L. M. Robeson, Correlation of separation factor versus permeability for polymeric membranes. *J. Membr. Sci.* **62**, 165-185 (1991).
23. S. Iijima, Helical microtubules of graphitic carbon. *Nature* **354**, 56-58 (1991).

24. H. Suda, K. Haraya, Gas Permeation through Micropores of Carbon Molecular Sieve Membranes Derived from Kapton Polyimide. *The Journal of Physical Chemistry B* **101**, 3988-3994 (1997).
25. N. B. McKeown, *Phthalocyanine materials: synthesis, structure, and function*. (Cambridge University Press, 1998).
26. M. Yang, B. D. Crittenden, S. P. Perera, H. Moueddeb, J. A. Dalmon, The hindering effect of adsorbed components on the permeation of a non-adsorbing component through a microporous silicalite membrane: the potential barrier theory. *J. Membr. Sci.* **156**, 1-9 (1999).
27. J. Caro, M. Noack, P. Kölsch, R. Schäfer, Zeolite membranes – state of their development and perspective. *Microporous Mesoporous Mater.* **38**, 3-24 (2000).
28. R. Mahajan, W. J. Koros, Mixed matrix membrane materials with glassy polymers. Part 1. *Polym. Eng. Sci.* **42**, 1420-1431 (2002).
29. R. Mahajan, W. J. Koros, Mixed matrix membrane materials with glassy polymers. Part 2. *Polym. Eng. Sci.* **42**, 1432-1441 (2002).
30. R. Mahajan, W. J. Koros, Factors Controlling Successful Formation of Mixed-Matrix Gas Separation Materials. *Ind. Eng. Chem. Res.* **39**, 2692-2696 (2000).
31. A. I. Skoulidas, D. M. Ackerman, J. K. Johnson, D. S. Sholl, Rapid Transport of Gases in Carbon Nanotubes. *Phys. Rev. Lett.* **89**, 185901 (2002).

-
32. D. M. Ackerman, A. I. Skoulidas, D. S. Sholl, J. Karl Johnson, Diffusivities of Ar and Ne in Carbon Nanotubes. *Molecular Simulation* **29**, 677-684 (2003).
33. B. J. Hinds *et al.*, Aligned Multiwalled Carbon Nanotube Membranes. *Science* **303**, 62-65 (2004).
34. N. B. McKeown *et al.*, Polymers of Intrinsic Microporosity (PIMs): Bridging the Void between Microporous and Polymeric Materials. *Chem. Eur. J.* **11**, 2610-2620 (2005).
35. H. Chen, D. S. Sholl, Predictions of selectivity and flux for CH₄/H₂ separations using single walled carbon nanotubes as membranes. *J. Membr. Sci.* **269**, 152-160 (2006).
36. E. E. Gonzo, M. L. Parentis, J. C. Gottifredi, Estimating models for predicting effective permeability of mixed matrix membranes. *J. Membr. Sci.* **277**, 46-54 (2006).
37. H. Cong, J. Zhang, M. Radosz, Y. Shen, Carbon nanotube composite membranes of brominated poly(2,6-diphenyl-1,4-phenylene oxide) for gas separation. *J. Membr. Sci.* **294**, 178-185 (2007).
38. S. Husain, W. J. Koros, Mixed matrix hollow fiber membranes made with modified HSSZ-13 zeolite in polyetherimide polymer matrix for gas separation. *J. Membr. Sci.* **288**, 195-207 (2007).
39. S. Himeno *et al.*, Synthesis and Permeation Properties of a DDR-Type Zeolite Membrane for Separation of CO₂/CH₄ Gaseous Mixtures. *Ind. Eng. Chem. Res.* **46**, 6989-6997 (2007).

40. J. van den Bergh, W. Zhu, J. Gascon, J. A. Moulijn, F. Kapteijn, Separation and permeation characteristics of a DD3R zeolite membrane. *J. Membr. Sci.* **316**, 35-45 (2008).
41. Y. Yoo, Z. Lai, H.-K. Jeong, Fabrication of MOF-5 membranes using microwave-induced rapid seeding and solvothermal secondary growth. *Microporous Mesoporous Mater.* **123**, 100-106 (2009).
42. S. Li *et al.*, Scale-up of SAPO-34 membranes for CO₂/CH₄ separation. *J. Membr. Sci.* **352**, 7-13 (2010).
43. A. Bétard *et al.*, Fabrication of a CO₂-selective membrane by stepwise liquid-phase deposition of an alkylether functionalized pillared-layered metal-organic framework [Cu₂L₂P]_n on a macroporous support. *Microporous Mesoporous Mater.* **150**, 76-82 (2012).
44. R. R. Nair, H. A. Wu, P. N. Jayaram, I. V. Grigorieva, A. K. Geim, Unimpeded Permeation of Water Through Helium-Leak-Tight Graphene-Based Membranes. *Science* **335**, 442-444 (2012).
45. H. W. Kim *et al.*, Selective Gas Transport Through Few-Layered Graphene and Graphene Oxide Membranes. *Science* **342**, 91-95 (2013).
46. H. Li *et al.*, Ultrathin, Molecular-Sieving Graphene Oxide Membranes for Selective Hydrogen Separation. *Science* **342**, 95-98 (2013).
47. A. F. Ismail, K. C. Khulbe, T. Matsuura, in *Gas Separation Membranes: Polymeric and Inorganic*. (Springer International Publishing, Cham, 2015), pp. 1-10.

-
48. L. M. Robeson, The upper bound revisited. *J. Membr. Sci.* **320**, 390-400 (2008).
49. S. Glasstone, K. J. Laidler, H. Eyring, *The theory of rate processes: the kinetics of chemical reactions, viscosity, diffusion and electrochemical phenomena.* (McGraw-Hill Book Company, Incorporated, 1941).
50. B. D. Freeman, Basis of Permeability/Selectivity Tradeoff Relations in Polymeric Gas Separation Membranes. *Macromolecules* **32**, 375-380 (1999).
51. A. A. Gusev, F. Müller-Plathe, W. F. Gunsteren, U. W. Suter, in *Atomistic Modeling of Physical Properties*, L. Monnerie, U. W. Suter, Eds. (Springer Berlin Heidelberg, Berlin, Heidelberg, 1994), pp. 207-247.
52. M. H. Cohen, D. Turnbull, Molecular Transport in Liquids and Glasses. *J. Chem. Phys.* **31**, 1164-1169 (1959).
53. C. Tzoumanekas, D. N. Theodorou, Topological Analysis of Linear Polymer Melts: A Statistical Approach. *Macromolecules* **39**, 4592-4604 (2006).
54. Y. P. Yampolskii, Methods for investigation of the free volume in polymers. *Russ. chem. rev.* **76**, 59-78 (2007).
55. R. J. Pace, A. Datyner, Statistical mechanical model for diffusion of simple penetrants in polymers. I. Theory. *Journal of Polymer Science: Polymer Physics Edition* **17**, 437-451 (1979).
56. P. Pandey, R. S. Chauhan, Membranes for gas separation. *Prog. Polym. Sci.* **26**, 853-893 (2001).

57. S. Kluiters, Status review on membrane systems for hydrogen separation. *Energy Center of the Netherlands, Petten, The Netherlands*, (2004).
58. G. T. Rochelle, Amine Scrubbing for CO₂ Capture. *Science* **325**, 1652-1654 (2009).
59. M. Pera-Titus, Porous Inorganic Membranes for CO₂ Capture: Present and Prospects. *Chem. Rev.* **114**, 1413-1492 (2014).
60. E. Favre, Carbon dioxide recovery from post-combustion processes: Can gas permeation membranes compete with absorption? *J. Membr. Sci.* **294**, 50-59 (2007).
61. H. Qi, H. Chen, L. Li, G. Zhu, N. Xu, Effect of Nb content on hydrothermal stability of a novel ethylene-bridged silsesquioxane molecular sieving membrane for H₂/CO₂ separation. *J. Membr. Sci.* **421–422**, 190-200 (2012).
62. H. Qi, J. Han, N. Xu, Effect of calcination temperature on carbon dioxide separation properties of a novel microporous hybrid silica membrane. *J. Membr. Sci.* **382**, 231-237 (2011).
63. S. Smart, J. F. Vente, J. C. Diniz da Costa, High temperature H₂/CO₂ separation using cobalt oxide silica membranes. *Int. J. Hydrogen Energy* **37**, 12700-12707 (2012).
64. S. Battersby *et al.*, Hydrothermal stability of cobalt silica membranes in a water gas shift membrane reactor. *Sep. Purif. Technol.* **66**, 299-305 (2009).

-
65. J. Yang, J. Chen, Hydrophobic modification and silver doping of silica membranes for H₂/CO₂ separation. *Journal of CO₂ Utilization* **3-4**, 21-29 (2013).
66. H. Wang, X. Dong, Y. S. Lin, Highly stable bilayer MFI zeolite membranes for high temperature hydrogen separation. *J. Membr. Sci.* **450**, 425-432 (2014).
67. Z. Tang, S.-J. Kim, G. K. Reddy, J. Dong, P. Smirniotis, Modified zeolite membrane reactor for high temperature water gas shift reaction. *J. Membr. Sci.* **354**, 114-122 (2010).
68. Y. Zhang, Z. Wu, Z. Hong, X. Gu, N. Xu, Hydrogen-selective zeolite membrane reactor for low temperature water gas shift reaction. *Chem. Eng. J.* **197**, 314-321 (2012).
69. X. Gu, Z. Tang, J. Dong, On-stream modification of MFI zeolite membranes for enhancing hydrogen separation at high temperature. *Microporous Mesoporous Mater.* **111**, 441-448 (2008).
70. S. R. Venna, M. A. Carreon, Metal organic framework membranes for carbon dioxide separation. *Chem. Eng. Sci.* **124**, 3-19 (2015).
71. S. Qiu, M. Xue, G. Zhu, Metal-organic framework membranes: from synthesis to separation application. *Chem. Soc. Rev.* **43**, 6116-6140 (2014).
72. Y.-S. Li *et al.*, Molecular Sieve Membrane: Supported Metal–Organic Framework with High Hydrogen Selectivity. *Angew. Chem. Int. Ed.* **49**, 548-551 (2010).

73. D. Parsley *et al.*, Field evaluation of carbon molecular sieve membranes for the separation and purification of hydrogen from coal- and biomass-derived syngas. *J. Membr. Sci.* **450**, 81-92 (2014).
74. A. Huang, W. Dou, J. Caro, Steam-Stable Zeolitic Imidazolate Framework ZIF-90 Membrane with Hydrogen Selectivity through Covalent Functionalization. *J. Am. Chem. Soc.* **132**, 15562-15564 (2010).
75. A. Huang, H. Bux, F. Steinbach, J. Caro, Molecular-Sieve Membrane with Hydrogen Permselectivity: ZIF-22 in LTA Topology Prepared with 3-Aminopropyltriethoxysilane as Covalent Linker. *Angew. Chem. Int. Ed.* **49**, 4958-4961 (2010).
76. A. Huang, J. Caro, Covalent Post-Functionalization of Zeolitic Imidazolate Framework ZIF-90 Membrane for Enhanced Hydrogen Selectivity. *Angew. Chem. Int. Ed.* **50**, 4979-4982 (2011).
77. Y. Peng *et al.*, Metal-organic framework nanosheets as building blocks for molecular sieving membranes. *Science* **346**, 1356-1359 (2014).
78. S. M. Saufi, A. F. Ismail, Fabrication of carbon membranes for gas separation—a review. *Carbon* **42**, 241-259 (2004).
79. W. N. W. Salleh, A. F. Ismail, T. Matsuura, M. S. Abdullah, Precursor Selection and Process Conditions in the Preparation of Carbon Membrane for Gas Separation: A Review. *Separation & Purification Reviews* **40**, 261-311 (2011).

80. S. C. Rodrigues, R. Whitley, A. Mendes, Preparation and characterization of carbon molecular sieve membranes based on resorcinol–formaldehyde resin. *J. Membr. Sci.* **459**, 207-216 (2014).

81. R. K. Joshi *et al.*, Precise and Ultrafast Molecular Sieving Through Graphene Oxide Membranes. *Science* **343**, 752-754 (2014).

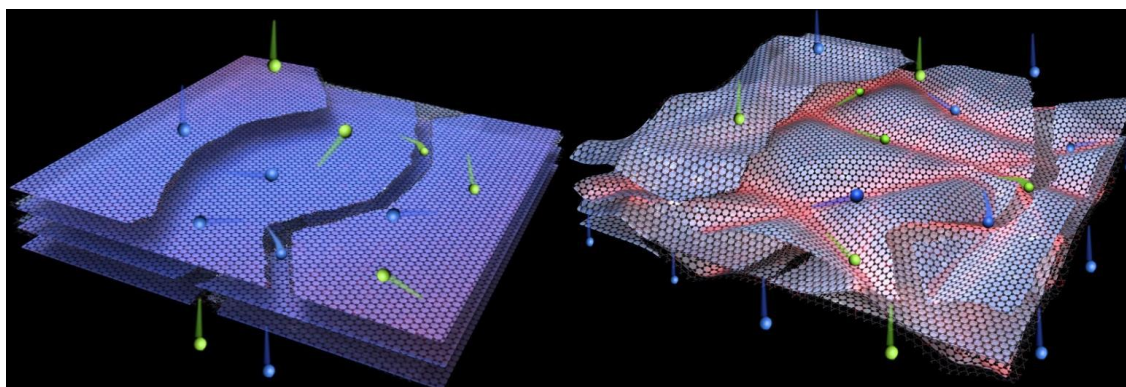
Chapter-2.2

Casting molecular channels through graphene oxide surface:

Effect of domain formation on gas permeation of Graphene oxide membranes.

Summary:

Recent progress on gas separation by graphene oxide (GO) membranes has generated a great deal of interest in the development of high performance membranes. However, it is crucial to enhance the permeability and study their performance at elevated temperatures for practical applications. We have demonstrated that by formation of oxygen rich and graphitic domains on GO surface the permeability of annealed GO membranes can be enhanced immensely up to 20 times without sacrificing their selectivity. We attribute this enhancement to the formation of molecular channels on GO surface which provide easy permeation pathway for gas molecules for better permeability. We have also demonstrated that these membranes perform very well for H₂/CO₂ separation compared to previously reported membranes and are well above the upper bound of polymeric membranes.



2.2.1. Introduction

Compared to other techniques (e.g. adsorption and cryogenic distillation) membrane based gas separation offers a cheap and energy efficient solution for separation of gas mixtures(1). From the late 1970s polymeric membranes have been commercially used for gas separation(2). An area of emerging interest in this field is separation and recapturing CO₂ from industrial processes (such as water gas synthesis, industrial exhaust purification etc.) for reuse and sequestration. Recent advances in membrane science and technology have led to the discovery and industrialization of polymer(3), zeolite(4, 5) and silicon(6) based membranes for these applications. However, permeability and separation factor are two key trade-offs in these membranes which limit their use. In last few years, the advent of graphene and graphene oxide membranes has opened a brand new era for fabrication of high performance membranes(7). Graphene and graphene oxide, due to their atomic level thickness, two dimensional structure, high mechanical strength and chemical inertness are perfect materials for such kind of membranes.

Single layer thick film of graphene has been proven theoretically to be impenetrable to even monoatomic gases such as Helium,(8) nevertheless, porous single layer graphene has been estimated to be an excellent material for water desalination in a study.(9, 10) But it is very difficult to have a defect free single layer graphene sheet big enough for any practical applications; moreover, precise control of the pore size in porous graphene is also very difficult. Membranes consisting of graphene oxide are expected to overcome these drawbacks. Graphene oxide has the advantages of easy synthesis and solution processability. Membranes consisting of graphene oxide have the advantage of being robust, flexible and having easy preparation procedure. These kind of membranes have been used for molecular separation,(11) water purification,(11, 12) dehydration of substances(13, 14) and gas separation. In one of the recent reports, Geim and co-workers showed GO membranes (500 nm to micrometre thick) were permeable to water but impermeable to helium even at high pressure.(15) Gas permeation through such kind of membranes is believed to occur through a tortuous path mechanism through the interlayer spaces of stacked sheets.(Figure 2.2.1a and b) More recently, Kim et. al. and Li et. al. have demonstrated that ultrathin GO membranes (few layer, 2-20 nm) are molecular sieving in nature and extremely efficient for H₂/CO₂ separation (16, 17). In their report, Kim et. al. tested the gas permeation properties of GO

membranes of thickness ranging from 1.8 nm to 18 nm. The membranes show high selectivity but the permeability value was low.(Figure 2.2.1c)

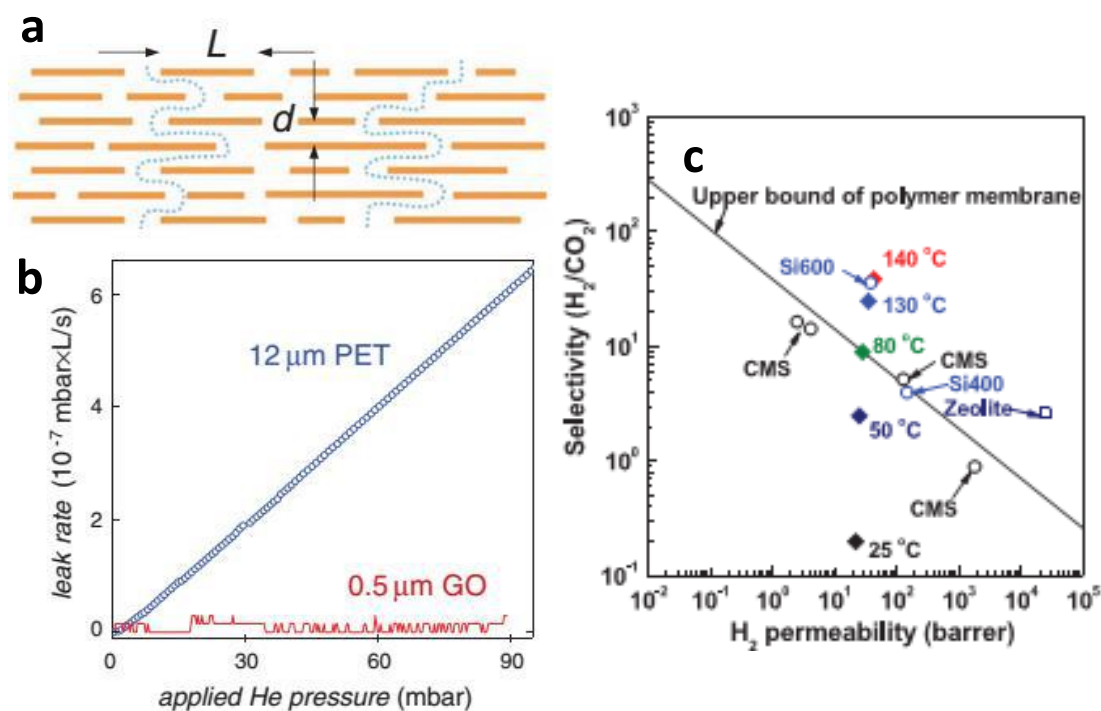


Figure 2.2.1. a) Mechanism of gas permeation through GO membranes through a tortuous pathway. Typical L/d is ~ 1000 . b) Examples of He-leak measurements for a freestanding submicrometer-thick GO membrane and a reference PET (polyethylene terephthalate) film (normalized per square centimeter). c) Comparison of gas separation performance between thermally treated GO membranes (Diamonds) and other membranes in the literature.(hollow circles) Adapted from ref (15, 17)

The mechanism of gas transport through ultrathin GO membranes (in contrast to submicrometer thick GO membranes) is believed to be due to two different factors 1) defects on GO sheets and 2) interlayer spacing formed by corrugation, wrinkles and ripples. For practical purposes, a relatively thicker membrane with high permeability is essential. Micrometre thick GO membranes as such do not show high gas flux. A very useful method to enhance permeability for layered membranes is to create ripples on the surface.

2.2.2. Scope of the present investigation:

GO, being a metastable state, slowly phase transforms to a partially reduced quasi equilibrium state at room temperature with a relaxation time of 35 days.(18) At

elevated temperature (80 °C), Grossman and co-workers showed the formation of oxygen rich and graphitic domains on GO sheet by the migration of oxygen functionalities. (Figure 2.2.2) (19) Such segregated domains on the GO surface is expected to create ripples and channels in a membrane made up of GO layers which in turn have implications on permeation and

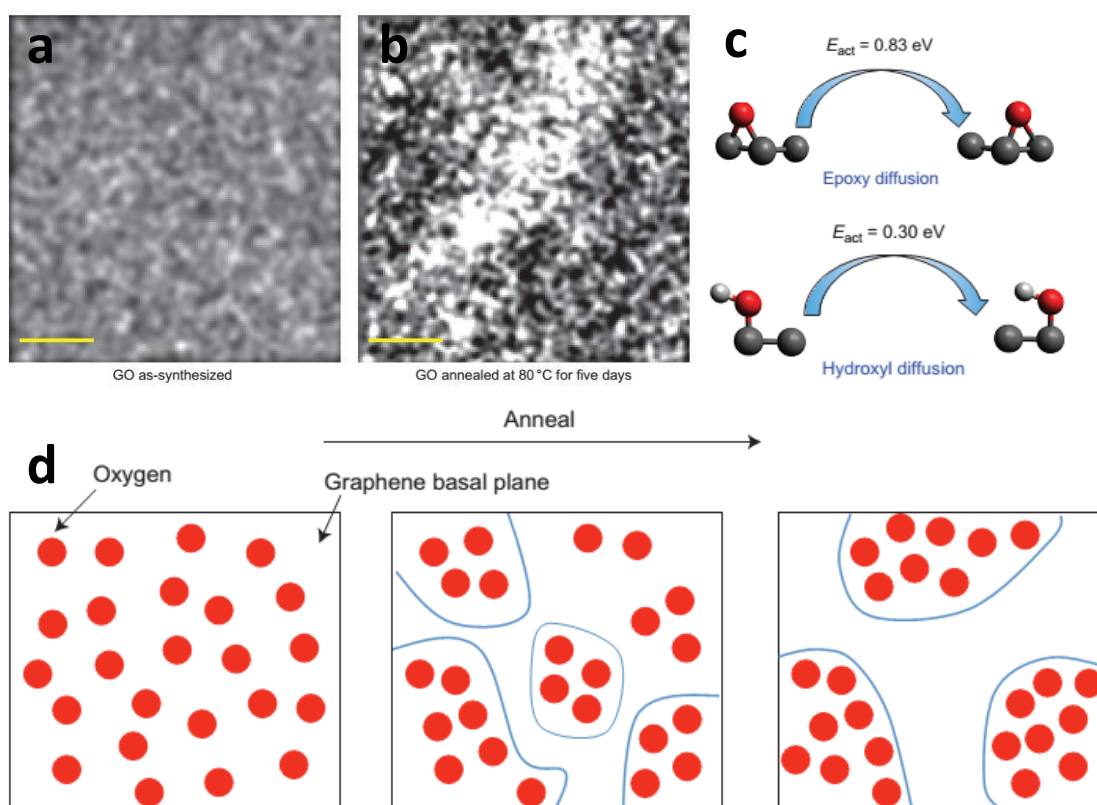


Figure 2.2.2. a) and b) AES oxygen mapping of as-synthesized and annealed GO films. The white spots indicate oxygen-rich regions and the black spots indicate oxygen-poor regions or, in other words, carbon-rich regions. Scale bar, 2 μm . c) Computed activation barriers for the diffusion of epoxy and hydroxyl functional groups on the graphene basal plane. d) Schematic depicting our proposed phase-separation process in as-synthesized GO structures. Synthetic procedures of GO lead to a mixed sp^2 – sp^3 phase that has the potential to separate into two distinct oxidized and graphene phases through diffusion of oxygen atoms on the graphene basal plane under the influence of an external stimulus. Adapted from ref (19)

separation performance of the membrane(20). Considering the huge potential of GO membranes (of thickness few nanometres to few 100 nm) in gas separation, water

purification and their possible utility at elevated temperature, it is highly important to study the effect of domain formation on the gas permeability. In this report, we have showed for the first time that the temperature induced domain formation on GO membranes enhances the gas permeability several fold (20 times) without compromising the separation factor of the H₂/O₂ and H₂/CO₂ gas mixtures.

2.2.3. Experimental procedure:

2.2.3.1. Materials and Characterization techniques:

Graphite powder (20 micron) (Sigma Aldrich), NaNO₃ (Sigma Aldrich), KMnO₄ (S D Fine chemicals), H₂SO₄ (98%, AR grade), were used without any further purification.

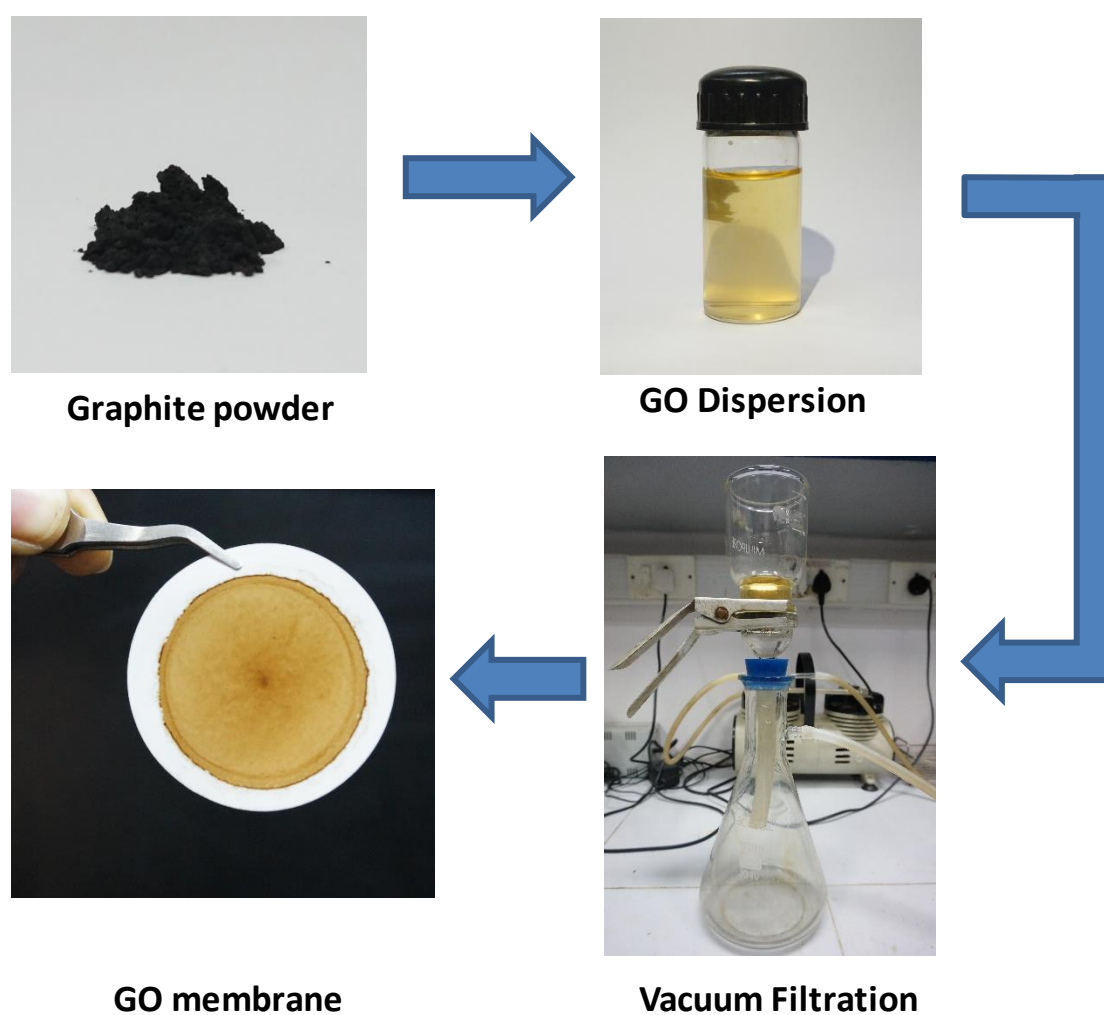
Powder X-ray diffraction (PXRD) patterns were recorded using Rigaku diffractometer using Cu K α radiation, ($\lambda=1.54$ Å). Field-emission scanning electron microscopy (FESEM) images were obtained by using FEI (Nova-Nano SEM-600 Netherlands) equipment. TEM measurements and elemental mapping were performed on a TEM (TECNAI T20) operating at an acceleration voltage (dc voltage) of 100 kV. Samples were prepared by placing a drop of dispersion on a TEM grid (holey carbon). Electronic absorption spectra were recorded on a Perkin Elmer Lambda 750 UV-Vis-NIR Spectrometer. 1 mm path length cuvette was used for recording the spectra.

2.2.3.2. Preparation of Graphene Oxide

Graphene oxide (GO) was obtained from graphite by Hummer's method (21). In a typical procedure, 23 mL of concentrated H₂SO₄ was mixed with 1 g of graphite and 0.5 g NaNO₃ in a 250 mL round bottom flask cooled in an ice bath at 0 °C. 3 g KMnO₄ was added slowly to the mixture in small portions with vigorous stirring. Temperature was maintained below 20 °C during this time. The ice bath was then removed and the reaction was brought to 30-35 °C, where it was maintained for 30 min. To this 46 mL water was added slowly causing violent effervescence and rise of temperature to 98 °C. The resultant brown coloured suspension was maintained at this temperature for 15 minutes. The suspension was then brought to room temperature and 140 ml water was added. The mixture was then treated with 1 mL of 30% H₂O₂ to reduce any unreacted permanganate. The bright yellow reaction mixture was then centrifuged at 5000 rpm, washed several times with distilled water and dialysed until pH of the solution turns neutral.

2.2.3.3. Preparation of GO membrane:

In a typical procedure, GO solution (~14 mg/ mL, 0.5 mL) was diluted to 30 mL and centrifuged at 14500 rpm for 15 min. The resultant solution was filtered through a Millipore filter paper (polycarbonate, pore size 200 nm) to obtain the membranes. For thicker membranes, 1 mL of the concentrated GO solution was diluted to 30 mL, centrifuged and filtered. Scheme 2.2.1 represents schematic of preparation of a typical GO membrane.



Scheme 2.2.1. Schematic for preparation of GO membrane.

2.2.3.4. Gas Permeation Measurements:

Gas permeation measurements were carried out in a custom made permeation cell as shown in figure. 2.2.3. Accurate gas flow was maintained through mass flow controllers (MKS and Hitachi). Pure H_2 , O_2 and N_2 were used as feed gases. Gas flow on the feed stream was kept constant at 100 sccm for individual gases and 50 sccm each for mixed gas permeation. On the the other hand, N_2 was used as sweep gas and the flow was kept

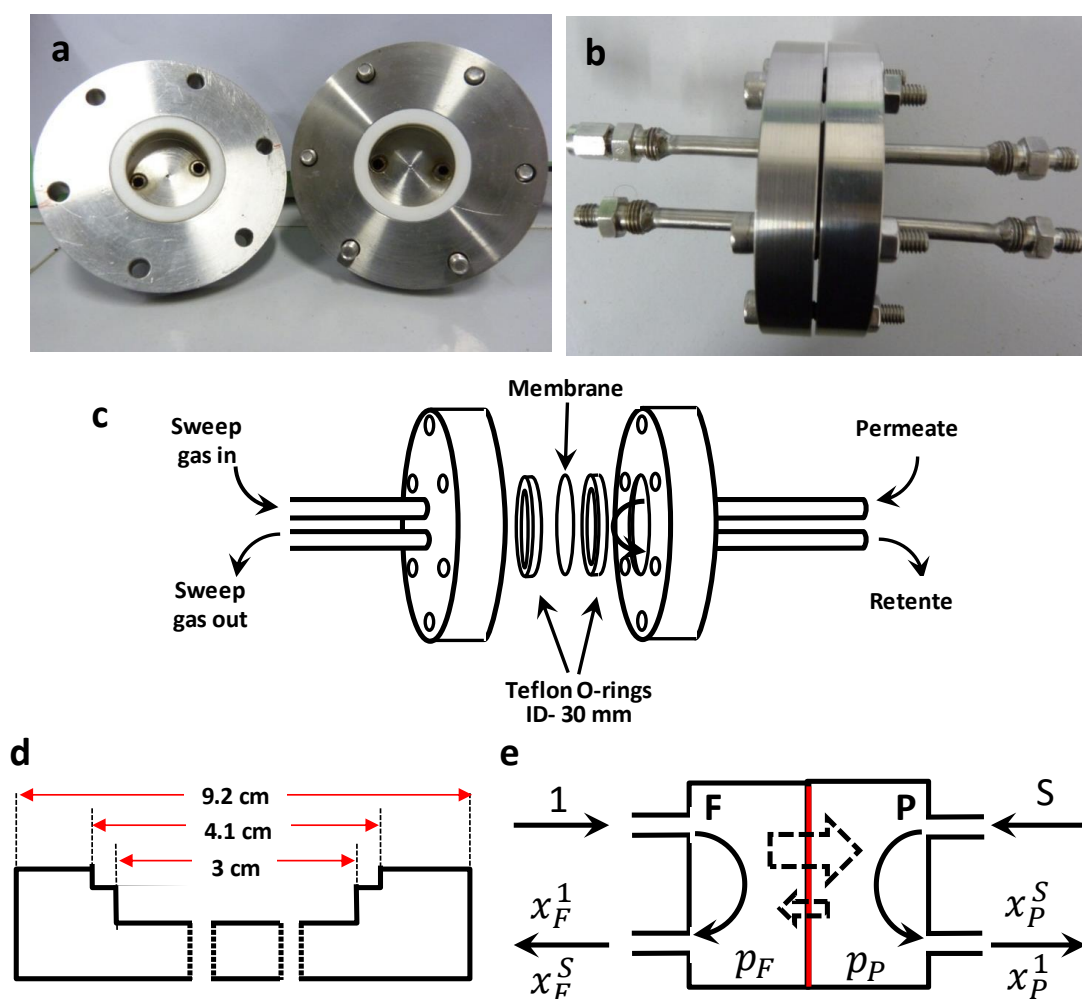


Figure 2.2.3. a, b) Images of the permeation cell, c) Schematic diagram of the permeation cell with membrane. d) Cross sectional view of the permeation apparatus. e) Schematic of gas permeation inside the permeation apparatus. F denotes the feed side, P denotes the permeate side. I is the feed gas while S is the sweep gas. p_F and p_P denoted pressures in the feed and permeate side respectively. x denotes the mole fraction of the respective components.

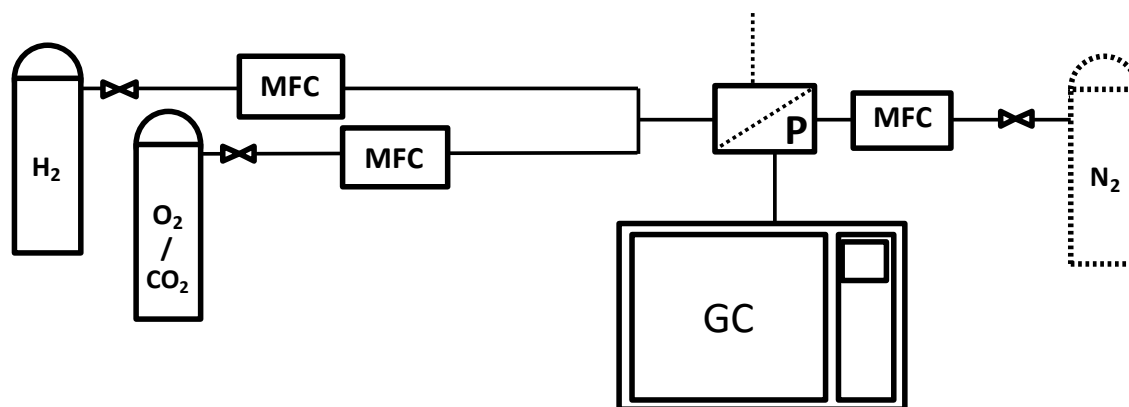


Figure 2.2.4. Schematic of the gas permeation setup. MFC- Mass flow controller, P- permeation cell, GC- Gas Chromatograph.

constant at 50 sccm. The concentration of the gases in the permeate stream was analysed through gas chromatographs (Agilent 7890 A) fitted with packed molecular sieve columns for H₂ and O₂ separation and capillary molecular sieve columns for CO₂ separation. (Figure 2.2.4) The permeation values were calculated according to the following equation (22):

$$P_1 = \frac{x_p^1 f t}{x_p^S \cdot A \cdot (p_F x_F^1 - p_P x_P^1)}$$

Where P_A = Permeability of gas 1. $x_F^1 x_P^1$ = Mole fraction of gas 1 in feed and permeate stream, x_p^S = mole fraction of sweep gas in the permeate stream, p_F, p_P = pressure in the feed side and permeate side respectively, A = area of the membrane, t = thickness of the membrane, f = flow rate of the sweep gas.

And separation factor or selectivity $\alpha = \frac{P_1}{P_2}$

For temperature dependent permeation measurements, permeation cell fitted with GO membranes were heated at 80 °C for different amount of time, cooled down to room temperature and permeation measurements were carried out.

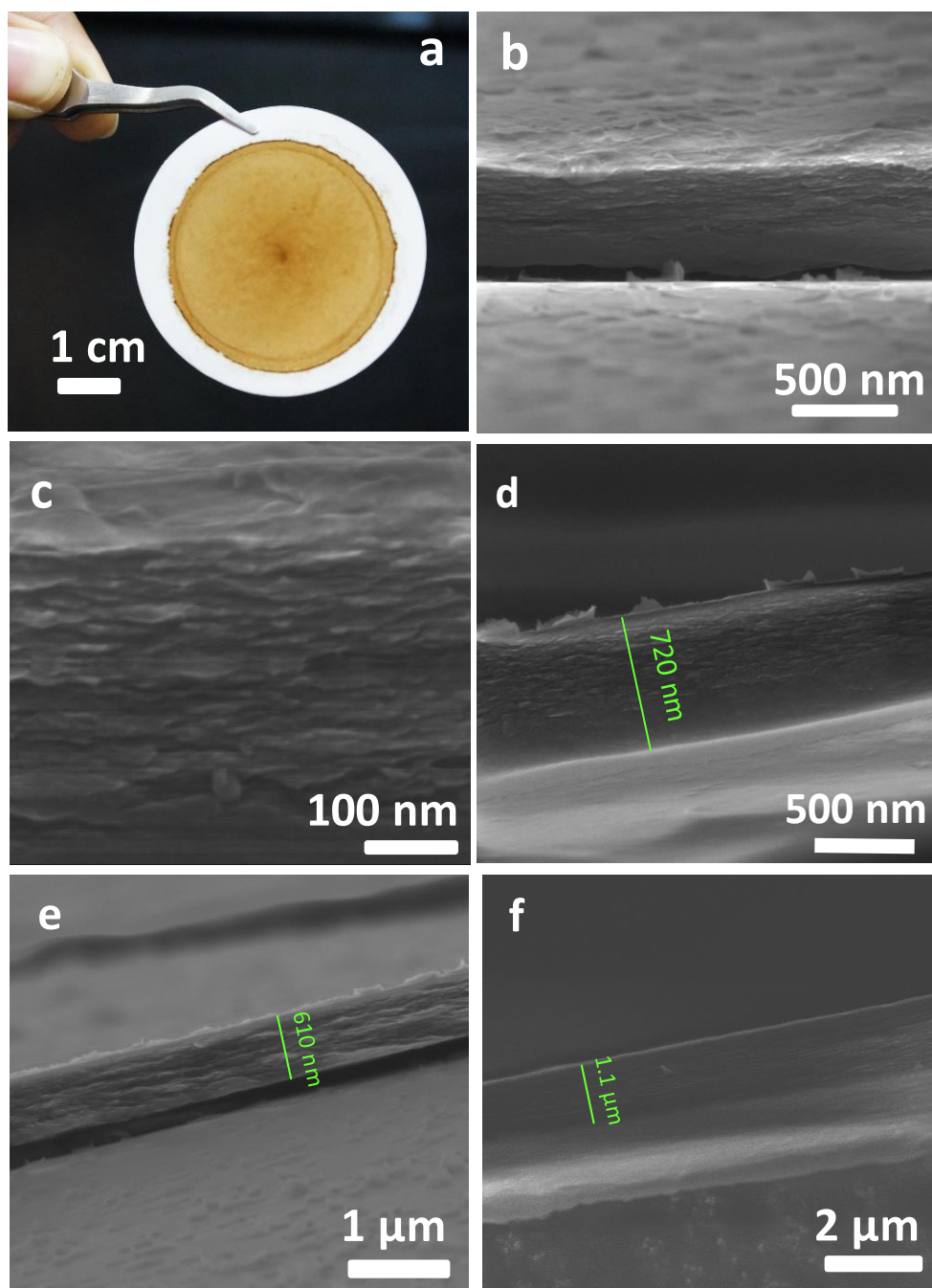
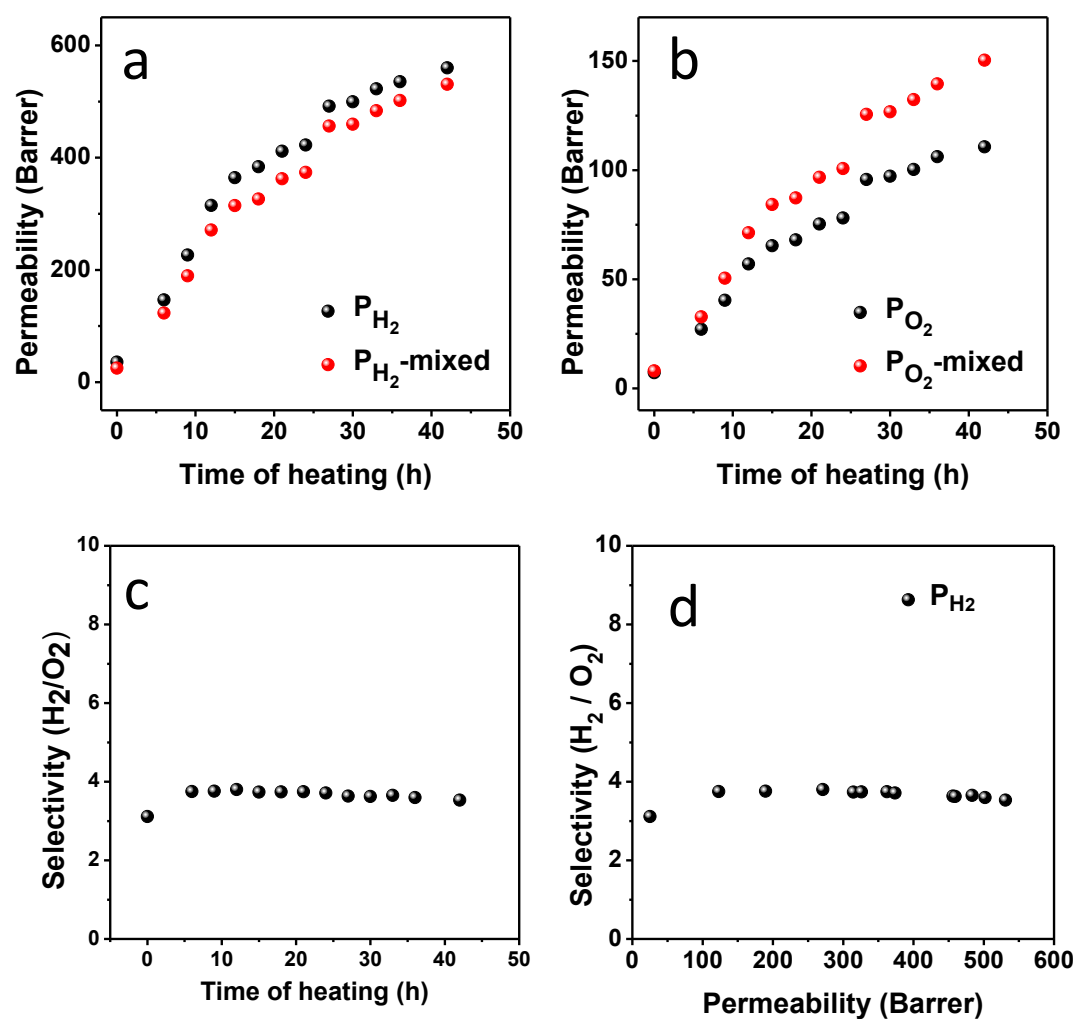


Figure 2.2.5. a) Optical image of a Graphene oxide membrane prepared by vacuum filtration of GO solution through a polycarbonate membrane (200 nm pore size), b) cross sectional view of the GO membrane after peeling off the polycarbonate support c) Magnified image of the cross section showing stacked GO sheets. d)-f) Cross sectional FESEM images of membranes with different thickness. d) membrane with average thickness of approx. 700 nm, e) membrane with average thickness of approx. 600 nm and f) membrane with average thickness of approx. 1000 nm

2.2.4. Results and Discussion:

The graphene oxide (GO), prepared via a modified Hummer's method was used to fabricate GO membranes over porous polycarbonate support via vacuum filtration as described in the experimental section. The optical image (Figure 2.2.5a) shows that the GO membrane is yellow in colour, associated with typical unreduced GO. Field emission scanning electron microscopy (FESEM) images of the cross section of the



membranes

Figure 2.2.6. a-c) Permeability and selectivity of H_2 and O_2 as individual gases and as 1:1 gas mixture through a GO membrane of 700 nm thickness. Figure a) and b) show permeability of H_2 and O_2 respectively measured with neat gases and 1:1 gas mixture in the feed stream over the annealed membranes (at 80 °C) at different intervals of time. Figure c) shows the variation of separation factor for H_2/O_2 for 1:1 gas mixtures

after different intervals of heating at 80 °C. d) Variation of H₂/O₂ selectivity with H₂ permeability

reveal that these membranes have uniform thickness (Figure 2.2.5b) and have a pronounced layered structure (Figure 2.2.5c). Membranes with different thickness were fabricated by controlling the concentration of GO in the stock solution as depicted in figure 2.2.5 d-f.

Gas permeation studies over GO membranes (700 nm thick) were carried out with neat H₂, O₂ and CO₂ gases as well as H₂:O₂ (1:1) and H₂:CO₂ (1:1) mixtures at room temperature in a custom made apparatus (Figure 2.2.3 and 2.2.4). The composition of the permeated gas mixture was analysed through an on-line gas chromatograph. The as-prepared membranes show very low permeability for H₂, and O₂ both in 1:1 (v/v) mixed gas measurements (permeability of 25 and 8 barrer respectively) and individual gas measurements (35.8 barrer for H₂ and 7.2 barrer for O₂) with a separation factor of around 3.7 (Figure 2.2.6 a-c). This value is very close to the separation factor 4 calculated from Knudsen diffusion, where the mean free path of the gas molecules is larger than the interlayer spacing/ pore diameter.(23, 24) Heating GO membranes at 80 °C results in the segregation of oxygen rich and graphitic domains as the oxygen functional groups in graphene oxide layers are mobile at this temperature.(25) The influence of domain formation on gas permeation properties was investigated by annealing the GO membranes at 80 °C for desired time periods and then brought to room temperature before carrying out the permeability studies. We observed a huge increase in permeability for both H₂ and O₂ after annealing the membranes at 80 °C. The H₂ permeability of as synthesized GO membrane increases from 25 barrer to 315 barrer on annealing it at 80 °C for 12h. Prolonged annealing at 80 °C for 42 h further increases the H₂ permeability to 560 barrer, 20 times higher than the as synthesized GO membrane. Similarly, the permeability of O₂ increases to 71 barrer after 12 h annealing at 80 °C and further to 140 barrer after 42 h annealing (Figure 2.2.6 a-c). It is interesting to note that the selectivity of the membrane (permeability ratio of H₂:O₂) remains the same (around 3.7). The plot of selectivity vs H₂ permeability shows that the selectivity remains constant with increase in H₂ permeability (Figure 2.2.6 d), which is quite anomalous considering the inverse relationship generally observed between permeability and selectivity.(2) Similar trend was observed in GO membranes with higher thickness (1000 nm) (Figure 2.2.7 a-c).The performance of annealed (at 80 °C

for 42 h) GO membrane is very close to the earlier reports for H₂/O₂ separation membranes as shown in the figure 2.2.7d.

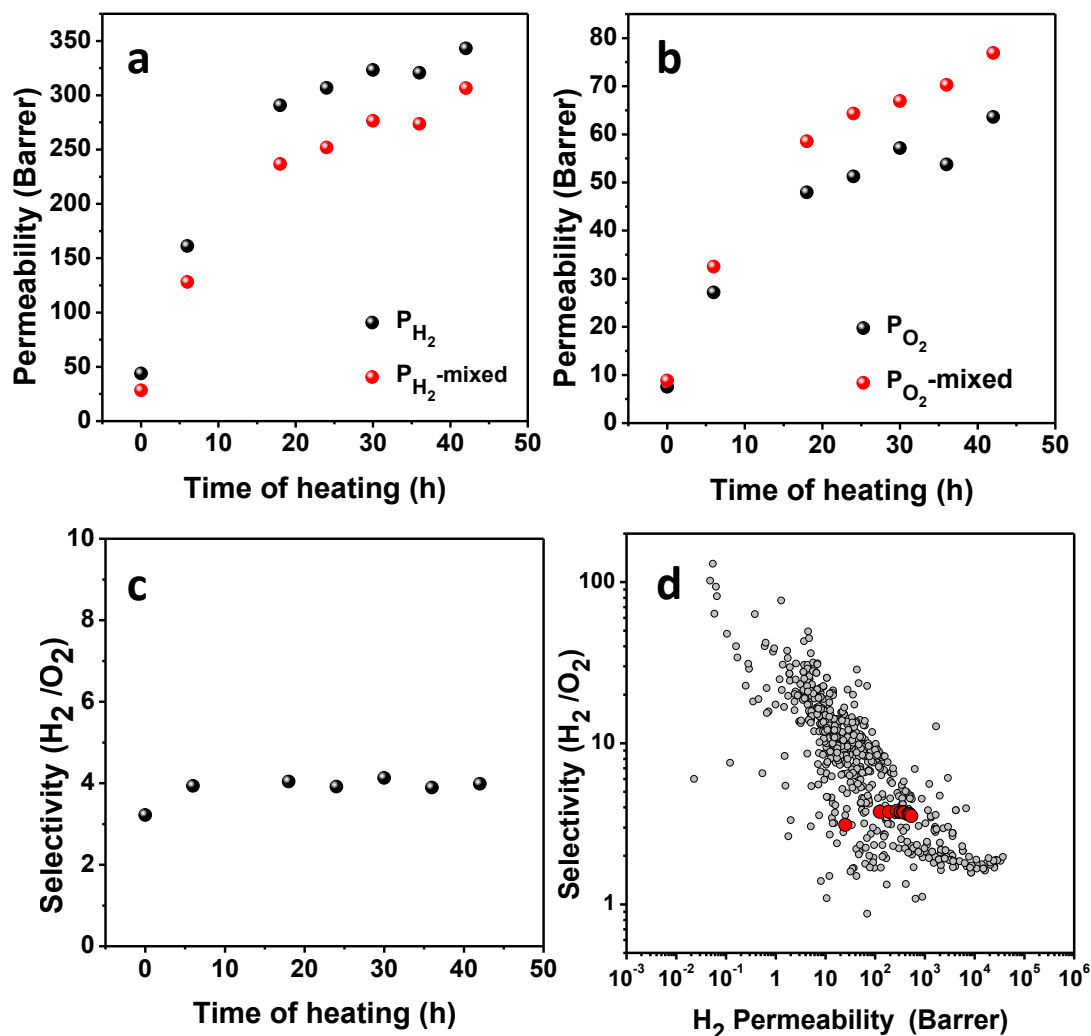


Figure 2.2.7. a-c- Permeability and selectivity of H₂ and O₂ as individual gases and as 1:1 gas mixture through a GO membrane of 1000 nm thickness. Figure a- and b- show permeability of H₂ and O₂ respectively measured with neat gases and 1:1 gas mixture in the feed stream over the annealed membranes (at 80 °C) at different intervals of time. Figure c) shows the variation of separation factor for H₂/O₂ for 1:1 gas mixtures after different intervals of heating at 80 °C. Comparison of H₂/ O₂ separation with respect to other membranes. The red dots indicate the permeability and selectivity for current report at different intervals of heating at 80 °C. The grey dots indicate previously reported values for polymeric membranes.(26)

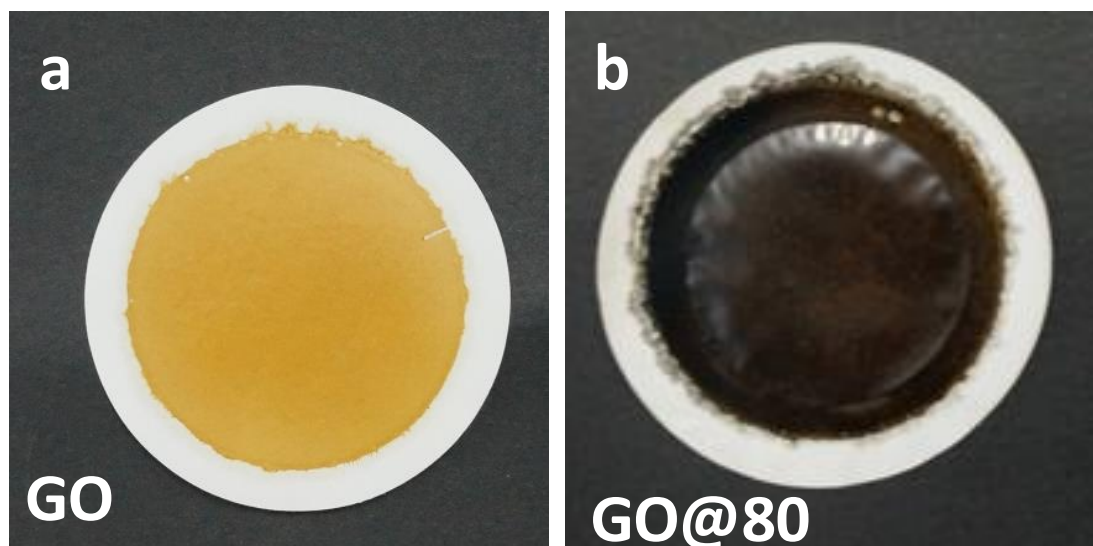
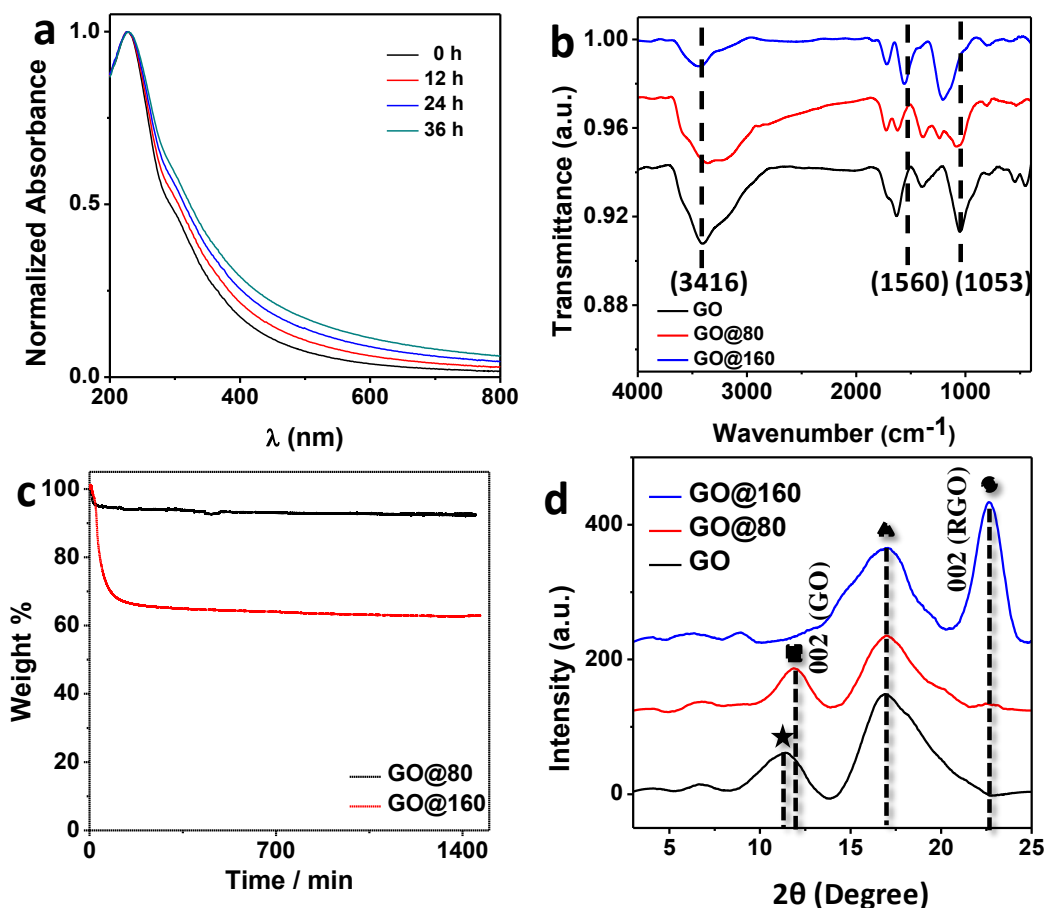


Figure 2.2.8. a) and b) optical images of a graphene oxide membrane before and after annealing at 80 °C for 42 h.

It is to be noted that on heating at 80 °C, the colour of the GO membranes changed from yellow to dark brown over the course of 42 h (Figure 2.2.8 a and b) which is similar to that of the colour change observed for aqueous dispersion of as prepared GO on heating at 80 °C by Kumar et. al.(19) The increase in absorption in the visible range of the spectrum (of the GO dispersion) is a direct indication of the darkening of the solution (Figure 2.2.9 a). These as prepared GO samples show a pronounced absorption peak at ~230 nm, attributed to the $\pi - \pi^*$ transition of C=C and a broad absorption at visible region (27). After annealing at 80 °C for 36 h, the main absorbance peak at 230 nm remains intact while the absorbance in the visible range increases, consistent with darkening of colour. This increase in absorbance was attributed to the oxygen diffusion occurred at the annealing temperature to form distinct oxidized and graphitic regions, having larger π conjugated domains, resulting in higher absorbance in the visible region (25).

Furthermore, GO shows typical IR peaks at frequencies 1053 cm^{-1} , 1724 cm^{-1} and 3416 cm^{-1} , corresponding to C-O and C-OH stretching, C=O stretching from carbonyl and carboxylate groups and O-H stretching from adsorbed water and hydroxyl groups respectively (Figure 2.2.9 b).(28) In GO sample after 42 h heating at 80 °C (GO@80) all these peaks are retained, while after heating at 160 °C for 42 h (GO@160) the oxygen functional group peaks diminish and new peak at 1560 cm^{-1} , corresponding to skeletal vibrations of graphene domains arise. Isothermal TGA studies of GO samples

were performed at 80 °C and 160 °C for 24 h (Figure 2.2.9c). GO annealed at 80 °C show minimal weight loss (~10 %), which can be attributed to the loss of water molecules physisorbed on the surface. On the other hand, at 160 °C about 40% weight loss is observed. As most of the structural oxygenated functional groups are lost, the



sample converts to thermally reduced rGO.

Figure 2.2.9. a) UV-Vis absorbance spectra of GO dispersion heated at 80 °C for different times. The spectra have been normalized to the peak at 230 nm. b) IR spectra of as prepared GO, GO annealed at 80 °C and 160 °C for 42 h. c) Isothermal TGA studies of GO samples at 80 °C and 160 °C for 24 h. d) XRD profiles of as prepared GO membranes along with membranes heated at 80 °C and 160 °C. ★ Represents the GO peak of as-prepared GO membranes, it shifts to higher 2θ value (■) after annealing at 80 °C, while after annealing at 160 °C, a new peak appears at $2\theta = 22.6^\circ$ (●) corresponding to graphitic stacking. The peak at $2\theta = 17^\circ$ (▲) can be assigned to polycarbonate membrane.

The as-prepared GO membrane shows typical low angle XRD peak at $2\theta = 11.3^\circ$, corresponding to the interlayer spacing, 0.78 nm. The membrane annealed at 80°C for 42 h shows no significant reduction in interlayer spacing ($2\theta = 11.9^\circ$, $d = 0.74$ nm) (Figure 2.2.9 d) further confirming no loss of oxygenated functional groups.

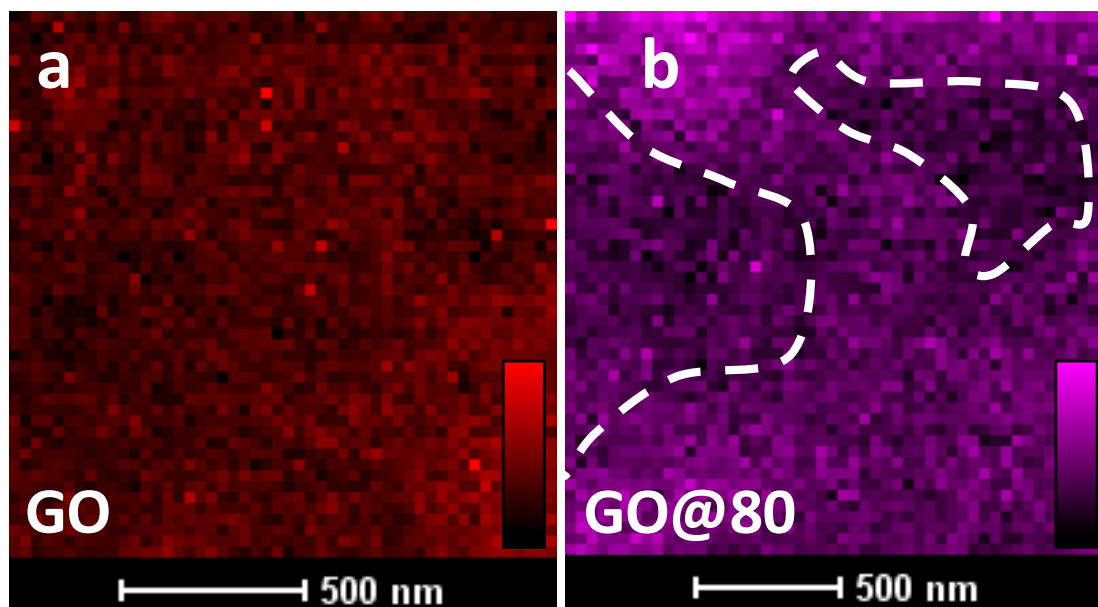


Figure 2.2.10. Elemental mapping of oxygen on GO sheets a) before and b) After heating at 80°C for 42 h. The colored regions represent oxygen rich domains. Distribution of oxygen is uniform on the as-prepared GO, whereas there is clear indication formation of oxygen rich and oxygen deficient regions after annealing.

Figures 2.2.10 a and b show the elemental mapping of oxygen on as prepared GO sheets and those annealed at 80°C . Annealed GO shows oxygen rich and poor domains as against the uniform distribution of oxygen observed over as prepared GO.

From these experiments it can be confirmed that heating GO membranes at 80°C induces migration of surface functional groups creating domains without any loss of oxygen content as observed previously.⁽²⁵⁾ We believe that the formation of such oxygen rich- and oxygen-deficient domains on the surface of annealed layers in the GO membrane could create additional channels between the layers for the gas molecule to diffuse fast. A schematic of such process is depicted in Figure 2.2.11 a and b. Similar enhancement of flux were reported earlier in case of fluid transport through GO and WS_2 membranes

with artificially incorporated surface ripples.(20, 29) This mechanism also explains the constant H_2/O_2 selectivity with increase in H_2 permeability.

The slightly low permeability of the lighter gas (here H_2) in mixed transport compared to the individual permeation (and the reverse trend for heavier O_2 gas) can be attributed to the momentum transfer mechanism in mixed gas systems(30). , wherein, the lower molecular weight gas molecules, having a higher velocity (in this case H_2) collide with gas molecules of higher molecular weight, having lower velocity (in this case O_2). This results in transfer of some of the momentum of the higher velocity H_2 molecules to the low velocity O_2 molecules and hence increase their permeability value. This would also explain the slightly lower separation factor that we obtained for mixed gases.

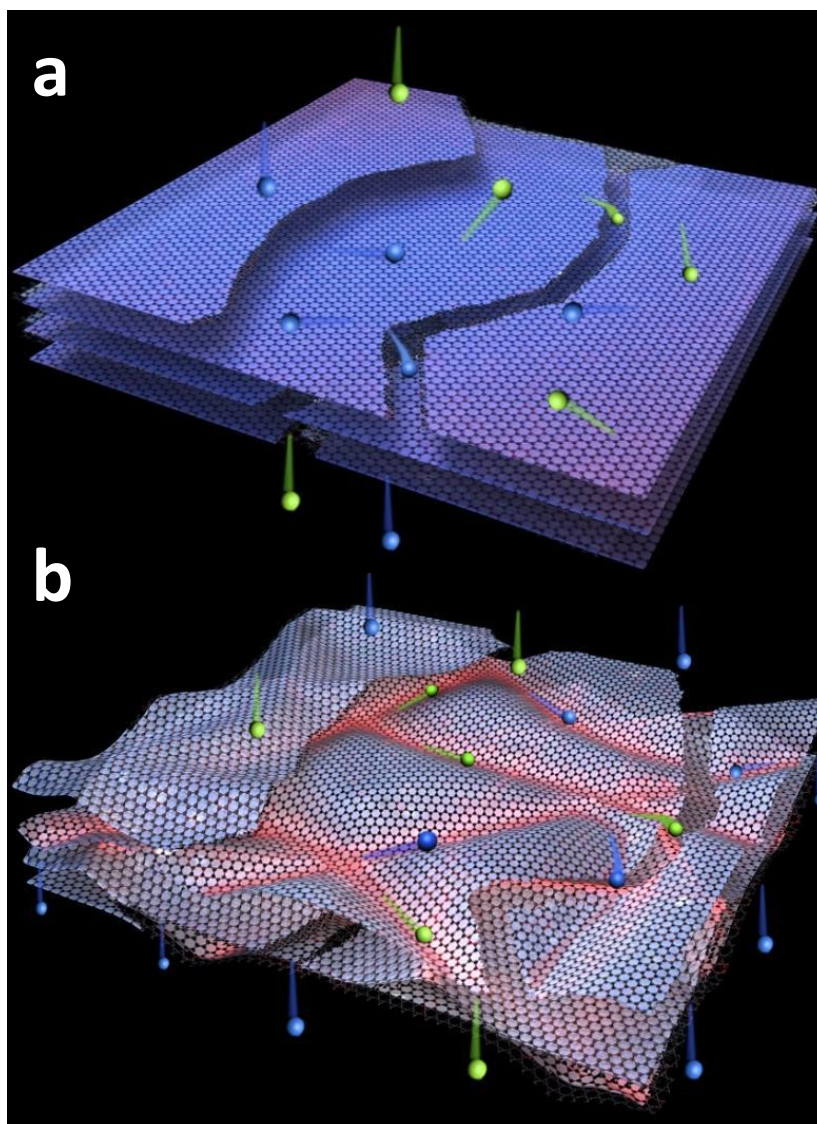


Figure 2.2.11. a) and b)- schematic of gas permeation mechanism through as-synthesized and domain formed GO membranes.

The permeability of both hydrogen and oxygen increases sharply with increase in annealing time up to 12 hours after which it saturates.(Figure 2.2.6 a,b and 2.2.7 a,b) This suggests that the major part of oxygen migration and formation of domains happen within 12 h at 80 °C, which was not realised from spectroscopic techniques before.(25)

Formation of channels on graphene sheets is also evident from N₂ adsorption isotherms of as-prepared GO membranes and GO membranes heated at 80 C for 36 h. (Figure 2.2.12) Continuous increase in N₂ uptake above P/P_o > 0.3 indicate enhanced pore openings of GO membranes annealed at 80 °C (Pore volume 3.026x10⁻² cc/g) compared to as prepared GO membranes (Pore volume 1.837x10⁻² cc/g) confirms creations of channels in the interlamellar region.

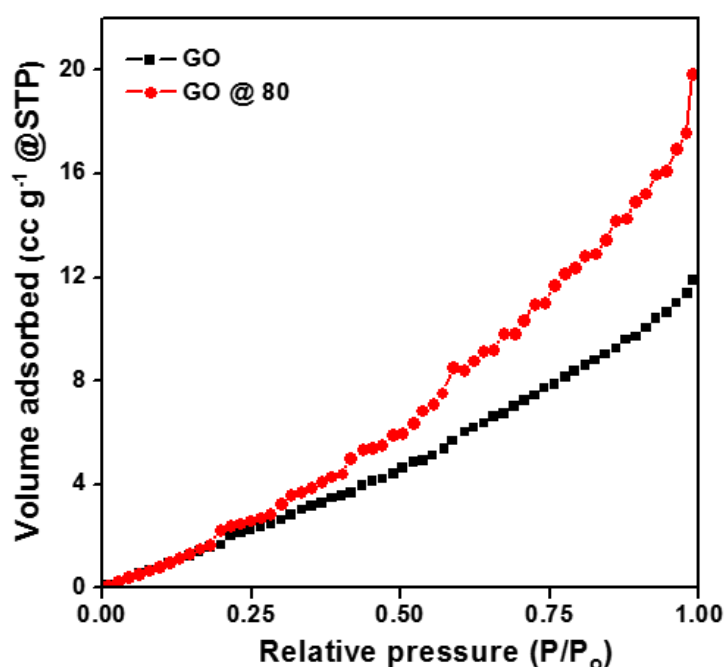


Figure 2.2.12. N₂ adsorption isotherms (77 K) of as-prepared GO membrane and GO membrane heated at 80 °C.

GO annealed at 160 °C for 42 h on the other hand, loses most of its oxygen functional groups, as evident from the TGA and IR studies (Figure 2.2.9 b and c respectively). The GO membrane annealed at 160 °C for 42 h does not show any characteristic GO peak at $2\theta = 11.9^\circ$, instead, a new peak appears at 22.6° corresponding to the graphitic interlayer

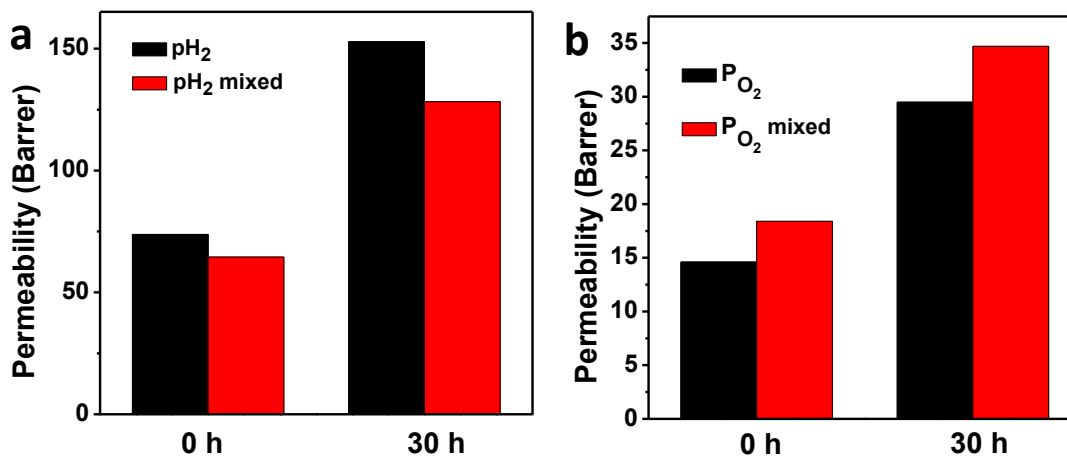


Figure 2.2.13. a) and b) Permeability of H₂ and O₂ respectively as individual gases and as 1:1 gas mixture through an as prepared 700 nm thick GO membrane and after heating the membrane at 160 °C for 42 h.

spacing (Figure 2.2.9 d). This suggests that at 160 °C the GO layers transform to thermally reduced graphene oxide (rGO) layers. The permeability studies show little increase in permeability (74 barrer to 153 barrer in case of H₂ and 14.6 barrer to 29.5 barrer in case of O₂) even after 42 hours of heating at 160 °C (Figure 2.2.13 a and b), showing the huge importance of domain formation on increase of gas permeability.

The permeation and selectivity studies for H₂ and CO₂ were carried out in a separate GO membrane of thickness 600 nm after annealing it at 80 °C for different time periods. We have observed a slight variation in hydrogen permeability over the 600 nm thick membrane as compared to 700 nm thick membrane, probably due to different batches of GO having slightly different oxygen content and/or inherent inhomogeneity at the time of membrane preparation. Nevertheless, the permeation behaviour of H₂/CO₂ over annealed GO membranes (Figure 2.2.14 a-c) shows similar trend as that of H₂/O₂ permeation behaviour. Furthermore, the separation factor for H₂: CO₂ (~6), is much higher than their Knudsen separation factor (~4.7) owing to the low permeability of CO₂ due to its interaction with the GO membrane through quadrupole moment.^(17, 31) In figure 2.2.14 d the H₂/CO₂ separation performance of these membranes are compared against the upper bound of polymeric membranes,⁽²⁾ carbon molecular sieve,^(32, 33) zeolite,⁽³³⁾ SiO₂,⁽⁶⁾ and GO⁽¹⁷⁾ membranes previously reported in

literature. Performance of the GO membranes can be enhanced by annealing them at 80 °C after which they perform much better than the polymeric membranes.

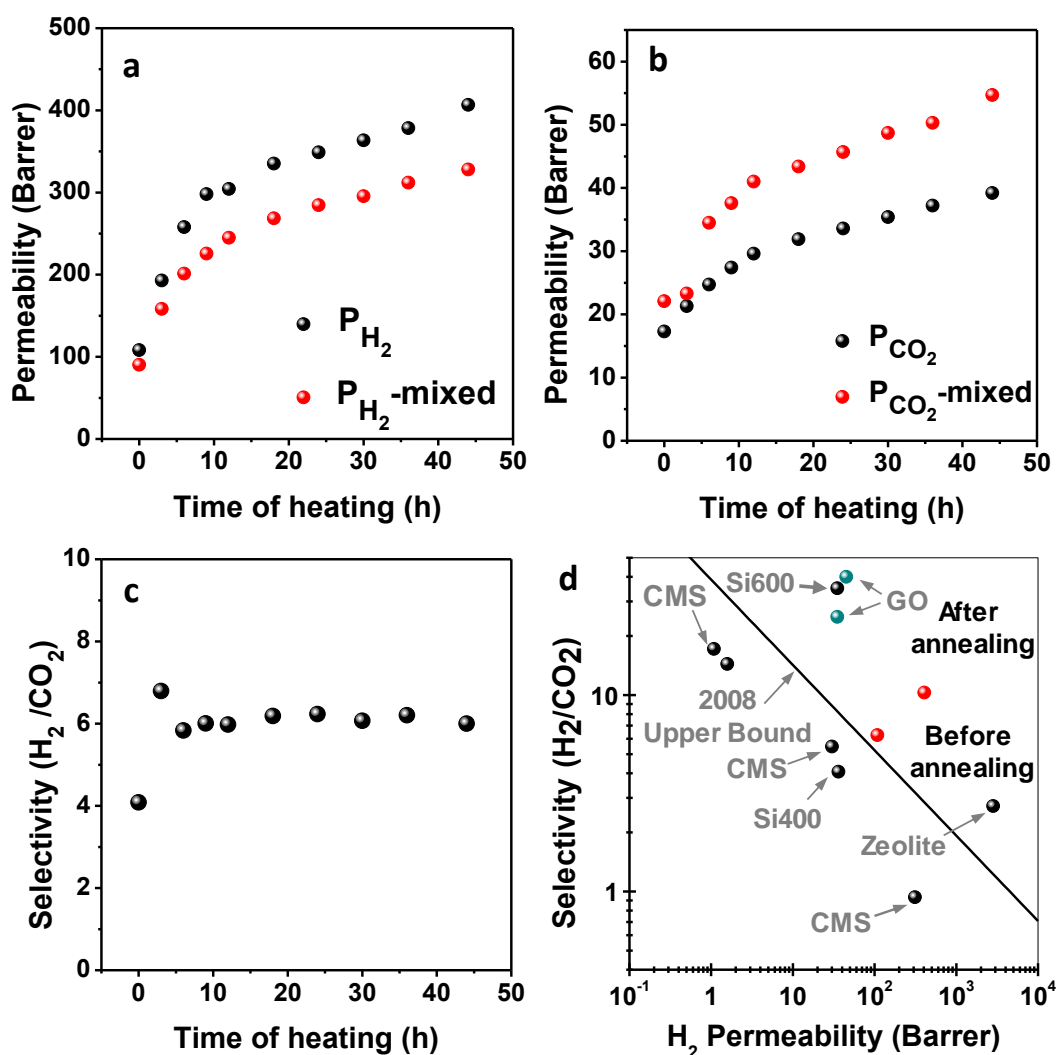


Figure 2.2.14. a-c)-Permeability and selectivity of H_2 and CO_2 as individual gases and as 1:1 gas mixture through a GO membrane of 600 nm thickness. Figure a) and b) shows permeability of H_2 and CO_2 respectively as individual gases and 1:1 gas mixture after different intervals of heating at 80 °C. Figure c) shows the variation of selectivity of H_2/CO_2 for 1:1 gas mixtures after different intervals of heating at 80 °C. Figure d)- Comparison of ideal H_2/CO_2 gas separation performance (for individual gases) of the GO membrane with other membranes. The black line represents the 2008 upper bound of polymeric membrane (2) black dots represent the CMS, (32,33) silica (6) and zeolite (33) membranes from the literature. Blue dots represent GO membranes reported

previously (17) and the red dots represent the performance of GO membranes in this study before and after annealing at 80 °C for 42 h.

2.2.5. Conclusion:

In conclusion, we have demonstrated that by annealing the GO membranes at 80 °C their permeability can be enhanced substantially in an easy and facile method without sacrificing their selectivity. The migration of oxygen functional groups on the GO surface at 80 °C create oxygen rich and graphitic regions, thus forming channels for easy permeation of gas molecules. Thus, treated GO membranes offer high throughput H₂/CO₂ separation superior to previously reported membranes.

2.2.6. References:

1. H. Strathmann, L. Giorno, E. Drioli, *Introduction to membrane science and technology*. (Wiley-VCH Verlag & Company, 2011), vol. 544.
2. L. M. Robeson, The upper bound revisited. *J. Membr. Sci.* **320**, 390-400 (2008).
3. L. M. Robeson, Polymer membranes for gas separation. *Curr. Opin. Solid State Mater. Sci.* **4**, 549-552 (1999).
4. Z. Lai *et al.*, Microstructural Optimization of a Zeolite Membrane for Organic Vapor Separation. *Science* **300**, 456-460 (2003).
5. M. Yu, R. D. Noble, J. L. Falconer, Zeolite Membranes: Microstructure Characterization and Permeation Mechanisms. *Acc. Chem. Res.* **44**, 1196-1206 (2011).
6. R. M. de Vos, H. Verweij, High-Selectivity, High-Flux Silica Membranes for Gas Separation. *Science* **279**, 1710-1711 (1998).
7. Graphene opens up to new applications. *Nat Nano* **10**, 381-381 (2015).
8. J. S. Bunch *et al.*, Impermeable Atomic Membranes from Graphene Sheets. *Nano Lett.* **8**, 2458-2462 (2008).

9. K. Sint, B. Wang, P. Král, Selective Ion Passage through Functionalized Graphene Nanopores. *J. Am. Chem. Soc.* **130**, 16448-16449 (2008).
10. J. Schrier, Helium Separation Using Porous Graphene Membranes. *J. Phys. Chem. Lett.* **1**, 2284-2287 (2010).
11. K. Huang *et al.*, A Graphene Oxide Membrane with Highly Selective Molecular Separation of Aqueous Organic Solution. *Angew. Chem. Int. Ed.* **53**, 6929-6932 (2014).
12. H. Liu, H. Wang, X. Zhang, Facile Fabrication of Freestanding Ultrathin Reduced Graphene Oxide Membranes for Water Purification. *Adv. Mater.* **27**, 249-254 (2015).
13. T.-M. Yeh, Z. Wang, D. Mahajan, B. S. Hsiao, B. Chu, High flux ethanol dehydration using nanofibrous membranes containing graphene oxide barrier layers. *J. Mater. Chem. A* **1**, 12998-13003 (2013).
14. R. Nair, P. Budd, A. Geim. (Google Patents, 2014).
15. R. R. Nair, H. A. Wu, P. N. Jayaram, I. V. Grigorieva, A. K. Geim, Unimpeded Permeation of Water Through Helium-Leak-Tight Graphene-Based Membranes. *Science* **335**, 442-444 (2012).
16. H. Méndez *et al.*, Doping of Organic Semiconductors: Impact of Dopant Strength and Electronic Coupling. *Angew. Chem. Int. Ed.* **52**, 7751-7755 (2013).
17. H. W. Kim *et al.*, Selective Gas Transport Through Few-Layered Graphene and Graphene Oxide Membranes. *Science* **342**, 91-95 (2013).
18. S. Kim *et al.*, Room-temperature metastability of multilayer graphene oxide films. *Nat Mater* **11**, 544-549 (2012).
19. P. V. Kumar *et al.*, Scalable enhancement of graphene oxide properties by thermally driven phase transformation. *Nat Chem* **6**, 151-158 (2014).

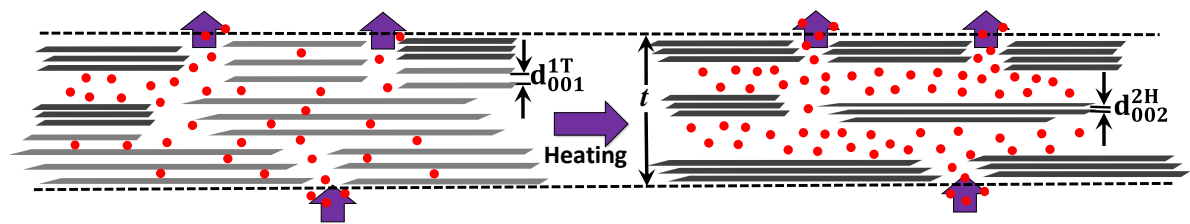
20. H. Huang *et al.*, Ultrafast viscous water flow through nanostrand-channelled graphene oxide membranes. *Nat Commun* **4**, (2013).
21. W. S. Hummers Jr, R. E. Offeman, Preparation of graphitic oxide. *J. Am. Chem. Soc.* **80**, 1339-2678 (1958).
22. S. Wiederhorn *et al.*, in *Springer Handbook of Materials Measurement Methods*, H. Czichos, T. Saito, L. Smith, Eds. (Springer Berlin Heidelberg, 2006), chap. 7, pp. 283-397.
23. R. D. Present, A. J. Debethune, Separation of a gas mixture flowing through a long tube at low pressure. *Phys. rev.* **75**, 1050 (1949).
24. M. Knudsen, Die Gesetze der Molekularströmung und der inneren Reibungsströmung der Gase durch Röhren. *Ann. d. Physik* **333**, 75-130 (1909).
25. P. V. Kumar *et al.*, Scalable enhancement of graphene oxide properties by thermally driven phase transformation. *Nat. Chem.* **6**, 151-158 (2014).
26. L. B. de Paiva, A. R. Morales, F. R. V. Diaz, Organoclays: Properties, preparation and applications. *Applied Clay Science* **42**, 8-24 (2008).
27. G. Eda *et al.*, Blue Photoluminescence from Chemically Derived Graphene Oxide. *Adv. Mater.* **22**, 505-509 (2010).
28. G. Yang *et al.*, A new approach to reduced graphite oxide with tetrathiafulvalene in the presence of metal ions. *J. Mater. Chem.* **22**, 4391-4395 (2012).
29. L. Sun *et al.*, Ultrafast Molecule Separation through Layered WS₂ Nanosheet Membranes. *ACS Nano* **8**, 6304-6311 (2014).
30. R. D. Present, A. J. Debethune, Separation of a gas mixture flowing through a long tube at low pressure. *Physical review* **75**, 1050 (1949).

31. P. M. Sudeep *et al.*, Covalently Interconnected Three-Dimensional Graphene Oxide Solids. *ACS Nano* **7**, 7034-7040 (2013).
32. M. B. Shiflett, H. C. Foley, Ultrasonic Deposition of High-Selectivity Nanoporous Carbon Membranes. *Science* **285**, 1902-1905 (1999).
33. D. Shekhawat, D. R. Luebke, H. W. Pennline, "A Review of Carbon Dioxide Selective Membranes: A Topical Report," (*Report DOE/NETL 2003/1200, U.S. Department of Energy, National Energy Technology Laboratory, Pittsburgh, PA, 2003*) (2003).

Chapter-2.3

High performance MoS₂ membranes: Effect of thermally driven phase transition on CO₂ separation efficiency

Summary: Submicrometer thick MoS₂ membranes were investigated for their gas permeation properties and efficiency of H₂/CO₂ separation. These membranes show high H₂/CO₂ separation at very high H₂ permeability. Thermal stability of the membrane and the effect of phase transition of MoS₂ from 1T to 2H phase on gas permeability and H₂/CO₂ separation was investigated by heating the membrane at different temperatures. The MoS₂ membranes were found to be thermally stable up to 160 °C and a significant increase in gas permeability was observed. The mechanism of gas permeation through MoS₂ membranes was found to be through interbundle spaces instead of interlayer spaces of individual MoS₂ sheets.



2.3.1. Introduction:

Separation of H₂ from other gases carry huge environmental and industrial implications in processing of hydrogen as next generation clean energy source. Industrial processes of producing hydrogen by gasification or steam reforming reactions produce a mixture of gases including CO₂, CH₄, N₂ etc. with H₂. This requires a separation process to obtain pure H₂. On the other hand, separation of CO₂, the main contributor in greenhouse gases from gas mixtures remain a major challenge in encountering global warming. Industrial processes such as Fischer Tropsch reaction and water gas shift reaction produce a mixture of H₂ and CO₂ which needs to be separated before treatment.

Membrane based gas separation techniques are becoming an integral part of many industries for recovery and purification of gases. Due to its low cost(1) operation and minimal capital investments it is gaining greater acceptance in industrial scale(2). Gas separation membranes have found diverse application in numerous processes involving hydrogen separation from petrochemicals(3), CO₂ separation from natural gases(4-6), water gas enrichment(7) and many others. Polymeric membranes have been used commercially for gas separation from the late 1970s. However, they suffer from the drawbacks such as low permeance and low stability over time.(8, 9) The quest for new membranes with higher flux and selectivity has paved the way for use of new membrane materials. Recent advances in this regard has led to the fabrication of zeolite, (10) silicon, (11) carbon molecular sieve, (12) and metal organic framework (13, 14) membranes as selective gas barriers. But the accomplishment of highly selective membranes with significant flux still remains a challenge.

In the last few years usage of two dimensional layered materials such as graphene and graphene oxide as perm selective membranes for gas separation (15) has opened up new possibilities in the field of gas selective membranes. Nair et. al. (16) first demonstrated ultralow helium permeance in a submicrometer thick GO film while it was permeable to water and has a high H₂/CO₂ separation factor. Kim et. al. (17) and Li et. al. (18) have demonstrated that ultrathin (2-20 nm) GO films are molecular sieving in nature. Though, GO membranes are highly selective for H₂, their permeability values leave much to be desired. For all practical purposes an ideal gas separation membrane needs to have a fairly high selectivity with high permeance. Other inorganic analogues

of graphene such as layered chalcogenides are very little explored in this direction as membrane materials. In this report, we have employed MoS_2 for fabricating gas selective membrane which carries the advantages of easy availability and easy exfoliation process and explored mostly for its electronic properties. In a recent report it has been demonstrated that the defect sites on MoS_2 lattice can have significant interaction with gas molecules, specifically CO_2 , making it a perfect material for H_2 selective gas separation.

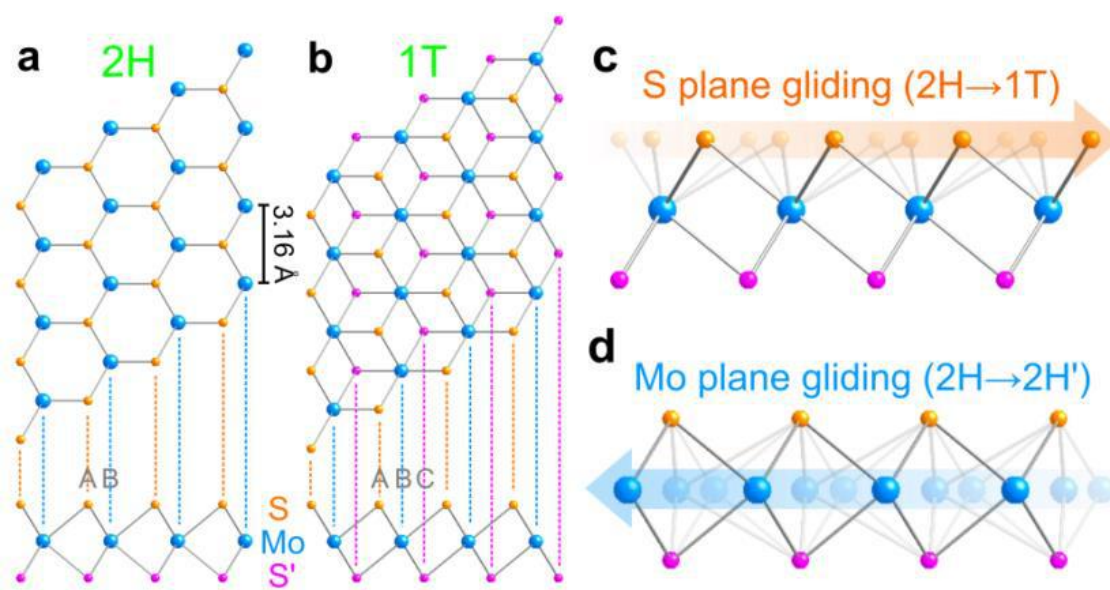


Figure 2.3.1. Polymorphs of single-layered MoS_2 . *a, b*, Schematic models of single-layered MoS_2 with 2H (*a*) and 1T (*b*) phases in basal plane and cross-section views. Mo, blue; top S, orange; bottom S', purple. The 2H phase shows a hexagonal lattice with threefold symmetry and the atomic stacking sequence (S–Mo–S') ABA. The 1T phase shows the atomic stacking sequence (S–Mo–S') ABC, with the bottom S' plane occupying the hollow centre (HC) of a 2H hexagonal lattice. *c*, The S plane glides over a distance equivalent to $a/\sqrt{3}$ ($a = 3.16 \text{ \AA}$), and occupies the HC site of the 2H hexagon, which results in a 2H→1T phase transition. *d*– Gliding of the Mo plane results in a 2H→2H' transition. The shadow atomic model shows the original 2H- MoS_2 structure. The three planes (Mo, S and S') in single-layer MoS_2 can glide individually to give different transitions. Adapted from ref (19)

MoS_2 crystal is built up on atomic layers stacked up by van der Waals force. Each layer consists of strong in-plane bonded S–Mo–S atomic planes. One of the unique features of MoS_2 is its polymorphism with distinct electronic properties. Depending on the

arrangement of sulfur atoms, single layer MoS₂ can exist in two different symmetries, 2H with trigonal prismatic D_{3h} symmetry and 1T with octahedral symmetry. These two phases display totally different electronic properties. While 2H phase is semiconducting, 1T phase is metallic. Both phases can easily be converted to each other through an intra-layer atomic plane gliding. The 1T phase was first reported to be obtained from 2H-MoS₂ by Li and K intercalation(20-23) while it is also known to be stabilized by substitutional doping of Re, Tc, and Mn atoms which serve as electron donor(24). The phase transitions between 2H, 1T and 2H' phases due to the atomic plane gliding are presented in Fig. 2.3.1c and d.

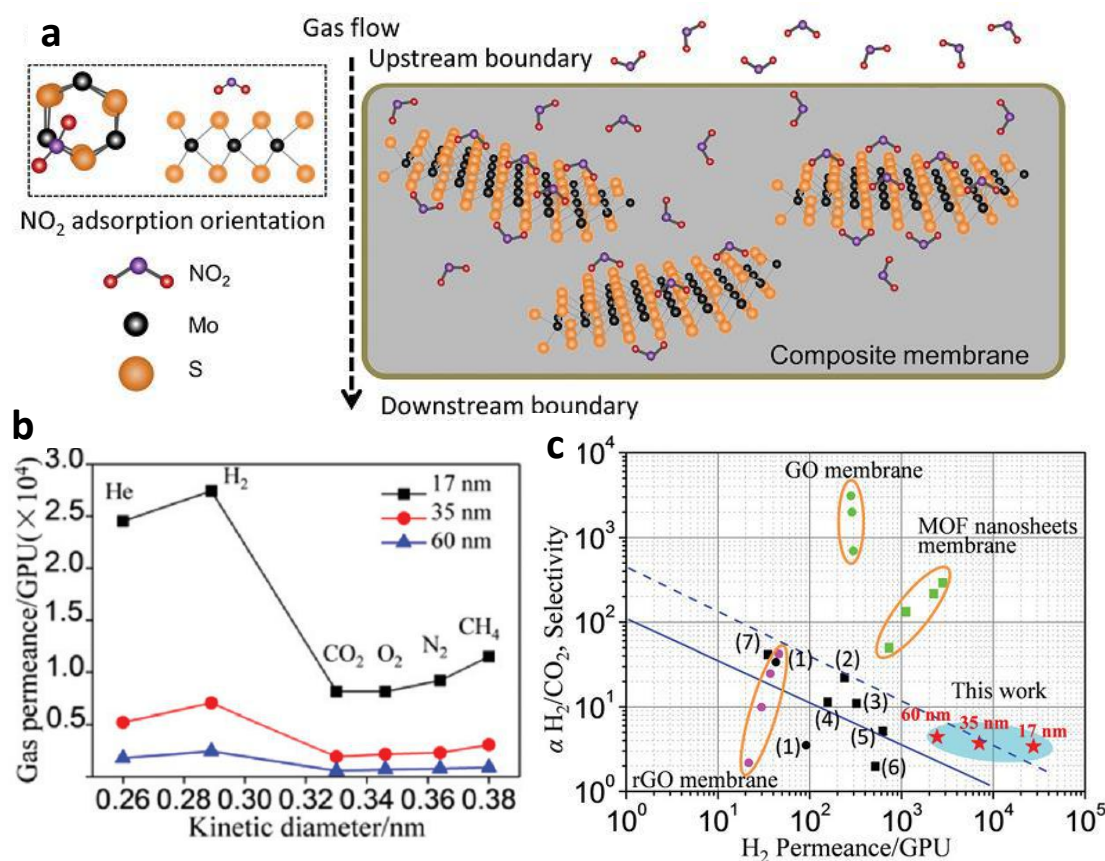


Figure 2.3.2. a) NO₂ gas adsorption and orientation onto 2D MoS₂ flakes grafted in PDMS membrane. Adapted from ref (25). b- gas permeance of MoS₂ membranes as a function of gas dynamic diameter and c) Comparison of MoS₂ membranes with polymeric membranes and inorganic microporous membranes for H₂/CO₂ separation. Adapted from ref (26)

2.3.2. Scope of the present investigation:

Herein, we have fabricated lamellar MoS₂ membranes for size selective permeation of gases. Very few reports exist in the literature which employs MoS₂ for gas separation purposes. K.J. Berean et. al. reported 2D MoS₂ and PDMS mixed matrix membranes for NO₂ separation(25). To the best of our knowledge only report that employs lamellar MoS₂ membranes for gas separation is by Wang. et. al(26)., which have gas selectivity far below the Knudsen value. In this report, it is demonstrated that the as prepared MoS₂ membranes on AAO disc has high permeability and superior selectivity for H₂/CO₂ separation. Further, temperature dependent permeation studies up to 160°C were performed to manifest its high thermal and stability and more importantly, the effect of phase transition on permeation.

2.3.3. Experimental Methods:

2.3.3.1. Materials and characterization techniques:

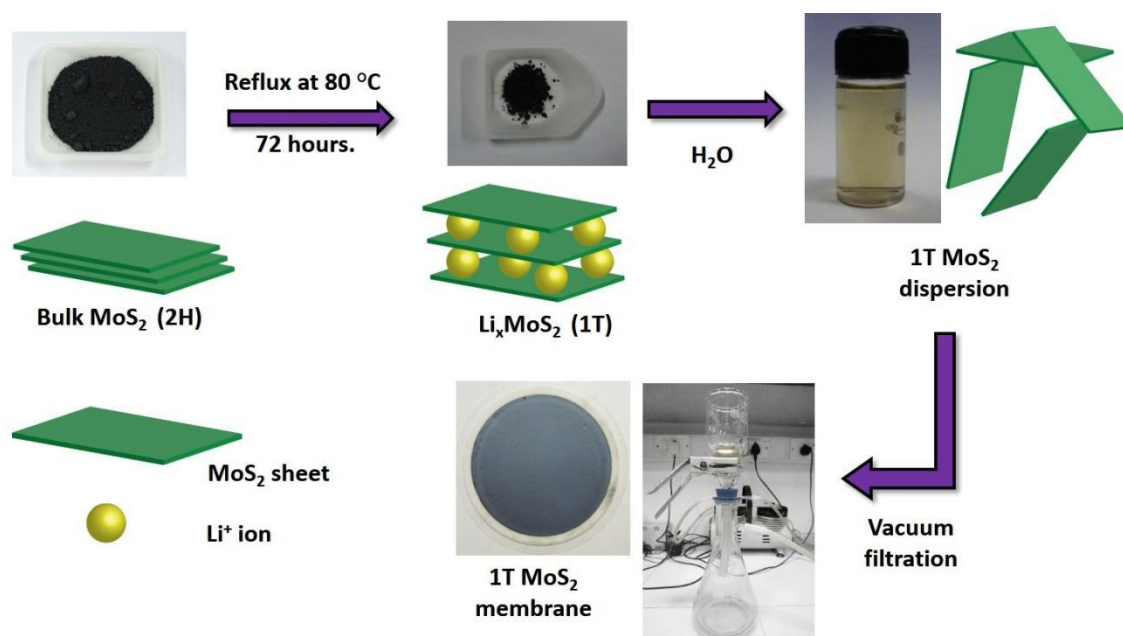
Bulk MoS₂ (< 2micron size, Sigma Aldrich), n-Butyl lithium (2.5M in hexane, Avra chemicals), Sodium Do-decylsulphate (Merck) were used without any further purification.

Rigaku diffractometer (Cu K α radiation, $\lambda=1.54$ Å) and Bruker-D8 diffractometer, (Cu K α radiation, $\lambda=1.54$ Å, step size: 0.02, current: 30 mA and voltage: 40 kV) were used to record Powder x-ray diffraction (PXRD) patterns. Field-emission scanning electron microscopy (FESEM) images were obtained by using FEI (Nova-Nano SEM-600 Netherlands) equipment. TEM measurements were performed on a TEM JEOL acceleration voltage (dc voltage) of 300 kV. Samples were prepared by placing a drop of dispersion on a TEM grid (copper grid). Electronic absorption spectra were recorded on a Perkin Elmer Lambda 750 UV-Vis-NIR Spectrometer. 1 mm path length cuvette was used for recording the spectra. XPS analysis was done in Omicron EA 125 X-ray photoelectron spectrometer with Al K α radiation of 1486.6 eV. Raman spectra were recorded at different locations of the sample using Jobin Yvon LabRam HR spectrometer with 632 nm Ar laser.

2.3.3.2. Exfoliation of bulk MoS₂:

Aqueous dispersion of 1T MoS₂ was prepared by previously reported lithium intercalation method(27). Typically, 300 mg of bulk MoS₂ was dissolved in 5 mL of dry hexane, to which 2 mL of 2.5 M n-butyl lithium was added under argon atmosphere. The reaction was refluxed at 80 °C for 72 hours. Obtained product (Li_xMoS₂) was purified by washing with n-hexane several times to remove excess organic lithium and unreacted MoS₂. The powder was dried in an oven at 60°C and dispersed in water (1mg/1mL) by sonication for 1 h. The dispersion was centrifuged repeatedly to remove LiOH and other impurities.

For membrane preparation, diluted solution of MoS₂ dispersion was vacuum filtered on AAO disc of pore size (100nm) as depicted in the following scheme.(Scheme 2.3.1)



Scheme 2.3.1. Schematic of preparation of lithium intercalated MoS₂ dispersion and vacuum filtration.

2.3.3.3. Gas permeation experiments:

Gas permeation measurements were carried out in a custom made permeation cell as shown in figure 2.2.3. Accurate gas flow was maintained through mass flow controllers (MKS and Hitachi). All the gases used were of high purity. Gas flow on the feed stream were kept constant at 100 sccm for individual gases and 50 sccm each for mixed gas (H₂/CO₂) permeation. On the other hand, N₂ was used as sweep gas and the flow

was kept constant at 20 sccm. The concentration of the gases in the permeate stream was analyzed through online gas chromatographs (Agilent 7690 A). (Figure 2.3.4)

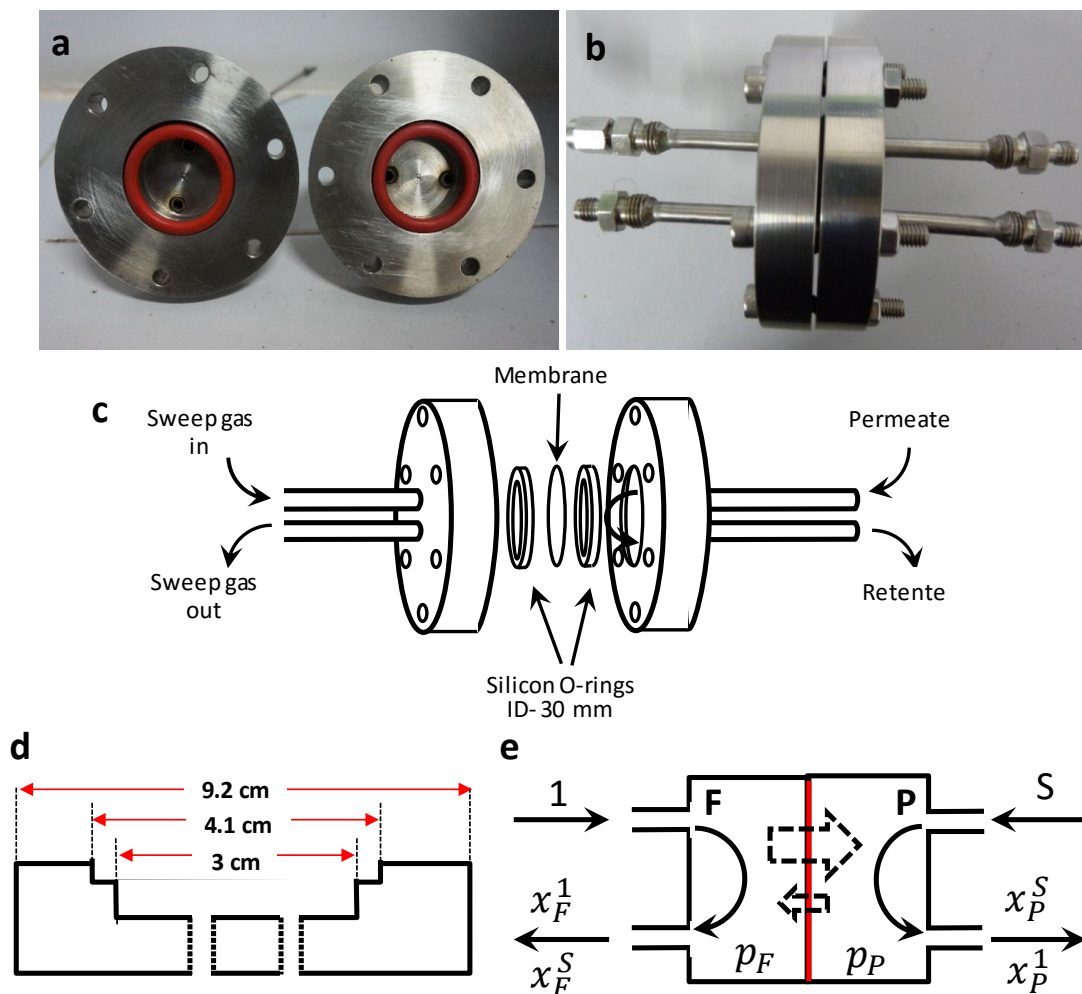


Figure 2.3.3. a, b)-Images of the permeation cell, c) Schematic diagram of the permeation cell with membrane d) Cross sectional view of the permeation apparatus. e) Schematic of gas permeation inside the permeation apparatus. *F* denotes the feed side, *P* denotes the permeate side. *A* is the feed gas while N_2 is the sweep gas. p_F and p_P denoted pressures in the feed and permeate side respectively. x denotes the mole fraction of the respective components.

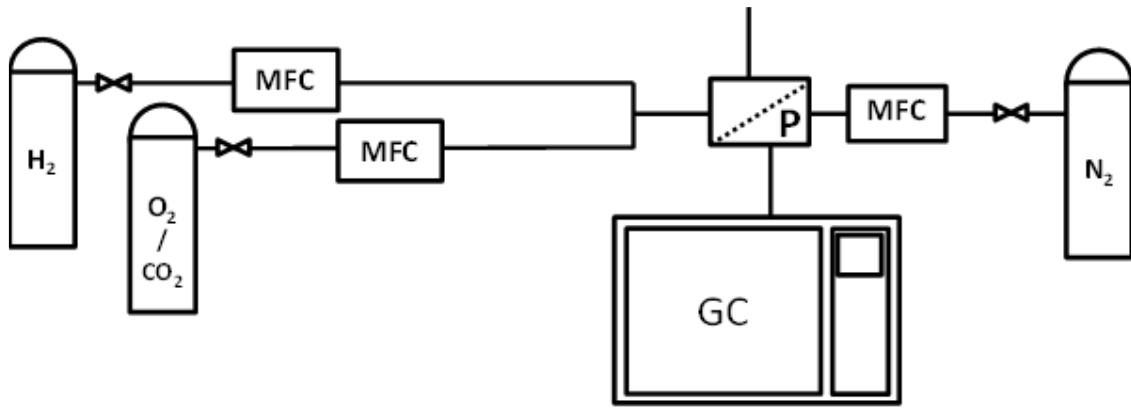


Figure 2.3.4. Schematic of the gas permeation setup. MFC- Mass flow controller, P- permeation cell, GC- Gas Chromatograph.

The permeation values were calculated according to the following equation(28):

$$P_1 = \frac{x_p^1 f t}{x_p^S \cdot A \cdot (p_F x_F^1 - p_P x_P^1)}$$

Where P_A = Permeability of gas 1. $x_F^1 x_P^1$ = Mole fraction of gas 1 in feed and permeate stream, x_P^S = mole fraction of sweep gas in the permeate stream, p_F, p_P = pressure in the feed side and permeate side respectively, A = area of the membrane, t = thickness of the membrane, f = flow rate of the sweep gas.

And separation factor or selectivity $\alpha = \frac{P_1}{P_2}$

For temperature dependent permeation measurements, permeation cell fitted with MoS₂ membranes were heated at different temperatures for two hours, cooled down to room temperature and permeation measurements were carried out.

2.3.4. Results and discussion:

Submicrometer thick MoS₂ membranes were prepared from the monolayer MoS₂ dispersion obtained by exfoliating the lithium intercalated MoS₂ in water as described in the experimental section (Scheme 2.3.1). Bulk MoS₂ exists in thermodynamically stable 2H symmetry with trigonal prismatic co-ordination(19). Intercalation with lithium induces phase transformation from 2H to octahedral 1T phase (metastable state) due to charge transfer from butyl lithium to MoS₂.(29) Membranes were formed by vacuum filtration of MoS₂ dispersion on an anodic aluminium oxide (AAO) substrate having 100 nm pore size.

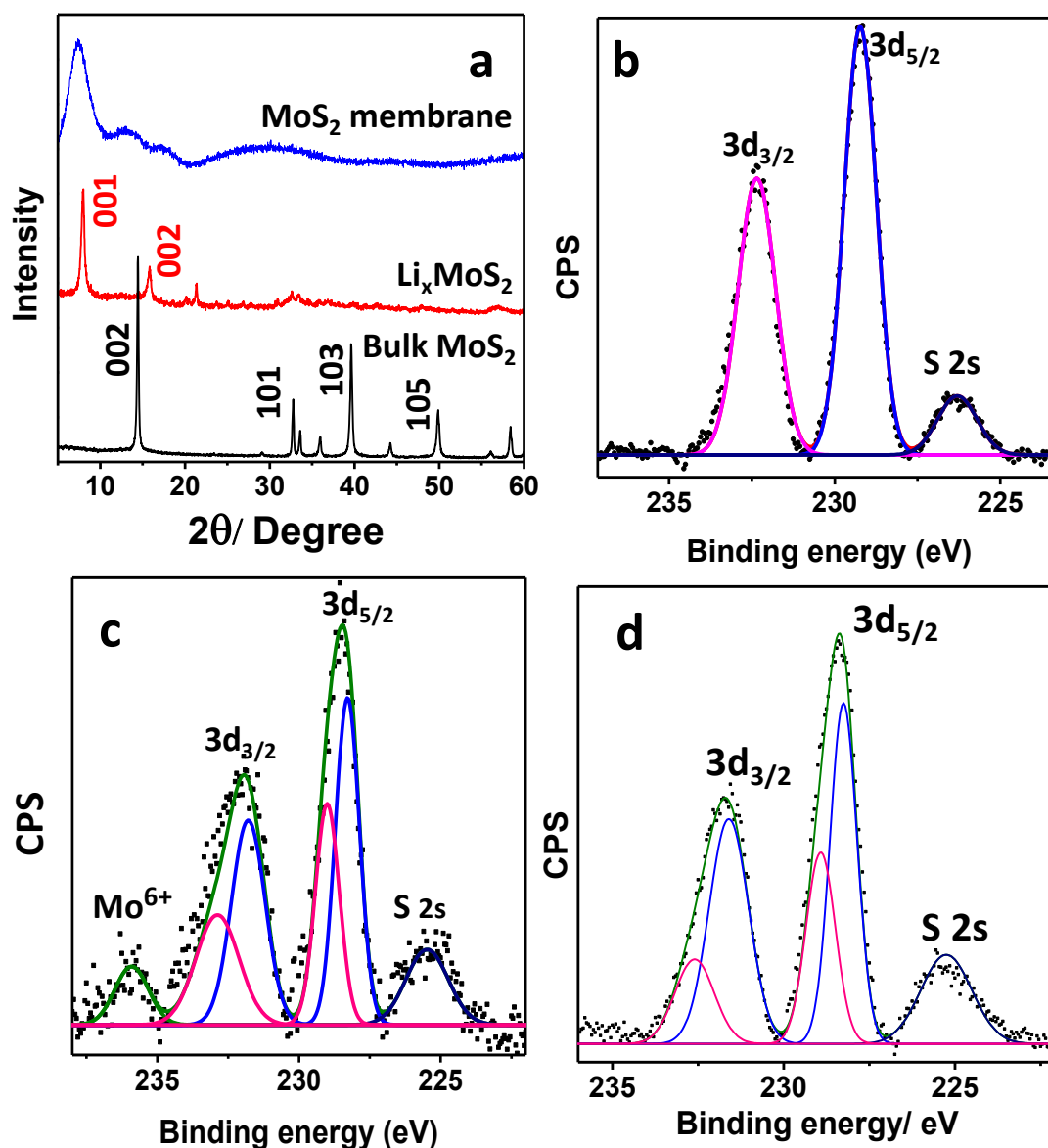


Figure 2.3.5. a) XRD pattern of bulk MoS₂ (Black) and lithiated MoS₂ (Red). Blue graph is the XRD pattern recorded for as prepared membrane Fitted XPS spectra (Mo⁺⁴ 3d) of b- bulk MoS₂ powder, c- lithiated MoS₂ powder and d- as prepared 1T membrane (black dots). Contributions from the 2H and 1T phase are indicated by red and blue lines, respectively. Green lines represent the resultant curve. Whereas bulk MoS₂ shows pure 2H phase, lithiated MoS₂ and as prepared 1T membrane shows a mixture of 1T and 2H phase.

An obvious (002) peak for bulk MoS₂ is associated with interlayer spacing of 6.12Å ($2\theta=14.4^\circ$), between the sheets.(Figure 2.3.5a) For lithiated MoS₂, an intense 001 peak

(at $2\theta=7.8^\circ$) arises with the spacing of 11.32\AA due to the increased spacing between Mo Planes, characteristic of 1T phase(30).

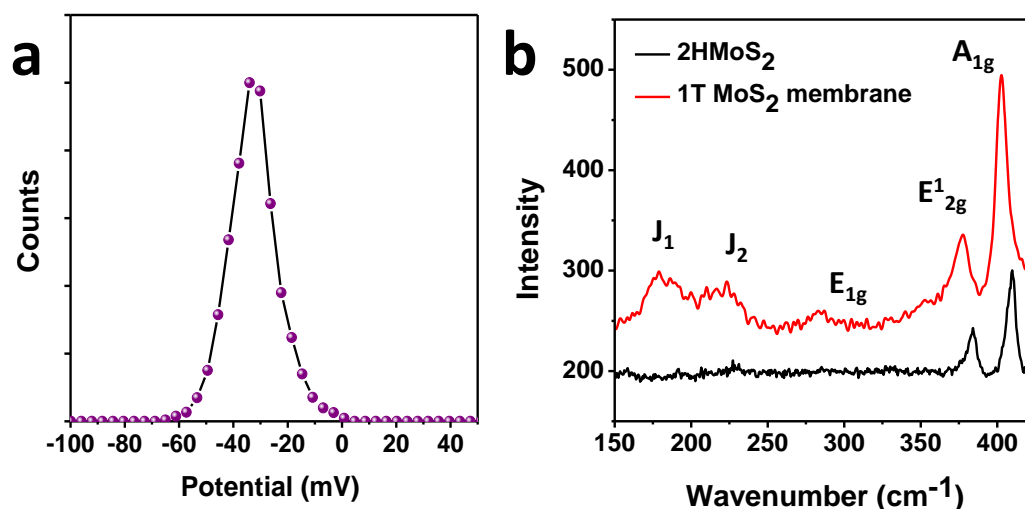


Figure 2.3.6. a) Zeta potential of 1T MoS₂ dispersion indicating highly negatively charged sheets and b) Raman spectra of bulk 2H MoS₂ and 1T MoS₂ membrane.

The increase in interlayer spacing from 6.12\AA to 11.32\AA on lithium intercalation is attributed to the presence of water bilayers of thickness 2.6\AA each adsorbed on the MoS₂ sheets.(19) XRD pattern of as prepared MoS₂ membranes prepared from lithiated MoS₂ (Figure 2.3.5a) reveals relatively strong (001) spacing, signifying the prevalence of octahedral 1T phase in contrast to thermodynamically stable 2H phase with trigonal prismatic co-ordination observed in the bulk MoS₂. We further confirmed the metallic 1T phase of the deposited membranes by XPS Analysis (figure 2.3.5 b-d). It has been formerly reported that binding energies of 3d states of 1T polytype of MoS₂ appears at $\sim 0.8\text{-}0.9\text{eV}$ lesser than that of 2H MoS₂.(31) The Mo 3d spectra of bulk 2H phase consists of spin orbit doublet Peaks at 228.90 and 232.53eV corresponding to $\text{Mo}^{4+} 3d_{5/2}$ and $\text{Mo}^{4+} 3d_{3/2}$.(Figure 2.3.5b) while in 1T counterparts, these peaks are shifted to lower binding energies, appearing at 228.17 and 231.61eV respectively.(Figure 2.3.5c) This is because of the increased electron density on the Mo atoms after intercalation. The peak at 225.27eV is due to 2s region of sulphur. The percentage of 1T phase (blue curve) in lithiated sample, is found to be around 60%. A small peak at 236eV is attributed to $\text{Mo}^{6+} 3d_{5/2}$ state, caused due to oxidation when exposed to air. From the deconvoluted peaks we have estimated that the as-prepared membrane consists of 72% of 1T and 28% of 2H MoS₂.(Figure 2.3.5c) Zeta potential measurement of lithiated

MoS₂ dispersion shows a highly negative value of -35 mV due to charge transfer from Li (Figure 2.3.6 a). The electrostatic repulsion between the MoS₂ sheets due to negative charge on the sulphur atom(30) helps in dispersion in aqueous medium. Raman spectroscopy too, offers substantial information on phase transformation of MoS₂. Raman spectra of MoS₂ membrane and bulk MoS₂ powder is shown in the figure 2.3.6 b. For bulk MoS₂, two prominent peaks appear at 384cm⁻¹ and 409cm⁻¹ which can be assigned to E¹_{2g} and A_{1g} first order phonon modes. E¹_{2g} arises because of the in plane vibration of two S atoms, whereas A_{1g} is attributed to out of plane modes of sulphur in opposite directions. For 1T MoS₂, additional peaks appear due to second order phonon modes. The induced distortion in the 1T MoS₂ creates numerous Raman active modes resulting in huge number of second order peaks and a rich Raman spectrum. Accordingly, 1T spectra show two main deviations with respect to 2H- MoS₂. 1) Disappearance of E¹_{2g} mode 2) emergence of J₁, J₂ and J₃ modes attributed to the superlattice structure of 1T phase. However, we do not see complete absence of E¹_{2g} mode as our sample contains mixed phase.

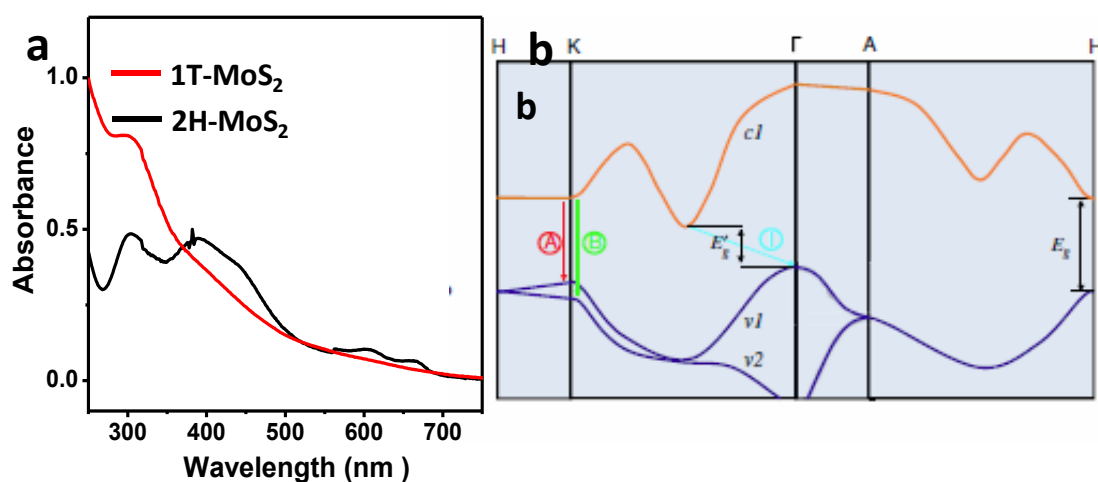


Figure 2.3.7. a) UV-Vis spectra of 1T and 2H MoS₂ dispersion and b) Simplified band Lattice structure of MoS₂ in both the in and out-of-plane directions and simplified band structure of bulk MoS₂, showing the lowest conduction band c1 and the highest split valence bands v1 and v2. A and B are the direct-gap transitions, and I is the indirect-gap transition. Adapted from reference (32)

Figure 2.3.7a depicts the extinction spectra of 1T and 2H MoS₂. The 2H- MoS₂ dispersion is prepared using well established surfactant intercalation method.

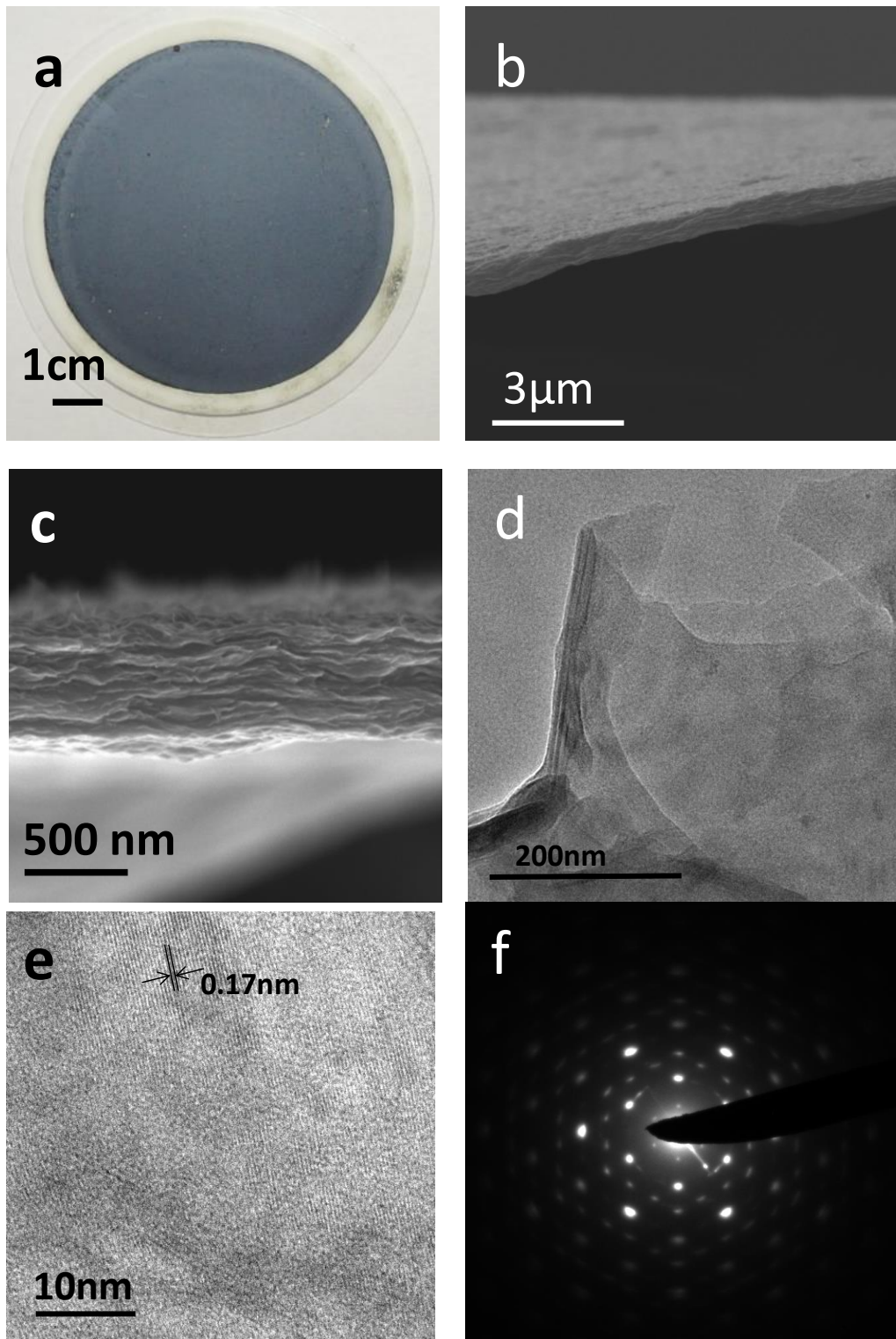


Figure 2.3.8. a) Optical image of the as prepared MoS₂ membrane on AAO Disc b) Cross-sectional image of MoS₂ membrane as seen in FESEM. c) High magnification FESEM image MoS₂ membrane showing layered structure. d, e- TEM image of dispersion of 1T MoS₂, showing single layered structure. f) Electron diffraction pattern recorded from single layer MoS₂ showing typical 1T structure.

Figure 2.3.7b shows the simplified band diagram of bulk 2H MoS₂. 2H-MoS₂ shows characteristic doublet peaks at 609nm and 670nm due to B1 and A1 excitonic transitions from K-point of Brillouin zone with the energy split from spin orbit coupling of valence band.⁽³¹⁾ Convolved peaks centered between 360 and 450nm corresponds to D and C excitons from the M point in the Brillouin zone. Whereas in 1T phase, no such transitions are seen because of the lattice distortion.⁽³¹⁾ Furthermore, UV visible spectroscopy can also be used to determine the presence of mixed phase in lithium exfoliated sample.⁽³³⁾ The absorption peak at 410 nm due to C exciton is a strong contribution for the 2H-phase. The occurrence of this transition in the 1T phase suggests the contribution from the 2H-phase.⁽³³⁾ However, this transition at 410nm in our lithium intercalated dispersion is very less intense, indicating efficient transformation of pristine MoS₂ to 1T phase.

Figure 2.3.8 a displays the optical image of the MoS₂ membrane on AAO support (of 47 mm diameter) which is uniform and crack free from naked eye observation. Field Emission Scanning Electron Microscopy (FESEM) images of cross section of the membrane (Figure 2.3.8b) and the corresponding magnified image (Figure 2.3.8c) clearly shows uniform thickness (~500 nm) with pronounced assembly of MoS₂ nanosheets. TEM image of 1T MoS₂ dispersion shows single to few layer bundles (Figure 2.3.8.d,e). Electron diffraction pattern (Figure 2.3.8f) of the exfoliated sheets show typical 1T pattern. The bright spots correspond to Mo atoms whereas the weak spots in between correspond to the sulphur atoms.

Gas permeation studies over these membranes were carried out in a custom made permeation cell attached with an online gas chromatograph. Permeability of various gases as a function of their kinetic diameter is outlined in the figure 6.8.a. As anticipated, hydrogen exhibited highest permeability of 1175 barrer. Permeation of carbon dioxide (142 barrer) is immensely reduced as compared to hydrogen, making these membranes highly efficient for H₂/CO₂ separation. The observed ideal H₂/CO₂ selectivity is 8.29 (Figure 2.3.9a, at room temperature), much higher than ideal Knudsen selectivity (4.69),⁽¹⁸⁾ demonstrating the remarkable separating ability of the membrane even at high flux. The same trend was observed over a membrane of larger thickness (650nm) (Figure 2.3.9b) with similar selectivity.

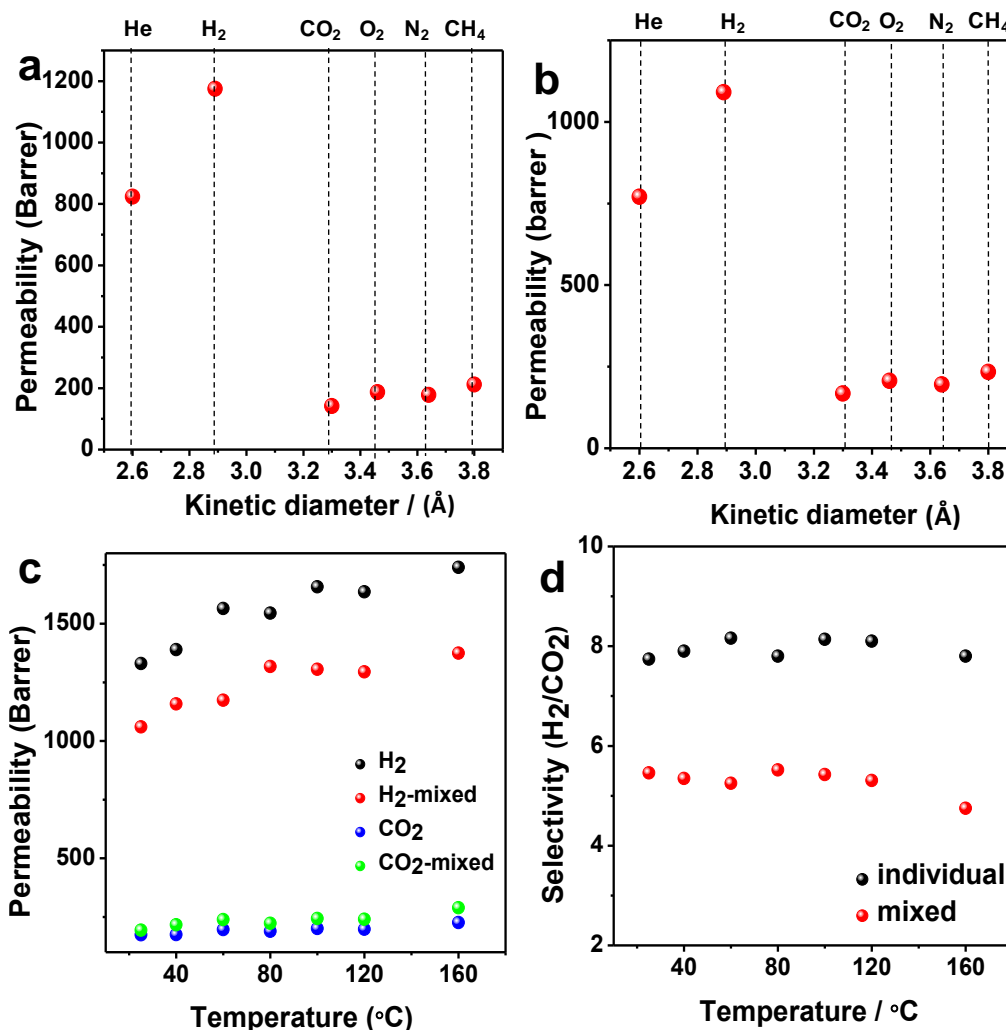


Figure 2.3.9. a) and b) Permeability of different gases through MoS₂ membranes of thickness 500 nm and 650 nm as a function of their kinetic diameter. c) Variation of permeability of H₂ and CO₂ with temperature. Permeability of H₂ as individual gas (black) and in mixed gas (1:1 H₂/CO₂, red), Permeability of CO₂ as individual gas (blue) and in mixed gas (1:1 H₂/CO₂, green). d) H₂/CO₂ selectivity calculated from the individual permeability of H₂ and CO₂ (black) and selectivity calculated from the permeability of H₂ and CO₂ gases in mixed gas permeability experiments (red) as a function of temperature.

Phase transition in MoS₂ is an important factor which can have an impact on its gas permeation properties. At higher temperatures (>80 °C), metastable 1T MoS₂ is reported to convert into stable 2H phase.(31, 34) We have systematically studied the

effect of temperature and phase transition on gas permeation and selectivity (H_2/CO_2) of 1T MoS_2 membranes (with a membrane of thickness $1\ \mu\text{m}$). The membrane was heated at different temperatures (from room temperature to $160\ ^\circ\text{C}$) for 2 h, cooled down to room

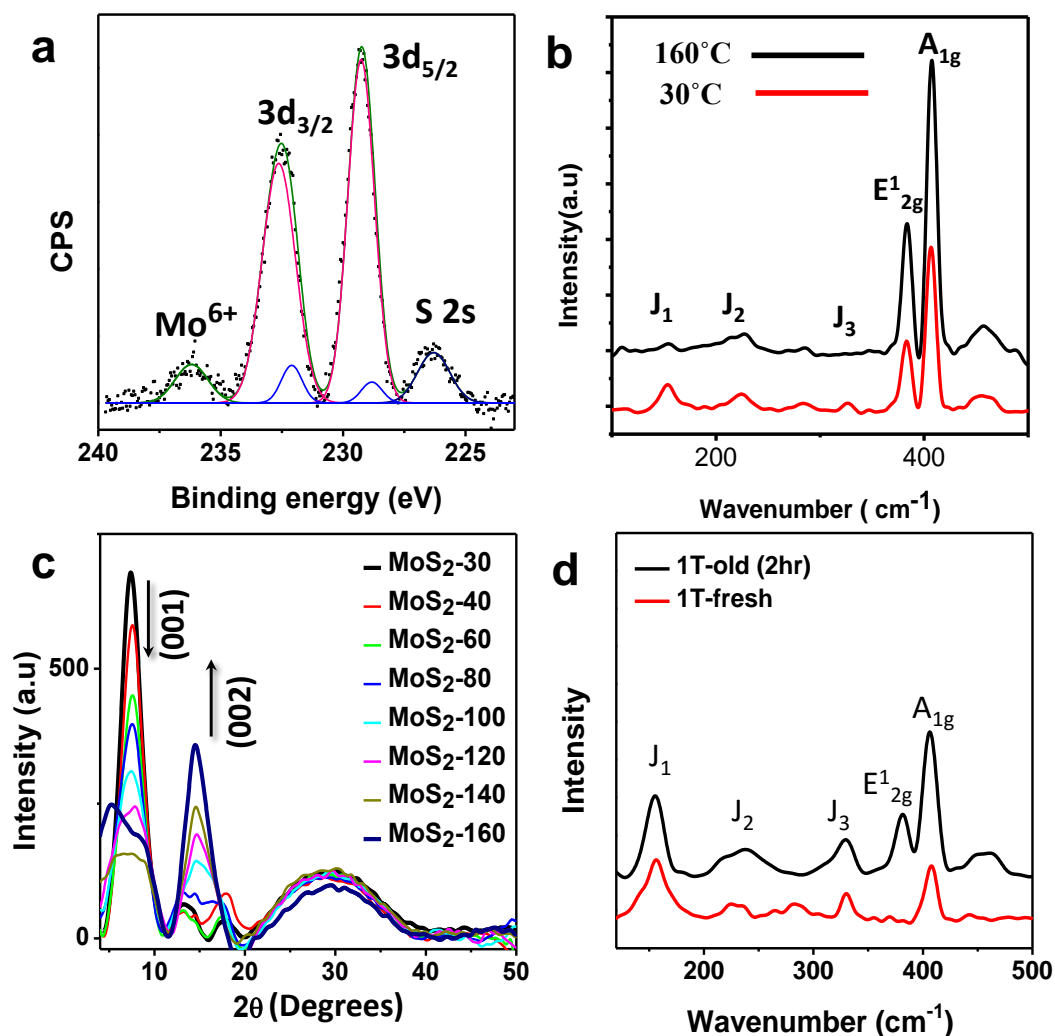
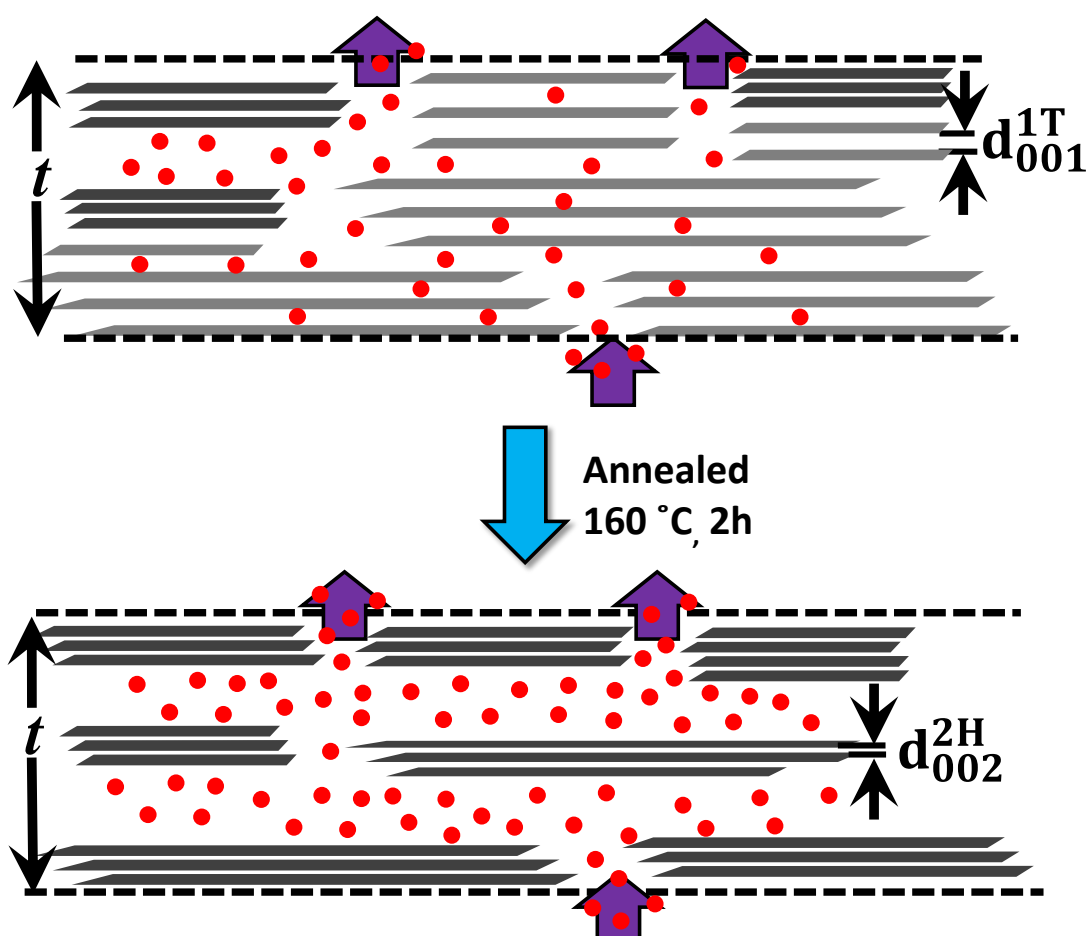


Figure 2.3.10. a) XPS spectra of Mo^{4+} 3d region of heated ($160\ ^\circ\text{C}$) MoS_2 membrane (black dots). Contributions from 2H and 1T are represented in red and blue lines respectively. The resultant curve is shown in green line. Mo^{6+} peak is due to the oxidation of Mo^{4+} while heating. b) Raman spectra of as-prepared MoS_2 membrane and MoS_2 membrane heated at $160\ ^\circ\text{C}$. c) XRD pattern of MoS_2 membrane at different temperatures (30 - $160\ ^\circ\text{C}$), indicating phase transformation induced change in d-spacing. d) Raman spectra of dispersion of freshly prepared 1T MoS_2 (Red) and the same after standing for 2 hours (black).

temperature and then the permeability was measured for H₂, CO₂ and their 1:1 (v/v) gas mixture. Figure 2.2.9c and d represents the variation in gas permeability and selectivity after heating the membrane at different temperatures. The permeability of hydrogen in 1:1 gas mixture was little lower than the pure hydrogen. On the other hand, for CO₂, the reverse was true (194 barrer in H₂/CO₂ mixture and 174 barrer for pure CO₂). This phenomenon can be explained by momentum transfer theory for a mixture of gases flowing through a narrow tube, where the smaller gas molecules (having higher velocity) can collide with heavier gas molecules (having lower velocity) and transfer some of their momentum, which reduces the gas selectivity.(35, 36)



Scheme 2.3.2. Schematic of gas permeation pathway over as-prepared and annealed MoS₂ membranes. After heating the 1T MoS₂ (Grey sheets) converts to 2H phase (Black sheets) which decreases the interlayer spacing without altering the overall thickness of the membranes (t). The decrease in d -spacing creates empty spaces or channels inside the membranes through which gas molecules can diffuse fast. This results in increase in gas permeability.

Interestingly, we have observed a significant increase (30%) in permeability (1740 barrer in case of pure H₂ and 289 barrer in case of pure CO₂) for the heat treated membrane (160 °C) as compared to the as prepared 1T MoS₂ membrane without compromising its selectivity. XPS spectra of the annealed (at 160 °C for 2h) MoS₂ membrane (Figure 2.3.10a) confirms the transformation from 1T phase MoS₂ to 2H phase(31, 33). The relative proportion of 2H phase estimated from the deconvoluted peaks was about 91%. Raman spectra (Figure 2.3.10b) also support this phase transition. We have observed the emergence of J₁, J₂, and J₃ modes (of 1T phase) after heating the membrane at 160 °C for 2h. The X-ray diffraction profile of the membrane (Figure 2.3.10c) shows gradual decrease of (001) peak assigned to 1T phase ($2\theta=7.8^\circ$, $d=11.3 \text{ \AA}$) with increase in annealing temperature. A concomitant increase of 002 ($2\theta=14.7^\circ$) peak of 2H phase associated with decrease of d -spacing from 11.32 Å to 6.12 Å further confirms the phase transition of MoS₂ layers from 1T to 2H phase while heating.(37) If one were to assume the gas permeation through the conventional tortuous path mechanism as observed in many GO and clay membranes(16, 38) it is obvious that the permeability would decrease when the interlayer spacing decreases. In contrast, we have observed a significant increase in the gas permeability in spite of noticeable reduction in d -spacing by phase transition (11.32 Å to 6.12 Å going from 1T to 2H phase, Figure 2.3.10c). We believe that the gas permeation is most likely to occur through inter-bundler space, as represented in scheme 2.3.2, rather than being through the interlayer spacing. The highly favourable co-stacking nature of 1T MoS₂ layers tends to form few layer bundles in solution, which gets deposited as membrane. As the main permeation pathway of gas molecules is through the space between preformed MoS₂ bundles, decrease in d -spacing does not result in reduction of gas permeability. Moreover, the FESEM images of membrane cross sections before and after heating at 160 °C do not show any significant shrinkage in the thickness (Figure 2.3.11 a and b). Thus, decrease in d -spacing by phase transition from 1T to 2H phase leads to the increase in inter-bundler spaces leading to the observed increase in permeability of the gases. (Scheme 2.3.2)

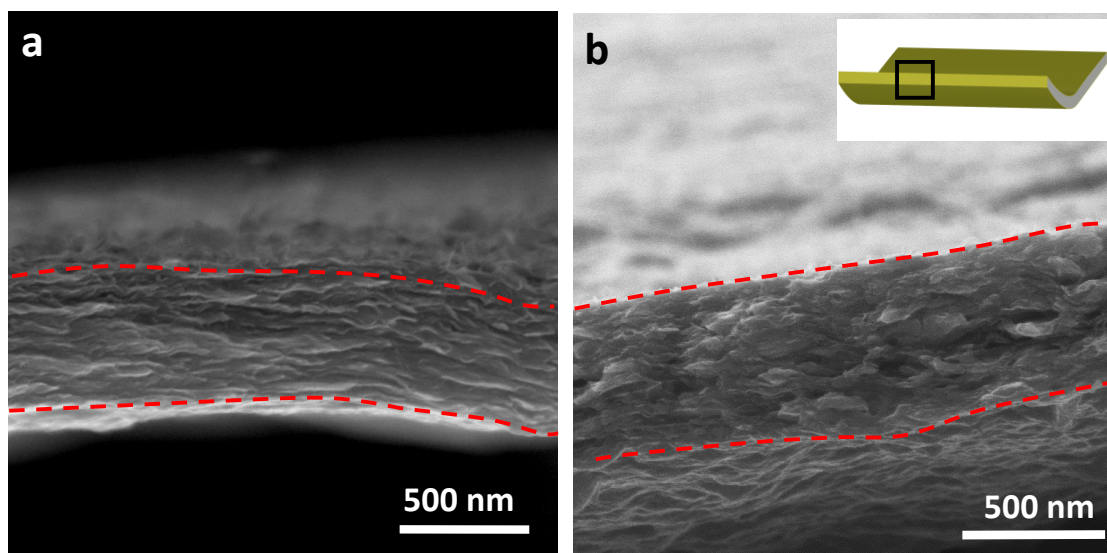


Figure 2.3.11. FESEM images of the as prepared (a) and annealed membrane (b) at 160 °C. The as prepared membrane shows tightly packed MoS₂ bundles, after heating we observe formation of irregularities in the membrane cross section. Figure b inset shows orientation of the membrane.

The appearance of inter-bundle spaces is also evident from the cross sectional FESEM image of the membrane after heating at 160 °C (Figure 2.3.11). Further, formation of MoS₂ bundles in the dispersion is evident from the Raman studies (Figure 2.3.10d). Raman spectra of freshly prepared MoS₂ dispersion (lithiated) shows characteristic 1T phase, identified by the disappearance of E_{2g}¹ mode, (which is a characteristic feature of bulk MoS₂ sample) and emergence of J₁(156 cm⁻¹), J₂ (226 cm⁻¹) and J₃(333 cm⁻¹), attributed to the superlattice structure of 1T phase(31, 37, 39, 40). On the other hand, the dispersion on standing for 2h, shows reappearance of the E_{2g}¹ (386 cm⁻¹) band in Raman spectra, indicating the partial phase transition back to stacked 2H phase, in the solution state.(40) Since the membrane formation typically takes few hours, it is expected that MoS₂ sheets deposit as few layer bundles in the membrane. This is indicated in the XPS spectra of the as prepared membrane also, which shows fairly high amount of 2H phase. (Figure 1b)

The performance of our MoS₂ membranes stands out better in terms of permeability and selectivity for H₂/CO₂ separation as compared to the upper bound of polymeric membranes,(41) zeolite,(10, 42) carbon molecular sieve (CMS),(43) silica,(11) graphene oxide(18) and MoS₂ membranes(26) (Fig 2.3.12). Previously reported MoS₂ membranes(26) show very low selectivity which lie very close to the upper bound of

polymeric membranes. Moreover, the increase in selectivity observed with increase in membrane thickness is contrary to the Knudsen gas separation, indicating possibility of

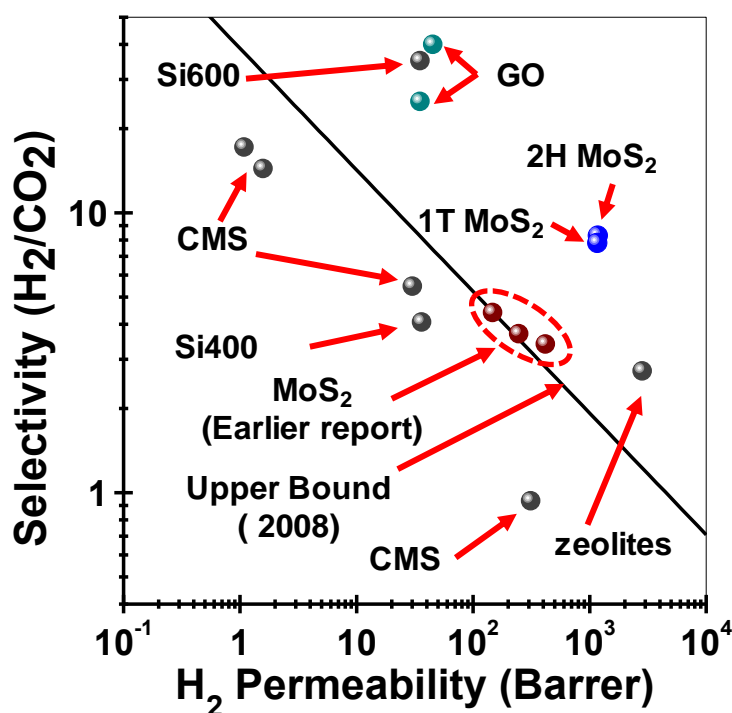


Figure 2.3.12. Comparison of ideal H_2/CO_2 gas separation performance of as prepared MoS_2 membrane (1T) and MoS_2 membrane annealed at $160\text{ }^\circ\text{C}$, (2H) with other membranes reported in the literature. The black line represents upper bound for polymeric membranes (2008),(41) black dots represent other inorganic membranes such as CMS(43), silica(11) and zeolite(10,42). Cyan dots represent GO membranes (18) and brown dots indicate MoS_2 membranes (26) reported previously. Blue dots represent the permeability and selectivity values of MoS_2 membranes in this report.

leaks in the membranes, which may contribute to the unusually high flux observed. MoS_2 membranes studied in this report retain more or less the same permeability and selectivity in all the experiments across different thickness. Moreover, the phase transition of MoS_2 from 1T to 2H on heating at $160\text{ }^\circ\text{C}$ enhances their performance, making them very useful for practical gas separation even at high temperatures.

2.3.5. Conclusion:

In conclusion, we have prepared high performance MoS₂ membranes by vacuum filtration of 1T MoS₂ solution. The as-prepared 1T MoS₂ membranes exhibit very high permeability and excellent selectivity for H₂ in H₂/CO₂ separation. We have also demonstrated for the first time, the phase transition induced enhancement in the gas permeability of the membranes without reducing the selectivity performance. We have also postulated a mechanism for gas permeation through these membranes which occur predominantly through inter bundler space.

2.3.6. References:

1. T. C. Merkel, H. Lin, X. Wei, R. Baker, Power plant post-combustion carbon dioxide capture: An opportunity for membranes. *J. Membr. Sci.* **359**, 126-139 (2010).
2. M. Freemantle, Membranes for Gas Separation. *Chemical & Engineering News Archive* **83**, 49-57 (2005).
3. N. W. Ockwig, T. M. Nenoff, Membranes for Hydrogen Separation. *Chem. Rev.* **107**, 4078-4110 (2007).
4. H. Yang *et al.*, Progress in carbon dioxide separation and capture: A review. *J. Environ. Sci.* **20**, 14-27 (2008).
5. L. Barelli, G. Bidini, F. Gallorini, S. Servili, Hydrogen production through sorption-enhanced steam methane reforming and membrane technology: A review. *Energy* **33**, 554-570 (2008).
6. R. W. Baker, B. T. Low, Gas Separation Membrane Materials: A Perspective. *Macromolecules* **47**, 6999-7013 (2014).
7. T. A. Peters, M. Stange, H. Klette, R. Bredesen, High pressure performance of thin Pd-23%Ag/stainless steel composite membranes in water gas shift gas

- mixtures; influence of dilution, mass transfer and surface effects on the hydrogen flux. *J. Membr. Sci.* **316**, 119-127 (2008).
8. M. Ulbricht, Advanced functional polymer membranes. *Polymer* **47**, 2217-2262 (2006).
 9. B. Van der Bruggen, M. Mänttari, M. Nyström, Drawbacks of applying nanofiltration and how to avoid them: A review. *Sep. Purif. Technol.* **63**, 251-263 (2008).
 10. N. Rangnekar, N. Mittal, B. Elyassi, J. Caro, M. Tsapatsis, Zeolite membranes - a review and comparison with MOFs. *Chem. Soc. Rev.* **44**, 7128-7154 (2015).
 11. B. Elyassi, M. Sahimi, T. T. Tsotsis, Silicon carbide membranes for gas separation applications. *J. Membr. Sci.* **288**, 290-297 (2007).
 12. Y. D. Chen, R. T. Yang, Preparation of Carbon Molecular Sieve Membrane and Diffusion of Binary Mixtures in the Membrane. *Ind. Eng. Chem. Res.* **33**, 3146-3153 (1994).
 13. S. Y. Lim *et al.*, New CO₂ separation membranes containing gas-selective Cu-MOFs. *J. Membr. Sci.* **467**, 67-72 (2014).
 14. A. Car, C. Stropnik, K.-V. Peinemann, Hybrid membrane materials with different metal-organic frameworks (MOFs) for gas separation. *Desalination* **200**, 424-426 (2006).
 15. H. Huang, Y. Ying, X. Peng, Graphene oxide nanosheet: an emerging star material for novel separation membranes. *J. Mater. Chem. A* **2**, 13772-13782 (2014).
 16. R. R. Nair, H. A. Wu, P. N. Jayaram, I. V. Grigorieva, A. K. Geim, Unimpeded Permeation of Water Through Helium-Leak-Tight Graphene-Based Membranes. *Science* **335**, 442-444 (2012).

17. H. W. Kim *et al.*, Selective Gas Transport Through Few-Layered Graphene and Graphene Oxide Membranes. *Science* **342**, 91-95 (2013).
18. H. Li *et al.*, Ultrathin, Molecular-Sieving Graphene Oxide Membranes for Selective Hydrogen Separation. *Science* **342**, 95-98 (2013).
19. Y.-C. Lin, D. O. Dumcenco, Y.-S. Huang, K. Suenaga, Atomic mechanism of the semiconducting-to-metallic phase transition in single-layered MoS₂. *Nat Nano* **9**, 391-396 (2014).
20. L. F. Mattheiss, Band Structures of Transition-Metal-Dichalcogenide Layer Compounds. *Phys. Rev. B* **8**, 3719-3740 (1973).
21. F. Wypych, R. Schollhorn, 1T-MoS₂, a new metallic modification of molybdenum disulfide. *J. Chem. Soc., Chem. Commun.*, 1386-1388 (1992).
22. R. Bissessur, M. G. Kanatzidis, J. L. Schindler, C. R. Kannewurf, Encapsulation of polymers into MoS₂ and metal to insulator transition in metastable MoS₂. *J. Chem. Soc., Chem. Commun.*, 1582-1585 (1993).
23. M. A. Py, R. R. Haering, Structural destabilization induced by lithium intercalation in MoS₂ and related compounds. *Can. J. Phys.* **61**, 76-84 (1983).
24. A. N. Enyashin *et al.*, New Route for Stabilization of 1T-WS₂ and MoS₂ Phases. *J. Phys. Chem. C* **115**, 24586-24591 (2011).
25. K. J. Berean *et al.*, 2D MoS₂ PDMS Nanocomposites for NO₂ Separation. *Small* **11**, 5035-5040 (2015).
26. D. Wang, Z. Wang, L. Wang, L. Hu, J. Jin, Ultrathin membranes of single-layered MoS₂ nanosheets for high-permeance hydrogen separation. *Nanoscale* **7**, 17649-17652 (2015).

27. A. Ambrosi, Z. Sofer, M. Pumera, Lithium Intercalation Compound Dramatically Influences the Electrochemical Properties of Exfoliated MoS₂. *Small* **11**, 605-612 (2015).
28. H. Czichos, T. Saito, L. R. Smith, *Springer handbook of materials measurement methods*. (Springer Science & Business Media, 2006).
29. W. Zhou, Electron microscopy: A phase transition glides into view. *Nat Nano* **9**, 333-334 (2014).
30. M. Acerce, D. Voiry, M. Chhowalla, Metallic 1T phase MoS₂ nanosheets as supercapacitor electrode materials. *Nat. Nanotechnol.* **10**, 313-318 (2015).
31. G. Eda *et al.*, Photoluminescence from Chemically Exfoliated MoS₂. *Nano Lett.* **11**, 5111-5116 (2011).
32. K. F. Mak, C. Lee, J. Hone, J. Shan, T. F. Heinz, Atomically Thin MoS₂: A New Direct-Gap Semiconductor. *Phys. Rev. Lett.* **105**, 136805 (2010).
33. K. C. Knirsch *et al.*, Basal-Plane Functionalization of Chemically Exfoliated Molybdenum Disulfide by Diazonium Salts. *ACS Nano* **9**, 6018-6030 (2015).
34. Q. H. Wang, K. Kalantar-Zadeh, A. Kis, J. N. Coleman, M. S. Strano, Electronics and optoelectronics of two-dimensional transition metal dichalcogenides. *Nat. Nanotechnol.* **7**, 699-712 (2012).
35. J. C. S. Wu, D. F. Flowers, P. K. T. Liu, High-temperature separation of binary gas mixtures using microporous ceramic membranes. *J. Membr. Sci.* **77**, 85-98 (1993).
36. R. D. Present, A. J. Debethune, Separation of a gas mixture flowing through a long tube at low pressure. *Phys. Rev.* **75**, 1050 (1949).
37. M. Acerce, D. Voiry, M. Chhowalla, Metallic 1T phase MoS₂ nanosheets as supercapacitor electrode materials. *Nat. Nanotechnol.* **10**, 313-318 (2015).

-
38. M. A. Priolo, D. Gamboa, K. M. Holder, J. C. Grunlan, Super Gas Barrier of Transparent Polymer–Clay Multilayer Ultrathin Films. *Nano Lett.* **10**, 4970-4974 (2010).
 39. A. Molina-Sánchez, L. Wirtz, Phonons in single-layer and few-layer MoS₂ and WS₂. *Phys. Rev. B.* **84**, 155413 (2011).
 40. D. Yang, S. J. Sandoval, W. M. R. Divigalpitiya, J. C. Irwin, R. F. Frindt, Structure of single-molecular-layer MoS₂. *Phys. Rev. B: Condens. Matter* **43**, 12053-12056 (1991).
 41. L. M. Robeson, The upper bound revisited. *J. Membr. Sci.* **320**, 390-400 (2008).
 42. Y. Li, F. Liang, H. Bux, W. Yang, J. Caro, Zeolitic imidazolate framework ZIF-7 based molecular sieve membrane for hydrogen separation. *J. Membr. Sci.* **354**, 48-54 (2010).
 43. D. Shekhawat, D. R. Luebke, H. W. Pennline, "A Review of Carbon Dioxide Selective Membranes: A Topical Report," (*Report DOE/NETL 2003/1200, U.S. Department of Energy, National Energy Technology Laboratory, Pittsburgh, PA, 2003*) (2003).

Conclusions and future outlook

In today's material science layered materials reserve a huge chunk of interest for their myriad of applications in various fields. This thesis focuses on different applications of layered materials such as clay based hybrid materials for solubilization of graphene and fullerene and biomolecule uptake. We also explored the mechanism of gas permeation through layered materials membranes like GO and MOS_2

The impact the layered materials create in daily life are enormous and proper research is obviously needed to explore their applicability. For example, in chapters 1.2 and 1.3 we have explored clay based materials for dispersion of water insoluble components. This technique can be easily extended for biomedical applications, using clay based hybrid materials as host for drug delivery

In chapter 2.2 and 2.3 we have explored the mechanism of gas permeation through GO and MOS_2 membranes and achieved high H_2/CO_2 separation performance. Permeation properties of different layered and hybrid materials can be studied in this method to optimize performance.

List of publications

1. **A. Achari**, K. K. R. Datta, M. De, V. P. Dravid and M. Eswaramoorthy, Amphiphilic aminoclay-RGO hybrids: A simple strategy to disperse high concentration of RGO in water, *Nanoscale*, 5, 5316 - 5320 (2013)
2. K. K. R. Datta, **A. Achari** and M. Eswaramoorthy, Aminoclay: A Functional Layered Material with Multifaceted Applications (Review), *J. Mater. Chem. A*, 1, 6707 - 6718 (2013)
3. A. Jain, **A. Achari**, N. Mothi, M. Eswaramoorthy and S. J. George, Shining the Light on Clay-Chromophore Hybrids: Layered Templates for Accelerated Ring Closure Photo-Oxidation. *Chem. Sci.*, 6, 6334-6340 (2015).
4. A. Jain, **A. Achari**, M. Eswaramoorthy and S. J. George Light Induced in-situ post-modification of clay-chromophore hybrids for multiple white light emissions, *J. Mater. Chem. C*, 4, 2748-2751 (2016)
5. **A. Achari**, Sahana. S and M. Eswaramoorthy, High performance MoS₂ membranes: Effect of thermally driven phase transition on CO₂ separation efficiency **Energy Environ. Sci.** (2016)
6. **A. Achari**, M. Eswaramoorthy, Highly water dispersible clay- Fullerene hybrids: Surface enhanced quenching of Cyanine dyes. (Under Preparation)
7. **A. Achari**, M. Eswaramoorthy, Casting molecular channels through domain formation: High performance graphene oxide membranes for H₂/CO₂ separation. (Submitted)

